The ultrastructural features of the surface of macrophages and the mechanics of phagocytosis

Jaime Obguia Cañedo

A thesis submitted in partial fulfilment of the requirements for the degree of
Doctor of Philosophy

Department of Infection, Immunity & Cardiovascular Disease

School of Medicine, Dentistry & Health

The University of Sheffield

February 2022

Abstract

Macrophages are highly dynamic cells, both structurally and functionally, that perform many important roles in the body. They provide immunity by surveying tissues for the presence of infectious particles and physically engulfing them in a process called phagocytosis. They also restore damaged tissues by secreting molecular factors which stimulate growth and repair. In spite of their various roles, they possess conserved features which are manifested in generating different types of membrane protrusion. Amongst the well-described types are lamellipodia, filopodia and dorsal ruffles. In this thesis, I will present my investigation on a novel type of membrane protrusion amongst macrophages and phagocytes I referred to as membrane ridge. Due to its nanoscopic size, electron and superresolution microscopy techniques are required to interrogate its actin-rich architecture. These revealed its highly consistent thickness property which is strikingly conserved across different types of macrophages and phagocytic cells I examined. Moreover, by tracking its development, I found its thickness to be highly maintained from its inception up to its recovery back to the membrane surface, indicating a tightly regulated process in generating these structures. By subjecting macrophages to different chemical, mechanical and genetic manipulations, I found an inherent sensitivity of membrane ridges to these factors, suggesting their possible roles in diverse activities of macrophages such as inflammatory response, osmoregulation and homeostasis. Finally, I explored the phagocytosis of spherical particles by macrophages and found that target size, target surface property and possession of membrane ridges largely influence phagocytic uptake. Increase in size of a spherical target and loss of membrane ridges impair phagocytosis, whilst target opsonisation with antibodies enhances phagocytic uptake. Taken together, I described the nanoscopic architecture of a highly conserved membrane protrusion amongst phagocytic cells I referred to as membrane ridge and examined the effect of its loss along with size and surface properties of a spherical target in phagocytic process.

Acknowledgements

To my family back home who has been the pillar of my strength and my best supporters, thank you. To my mum who was my inspiration in everything I do, I know you would have been proud to see me finish, thank you and I love you always.

5

Table of Contents

8

9

List of abbreviations

ANOVA: analysis of variance

APC: antigen-presenting cells

Arp2/3: actin-related protein 2/3

BAL: bronchoalveolar lavage

BATF3: basic leucine zipper transcriptional factor ATF-like 3

BMDM: bone-marrow derived macrophage

BSA: bovine serum albumin

CCL: cc ckemokine ligand

CRISPR: clustered regularly interspaced short palindromic repeats

CD: cluster of differentiation

cDC: classical/conventional dendritic cell

Cdc42: cell division control protein 42

CFU: colony forming unit

Cn: *Cryptococcus neoformans*

CO_2: carbon dioxide

CR: complement receptor

DAPI: 4',6-diamidino-2-phenylindole

DC: dendritic cell

DC-SIGN: dendritic cell-specific intercellular adhesion molecule-3-grabbing non-integrin

dH_2O: distilled water

DIC: differential interference contrast

ECP: eosinophil cationic protein

EDTA: ethylenediamine tetraacetic acid

EDN: eosinophil-derived neurotoxin

Ena/VASP: enabled/vasodilator-stimulated phosphoprotein

EPO: eosinophil peroxidase

EtOH: ethanol

FBS: foetal bovine serum

FcγR: Fcγ receptor

FITC: fluorescein isothiocyanate

GA: glutaraldehyde

GAP: GTPase-activating protein

GEF: guanine nucleotide exchange factor

GFP: green fluorescent protein

GM-CSF: granulocyte–macrophage colony-stimulating factor

GTP: guanosine triphosphate

GXM: glucuronoxylomannan

GXMGal: glucuronoxylomannogalactan

HIF-1α: hypoxia-inducible factor 1α

HIM: helium ion microscopy

HMDM: human monocyte-derived macrophage

HMGB1: high-mobility group box 1

HSC: haematopoietic stem cell

IFN-γ: interferon- γ

IDO: indole amine 2,3 dioxygenase

Ig: immunoglobulin

IGF-1: insulin-like growth factor 1

IL: interleukin

ILC: innate lymphoid cell

iNOS: inducible nitric oxide synthase

IRF4: interferon-regulatory factor 4

ITAM: immunoreceptor tyrosine-based activation motif

LPS: lipopolysaccharide

KC: Kupffer cell

kV: kilovolt

LAT: linker for activation of T cells

LLS: lattice light sheet

LUT: look-up table

MΦ: macrophage

MAPK: mitogen-activated protein kinase

MARCO: macrophage receptor with collagenous domain

M-CSF: macrophage colony-stimulating factor

MDSC: myeloid-derived suppressor cell

MHC: major histocompatibility complex

Mincle: Macrophage inducible Ca^{2+}-dependent lectin receptor

mN/m: millinewton per meter

MOI: multiplicity of infection

MPS: mononuclear phagocytic system

MS: multiple sclerosis

NA: numerical aperture

NaCl: sodium chloride

NET: neutrophil extracellular trap

NH_4Cl: ammonium chloride

NK: natural killer

nm: nanometre

NOD: nucleotide-binding oligomerization domain

N-WASP: Neuronal Wiskott-Aldrich Syndrome Protein

PA: particle anlaysis

PAH: pulmonary arterial hypertension

PAK: p21-activated *kinase*

PAMP: pathogen associated molecular pattern

PBMC: peripheral blood mononuclear cell

PFA: paraformaldehyde

PBS: phosphate buffer saline

pDC: plasmacytoid dendritic cell

PI: post infection

PI3K: phosphatidylinositol-3-kinase

PIP_2: phosphatidylinositol 4,5-bisphosphate

PIP_3: phosphatidylinositol 3,4,5-trisphosphate

PMA: phorbol 12-Myristate 13-Acetate

PRR: pathogen recognition receptor

PS: phosphatidylserine

RD: *ridge detection*

RBC: red blood cell

RNA: ribonucleic acid

ROS: reactive oxygen species

RT: room temperature

RVD: regulatory volume decrease

SD: standard deviation

SEM: scanning electrom microscope

SFK: Src-family kinase

SLP: SH2 domain-containing leukocyte protein

SR: scavenger receptor

STAT3: signal transducer and activator transcription 3

Syk: spleen tyrosine kinase

TCR: T cell receptor

TEM: transmission electron microscope

TGF-β: transforming growth factor-β

Th2: T helper 2

TIM: T cell immunoglobulin mucin domain

TLR: toll-like receptor

TNF: tumor necrosis factor

trib: tribbles homolog

TRITC: tetramethyl rhodamine iso-thiocyanate

μm: micrometre

WASH: Wiskott Aldrich syndrome protein and Scar Homologue

WASP: Wiskott-Aldrich syndrome protein

WAVE: WASP-family verprolin-homologous protein

YNB: yeast nitrogen base

YPD: yeast extract peptone dextros

15

List of figures

16

19

List of tables

20

CHAPTER 1

Introduction

Infection is a complex process that shows a dynamic interplay between a host organism and a pathogen. The host, usually being a larger organism, is exploited by the pathogen for its survival and persistence, leading to an 'arms race' relationship that is characterised by the pressure for the host to evolve resistance against the invading pathogens whilst pathogens developing countermeasures that enable continual infection. This relationship throughout the course of evolution had shaped the landscape of immunity allowing genetic and structural diversifications (reviewed by Sironi et al., 2015) which encompass our understanding of the components and events of infectious diseases.

The responses of a host against foreign threats can be considered as basic physiological reactions to maintain cellular integrity and homeostasis and, more importantly, to ensure host survival. Defence mechanisms against pathogens appeared as early as in prokaryotic cells (i.e. bacteria and archaea) wherein a mechanism based on Cas enzyme and clustered regularly interspaced short palindromic repeats (CRISPR) confers resistance against bacteriophages (Barrangou et al., 2007). This is also regarded as a 'nucleic acid-based immunity' by which integration of new phage-derived genetic elements, called spacers, to the bacterial genome enables identification of phages and their subsequent destruction by Cas enzymatic system (Barrangou et al., 2007). Meanwhile, eukaryotes have developed more sophisticated systems to counter threats from infectious agents. Unicellular amoebae established an ability to internalise foreign materials in a process called phagocytosis (described in detail in section 1.3), which does not only provide a means of controlling microbial threats but also of acquiring nutrients (Halanych, 2004). This mechanism is highly conserved throughout evolutionary history and became the basis of innate immunity in multicellular organisms (Buchmann, 2014).

The immune system requires a mechanism that can efficiently detect and destroy foreign particles. This is achieved by specific interactions between pathogen recognition receptors (PRRs), usually on the membrane surface of host or immune cell, and pathogen associated molecular patterns (PAMPs) on the pathogen's surface. The repertoire of PRRs is very extensive which includes different classes of scavenger receptor (SR), toll-like receptor (TLR) and nucleotide-binding oligomerization domain (NOD)-like receptor that are able to bind and therefore recognise a wide range of pathogens (Mogensen, 2009). On the other hand, amongst well-described PAMPs are lipopolysaccharide (LPS), peptidoglycans, double-stranded RNA and flagellins which are invariant amongst different pathogen classes (Janeway,

1989) and enable the discrimination of viruses, bacteria, fungi, protozoans and helminths by the host (Buchmann, 2014). Following PAMP recognition, PRRs initiate antimicrobial and pro-inflammatory responses by a cascade of intracellular signalling pathways (reviewed in detail by Mogensen, 2009) including adaptor molecules, kinases and transcription factors. These ultimately lead to gene activation and synthesis of a broad range of molecules including cytokines, chemokines, cell adhesion molecules and immunoreceptors, which orchestrate an early response to infection and serve as an important link to the adaptive immune response (Akira et al., 2006).

Whilst innate immunity is usually able to eliminate pathogens efficiently through phagocytosis, initial clearance can fail due to a high number or virulence factors from these invading pathogens (Netea et al., 2019). In these instances, the development of another arm of the immune system known as adaptive immunity is a critical evolutionary step to reinforce host protection against infectious agents (Flajnik and Du Pasquier, 2004). Antigen-presenting cells such as granulocytes (Kambayashi and Laufer, 2014), macrophages (Muntjewerff et al., 2020), dendritic cells (Hilligan and Ronchese, 2020) are able to activate lymphocytes, which leads to specific recognition and elimination of pathogens through antibody secretion and enhanced killing through phagocytosis by innate immune cells (Alberts et al., 2015). The establishment of adaptive immunity requires one to two weeks (Netea et al., 2019) and is crucial to establish an immunological memory that responds more efficiently to reinfection (Farber et al., 2016).

In the following sections, I will further describe the current knowledge on the ontogenetic and functional properties of different classes of immune cells. I will provide more details on innate immune cells especially macrophages as they are the central theme of this dissertation. I will then discuss critical aspects of macrophage biology including phagocytosis, their fundamental structural features called membrane protrusions and their role in Cryptococcal infection. Lastly, I will present the general and specific aims of my thesis.

1.1 Innate Immune System

As the first line of host defence against infection, the innate immune system plays crucial role in the early recognition and subsequent pro-inflammatory response to infectious agents (Medzhitov and Janeway, 2000). Broadly defined, the innate immune system includes all aspects of the host's immune defence mechanism such as epithelial cell layers, secreted mucus layers, soluble proteins, bioactive small molecules (complement proteins, defensins, ficolins, cytokines, chemokines etc.) and innate immune cells which are all genetically encoded in the host's mature form (Chaplin, 2010). For simplicity of discussion, I will focus on the cellular component of the innate immune system (Figure 1.1).
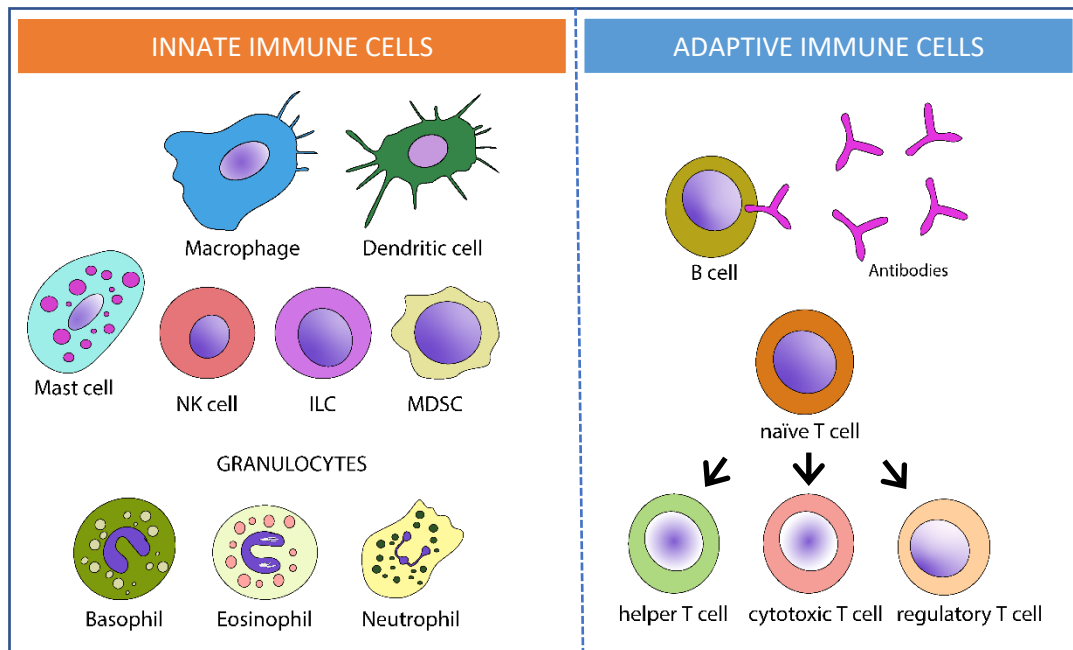
Figure 1.1 | The different types of immune cells in vertebrates

Innate immune cells comprise a broad and expanding range of myeloid and lymphoid cells originating from hematopoietic stem cells (Gasteiger et al., 2017). The well-known innate immune cells are neutrophils, dendritic cells, natural killer cells, mast cells, basophils, eosinophils and macrophages; though studies on the importance of myeloid-derived suppressor cells (MDSCs) and innate lymphoid cells (ILCs) in different aspects of innate immunity are keeping pace (Talmadge and Gabrilovich, 2013; Klose and Artis, 2020). These cells are considered not to possess any immunological memory and rely on invariant receptors to recognise common features of the pathogen (Janeway et al., 2001). Although this view is recently challenged with epigenetic and metabolic reprogramming observed amongst innate immune cells during inflammatory encounters leading to the concept of trained immunity (Netea et al., 2020).

1.1.1 Neutrophils

Neutrophils are the most common type of granulocyte, a morphological classification amongst leucocytes (white blood cells) based on staining properties that reflect their secretory roles (Alberts et al., 2015). Tracing *in vivo* through healthy volunteers, the average lifespan of neutrophils was found to be 5.4 days (Pillay et al., 2010). Classically, neutrophils are believed to originate from hematopoietic stem cells through common myeloid progenitors, granulo-monocytic progenitors (Cowland and Borregaard, 2016) and the recently identified unipotent neutrophil progenitors in the bone marrow (Zhu et al., 2018) although the actual path of generating neutrophils is suspected to be more molecularly complex (Paul et al., 2015).

Differentiation into neutrophils is characterised by condensation and multilobular appearance of the nucleus and the emergence of cell-type specific intracellular granules (Bainton et al., 1971). Mature neutrophils contain three types of granules- primary, secondary and tertiary granules, as well as secretory vesicles of endocytic origin (Cowland and Borregaard, 2016). These compartments are packed with antimicrobial factors which enhance killing when liberated into phagosome or extracellular space (Cowland and Borregaard, 2016).

As a critical component of innate immunity, neutrophils immediately respond to microbial threats by phagocytosing them. Enzymatic components of their granules enable them to migrate to sites of infection and also efficiently degrade bacterial and fungal proteins (Hager et al., 2010). Another important antimicrobial property of neutrophils is their ability to extrude their DNA components to form neutrophil extracellular traps (NETs) which allow them to capture and destroy pathogens using chromatin threads with microbicidal proteins from their granules (Brinkmann et al., 2004).

1.1.2 Dendritic cells

Phagocytosis of microbes by immature dendritic cells is believed to be the initial step to stimulate an adaptive immune response (Janeway et al., 2001). These phagocytic cells reside in skin, spleen, liver, lung, intestine and lymphoid tissues (Guilliams et al., 2014). They are well-known for their role in presenting antigens to T cells, a kind of lymphocyte (discussed in section 1.2), which leads to activation of these cells characterised by their proliferation and differentiation. Due to this, they are considered as key immune cells at the interface of innate and adaptive immune response (Worbs et al., 2017).

Dendritic cells (DCs) are a part of the mononuclear phagocyte system and can be classified according to distinct sets of transcription factors regulating differentiation of the common precursor DCs (Guilliams et al., 2014). The three major DC classes proposed by Guilliams (2014) and colleagues are: *cDC1* (classical or conventional type 1 DC), *cDC2* and *pDC* (plasmacytoid DC). Basic leucine zipper transcriptional factor ATF-like 3 (BATF3)-deficient mouse were associated with abnormal cDC1 development (Hildner et al., 2008), whereas interferon-regulatory factor 4 (IRF4) was found to strongly regulate cDC2 differentiation (Tamura et al., 2005). Meanwhile, pDC development was found to be controlled by the transcription factor E2-2 which directly counteracts cDC1- and cDC2-regulatory factors (Ghosh et al., 2010; Cisse et al., 2008).

DCs possess stellate morphology and show the canonical antigen-presentation capability to activate T cells belong to cDC group whilst interferon-producing cells that are morphologically similar to plasma cells are exhibited by pDCs. The physical interaction between DCs and T cells is mediated by major histocompatibility complex (MHC) molecules

which are cell surface gylcoproteins that bind protein fragments either synthesised within the host cell (class 1 MHC) or from microbial residues that have been proteolytically processed (class II MHC) (Chaplin, 2010).

1.1.3 Natural killer cells

Natural killer (NK) cells are subsets of innate lymphocytes that possess anti-tumour and anti-viral properties (Abel et al., 2018). They do not require previous antigen exposure to mediate their anti-tumour effects (Kiessling et al., 1975), and they are recruited early at the site of inflammation to destroy virus-infected cells by inducing them to undergo apoptotic cell death (Alberts et al., 2015).

NK cells were initially thought to develop exclusively in the bone marrow; however, recent evidence in humans and mice suggest that they can also develop and mature in lymphoid tissues such as tonsils, spleens and lymph nodes (Scoville et al., 2017). Their development is regulated by critical transcription factors T-bet and eomesodermin (Simonetta et al., 2016). They are distinguished by their unique functions and expressions of surface antigen. For instance, NK cells lack the clonotypic T cell receptor (TCR) of T and NKT cells and its associated signal-transducing adaptor, CD3ε (Abel et al., 2018).

1.1.4 Mast cells

Mast cells are cells of the innate immunity that respond to signals from both innate and adaptive immunity through modulation of the release of inflammatory mediators such as proteoglycans, serine proteases, histamines etc. (Stone et al., 2010). The best-known activation mechanism is by immunoglobulin E (IgE)-FcεRI interaction which is also implicated in various pathological conditions such as allergy, anaphylaxis and asthma (Draberova et al., 2021). Mast cells are capable of phagocytosing bacteria (Malaviya et al., 1994), however this is believed to be a negligible role in providing immunity (Draberova et al., 2021). They are better known in controlling bacterial infection by rapid degranulation associated with release of pro-inflammatory mediators, cytokines and chemokines, which can then cause influx of other immune cells, mainly neutrophils, to the site of infection (Draberova et al., 2021). Once recruited, neutrophils not only phagocytose and destroy bacteria, but also become activated and secrete inflammatory mediators, leading to amplification of the anti-bacterial inflammatory response (Gekara and Weiss, 2008).

Mast cells are located primarily in blood vessels and epithelial surfaces where they act as potent immune sensors of the tissue microenvironment (Drabevora et al., 2021). They are not only involved in antimicrobial response (Malaviya et al., 1996) but are also implicated in homeostatic regulations such as during allergic response and autoimmune diseases (reviewed extensively by Ryan et al., 2007).

1.1.5 Basophils

Closely related to mast cells but with distinct lineage, morphological and functional properties are basophils. They are well known for their role in secreting histamine, as previously stated, a type of mediator that can induce both pro-inflammatory (Falus, 1994; Wu and Baldwin, 1992) and anti-inflammatory (Falus and Meretey, 1992) effects. In general, its inflammatory effects are mediated by histamine H_1 receptors (Sirois et al., 2000), whereas various immunoregulatory effects of histamine, such as induction of suppressor cells (Rocklin and Greineder, 1977) and inhibition of lymphocyte proliferation (Ogden and Hill, 1980) are mediated by H_2 receptors. Furthermore, histamine appears to modulate the release of various cytokines such as interleukin-1 (IL-1) (Dohlsten et al., 1988), IL-5 (Krouwels et al., 1998), IL-6 (Delneste et al., 1994), IL-8 (Jeannin et al., 1994), interferon- γ (IFN-γ) (Lagier et al., 1997), and tumor necrosis factor (TNF) (Vannier et al., 1991) reiterating its critical role in immunomodulation.

Like mast cells, basophils highly express FcεRI on their surfaces which upon activation with IgE leads to release of preformed mediators such as histamine and platelet-activating factor from the secretory granule (Galli et al., 2000). This is then followed by generation of newly synthesised mediators including substances from arachidonic acid metabolism and different classes of cytokines (Varricchi et al., 2018).

1.1.6 Eosinophils

Eosinophils are granulocytes named after their striking capacity to be stained by an aniline dye called eosin (Kay, 2015). They develop in the bone marrow and are released into the circulation following stimulation by IL-5, IL-3 and granulocyte–macrophage colony-stimulating factor (GM-CSF) although a large number of mature eosinophils remain in the bone marrow (Stone et al., 2010). They play important roles in killing parasites, though this is quite controversial (Rosenberg et al., 2012), and modulating allergic inflammatory responses (Alberts et al., 2015).

IL-5 has a pivotal role in all aspects of eosinophil development, activation and survival (Rosenberg et al., 2012). Eosinophils pursue maturation and proliferation in response to IL-5, which leads to production of eosinophil cationic protein (ECP), major basic protein, eosinophil peroxidase (EPO), and eosinophil-derived neurotoxin (EDN) stored in cytoplasmic granules (Roufosse, 2018). Amongst important contributors of IL-5 are T helper 2 (Th2) cells and although eosinophil development and maturation are influenced by these lymphocytes, eosinophils can in turn modulate the functions of T and B cells by production of IL-6 cytokine (Chu et al., 2011) and chemokines, CCL17 and CCL22 (Jacobsen et al., 2008), which activate

and recruit these cells during inflammatory response, and also by antigen presentation through MHC class II (Wang et al., 2007).

1.1.7 Macrophages

Together with monocytes and DCs, macrophages (MΦ) constitute a subset of innate immune cells known as mononuclear phagocytic system (MPS) (Hume, 2008). They are amongst the first responders to infectious threats and thus are critical in rapid clearance of pathogens. Moreover, they are also known for their roles in development and tissue homeostasis (Pollard, 2009) which show their diverse functional properties.

1.1.7.1 Origin

Ontogenetically, MΦ in vertebrates are derived from at least three distinct structures: yolk sac, foetal liver and bone marrow (Theret et al., 2019). They emerge at different stages of development and can reside at different tissues and organs; hence it is not surprising that they have achieved regulatory functions as well (reviewed by Epelman et al., 2014). During primitive haematopoiesis (blood cell generation) from embryonic day (E)6.5 to E11 in mice, tissue resident MΦ such as microglia and Langerhans cells appear in their respective tissues (Theret et al., 2019). Later in development (E8.5 to E12), immature haematopoietic stem cells (HSCs) are generated which give rise to Kupffer cells and alveolar MΦ (Theret et al., 2019), the resident MΦ of liver and lung, respectively. These immature HSCs would eventually colonise the foetal liver. From E10 to E19, the foetal liver starts generating all immune cells and tissue-resident MΦ within the cardiac system, skeletal system, demis and gut (Theret et al., 2019). Soon after birth (beyond E19), foetal liver HSCs migrate to the bone marrow and give rise to mature HSCs that produce all blood cell components by definitive haematopoiesis throughout adulthood(Theret et al., 2019).

1.1.7.2 Activation

The role of MΦ during inflammation is commonly categorised into two phenotypes: M1- pro-inflammatory/classically activated and M2- anti-inflammatory/alternatively activated. M1 MΦ are highly efficient in responding to infection as they can secrete antimicrobial compounds such as reactive oxygen and nitrogen species. These cells have also upregulated pro-inflammatory cytokine profile which include IFNγ, TNF-α, IL-1 and IL-6 (Mantovani et al., 2004). On the other hand, MΦ with M2 phenotype promote wound healing and secrete growth factors such as transforming growth factor-β (TGF-β) and insulin-like growth factor 1 (IGF-1) which are essential for tissue repair (Mantovani et al., 2004).

1.1.7.3 Tissue-resident macrophages

Specialised MΦ called tissue-resident MΦ are strategically located throughout the body to perform an important immune surveillance function. They constantly survey their immediate surroundings for signs of tissue damage or invading organisms and are poised to

stimulate lymphocytes and other immune cells to respond to any threats and maintain tissue homeostasis (Murray and Wynn, 2011). I will only discuss two types of tissue resident MΦ in here, alveolar and Kupffer cells, which are further investigated in the succeeding chapter (3), for a comprehensive review of other tissue-resident MΦ such as osteoclasts, microglia etc., the reader is referred to Davies et al., (2013).

1.1.7.3.1 Alveolar macrophages

Microbes and other particles entering the lung usually encounter its resident MΦ first called alveolar MΦ. With their inherent plasticity, alveolar MΦ can efficiently react to environmental stimuli which leads to rapid and reversible changes in their inflammatory phenotype (Byrne et al., 2015). During inflammation, alveolar MΦ constantly communicate with different cells in their microenvironment such as epithelial cells, microvascular endothelial cells, neutrophils, lymphocytes, tissue progenitor cells and fibroblasts to regulate immune response against invading pathogen and restore lung homeostasis (Divangahi et al., 2015; Misharin et al., 2017). These enable them to efficiently clear out any unnecessary materials in the lung and also regulate its composition such as its surfactant level (Carey and Trapnell, 2010).

Alveolar MΦ are shown to have multiple origins during development. They could arise from circulating adult monocytes or, as previously mentioned, immature HSCs (Guilliams et al., 2013; Theret et al., 2019). It was shown by Guilliams (2013) and colleagues that foetal monocytes contribute significantly to the population of alveolar MΦ whilst monocytes' contribution is very minimal although during respiratory stress and damage monocyte differentiation to alveolar MΦ is highly favoured (Maus et al., 2006).

1.1.7.3.2 Kupffer cells

As resident MΦ of the liver, Kupffer cells (KCs) participate in the detection and clearance of toxins, dead cells and pathogens from the blood. Liver, as an organ that filters blood content, requires a strategy that can suppress unnecessary activation of immune cells from innocuous dietary and microflora antigens (Robinson et al., 2016). This is achieved by immunotolerance where anti-inflammatory cytokines, such as IL-10, play a very significant role (Crispe, 2014; Erhardt et al., 2007).

KCs constitute 80-90% of the tissue-resident MΦ in the body (Ishibashi et al., 2009). They are key players in maintaining liver homeostasis which, as a result, implicates them in various liver diseases such as chronic cholangiopathies (Jemail et al., 2018). Kupffer cells are known to be amongst the major sources of IL-10 in the liver (Erhardt et al., 2007) which downregulates MHC class II expression and receptor-mediated antigen uptake leading to inhibition of T cell activation (Freitas-Lopes et al., 2017). This further highlights their critical

role in maintaining liver homeostasis. Lastly, they are also important in iron homeostasis by phagocytosing damaged or senescent red blood cells and recycling their iron contents (Davies et al, 2013).

1.1.7.4 Macrophage cell lines

Different genetic manipulation techniques enabled immortalisation of MΦ leading to generation of different cell lines. They are indispensable in macrophage studies as they permit easy and rapid experimentation to probe different aspects of macrophage biology. Gene editing could be mediated by adenoviruses, adeno-associated viruses and retroviruses which are common means of manipulating mammalian cells (Zhang et al., 2009). Transfection of MΦ has proven to be a challenge though as they possess many potent degradative enzyme that can disrupt nucleic acid integrity (Zhang et al., 2009).

1.1.7.4.1 J774 macrophage-like cells

J774 cells were first introduced by Hirst (1971) and colleagues from reticulum cell sarcoma of BALB/c mice. Since then, they had become a very important model to understand macrophage structures, functions and dynamics in diseases (Lam et al., 2009; Lemaire et al., 2014; Lee et al., 2019). They possess biophysical properties comparable to naturally-derived macrophages shown by their capacity to produce different types of membrane protrusion and to probe and migrate within their respective environments (Lam et al., 2009). They also possess an arsenal of antimicrobial products (Lemaire et al., 2014) and are able to produce cytokines to modulate their inflammatory activities (Morita et al., 2002). Finally, they are proven to be indispensable in describing the interaction of macrophages with different types of pathogen (Morita et al., 2002; Lee et al., 2019; Johnston and May, 2013; Pline, 2019)

1.1.7.4.2 RAW264.7 macrophage-like cells

Ralph and Nakoinz (1977) first generated RAW264.7 cells by tumour induction in BALB/c mice using Abelson murine leukaemia virus. Like J774 cells, RAW264.7 cells were also remarkably similar to MΦ that are produced naturally in the body with respect to their general structures, metabolism and functions. There are however some differences on cytokine profile, gene expression and pathogenic response between these cell lines. Lindmark (2004) and collaborators showed that J774 cells were more similar to peritoneal MΦ than RAW264.7 cells with respect to gene expression profile despite both cell types having similar origin. Heming (2001) and colleagues showed that following LPS stimulation, RAW264.7 were found to produce 30-fold higher TNF-α mRNA than J774. Moreover, during infection with *Streptococcus iniae* RAW264.7 exhibited higher respiratory burst, the production of reactive oxygen species (ROS) and its subsequent metabolism, than J774 cells (Aamri et al., 2015). Lastly, exposure to the intracellular parasite *Toxoplasma gondii* reduced the levels of the

enzyme inducible nitric oxide synthase (iNOS) in J774 but not in RAW264.7 cells. Nitric oxide is amongst the microbicidal compounds synthesised through iNOS.

1.1.8 Myeloid-derived suppressor cells

Another type of innate immune cells are myeloid-derived suppressor cells (MDSCs). As their name implies, they act to suppress the activation of T cells (discussed in section 1.2) which they carry out through various mechanisms (reviewed by Mantovani, 2010). A plethora of key effectors and signalling pathways involved in suppressive activities of MDSCs are identified which include granulocyte-macrophage colony-stimulating factor (GM-CSF), signal transducer and activator transcription 3 (STAT3), indole amine 2,3 dioxygenase (IDO), calcium-binding S100 proteins, high-mobility group box 1 (HMGB1), hypoxia-inducible factor 1α (HIF-1α), IL-1β, arginase-1, iNOS, IL-6, TNF-α, and ROS production (Nagaraj and Gabrilovich, 2007).

1.1.9 Innate lymphoid cells

Innate lymphoid cells (ILCs) play a more regulatory role during immune response. Their lack of somatically-recombined antigen receptor classified them as innate immune cells (Bedoui et al., 2016). ILCs are commonly grouped into three classes: ILC1, ILC2 and ILC3, by which depending on their type are capable of producing cytokines such as IL-4, IFN-γ and IL-17 to elicit an appropriate immune response to a specific pathogen (Marshall et al., 2018).

1.2 Adaptive Immune System

Compared to the innate immune response, the adaptive immune response is slower and more specific (Alberts et al., 2015). It can take one to two weeks for adaptive immunity to be established (Netea et al., 2019), however it provides a more specific response which is based on antigen-specific receptors expressed on the surfaces of its cellular constituents called lymphocytes. The innate and adaptive immune systems are often described as separate and contrasting arms of the immune system; however, they usually act together in modulating infection response and restoring tissue homeostasis (Chaplin, 2016). For instance, DCs and ILCs of innate immunity can influence the activity of T cell lymphocytes through production of cytokines and antigen presentation by contact between cells (Gasteiger and Rudensky, 2014). The two types of adaptive immune cells are T and B cells which are named based on the organs where they develop, the thymus and the bone marrow, respectively (Chaplin, 2016).

1.2.1 T lymphocytes

T cells originate from the bone marrow through common lymphoid progenitor cells that migrate to the thymus for maturation, selection and export to peripheral locations in the body (Kumar et al., 2018). They populate virtually every organ and tissue in the body including primary and secondary lymphoid tissues, mucosal and barrier sites, exocrine organs,

adipose tissue, and even the brain for immune surveillance and response (Kumar et al., 2018). Their functions range from infection control to developmental regulation which is reflected on their diverse phenotypes and activation states (Davenport et al., 2020; Kumar et al., 2018). As they are not the main subject of this thesis, I will focus on processes that link them to innate immune cells, more specifically the phagocytic cells.

As previously stated, T cells are activated through presentation of foreign antigens from an invading pathogen by antigen-presenting cells (APCs) such as dendritic cell, macrophage and eosinophil. APCs are required since T cells can only recognise fragments of protein antigens that have been produced by partial proteolysis inside a host cell (Alberts et al., 2015). Antigen presentation is initiated by internalising foreign antigens. These are then degraded into peptides that bind to MHC class II. The peptide-MHC II complex is subsequently displayed on the surface of APC for recognition of naïve (i.e. mature but not yet activated) T cells. Upon successful antigen recognition, T cells then proliferate and differentiate into activated effector cells with specialised roles in responding to infection (Alberts et al., 2015; Kumar et al., 2018). APCs are activated through induction with cytokines such as IL-12 (Kalinski et al., 2001). However, certain cytokines, such as IL-10, are also able to inhibit APC maturation to suppress unnecessary immune activation (Mittal and Roche, 2015).

1.2.2 B lymphocytes

B cells are also derived from lymphoid progenitor cells, but unlike T cells, they complete their maturation in the bone marrow. In response to infection, they produce antibodies that can bind with other proteins to directly kill the pathogen or enhance phagocytic uptake by macrophages and other professional phagocytes of the innate immune system (Chaplin, 2010). B cells can recognise antigens on the surface of pathogens even without initial processing, and this subsequently leads to modulation of the corresponding anti-microbial immune response (Alberts et al., 2015).

1.3 Phagocytosis – the cellular basis of innate immunity

Phagocytosis is a conserved feature amongst eukaryotic cells that serves different biological purposes. Free-living, unicellular organisms such as amoebae and ciliates use it for nutrition (Halanych, 2004) whilst it evolved as a critical part of the immune system in multicellular animals for controlling infection, regulating development and restoring homeostasis (Gordon, 2016). Cells of the innate immune system called professional phagocytes are particularly effective in carrying out a phagocytic role (Rabinovitch, 1995). Neutrophils, macrophages, dendritic cells and eosinophils are key phagocytes of the immune system that clear out pathogenic microbes, apoptotic cells, necrotic cells and cellular debris (Gordon, 2016).

Phagocytosis requires different cellular components that enable the phagocyte or host cell to engulf different types of large (i.e. > 0.5 um) particles (Figure 1.2). It relies on receptors found on the plasma membrane or cell membrane, which upon activation can trigger actin polymerisation directly beneath it that enables the host cell to extend its membrane around the target and internalise it (Ostrowski et al., 2016; Perrone et al., 2016). Typically, a phagocytic target (Figure 1.2, red) is detected by a protrusion (discussed in detail in section 1.4) on the cell surface. These protrusions are believed to be essential to increase the cell's surface area and to expose cognate receptors which both increase the likelihood of contacting the target (Jaumouillé & Grinstein, 2011; Ostrowski et al., 2016). Cells unable to form protrusions were observed to have impaired phagocytic capacity (Flannagan et al., 2010). Further receptor activation results to a feature known as phagocytic cup (Figure 1.2D and 1.2E red arrow). This reflects how the actin rich pseudopodia advance around the target, which is also believed to generate a protrusive force for target internalisation that results from the actin growth that pushes the membrane (Herant, 2006; Ostrowski et al 2016). Finally, opposite ends of the phagocytic cup meet and fuse to complete the engulfment process (Figure 1.2F). The end product is a phagocytic vesicle or phagosome which contains the target and delivers it towards the cell's interior for further processing by biochemical degradation (Underhill & Goodridge, 2012).

The events of phagocytic engulfment highlight both the molecular and mechanical nature of this process. It does not only emphasise the importance of specific molecular components in the host cell to internalise a target but also the mechanical requirements, such as extending and bending the host cell membrane, for successful target uptake. Both of these aspects are equally important to fully grasp the complexities of phagocytic uptake and understand its limits with respect to changes in the physical properties of the target or the host cell (further explored in chapters 4 and 5).
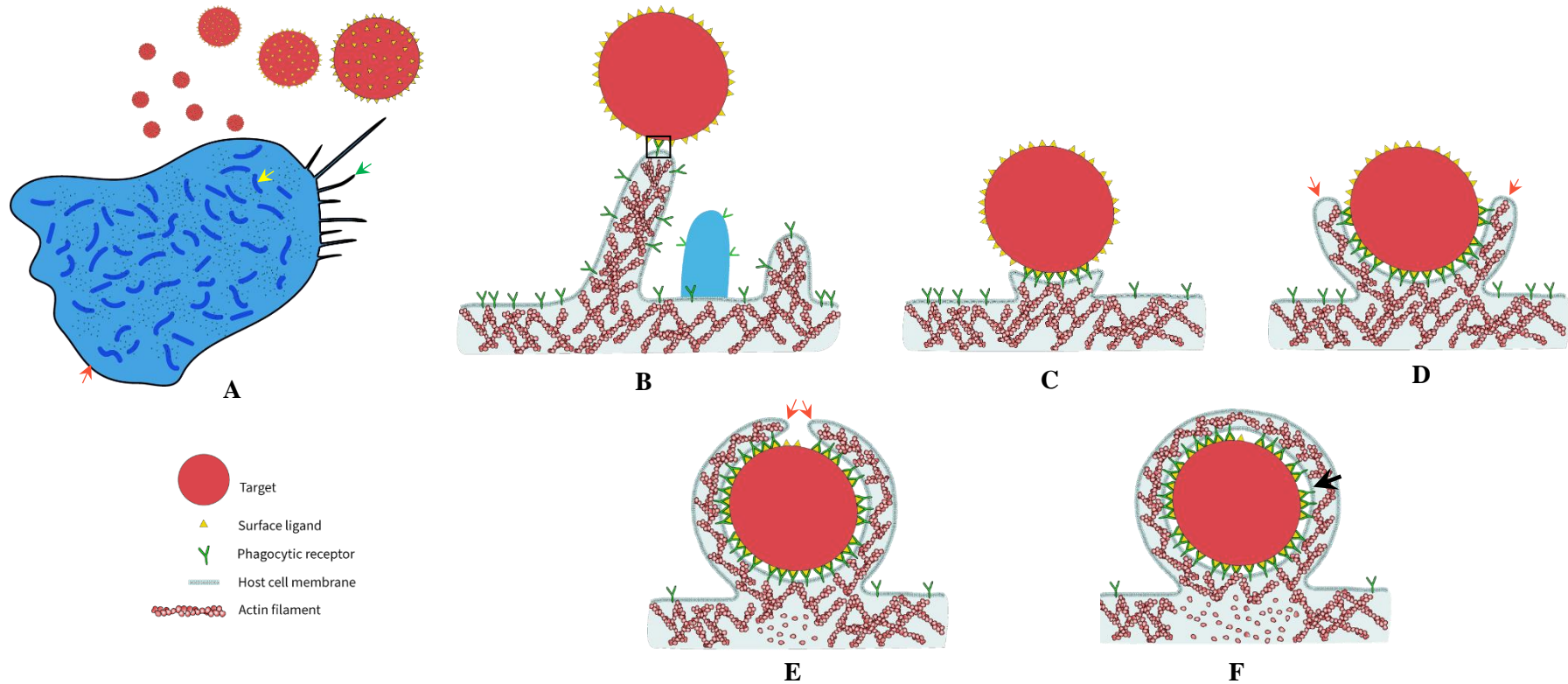
Figure 1.2 | A cartoon depicting phagocytosis of a spherical target (red) by a phagocyte (blue). (A) Showing surface features of the target and the phagocyte, with ligands (yellow) decorating the target surface whilst phagocytic receptors (green puncta) and different membrane protrusions (filopodia – green arrow, ridges – yellow, and lamellipodia – red) on the host cell surface, **(B-F)** Cross-sectional illustrations of phagocytic interaction, *B*: target recognition is mediated by ligand-receptor interaction (box), *C-E:* further receptor recruitment and binding with ligands result to a phagocytic cup (red arrow) surrounding the target, *F:* opposite ends of the phagocytic cup meet and fuse to form the phagosome (arrow).

1.3.1 The host cell membrane during phagocytosis

The host cell membrane, which acts as a structural interface between the phagocyte and its target, reveals many important aspects of the early phagocytic events. As previously mentioned, molecular receptors found on the cell surface initiate contact with the target leading to cascades of intracellular signals that promote actin growth that subsequently results in target engulfment. Therefore, it is not surprising that the type of receptor, its mobility and the signalling pathways it is involved in are important factors that determine the phagocytic capacity of a host cell (Jaumouillé & Grinstein, 2011; Underhill & Goodridge, 2012).

1.3.1.1 Phagocytic receptors and their membrane mobilities

A phagocytic receptor is usually classified whether it can bind directly or indirectly to its target. Receptors that require antibody or complement protein to recognise the target are called opsonic, whilst those that can directly bind to the target's surface ligands are called non-opsonic (Gordon, 2016). Some of the known phagocytic receptors and the ligand/s they recognise are summarised in table 1.1.

The binding of a particle to the surface of a phagocytic cell does not always result to engulfment (Swanson, 2008). A sufficient number of receptors and its continuous engagement with ligands are critical for target internalisation (Ostrowski et al., 2016). However, receptors usually have heterogenous distributions in the plasma membrane (Jaumouillé & Grinstein, 2011) which therefore require recruitment to the site of target contact. In addition, the complex feature of the cell membrane possessing physical obstacles (Figure 1.3) is another challenge for receptor mobility that needs to be overcome to interact with ligands and signal cytoskeletal remodelling and actin growth.

The cell membrane is composed of a heterogenous population of large molecules including glycoproteins, glycolipids and polysaccharides, collectively called the glycocalyx. This can form a barrier that can impede free diffusion of receptors along the membrane (Alberts et al., 2015). Recent evidences using single particle tracking technique suggest that passive diffusion or Brownian motion may not be able to describe the mobility of receptors observed *in vitro* (Jaumouillé & Grinstein, 2011). Jaumouille and Grinstein (2011) reported that FcγRIIa forms clusters in the membrane with submicron dimensions suggesting confinement of immunoreceptors. This observation conforms with the physical features of the cell membrane previously described by Kusumi (2005) and colleagues, exploiting advances in imaging and image analysis with nanometre resolution. In this model (Figure 1.3), the cell membrane is believed to be compartmentalised with the underlying actin scaffold acting as a "fence" where proteins spanning the membrane can attach to. These stationary proteins serve as "pickets" limiting the mobility of molecules, more importantly, the receptors enclosed by each compartment (Kusumi et al., 2005). This possibly explains the observed restricted

diffusion of membrane receptors FcγRIIa (Jaumouillé & Grinstein, 2011) and Dectin-1 (Ostrowski et al., 2016) which are otherwise unattached to the cytoskeleton and hence could diffuse freely.

Phagocytic receptor (Alternative name/s)	Ligand/s
α5β1	Fibronectin, Vitronectin (Blystone et al., 1994)
CD44 (HCAM)	Hyaluronic acid (Vachon et al., 2006)
CR1 (CD45)	Mannan-binding lectin, C1q, C4b, C3b (Ghiran et al, 2000)
CR3 (αMβ2, CD11b/CD18, Mac1)	iC3b (Ross et al., 1992)
CR4 (αvβ2, CD11c/CD18, gp150/95)	iC3b (Ross et al., 1992)
FcαRI (CD89)	IgA1, IgA2 (van Spriel., 1999)
FcεRI	IgE (Daeron et al., 1994)
FcγRI (CD64)	IgG1, IgG3, IgG4 (Anderson et al., 1990)
FcγRIIa (CD32a)	IgG3, IgG1, IgG2 (Anderson et al., 1990)
FcγRIIIa (CD16a)	IgG (Anderson et al., 1990)
αvβ5	Apoptotic cells (Albert et al., 2000)
BAI-1	Phosphatidylserine (Park et al., 2007)
CD14	Lipopolysaccharide-binding protein (Schiff et al., 1997)
CD36	*Plasmodium falciparum*-infected erythrocytes, Oxidised phosphatidylserine (Greenberg et al., 2006)
DC-SIGN	Fucosylated glycans, mannose-rich glycans (van Liempt et al., 2006)
Dectin-1 (CLEC7A)	β 1,3-glucan (Herre et al., 2004)
Dectin-2 (CLEC6A)	α-mannan (Zhu et al., 2013)
Dectin-3 (CLEC4D)	α-mannan (Zhu et al., 2013)
Mannose receptor (CD206)	Mannan (Ezekowitz et al., 1990)
MARCO	Bacteria (van der Laan et al., 1999)
Mincle	Trehalose dimycolate (Ishikawa et al., 2009)
Scavenger Receptor A (CD204)	Lipopolysaccharide, Lipoteichoic acid (Peiser et al., 2000; Peiser et al., 2006)
Stabilin-2	Phosphatidylserine (Park et al., 2008)
TIM-1	Phosphatidylserine (Kobayashi et al., 2007)
TIM-4	Phosphatidylserine (Kobayashi et al., 2007)

Table 1.1 | Phagocytic receptors and their ligands. (Bold letters: opsonic receptor, Italicised: non-opsonic receptor)

Lateral diffusion of these pickets is required to free receptors and increase their membrane mobility (Ostrowski et al., 2016). Hence, events disrupting linkages between the protein pickets and the underlying cytoskeleton favour diffusion of membrane receptors, which is important to engage with target ligands and to proceed with the next stages of phagocytosis characterised by signalling pathways that promote cytoskeletal remodelling and actin growth.
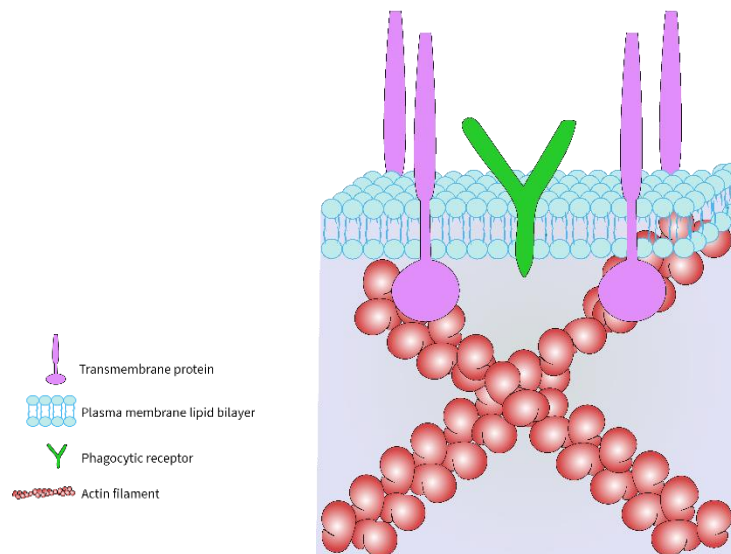
Figure 1.3 | A cartoon depicting the "fence" (actin filament) and "picket" (transmembrane proteins attached to actin) cell membrane model

1.3.1.2 Signalling events via receptors

Receptors are capable of triggering phagocytosis through their specific regions that initiate an intracellular cascade of signals. There might be variations in ligand binding and signalling mechanisms amongst receptors, but FcγR (Figure 1.4) serves as a canonical model to understand receptor signalling during phagocytosis (Jaumouillé & Grinstein, 2011). FcγR uses an immunoreceptor tyrosine-based activation motif (ITAM) to deliver signal of ligand binding (Jaumouillé & Grinstein, 2011). The molecular details of this signalling pathway are reviewed extensively by Ostrowski (2016) and colleagues, and the following discussions will only highlight the key events leading to membrane and cytoskeletal remodelling.

Upon binding with its ligand (IgG), FcγR requires clustering for activation which is then phosphorylated by Src-family kinases (SFK). The phosphorylated site becomes the docking site for various kinases, phosphatases and adaptor molecules which enable recruitment of important GTPases and effector molecules for cytoskeletal remodelling and actin growth (Jaumouillé & Grinstein, 2011). Spleen tyrosine kinases (Syk) are recruited to the membrane which activates key regulators of actin skeleton such as Vav,

phosphatidylinositol-3-kinases (PI3K), phospholipase C (PLC), SH2 domain-containing leukocyte protein (SLP), and linker for activation of T cells (LAT) (Mócsai, Ruland, & Tybulewicz, 2010). This recruitment allows activation of Rac and Cdc42 GTPases by nucleotide exchange factors which favours actin nucleation through WAVE, WASP and Arp2/3 using actin monomers to assemble an entire filament (Figure 1.4, Jaumouillé & Grinstein, 2011). These events then change the dominant Rho/formin/myosin linear actin scaffold to a branched Arp2/3 dependent cytoskeleton (Ostrowski et al., 2016) which is amongst the key features of phagocytosis.

Phosphoinositides are membrane components which are found to be critical in signalling events during phagocytosis. In early stages of phagocytosis, phosphatidylinositol 4,5-bisphosphate or PIP_2 dominates the membrane and is able to recruit WASP which in turn activates Arp2/3 and profilin, favouring formation of a branched actin network (Sarantis & Grinstein, 2012). Profilin is a capping protein that interacts with WASP family proteins, specifically WASP's proline-rich domain to promote filament growth (Beiling et al., 2018). In later phagocytic stages, PIP_2 is converted to phosphatidylinositol 3,4,5-*tris*phosphate or PIP_3 by PI3K which destabilises the underlying cytoskeleton and closes the phagocytic cup (Sarantis & Grinstein, 2012).
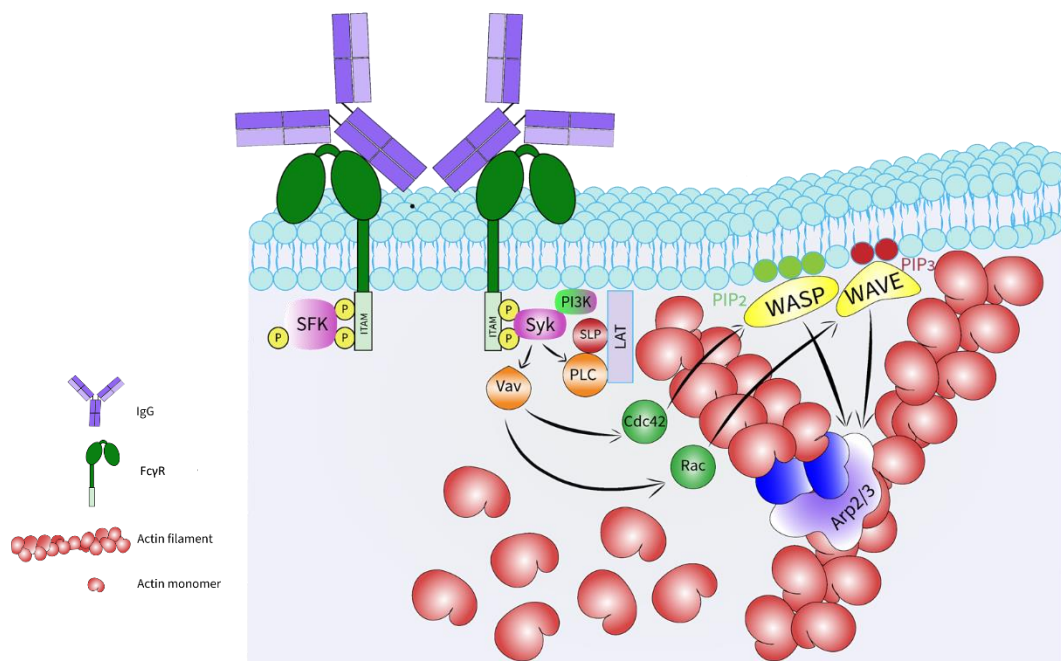
Figure 1.4 | FcγR activation during phagocytosis and the subsequent actin filament growth

1.3.2 Target engulfment

During particle uptake, the physical properties of the target and the phagocyte require as much attention as the multitude of molecular processes that define phagocytosis. Variations in the size, shape and stiffness of the target were reported to have profound effects on its phagocytic uptake (Beningo & Wang, 2002; Padmore et al., 2017; Paul et al., 2013; Serda et al., 2009; Sosale et al., 2015). Phagocytes respond to targets with different physical properties by modulating its mechanical properties, essentially by remodelling its cytoskeletal framework (Herant et al., 2011). This has important implications in target engulfment which shows various degrees of cytoskeletal rearrangement (Herant et al., 2011).

1.3.2.1 Size, shape and rigidity of the target

In biological settings, microbes and other particles targeted for phagocytosis possess different sizes, rigidities and shapes (Möller et al., 2012). These confront the phagocyte to generate an effective mechanism to internalise these physically diverse targets. Alveolar macrophages were observed to phagocytose shorter length fibres more efficiently than longer ones (Padmore et al., 2017), indicating the importance of target size in phagocytic uptake. Moreover, the maximum length of fibre that can be taken up by these phagocytes was found to be 16 um (Padmore et al., 2017). Interestingly, uptake of longer fibres resulted to increase in inflammatory biomolecules secreted by these macrophages, suggesting that phagocytosis could be linked to cellular activation during immune response.

Beningo and Wang (2002) reported that rigidity or stiffness is an important criterion for particle uptake. They found that rigid beads (0.2% bis-acrylamide) were more likely to be internalised than soft ones (0.05% bis-acrylamide). By modulating molecular pathways involved in phagocytosis through Rac1 but not RhoA GTPase, they showed that phagocytosis of soft beads by macrophages could be enhanced. Sosale (2015) and colleagues confirmed the mechanosensitive property of phagocytosis by comparing uptake of rigid (chemically modified) red blood cells (RBCs) and normal RBCs. They found that target stiffness determines particle uptake which is dependent on myosin-II, an important effector during late-stage contraction of phagocytosis (Kovari et al., 2016). Overall, this underscores the mechanosensitive nature of phagocytosis which allows target discrimination. An important implication is in clearing out senescent and diseased cells with altered stiffness property.

The effects of particle shape had been elegantly shown in the experiments of Champion and Mitragotri (2009). Geometric properties of the target, specifically its curvature at the point of contact, determines whether phagocytosis would be initiated or not (Champion & Mitragotri, 2009). Increase in local curvature in non-spherical targets results to higher phagocytic uptake (Champion & Mitragotri, 2009; Möller et al., 2012; Tollis et al., 2010). For

instance, engulfment of spheroids is faster when the cell contacts the more highly-curved tip first (Champion & Mitragotri, 2006). Furthermore, Möller (2012) and colleagues reported that uptake of rod-shaped bacteria only happens when the macrophage contacts the target on its tip and not along its axial length. The speed of engulfment is constant for each bacterial cell and internalisation seems to be determined by bacterial length highlighting the importance of size as well in the phagocytic uptake of this type of target (Möller et al., 2012).

A model of target shape and engulfment was further explored in relation to receptor behaviour during phagocytosis. Richards and Endres (2014) divided the process into two stages: a slow first stage that further decreases as engulfment ensues and a faster second stage which covers the final stages of engulfment. The first stage is due to the passive movement of receptors to the contact site whilst the second stage is believed to be caused by an active process of receptor recruitment (Richards & Endres, 2014). This model seems to explain why standing ellipsoids are engulfed faster than lying down ellipsoids since the time requirement to finish the first stage in the former is shorter than the latter, allowing the second stage to start earlier in taking up standing ellipsoids (Richards & Endres, 2017).

1.3.3 Mechanical properties of the phagocyte

Phagocytes are highly specialised in reacting to various mechanical forces in its environment. They are endowed with sophisticated cytoskeleton composed primarily of actin, which are highly flexible molecules with a rapid turnover rate (Moeendarbary & Harris, 2014). Furthermore, actin can form higher levels of organisation (i.e. linear or branched filaments), allowing them to sustain the mechanical stress experienced by the cell (Moeendarbary & Harris, 2014). In phagocytosis, extensive reorganisation of cytoskeleton and membrane remodelling are a key feature for successful target internalisation.

1.3.3.1 Membrane deformation

Deformations of the cell membrane are highly featured during phagocytic uptake. Membrane deformations to accommodate the target during internalisation require a phagocyte to resist mechanical tension that might otherwise cause it to rupture. Agudo-Canalejo and Lipowski (2016) studied the conditions required for the stability of membranes during engulfment. They used a spontaneous curvature model which describes the membrane by its bending rigidity κ and its spontaneous curvature m given by the following equation:

$$E_{be} = 2\kappa \int \mathrm{d}A \, (\mathrm{M} - \mathrm{m})^2 \qquad (1.1).$$

M is the mean curvature of the membrane and the integral is over the area of the whole membrane surface. This model is similar to the one proposed by Helfrich (1975) which

describes the elastic membrane property in terms of bending and stretching energies. However, they neglect the surface tension contribution and only considered the importance of bending energy to deform the membrane. This assumes that phagocytes have a large pool of membrane reserves during phagocytic uptake. This is supported by previous observations of local membrane remodelling by exocytosis in the site of developing phagocytic cup (Lee et al., 2007), fusion of the plasma membrane with endoplasmic reticulum membrane during phagocytosis (Becker et al., 2005) and potential unfurling of membrane protrusions on the plasma membrane, such as the membrane ridges, which I will discuss in the succeeding chapter (3).

1.3.3.2 Cortical tension and viscosity

Increase in surface area of the phagocyte is regulated by an interfacial tension known as cortical tension (Heinrich, 2015). This maintains cell shape and resist deformations that might be induced by mechanical forces acting upon the cell. Cortical tension in cells has both a passive component (Smeets et al., 2018), which might be due to the inherent property of the material (Hawkins personal communication), and an active component due to the interaction of actin and myosin molecules beneath the cell membrane (Salbreux et al., 2012). It is recorded to be in the range of 0.1 to 1 mN/m (Herant, 2006; Wolfe et al., 1986). The physiological state of the phagocyte and the mechanical forces it encounters determine the present cortical tension within the cell. In unstimulated neutrophils, small deformations change cortical tension very little; whilst, it is found to rise sharply when cell surface area is increased by approximately 30% (Herant et al., 2005). Furthermore, tension varies in events of passive deformation (e.g. changes in cell shape due to movement in narrow blood vessels) with that of active processes (e.g. phagocytosis and migration) suggesting that cortical tension is tightly monitored (Heinrich, 2015).

Whilst cortical tension maintains cell shape and resists deformations, cytoplasmic viscosity is another important property that serves to counteract cell shape changes (Evans & Yeung, 1989; Hochmuth et al., 1993). It was observed that both cortical tension and cytoplasmic viscosity can vary in many types of phagocytes, but, remarkably, tension/viscosity ratio appears to be conserved in phagocytic cells (Lam et al., 2009). This suggests the importance of regulating these physical parameters for phagocytes to efficiently carry out their cellular functions such as phagocytosis. A very high viscosity leads to a less fluid cell interior which inhibits cell shape changes necessary for particle engulfment and, similarly, too high cortical tension negatively affects phagocytic uptake by preventing formation of local protrusions (Heinrich, 2015) which are important for target contact (Flannagan et al., 2010). Meanwhile, if viscosity is very low, no support can be provided for the developing local protrusions, whilst too low cortical tension prevents the phagocyte to

round up after engulfment and affects its transport through the body circulation (Heinrich, 2015).

1.3.4 Force generation during phagocytosis

Upon activation of phagocytic receptors, polymerisation of actin filaments against the cell membrane results to an engulfment force manifested by the host cell membrane spreading over the target. As shown in figure 1.2, this results to a phagocytic cup that is then closed by fusion of its opposite ends to form a phagosome.

1.3.4.1 Cell-target adhesion

Physical contact with the target is a crucial event that determines the success of phagocytosis. Despite its importance, less is known about the underlying mechanism of interaction. Cell-target adhesion is believed to be driven mainly by specific weak bonds (i.e. noncovalent interactions) (Heinrich, 2015). However, it is not clear whether the described phagocytic receptors (table 1.1) or other membrane components, which do not trigger cytoskeletal rearrangement, are responsible for maintaining target adhesion. Underhill and Goodridge (2012) proposed a model that distinguishes these membrane molecules as "tethering" or "tickling". For instance, phagocytic receptors for apoptotic cells called phosphatidylserine (PS) receptors are necessary for cell uptake but show poor affinity with their counterpart ligands (Hoffmann et al., 2001). This suggests that other key molecules in the phagocyte's membrane must be important in tethering the target that needs to be internalised. The most likely candidates are integrins, which are surface molecules activated during phagocytosis and physically link the target and cytoskeleton through actin-binding proteins (Ostrowski et al., 2016).

Other studies inferred a combination of different receptors enables target adhesion and phagocytic uptake. For instance, the number of FcγRIIIb which reaches around 3500 copies per square micrometre in human neutrophils suggests that it might be important in FcγRIIa-mediated phagocytosis to compensate for FcγRIIa's low ligand affinity and low number (García-García et al., 2009; Rivas-Fuentes et al., 2010). Indeed, blocking of either FcγRIIIb or FcγRIIa impaired uptake of bacterial cells by neutrophils underscoring the cooperative role of these receptors during phagocytosis (Treffers et al., 2019; Golay et al., 2013; Fossati et al., 2002).

1.3.4.2 Forces during target internalisation

As shown in figure 1.2 and figure 1.4, activating intracellular signalling pathways by phagocytic receptors leads to actin polymerisation which generates the important forces for target internalisation (Herant et al., 2006). The phagocytic cup that surrounds the target is mainly supported by the newly polymerised actin network beneath the cell membrane (Figure

1.2D and 1.2E). This generates a protrusive force opposing the cortical tension and expanding over the target (Herant et al., 2011). Specific events that define actin dynamics such as nucleation, branching, capping and anti-capping and how they shape the membrane during phagocytic uptake were investigated *in silico* by our collaborators (Bradford, 2021). Our preliminary results revealed differences in timing to complete the engulfment of spherical targets with respect to their size (Chapter 4). Meanwhile, Herant (2006) and colleagues also used a computational approach to explore the mechanics of phagocytosis and, similarly, concluded the importance of actin in successful target engulfment. They proposed that phagocytic uptake is driven by two important forces: *a repulsive force* which acts at the edge of the phagocytic cup caused by a repulsion between the actin network and the free membrane (i.e. not attached to the target) in this region and a *flattening force* which is caused by a contractile force in the interface of phagocytic target and engulfing cell mainly driven by the actomyosin network and results to an inward pull of the target. However, these had not been evidenced *in vivo* due to the technical challenges in live imaging phagocytosis with molecular resolution and hence were only inferred using a micropipette experimental set-up where they monitored changes in the cortical tension and cell morphology during phagocytic uptake (Herant et al., 2006; Herant et al., 2005).

1.3.5 Phagocytosis in diseases

Problems in phagocytosis have been associated with several diseases, but little is known on its mechanistic detail. These underscore the importance of understanding means of clearing damaged cells, foreign particles and debris in the body to restore tissue homeostasis and achieve normal tissue functions.

1.3.5.1 Chronic neurological disease

In multiple sclerosis (MS), a neurodegenerative disorder affecting the central nervous system (Frohman et al., 2006), failure in engulfing defective neuronal cells by the resident macrophage, microglia, is believed to contribute to the progression of the disease (Prineas et al., 2001). Blood-derived macrophages were also observed to aggregate at sites of injury in early MS (Fu et al., 2014), further highlighting the importance of phagocytosis to understand disease progression and pathology. Whilst recruitment of macrophages is believed to be caused by activation of complement system by injured neuronal cells (Prineas et al., 2001), events leading to unsuccessful phagocytosis remain to be examined.

1.3.5.2 Bacterial infection

1.3.5.2.1 *Porphyromonas gingivalis*

Periodontitis is a chronic inflammation of the oral epithelial tissue that is commonly associated with the bacterial pathogen *Porphyromonas gingivalis* (Eke et al., 2012; Werheim

et al., 2020). A number of studies associated this disease to the ability of *P. gingivalis* in manipulating and disrupting phagocytosis. Werheim (2020) and colleagues demonstrated the remarkable ability of *P. gingivalis* to escape and re-enter macrophages. Though the important factors enabling the bacterium to achieve these traits were not identified, a notable difference between the virulent (W83) and the non-virulent (33277) variants were the possession of capsule in the former and its absence in the latter (Werheim et al., 2020), suggesting a potential role of its capsule on its manipulation of phagocytosis.

Castro (2017) and colleagues on the other hand showed that cysteine proteases from *P. gingivalis* can cleave CD14 receptor which impairs phagocytosis of apoptotic neutrophils by macrophages. Moreover, this secreted product can inhibit migration of macrophages towards their targets (Castro et al., 2017). The accumulation of apoptotic neutrophils and pro-inflammatory effects of pathogen secretion exacerbate local tissue damage which may contribute to chronic inflammation (Castro et al., 2017). Overall, these reiterate the relevance of phagocytosis to broader subjects of infection and inflammation.

1.3.5.2.2 *Haemophilus influenzae*

In biological settings having actual pathogen, the dependence of phagocytosis to different parameters such as the availability of receptors on host membrane and pathogen density had also been described. *Haemophilus influenzae*, the most common pathogen associated with chronic obstructive pulmonary disease or COPD (Murphy et al., 2004), was found to be persistent in conditions with advanced airway inflammation and reduced lung function (Bresser et al., 2000). A well-studied factor that contributes to lung inflammation and subsequent diseases is smoking. Kirkham (2004) and collaborators showed that carbonyl compounds from cigarette smoke could affect macrophage phagocytosis and migration by sequestering membrane receptors and modifying substrate composition essential for migration. Moreover, the expression of important recognition receptors for phagocytosis was found to be significantly reduced in smoking individuals compared to non-smoking population (Hodge et al., 2007). This is believed to very likely explain the defective phagocytosis of *H. influenzae* by alveolar macrophages in smokers with COPD (Berenson et al., 2013).

Meanwhile, Liang (2014) and collaborators showed that bacterial density is important in understanding the phagocytic uptake of *H. influenzae*. In individuals with severe asthma, bacterial density was shown to negatively impact phagocytosis in both alveolar and monocyte-derived macrophages (Liang et al., 2014). Amongst the most common microbes found in the lungs of asthmatic patients is *H. influenzae* (Earl et al., 2015). Liang (2014) and colleagues showed that increase in *H. influenzae* burden leads to reduction in phagocytic uptake by macrophages. This scenario is further compounded by the presence of apoptotic neutrophils

that also require clearance by macrophages. Indeed, Ween (2016) and collaborators confirmed that an increase in number of *H. influenzae* in the lungs leads to reduction of phagocytosis of apoptotic cells by alveolar macrophages.

1.3.5.2.3 *Staphylococcus aureus*

S. aureus is a Gram-positive commensal bacterium (Harris et al., 2002) that could be associated with different types of infection such as endocarditis, necrotising pneumonia and skin infection to name a few (DeLeo et al., 2010). This is partly due to the emergence of different strains such as the methicillin-resistant *S aureus* (MRSA) that can evade phagocytosis and survive and proliferate within the human host (Greenlee-Wacker et al., 2014). Its broad medical relevance resulted to decades of investigations on biological and physical mechanisms that enable its survival within host cells, especially within professional phagocytes neutrophils and macrophages (reviewed extensively by Horn et al., 2018). As this pathogen is not the focus of this work, the reader is referred to the previously mentioned references for further reading.

The biophysical mechanics of *S. aureus* phagocytosis is poorly understood. It is a round-shaped pathogen with a diameter of 0.5 – 1.5 um that can divide in multiple planes to produce grape-like clusters (Harris et al., 2002). To initiate phagocytosis, coating by opsonins such as IgGs and complement proteins is believed to be an important prerequisite for its internalisation (van Kessel et al., 2014). Its size and shape make it a highly ideal target for phagocytosis by neutrophils and macrophages as demonstrated in experiments using beads (Pratten and Lloyd, 1986; Tabata and Ikada, 1988; Koval et al., 1998; Champion and Mitragotri, 2006; Paul et al., 2013). Similar with *H. influenzae*, *S. aureus* is a common pathogen that exacerbates asthma (Earl et al., 2015), and its phagocytosis is negatively impacted by bacterial burden (Liang et al., 2014).

1.3.5.3 *Fungal infection*

Phagocytosis is an important event in controlling fungal infection especially during its early onset (Bonnett et al., 2006; Bojarczuk et al., 2016). Most known fungal pathogens do not cause any disease unless there is disturbance in immune homeostasis such as in immunocompromised and immunosuppressed individuals (Romani, 2004; Drummond et al., 2014). Amongst the most common human fungal pathogens are *Candida* spp., *Aspergillus* spp., *Pneumocystis jirovecii* and *Cryptococcus* spp. (Drummond et al., 2014). For recognition and phagocytic uptake of these pathogens, cell wall components such as mannan and β-1,3-glucan are usually utilised by macrophages and other phagocytes via phagocytic receptors on their membrane surfaces (table 1.1). As this work focuses on *Cryptococcus* spp., the following subsection only discusses its biology and infection; however, the reader is referred to excellent

reviews of Pappas et al., 2018 (*Candida*), Thompson and Young, 2021 (*Aspergillus*) and Thomas and Limper, 2007 (*Pneumocystis*) for other common human fungal infections.

1.3.5.3.1 *Cryptococcus* spp.

1.3.5.3.1.1 Characteristics and classification

Cryptococcus is a unicellular fungus found ubiquitously in the environment with worldwide distribution (Lin and Heitman, 2006). It was first isolated by Sanfelice in 1894 in Italy and since then had been characterised as an important human pathogen causing cryptococcosis (Kwon-Chung et al., 2014). *Cryptococcus* can readily be differentiated from other pathogenic yeasts such as *Candida* by possession of a polysaccharide coating known as capsule, production of melanin and presence of urease activity, all of which contribute to its virulence (Kwon-Chung et al., 2014; Zaragoza, 2019). McClelland (2004) and colleagues identified capsule as the most important virulence factor of *Cryptococcus* which accounts for approximately 25% of its total virulence.

The exact native architecture of *Cryptococcus* capsule has not been completely resolved (Casadevall et al., 2019). This is largely due to its highly hydrated nature which preclude the use of high-resolution imaging such as electron microscopy in examining its native structure (Casadevall et al., 2019). However, previous reports of Maxson (2007) and collaborators showed that capsule is a highly dynamic and heterogenous structure which could be influenced by the age of the cell. Furthermore, biochemical studies revealed that it is about 90% composed of glucuronoxylomannan (GXM) with α-1,3-mannose backbone and β-1,2- and β-1,4-xylose and β-1,2-glucuronic acid substitutions (Merrifield and Stephen, 1980; Cherniak et al., 1980). Structural differences on this capsular component, specifically the complexity of mannose backbone substitution, give rise to antigenic differences allowing further subgrouping of *Cryptococcus* into five serotypes: A, B, C, D and AD (Casadevall et al., 2019). *Cryptococcus neoformans* contains A, D and AD serotypes whilst *C. gattii* includes the B and C subgroups (Belay et al., 1996). *C. neoformans* is commonly associated infecting immunocompromised individuals whilst *C. gattii* commonly infects immunocompetent or healthy hosts (Speed and Dunt, 1995); however how immune status affects predilection with *C. neoformans* or *C. gattii* infection remains to be investigated (Capilla et al., 2006).

1.3.5.3.1.2 Ecology and life cycle

Cryptococcus is widely distributed across different animal and plant species acting as its environmental reservoir. Pigeons are commonly associated with *C. neoformans* serotype A and D however other avian species such as chicken, goose, duck, eagle, owl, peacock and parrot could also be sources (Lin and Heitman, 2006). Meanwhile, eucalyptus trees, fruits,

vegetables, soil and decaying wood were also found to possess *Cryptococcus* isolates (Pfeiffer and Ellis, 1992; Cornelissen et al., 2003; Pal et al., 1990).

C. neoformans and *C. gattii* may have differences in geographical distribution which is an important factor to understand their epidemiological attributes. *C. neoformans* has a worldwide distribution and causes the vast majority of infection to immunocompromised host (Lin and Heitman, 2006) whilst *C. gattii* is believed to be endemic in tropical and subtropical regions (Kwon-Chung and Bennett, 1984). Global infection caused by *C. neoformans* was approximated to be 80% compared to 20% caused by *C. gattii* (Kwon-Chung et al., 2014). Whilst *C. gattii* infection is commonly recorded in tropical and subtropical areas, recent data indicate that the species might have colonised temperate regions as well. Recent infection outbreaks of *C. gattii* on Vancouver Island, Canada and the Pacific North-western United States are notable evidence of this expansion (Hoang et al., 2004; MacDougall et al., 2007). Moreover, strains of *C. gattii* (VGIIa and VGIIc, respectively) responsible for these outbreaks were found to be more virulent than other previous *C. gattii* variants (D'Souza et al., 2011; Byrnes et al., 2010). This suggests a fundamental shift in *Cryptococcus* pathogenicity and distribution which is potentially critical to adapt to changing ecological and climactic conditions.

In general, the life cycle of *Cryptococcus* reflects its highly successful mechanism of production and dispersal in the environment. Both *C. neoformans* and *C. gattii* are heterothallic (i.e. separate male and female individuals) haploid yeasts compose of two mating types, *MATα* and *MATa* (Kwon-Chung et al., 2014). The haploid cells propagate asexually by budding and can undergo dimorphic transition into a filamentous stage characterised by distinct differentiation pathways: mating and monokaryotic fruiting (Lin and Heitman, 2006). Both *MATa* and *MATα* cells are capable of secreting pheromones to ensure successful fusion and reproduction (McClelland et al., 2004). The fusion of haploid cells of different mating types (a and α yeast cells) produces dikaryotic filament, eventually leading to the formation of a basidium. In the terminal region of the basidium, nuclei from opposite mating types fuse to form a diploid nucleus which then undergoes meiotic division (Kwon-Chung, 1976). These haploid meiotic products then undergo mitotic division producing a bud of four long chains of basidiospores with *MATa* and *MATα* at remarkably equal ratios (Kwon-Chung, 1980). These spores are then readily dispersed in the environment to repeat the life cycle from unicellular haploid cells.

Meanwhile, another type of sexual reproduction amongst *Cryptococcus* that gives rise to morphologically similar basidiospores formed by two opposite mating types was also characterised (Lin et al., 2005). In this process, a monokaryotic hypha is produced from sexual

reproduction between two similar mating types (Lin et al., 2005). Cells become diploid either by endoduplication or by nuclear fusion to produce a monokaryotic hypha with unfused clamp connections (Lin and Heitman, 2006). This process is usually observed with α strains (Wickes et al., 1996), which is presumed to be the main reason for their predominance in clinical and environmental isolates (Lin and Heitman, 2006).

1.3.5.3.1.3 Host interaction and virulence

The interaction of *C. neoformans* with soil amoeba is believed to be a critical step in its evolution as a successful intracellular pathogen (Kwon-Chung et al., 2014). The ability of the fungus to survive within the amoeba allowed it to utilise the same strategy in colonising human innate immune cells such as macrophages (Steenbergen et al., 2001). Some of these well-known *Cryptococcus* traits which promote survival within the host are capsule possession (Jacobson et al., 1982), melanin production (Rhodes et al., 1982) and tolerance to mammalian body temperature (Perfect, 2006). Melanin provides antioxidant protection (Wang and Casadevall, 1994) and is also found to be essential against microbicidal peptides (Doering et al., 1999), growth at elevated temperature (>30 °C) is due to temperature-sensitive genes such as calcineurin which is involved in signalling cascade (Odom et al., 1997), whilst the capsule is believed to be the most important virulence factor for the following reasons.

The capsule of *Cryptococcus* serves as the outermost structure which can provide different means of protecting the pathogen. It enables survival during dehydrating conditions (Aksenov et al., 1973) and exposure to free radicals (Zaragoza et al., 2008). Furthermore, it is believed to permit the pathogen to evade phagocytosis by masking its ligands, such as cell wall mannan and β-1,3-glucan, important for receptor activation and phagocytic uptake (Kozel and Gotschlich, 1982; Cross and Bancroft, 1995;). However, the mechanism by which the capsule promotes this highly antiphagocytic property is largely unknown.

As previously mentioned, *Cryptococcus* capsule is primarily composed of water (Maxson et al., 2007) and large polysaccharides cross-linked into a matrix that decreases in density, porosity and stiffness as it extends outside from the cell wall (Casadevall et al., 2019). Its two main polysaccharides are glucuronoxylomannan (GXM) and glucuronoxylomannogalactan (GXMGal) (Zaragoza, 2019). *Cryptococcus* capsule is a very dynamic and sensitive structure that can undergo different rearrangements during infection (Zaragoza, 2011). For instance, immediately after *Cryptococcus* occupies the lung, a dramatic increase in capsule size was observed (Feldmesser et al., 2001). Some of the known factors that induce capsule growth are high CO_2 (Granger et al., 1985), low iron (Vartivarian et al., 1993), mannitol (Guimaraes et al., 2010) and mammalian serum (Zaragoza and Casadevall, 2004). As previously stated, capsule properties could also be affected by the age of the cell as

older cells exhibit higher rigidity, decrease permeability, electrometric potential and change in composition (Cordero et al., 2011).

In an *in vivo* study of Cryptococcal infection using zebrafish model by Bojarczuk (2016) and colleagues, the phagocytosis of *Cryptococcus* by macrophages was seen to be restricted very early in infection and, furthermore, there was preferential uptake of cells with smaller capsule. In the same study, about 3-fold increase in capsule size was observed after an overnight infection, enough to limit any further phagocytosis by macrophages (Bojarczuk et al., 2016). This further highlights the importance of capsule in the survival and pathogenesis of *Cryptococcus.*

1.4 Phagocyte membrane protrusions

Phagocytes are highly dynamic cells that usually rely on their membrane extensions to carry out important functions such as migration, probing of extracellular environment, fluid uptake and phagocytosis. They use the energy of actin polymerisation to generate a pushing force against the membrane, resulting to different types of membrane protrusions (Pollard, 2016). Some of their well-studied membrane protrusions are lamellipodia, filopodia, dorsal ruffles and podosomes.

1.4.1 Lamellipodia

Thin, sheet-like protrusions that are commonly found on the leading edge of migrating cells are called lamellipodia (Abercrombie et al., 1971). They generate large pushing forces that are mainly responsible for propelling the cell front (Svitkina, 2018). Aside from force generation, lamellipodia also play important roles in navigating through the extracellular matrix by guiding cell around obstacles, sensing soluble guidance cues, and probing the chemical and mechanical properties of the substratum (Svitkina, 2018).

Early studies on the structure of lamellipodia revealed a network of long diagonal actin filaments exhibiting polarity shown by their fast-growing barbed ends oriented towards the leading edge (Small et al., 1978). *In vitro* reconstitution of a branched actin network showed that its free barbed ends increase in density at increasing load or force opposite filament growth with concomitant increase in filament packing (Beiling et al., 2016). Further scrutiny of lamellipodial actin network revealed multiple branched actin filaments formed by the attachment of the slow-growing pointed end of one filament to the side of another filament at a consistent 70° angle (Svitkina and Borisy, 1999). More recent evidence though suggest that end branching is also a possible mechanism to maintain lamellipodial actin network (Vinzenz et al., 2012). This branching pattern was found to be established through actin-related protein (Arp) 2/3 nucleation (Mullins et al., 1998).

The mechanism of actin turnover in lamellipodia includes continuous nucleation of new daughter actin filaments from pre-existing mother filaments (Mullins et al., 1998). Daughter filaments then elongate and push on the plasma membrane. After a short period of elongation, their barbed end is capped, and elongation is terminated (Mullins et al., 1998). Disassembly of the network occurs through a combination of debranching and severing of actin filaments, followed by depolymerization of filament fragments (Svitkina and Borisy, 1999). Thus, individual filaments in the network do not treadmill, but are generated from a branchpoint, grow at the barbed end, become capped, and later dissipate by depolymerization (Pollard and Borisy 2003). Subsequent disassembly of filaments is accelerated by cofilin which serves to replenish the pool of free actin monomers for continuous assembly (Schaub et al., 2007). Given this sequence of reactions, the capping rate sets the limit for the length of actin filaments in lamellipodia, whereas the number of growing filaments is believed to be defined by the balance between branching and capping rates (Schaub et al., 2007). A high caping rate is expected to correlate with a high branching rate because of the need to produce new filaments to compensate for the loss of filaments due to capping (Schaub et al., 2007). The importance of filament geometry becomes apparent during force generation as short filaments are more efficient at pushing the plasma membrane forward in a Brownian ratchet mechanism (Mogilner and Oster, 1996; Peskin et al., 1993) as bending rigidity of the filament decreases at increasing length (Schaub et al., 2007). Meanwhile, the array of branched filaments in lamellipodia undergoes treadmilling as a whole by assembling at the front and disassembling throughout its body (Svitkina, and Borisy, 1999).

1.4.2 Filopodia

Finger-like extensions called filopodia are also commonly seen amongst phagocytic cells (Horsthemke et al., 2017). Like lamellipodia, they are involved in cell migration and other cellular processes such as mechanosensing of substrate topography (Albuschies and Vogel, 2013), chemical sensing (Matilla and Lappalainen, 2008) and cell-to-cell communication (Goodman et al., 2019). They are composed of a bundle of 10-30 parallel linear actin filaments whose barbed ends are able to push the plasma membrane similar to lamellipodia (Yang and Svitkina, 2011). It is generally believed that filopodia may control directionality and persistence of movement by promoting cell-matrix adhesion at the leading edge of advancing lamellipodia (Bornschlogl, 2013; Matilla and Lappalainen, 2008).

Many proteins that regulate the actin cytoskeleton have been shown to localise to filopodia and regulate its formation. During filopodial elongation, actin monomers are added to the filopodial tip through formin and enabled/vasodilator-stimulated phosphoprotein (Ena/VASP) which protect the barbed ends of the filament from capping proteins (Svitkina et al., 2003; Yang et al., 2007). Filopodial filaments are cross-linked to form bundles through

fascin, which enhances filopodial stiffness (Vignjevic et al. 2006). The high turnover of fascin within filopodia by constantly dissociating and rebinding to actin filaments enable phagocytes to release stresses within the bundle and finetune filopodial morphology to perform their important roles such as probing the external environment (Svitkina, 2018; Matilla and Lappalainen, 2008).

1.4.3 Dorsal ruffles

Dorsal ruffles are wavy, sheet-like protrusions arising from the dorsal surface of adherent cells (Stow and Condon, 2016). They are transient in nature which typically appear 2 minutes after stimulation and disappearing within 30 minutes of induction (Legg et al., 2007). Some of the known stimulants to generate dorsal ruffles in macrophages are LPS (Patel et a., 2008), PMA and M-CSF (Yoshida et al., 2015). They are well-known for their role in forming macropinosome for nonspecific fluid uptake (Bohdanowicz et al., 2013; Dowrick et al., 1993) and are also found to be important in recycling of membrane receptors (Orth et al., 2006), cell motility (Krueger et al., 2003) and pathogen uptake (Swanson, 2008).

Unlike lamellipodia and filopodia, the molecular basis of ruffle formation is not well understood, potentially due to its cellular localisation and fleeting nature which require technical skills during specimen preparation to prevent its collapse and examine it using electron microscopy. The formation of dorsal ruffles is believed to be initiated by various nucleators including Arp2/3 and formin and, similar to phagocytosis, the assembly of Arp2/3 is very likely to be controlled by WASP family of nucleation promoting factors, WASP and WAVE (Veltman et al., 2016). Furthermore, Rho GTPases such as Rac and Cdc42 that play important roles in signalling cascades during phagocytosis are also found during ruffle formation (Itoh et al., 2013; Mahankali et al., 2011). Other signalling molecules such as Ras, Akt, PI3K, MAPK, Src, and PAK1 were found to be enriched in ruffles, suggesting complex events of cytoskeletal reorganisation during ruffle formation (Hoon et al., 2012). Finally, maturation of ruffles to macropinocytic cups showed patches of PIP_3 in the membrane underscoring the importance of phosphoinositide signalling during ruffle development (Araki et al., 2003; Yoshida et al., 2009).

1.4.4 Podosomes

Podosomes are cone-shaped adhesion structures that are prominent in macrophages and dendritic cells which also play important roles in migration, degradation of extracellular matrix and cellular fusion (Faust et al., 2019). They are located at the ventral cell surface reaching heights of about 600 nm (Labernadie et al., 2010). Their defining molecular architecture is a core of actin filaments nucleated by Arp2/3 (Linder et al., 2000; Kaverina et al., 2003) that is surrounded by adhesive plaque of proteins including talin, vinculin and integrins (Zambonin-Zallone et al., 1989; Pfaff and Jurdic, 2001). In addition to Arp2/3,

dynamin (Ochoa *et al.*, 2000) and N-WASP (Mizutani et al., 2002) are also believed to be essential in actin polymerisation to generate podosomes.

Using superresolution microscopy, podosomes are seen to be organised into clusters forming a polygonal structure (van den Dries et al., 2013). They have regular spacing but are interconnected with a radial actin filament network (Luxenburg et al., 2007). They are highly dynamic with an actin turnover of about 30 seconds and a periodic oscillation of the core stiffness that depends on the activities of their actin filaments and myosin II (Labernadie et al., 2010). This allows them to exert a perpendicular force to the substratum and sense its mechanical properties such as its stiffness.

1.5 General and specific thesis aims

Our understanding of the biophysical underpinnings of host-pathogen interaction at the cellular level remain cursory even with the very striking mechanical features of the phagocytic process. This could be accounted to the highly dynamic nature of this process and the imaging resolution required to accurately illustrate the activities of its molecular components. Nonetheless, this thesis aims to investigate the biophysical properties of phagocytic cells to understand how they interact with different phagocytic targets. In my first results chapter (Chapter 3), I will demonstrate the morphological properties of a phagocytic surface using electron microscopy and superresolution microscopy to characterise the actin-based membrane protrusions of phagocytes. I will then describe the different chemical, physical and biological factors that affect their surface properties with respect to their membrane ridge protrusions. In my second results chapter (Chapter 4), I will present the effect of target size in the phagocytic uptake of spherical particles by macrophages. I will show how my experimental data compare with an *in silico* model of phagocytosis of spherical targets provided by our collaborators, that is based on actin's role in shaping the phagocyte's membrane during uptake. I will then use my experimental data to analyse the uptake of an actual spherical pathogen, *Cryptococcus neoformans,* and determine the role of size on its uptake. Along with size property, I will also examine how surface features of spherical targets influence their phagocytic uptake as this process mainly relies on receptors activated by interaction with ligands on the target's surface. Finally, in my last results chapter (Chapter 5), I will present the dynamics of macrophage surface during phagocytic interaction with *Cryptococcus*, focussing on two types of sheet-like protrusions: membrane ridges and dorsal ruffles. I will describe how the actin cytoskeleton play an important role in generating and maintaining structural features in macrophages during their phagocytic interaction with *Cryptococcus*.

CHAPTER 2

Methodology

2.1 Cell preparation, culture and maintenance

Different types of phagocytic cells were used in this study. I have done all specimen preparations unless otherwise stated where names of those who donated the samples were stated along with the methods they used for sample preparation.

2.1.1 J774 and RAW 264.7 macrophage-like cells

J774 (Hirst el al., 1971) and RAW264.7 (Ralph and Nakoinz, 1977) were obtained from cryovial stocks stored in liquid nitrogen dewars. Cryovials were defrosted for about 2 minutes in a 37 °C water bath. Cells were then resuspended in a 15 ml falcon tube with 4 ml complete Dulbecco's modified Eagle's medium (DMEM) with the following composition:

a. 88% DMEM (Sigma D5546)

b. 10% Fetal bovine serum (FBS) (Sigma F7524)

c. 1% 2mM L-glutamine (Sigma G7513)

d. 1% 100 units/ml Penicillin G and 0.1 mg/ml Streptomycin mixture (Pen/strep) (Sigma P4333)

The cell suspension was then centrifuged for 5 minutes at 1000x g. Supernant was discarded thereafter and resuspended in at least 10 ml complete DMEM. Cells were then seeded into a T75 tissue culture flask and incubated at 37 °C and 5% CO_2. Cells were passaged when flasks showed at least 80% confluency and only used up to passage 14.

2.1.2 THP-1

Undifferentiated THP-1 cells were a gift from Dr. Robbie Evans of University of Birmingham. Cells were grown in T75 culture flasks with 25 ml of complete Rosewell Park Memorial Institute (RPMI) media with the following components:

a. 89% RPMI (BioWhittaker)

b. 10% FBS

c. 1% Pen/strep

Flask confluency were maintained above 1×10^5 cells/ml before passaging up to 20. In differentiating THP-1 cells, confluent flasks were resuspended in 50 ml falcon tubes, spun at 1,250 rpm for 5 minutes and media was replaced by fresh complete RPMI. The number of live cells was estimated using trypan blue and haemocytometer. Cells were then seeded into a 24-well plate with cover slips at 2×10^5 cells/well density in 500 μl complete RPMI with 50 ng/ml

phorbol 12-Myristate 13-Acetate (PMA). Cells were incubated for 3 days at 37 °C and 5% CO_2. Thereafter, media was replaced with fresh complete RPMI and incubated for further 2 days. Differentiated cells were confirmed by examining their macrophage-like features such as adhesion to the plate or cover slip and possession of membrane protrusions. Cells were then prepared for SEM (2.3)

2.1.3 Mouse bone marrow-derived macrophages

Bone-marrow derived macrophages (BMDM) from mouse were prepared by Dr. Laura Martinez-Campesino of Department of Infection Immunity and Cardiovascular Disease, University of Sheffield. Briefly, wild and *trib3* knockout mice were euthanized with their femur and tibia recovered to extract bone marrow tissues. Cell suspensions were centrifuged for 5 minutes at 500x g before resuspending in a fresh complete DMEM with 10% L929 cell-conditioned medium. Cells were then seeded in a 24-well plate and incubated at 37 °C with 5% CO_2 for 5 days. Thereafter, media was replaced with new complete DMEM before using cells for SEM (2.3).

2.1.4 Human monocyte-derived macrophages

Human monocyte-derived macrophages (HMDM) were prepared by Dr. Chiara Niespolo of Department of Infection Immunity and Cardiovascular Disease, University of Sheffield. Briefly, donated blood was mixed with trisodium citrate dihydrate at 9:1 (citrate to blood) ratio. Peripheral blood mononuclear cells (PBMCs) were the extracted using a density centrifugation technique based on Ficoll media (Niespolo thesis, 2020). Following isolation of PBMCs, monocytes were isolated by positive selection using human anti-CD14 microbeads. Differentiation of monocytes was done by spinning monocyte suspension at 1500 rpm for 5 minutes and resuspending cells in complete RPMI media with 100 ng/ml rhM-CSF. Cells were then incubated at 37 °C and 5% CO_2. After 7 days, cells were treated accordingly with different cytokines to produce M1 and M2:

a. LPS (100 ng/ml) + IFNγ (20 ng/ml) – M1

b. IL4 (20 ng/ml) or IL10 (20 ng/ml) – M2

c. no stimulant (media only) – M0

After overnight stimulation, cells were then used for SEM (2.3).

2.1.5 HMDM from pulmonary arterial hypertension patient

HMDM derived from a pulmonary arterial hypertension (PAH) donor were prepared by Dr. Amira Zawia of Department of Infection Immunity and Cardiovascular Disease, University of Sheffield. As in the previous method (2.1.4), PBMCs were extracted using Ficoll media and resuspended in a complete RPMI. Cell were seeded in 24-well plate for 1-3 hours

at 37 °C and 5% CO_2. Thereafter, media was replaced with a fresh complete RPMI and further incubated for 14 days, changing the media every 3-4 days. When differentiation was completed, cells were treated respectively for polarisation:

    a. LPS (100 ng/ml) + IFNγ (50 ng/ml) – M1

    b. IL4 (20 ng/ml) – M2

    c. no cytokine/complete RPMI only – M0

2.1.6 Mouse alveolar macrophages

Mouse alveolar macrophages were prepared by Ms. Mahrukh Shameem of Department of Infection Immunity and Cardiovascular Disease, University of Sheffield. Briefly, mice were euthanised by intraperitoneal injection of sodium pentobarbital for bronchoalveolar lavage (BAL) procedure. After confirming death, lungs and the rest of respiratory tract were exposed by cutting through the ribs. Trachea was cut open to insert a cannula and fluid from the lungs was acquired by a syringe to retrieve the alveolar macrophages. Lung fluid extract were directly mixed with BAL media (0.4% Ethylenediamine tetraacetic acid EDTA, 0.5% FBS and 99.1% Phosphate buffer saline (PBS) solution). BAL fluid was further processed by spinning at 250x g for 10 minutes at 4 °C to isolate alveolar macrophages. Pellets were resuspended in a PCLS media (90% high glucose DMEM, 9% FBS and 1% Pen/strep), and cells were then seeded into a 24-well plate. Alveolar macrophages were incubated at 37 °C and 5% CO_2 before using for SEM (2.3).

2.2 Tissue preparation and imaging

Mouse lung and liver samples were also donated by Ms. Mahrukh Shameem. Lungs and liver were extracted from euthanised mouse (2.1.6) and fixed in 4% paraformaldehyde (PFA) for 10 minutes at room temperature (RT). They were then washed with PBS three times before fixing with 2.5% glutaraldehyde (GA) in 0.1 M sodium phosphate buffer overnight at 4 °C. Thereafter, samples were mounted on a block and sectioned using a vibratome through its frontal plane to produce tissue sections of 100 μm thickness. Sections were then washed at least three time before using for SEM (2.3).

2.3 Scanning electron microscopy

Cells ($1x10^5 – 2 x10^5$ cells/well) seeded in a 24-well plate with glass cover slips were fixed with 4% PFA at RT for 10 minutes. Samples were then washed three times with PBS and fixed with 3% GA in 0.1M sodium phosphate overnight at 4 °C. Thereafter, samples were washed twice in 0.1M phosphate buffer for 10 minutes at RT. Secondary fixation was done using 2% aqueous osmium tetroxide for 1 hour at RT which was by then followed by a series of dehydration steps using graded ethanol (EtOH) (75%, 95% and 100% twice). Samples

were then dried using Leica EM CPD300 with the following settings: CO_2 influx set to slow, a delay of 2 minutes before 24 exchange cycles, slow heating speed and slow gas out with 75% of normal speed. After drying samples were mounted on aluminium stubs, attached with carbon sticky tabs and coated with approximately 25 nm of gold using Edwards S150B sputter coater.

For SEM imaging, samples were examined using TESCAN Vega3 LMU Scanning Electron Microscope at an accelerating voltage of 10 – 30 kV accelerating voltage, 9 mm working distance, 63 nm spot size and 0° stage tilt. Magnifications of 500x up to 30000x were used in imaging depending on region of interest (i.e. cell population, individual cell or membrane protrusion).

2.3.1 Macrophage surface 3D reconstruction

A 3D reconstruction software (Alicona MeX v6.2) based on photometric stereoscopic SEM technique was used to render 3D images of the macrophage surface. An automated angular calibration was done by focussing on the ridges to calculate different imaging positions. 3D images were rendered by setting an automatic offset, after which profile analysis was done to determine the geometrical properties (width, length and height) of membrane ridges.

2.3.2 Ridge detection

Raw SEM images were analysed using Fiji (Schindelin et al., 2012). *Ridge detection* (Steger, 1999) was used to measure the thickness and length of membrane protrusions (ridges, filopodia, lamellipodia and dorsal ruffles). Ridge detection is a Fiji plug-in that can detect and analyse curvilinear structures in an image with an unbiased approach. For a detailed description of the algorithm, the reader is referred to Steger (1999). Briefly, parameters were set to determine linear structures in an image: sigma = 1-3, lower threshold = 0, upper threshold = 1-6. Images were then visually inspected after running the script to check that protrusions were correctly determined. A manual image analysis using TESCAN Vega3 LMU SEM software was also carried out to compare measurements derived from *ridge detection.*

2.3.3 Ridge curvature profiling

Ridges from SEM images were manually extracted by tracing its borders. *Ridge detection* was then run to determine ridge midline. A custom-built script (Appendix 1) written by Dr. James Bradford was used to determine the magnitude and direction of ridge curvature. Briefly, the script uses the coordinates of each linepoint (ridge midline) to estimate angular change from one end of the ridge up to the opposite end. Data of individual ridge curvature and combined ridge curvature were then plotted in a histogram.

2.3.4 Shape analysis

Low magnification (500x) SEM images were used to estimate cell surface area and its elongation (aspect ratio). A threshold was set to identify cells on each image, and each cell was manually inspected to check that borders were correctly identified. *Particle analysis* was then used to determine the surface area and aspect ratio of each cell.

2.4 Transmission electron microscopy

J774 cells ($1x10^5$ cells/well) seeded in a 24-well plate with glass cover slips were fixed with 3% GA in 0.1M sodium phosphate overnight at 4 °C. Samples were then washed twice in 0.1M phosphate buffer for 10 minutes at RT. This was then followed by secondary fixation using 2% aqueous osmium tetroxide for 1 hour at RT. A series of dehydration steps was then carried out using different EtOH concentrations (75%, 95% and 100% twice). Specimens were then placed in propylene oxide for 15 minutes twice. Infiltration was accomplished by placing the specimens in a 50/50 mixture of propylene oxide/araldite resin overnight at room temperature. Thereafter, specimens were left in full strength araldite resin for 6-8 hours at RT after which they were embedded in fresh araldite resin for 48-72 hours at 60 °C. Ultrathin sections, approximately 100 nm thick were cut on a Reichert Ultracut E ultramicrotome and stained for 25 mins with 3% aqueous uranyl acetate followed by staining with Reynold's lead citrate for 5 mins. Sections were examined using a FEI Tecnai Transmission Electron Microscope at an accelerating voltage of 80 kV.

2.5 Airyscan superresolution microscopy

A healthy culture of J774 cells ($1x10^5$ cells/well) seeded in 24-well plate with glass coverslips overnight at 37 °C and 5% CO_2 was fixed with 4% PFA at RT. Cells were then washed three time with PBS followed by incubation with TRITC-phalloidin for 20 minutes at RT. Specimens were again washed three times with PBS and distilled water (dH_2O) separately, before mounting onto a glass slide using mowiol and drying overnight. Airyscan confocal microscope LSM880 in superresolution mode was used to image actin cytoskeleton with 63x oil immersion objective (1.4 NA Plan Apo), 540 nm excitation laser, 570 nm emission wavelengths in z-stacks with 100 nm interval of 10-20 μm range.

2.5.1 Ridge and cortex extraction

Airyscan actin images were processed manually using Fiji. A 3D image projection was rendered to examine the entire actin cytoskeleton. Ridges were then extracted from each z section by tracing the border of each ridge as they project from the dorsal cell surface and actin cortex. After isolation of actin ridges, z-stacks were projected in 3D to confirm successful extraction. Similarly, actin cortex was also manually extracted by following its

edges around the cell in each z section and rendering 3D projections to confirm successful extraction.

2.5.2 Actin ridge and cortex measurements

Using Fiji, manually extracted actin ridges and actin cortex were then reoriented to yz plane. *Ridge detection* was then run on these images to measure their thicknesses. Images were visually inspected after automated analysis to verify structures were identified correctly.

2.6 Ridge immunofluorescence microscopy

Healthy cultures of J774 and RAW264.7 cells ($1x10^5$ cells/well) were seeded into 24-well plate with glass coverslips overnight at 37 °C and 5% CO_2. Cell were then fixed with 4% PFA at RT. Excess PFA was neutralised by applying 50 mM NH_4Cl for 5 minutes. Thereafter, cells were permeabilised using 0.1% Triton X-100 in blocking solution (5% Human IgG) for 3 minutes. Samples were then incubated with primary antibodies: anti-Arpc2 (Abcam ab133315), anti-TLR2 (Biolegend 12802) and anti-WASH1 (Atlas HPA002689) in blocking solution for 30 minutes. Samples were washed three times with PBS for 5 minutes before incubating with secondary antibody (anti-mouse-FITC) in blocking solution for 30 minutes. Lastly, samples were incubated with phalloidin-TRITC for 30 minutes. All staining steps were carried out using an improvised humidified chamber made up of wet plastic foam supporting a parafilm mounting platform cells were stained to avoid sample dehydration. After labelling, samples were then washed with PBS and dH_2O three times separately before mounting onto clean glass slides using mowiol. Two types of control were prepared: following the above steps up to permeabilisation and repeating the above steps without primary antibodies.

Slides were then imaged using 60x oil immersion objective lens (1.4 NA Plan Apo) in GFP (excitation: 470/40 nm, emission: 525/50 nm) and Cy3 (excitation: 545/25 nm, emission: 605/70 nm) channels of a Nikon Eclipse Ti widefield microscope. Images were blindly deconvolved (Ayers and Dainty, 1988) using NIS Elements deconvolution software and were analysed using NIS Elements v4.11.

2.7 Ridge timelapse imaging

2.7.1 Differential interference contrast imaging

A healthy culture of J774 cells ($1x10^4$ cells/well) was seeded in 96-well glass bottom plate with complete DMEM media at 37 °C and 5% CO_2. After overnight acclimatisation, live cells were imaged in a widefield microscope (Nikon Eclipse Ti) differential interference contrast (DIC) set-up using 60x oil immersion objective (1.4 NA Plan Apo). Polariser was adjusted to acquire a sharp contrast of the membrane ridges. When ridges are in focus, cells were imaged for 15 minutes capturing a frame every second using an Andor Neo SCC-02546

camera detector. Timelapse images were then processed using Fiji and *ridge detection* to analyse membrane ridges. Ridge thickness and lifetime were recorded and analysed accordingly.

2.7.2 Lattice light sheet imaging

Timelapse imaging data from Prof. Jennifer Stow's lab of University of Queensland were manually processed to isolate ridges from dorsal ruffles (for specimen preparation please refer to Condon et al., 2018). After isolation of ridges, they were then measured using *ridge detection* and tracked individually throughout their lifetimes (i.e. from emergence to collapse back on the surface). Thickness of membrane ridges were also recorded and analysed.

2.8 Osmosis

Osmosis experiments are summarised in Figure 2.1. A heathy culture of J774 cells ($1x10^5$ cells/well) was seeded into 24-well plate with glass coverslips at 37 °C and 5% CO_2. After overnight acclimatisation, cells were then exposed different media osmolarities by replacing old media with: distilled water, 0.2% NaCl, 0.5% NaCl, 0.9% NaCl, 1.5% NaCl, 2.5% NaCl and complete DMEM at 37 °C with 5% CO_2 for 30 minutes. Thereafter, cells were immediately fixed using 4% PFA at RT for 10 minutes and processed for SEM and fluorescence microscopy separately. For SEM preparation, please see section 2.3. For fluorescence imaging, fixed cells were washed three times and then incubated with phalloidin-TRITC for 20 minutes at RT. Specimens were then washed three times with PBS and dH_2O separately, before mounting onto a glass slide through mowiol and drying overnight. Samples were imaged using a Nikon Eclipse Ti widefield microscope by 60x oil immersion objective (1.4 NA Plan Apo) in Cy3 channel (excitation: 545/25 nm, emission: 605/70 nm) with z stacking of 100 nm interval and 20 μm thickness. Images were analysed using *ridge detection* (2.3.2) and shape analysis (2.3.4) of Fiji software.

Overnight culture of J774 cells

Replace old media with fresh comp DMEM or different concentrations of NaCl in dH_2O for 30 minutes

Process samples for fluorescence microscopy examination

Process samples for SEM examination
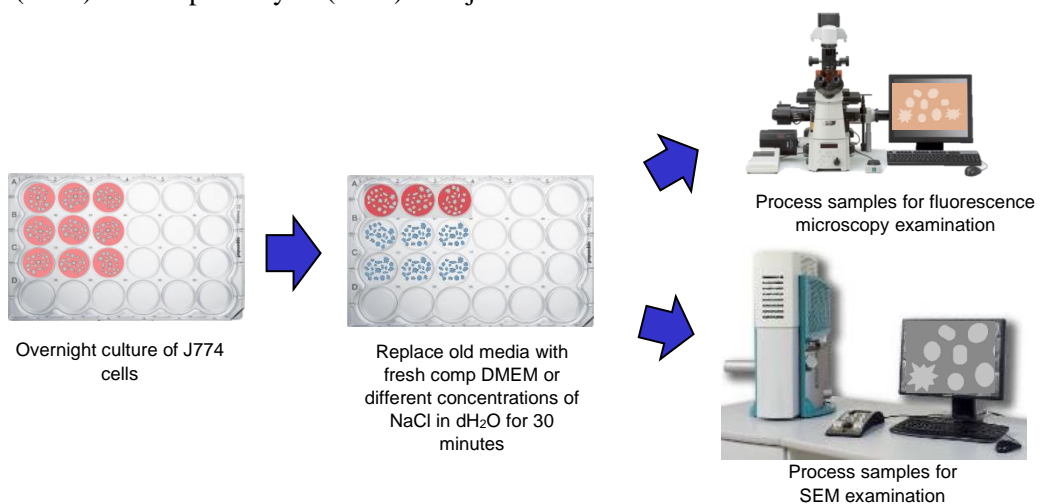
Figure 2.1 Osmosis experiment workflow summary

2.9 Phagocytosis assay using beads

The phagocytosis assay using beads is summarised in Figure 2.2. A healthy culture of J774 cells ($1x10^5$ cells/well) were seeded into a 24-well plate with glass coverslips and allowed to acclimatise overnight at 37 °C and 5% CO_2. Macrophages (MΦ) were then incubated with beads (Polysciences 17152-17156) in serum-free media (i.e. complete DMEM without FBS): 0.25 μm, 0.5 μm, 1.0 μm, 1.5 μm and 3.0 μm radius, in triplicates using a multiplicity of infection (MOI) of 1 MΦ: 10 beads. Each bead suspension was vortex mixed for at least 2 minutes before incubating with MΦ. After 30 minutes, samples were immediately fixed with 4% PFA for 10 minutes at RT, washed with PBS and dH_2O three times separately, mounted onto glass slides using mowiol and dried overnight. SEM imaging of bead phagocytosis was also performed using 2.3 after PFA fixation.

Samples were imaged using a 60x oil immersion objective lens (1.4 NA Plan-Apo) in modified DIC (all DIC parts except the polariser) and GFP channels (excitation: 470/40 nm, emission: 525/50 nm) of a Nikon Eclipse Ti widefield microscope. Imaging was done with z-stacking using different intervals depending on bead size (i.e. +0.5 of the bead diameter) and a range of 15 μm. Three images per replicate were taken, and phagocytosis was assessed by manually scoring each image for total MΦ, MΦ in phagocytosis (i.e. with internalised beads), number of beads attached to MΦ and number of beads internalised by MΦ using NIS Elements v4.11.

Overnight culture of J774 cells

Incubate with beads of different sizes in triplicates for 30 minute using 1MΦ:10beads MOI

Process samples for widefield imaging

Score for phagocytic uptake
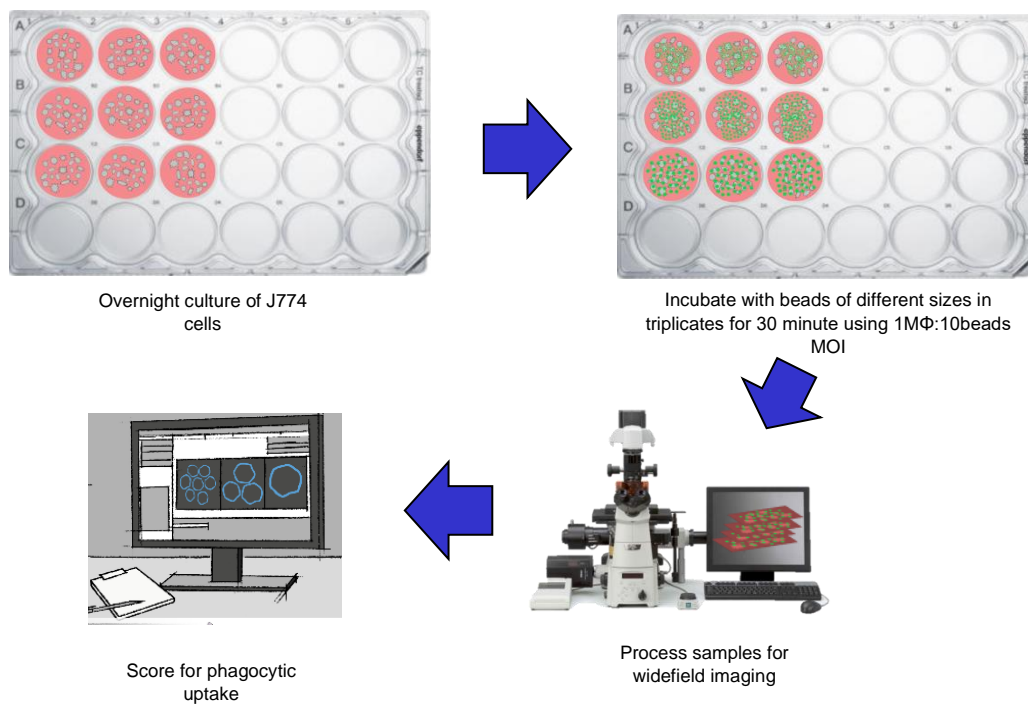
Figure 2.2 Beads *in vitro* phagocytosis assay workflow summary

2.9.1 Phagocytosis assay with amiloride

Phagocytosis assay with amiloride to inhibit MΦ macropinocytosis was performed. J774 cells ($1x10^5$ cells/well) seeded in 24 well-plate overnight at 37 °C and 5% CO_2 were exposed to 1 mM amiloride in serum-free media for 30 minutes. Immediately after, cells were incubated with 1 um beads (Polysciences 17154) suspended in serum-free media using an MOI of 1:10 for 30 minutes. After incubation, samples were processed and analysed as in section 2.9 for fluorescence microscopy and as in section 2.3 for SEM.

2.9.2 Bead settling assay

Beads (Polysciences 17152 - 17156) of different sizes (0.25 μm, 0.5 μm, 1.0 μm, 1.5 μm and 3.0 μm radius) suspended in serum-free media and at similar concentrations ($1x10^6$ beads/ml) were allowed to settle in a 24-well plate for 30 minutes. A triplicate for each bead size was prepared and an image of the central bottom of the well was taken after 30 minutes using Nikon Eclipse Ti with 20x objective lens (0.45 NA S Plan-Flour) in GFP channel (excitation: 470/40 nm, emission: 525/50 nm). Images were processed and analysed using Fiji. *Thresholding* was used to detect beads on each image and *watershed* segmentation was applied to separate beads in close contact. Bead count was then estimated using *particle analysis* (PA)*,* and the total number of beads settled was computed for each bead size. Beads were also counted manually to compare results with PA and compute the relative error.

2.9.3 Opsonised beads phagocytosis assay

Beads (Polysciences 17152 - 17156) were opsonised by incubating with filter sterilised 10 mg/ml bovine serum albumin (BSA, Fisher BioReagents BP9704) in PBS overnight with gentle spinning (20 rpm) at 4 °C. Thereafter, beads were washed three times with PBS and incubated with mouse monoclonal anti-BSA (Sigma B2901) with 1:1000 dilution for one hour with spinning (20 rpm) at RT. Beads were then washed with PBS three times and stored at 4 °C. A confirmatory test for bead opsonisation was done by incubating beads with anti-mouse IgG Alexflour647 (ThermoFisher A21237) for 30 minutes and imaging them with Nikon Eclipse Ti using 20x objective lens (0.45 NA S Plan-Flour) in GFP (excitation: 470/40 nm, emission: 525/50 nm) and Cy5 (excitation: 620/60 nm, emission: 700/75 nm) channels. Settling of opsonised bead was also quantitated as in 2.9.2.

After confirming successful opsonisation, beads were used in phagocytosis assay as in 2.9. Phagocytic uptake of unopsonised beads and opsonised beads by MΦ were then compared and analysed.

2.10 Phagocytosis assay using Cryptococcus

Two strains of *Cryptococcus neoformans* (Cn): H99 (serotype A) -wild type, capsular and CAP59- acapsular type, were used for phagocytosis assay. Bead stocks of these cells were recovered from -80 °C freezer, seeded and allowed to grow in yeast extract peptone dextrose (YPD) plates at 28 °C for two to three days. Colonies were re-streaked onto a new YPD plate, and yeast cells were allowed to grow for about 2-3 days until sufficient colonies were available for assay. A loopful of culture was then suspended into 5 ml culture tube containing 2 ml YPD with constant 20 rpm rotation at 28 °C. In parallel, a healthy culture of J774 cells ($1x10^5$ cells/well) were seeded in a 24-well plate with glass coverslips overnight at 37 °C and 5% CO_2. H99 and CAP59 Cn were then washed the following day before using in phagocytosis assay. H99 were washed three times with PBS whilst CAP59 were washed with 0.1% PBS-Tween to discourage cell clustering. Furthermore, CAP59 tubes were allowed to stand for 30 minutes, and only the topmost layer (~100 ul) of each tube was used to avoid picking cell clusters.

Washed H99 and CAP59 were incubated with calcofluor white (Sigma 18909) in 1:100 dilution for 20 minutes at RT. Cells were then washed with PBS, and concentration was adjusted to $1x10^6$ CFU/ml and suspended in a serum-free media for phagocytosis and settling assays. Old media of acclimatised J774 cells were replaced with 1 ml of either H99 or CAP59 suspension. A triplicate for each H99 and CAP59 infection was set up, and samples were incubated for 2 hours at 37 °C and 5% CO_2. After incubation, samples were fixed immediately using 4% PFA for 10 minutes at RT. Excess PFA was then neutralised by applying 50 mM NH_4Cl for 5 minutes. Thereafter, cells were permeabilised using 0.1% Triton X-100 for 3 minutes before incubating with 18B7 (Casadevall, 1998) for 20 minutes at RT for capsule staining. Samples were then washed with PBS three times before incubating with anti-mouse IgG-FITC for 20 minutes followed by another 20 minutes incubation with phalloidin-TRITC at RT. Samples were then washed with PBS and dH_2O three times separately before mounting onto clean glass slides using mowiol. Samples were imaged using a Nikon Eclipse Ti with 60x oil immersion objective (1.4 NA Plan-Apo) in DAPI (excitation: 436/20 nm, emission: 480/40 nm), GFP (excitation: 470/40 nm, emission: 525/50 nm) and Cy3 (excitation: 545/25 nm, emission: 605/70 nm) channels of a widefield microscope. Three fields of view were imaged per replicate (a total of nine images per variant) starting at the centre of each coverslip. Phagocytic uptake was scored as in the previous section (2.9) and capsule size of H99 taken up by MΦ was measured by drawing a line across the cell (through its largest diameter if not perfectly spherical) using the cell wall as a reference border.

Meanwhile, H99 and CAP59 cells that were not used in phagocytosis assay were then used for settling assay. One ml of each variant ($1x10^6$ CFU/ml) was placed in a 24-well plate

in triplicates and incubated for 2 hours at 37 °C and 5% CO_2. After incubation, samples were then imaged using a Nikon Eclipse Ti with 20x objective lens (0.45 NA S Plan-Flour) in phase contrast and DAPI (excitation: 436/20 nm, emission: 480/40 nm) channels. Imaging was optimised by using camera settings with no binning, automated exposure and ¼ gain of Andor Neo SCC-02546. The number of cells in each image was then counted using PA analysis as in previous 2.9.2.

H99 cells that were not used in phagocytosis assay were fixed onto coverslips using 4% PFA for 10 minutes at RT. They were then incubated with 50 mM NH_4Cl for 5 minutes before staining with 18B7 for 20 minutes at RT. Samples were then washed with PBS and dH_2O separately three times before mounting with mowiol onto glass slides and drying overnight. Samples were images using Nikon Eclipse Ti with 60x oil immersion objective (1.4 NA Plan-Apo) in DAPI (excitation: 436/20 nm, emission: 480/40 nm), GFP (excitation: 470/40 nm, emission: 525/50 nm). Capsule size was measured manually as in previous.
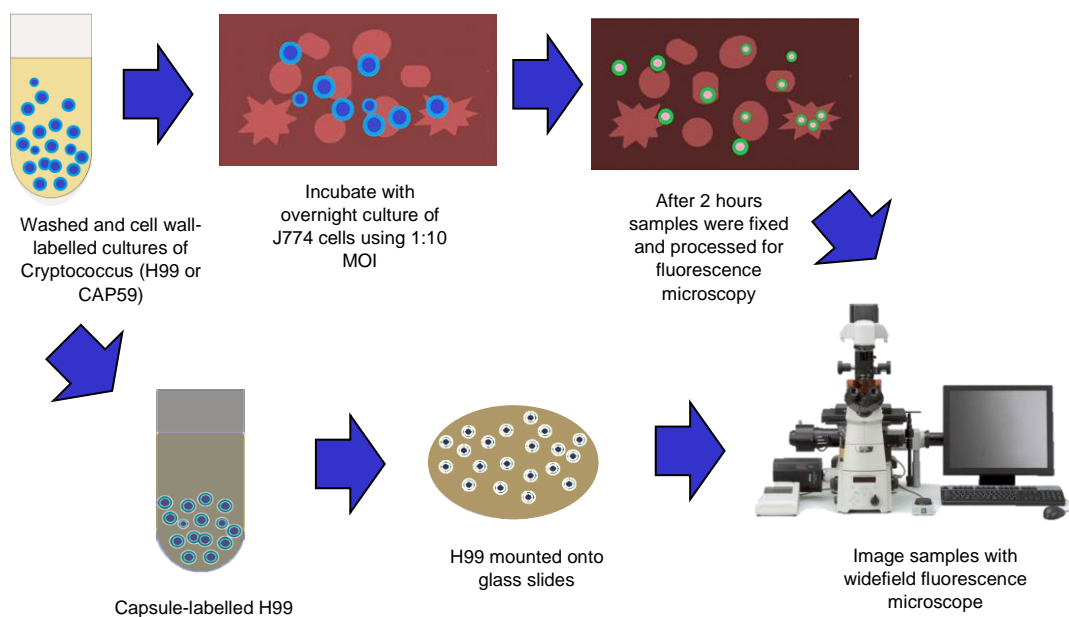
Figure 2.3 Cryptococcus *in vitro* phagocytosis assay workflow summary

2.10.1 Opsonised H99 phagocytosis assay

A phagocytosis assay comparing unopsonised and opsonised H99 cells was also carried out. H99 Cn that were prepared as in previous (2.10) were opsonised using 18B7 (1 ul per $1x10^6$ CFU) for one hour at RT with constant 20 rpm rotation. Opsonised H99 were then used in phagocytosis assay as in previous (2.10), and its uptake was compared with unopsonised H99.

2.10.2 Cryptococcus phagocytosis assay with ridge repression

Healthy cultures of J774 cells and H99 and CAP59 Cn were prepared as in previous (2.10). J774 cells were first incubated with CAP59 Cn for one hour using an MOI of 1 MΦ: 10 Cn, this was then followed by incubation with either H99 or CAP59 using the same MOI. A control was also setup by incubating J774 cells with H99 or CAP59 without pre-incubation with CAP59. Samples were fixed and processed thereafter for fluorescence microscopy as in previous (2.10). Finally, images were scored for phagocytic uptake and analysed as previously.

2.11 Cryptococcus SEM phagocytosis assay

A healthy culture of J774 macrophage-like cells was seeded into 24-well plate with glass coverslip overnight at 37 °C and 5% CO_2. They were then challenged with either H99 or CAP59 Cn (processed as in 2.10) at 0, 5, 10, 20, 30, 60 and 120-minute timepoints. Samples were then fixed and processed for SEM examination as in previous (2.3). Single cell SEM images were taken using 10 kV accelerating voltage, 9 mm working distance, 63 nm spot size and 0° stage tilt. Twelve images per timepoint were taken, and were processed manually using *ridge detection* (2.3.2) to measure their ridge and ruffle area densities separately. Area densities for each protrusion was derived by dividing the total cross-sectional area of the protrusion to total cross-sectional area of the cell.

CAP59 and H99 cells that were not used in phagocytosis assay were also processed separately for SEM by fixing them onto glass coverslips using 4% PFA. Succeeding steps of SEM sample processing (2.3) were then carried out.

2.12 Statistical analysis

All experiments were repeated independently at least three times. The specific statistical tests and post hoc tests used can be found in each figure legend in the results section (chapter 3-5). In all analyses, statistically significant results were considered if within 95% confidence limit. Statistical notations showing significance (asterisks) were not shown in comparisons with more than two groups which were otherwise shown in tables. All statistical tests and plots were done using GraphPad Prism v7.0a – 9.3.1.

CHAPTER 3

Identification and characterisation of actin containing membrane ridges on macrophages

3.1 Introduction

Macrophages are amongst the most numerous and diverse types of leucocytes in the body (Williams et al., 2018). They appear as early as day six of mammalian embryonic development and reside in different tissues and organs to participate in various events of homeostasis and development (Wynn et al., 2013; Theret et al., 2019). They are more commonly known for their canonical role in providing immunity by engulfment of pathogenic microbes and communicating with other immune cells to orchestrate a systemic response to infection (Turner et al., 2014).

Macrophages continuously monitor the surrounding milieu to shift their functional states in response to pathogenic microbes, apoptotic cells, tumours and tissue injury (Stow and Condon, 2016; Wynn et al., 2013). This requires rapid sensing of the extracellular environment and eliciting responses that will restore tissue homeostasis. The macrophage plasma membrane resembles similar architecture with other eukaryotic cells having a phospholipid bilayer framework with embedded proteins (Nachman et al., 1970); however, an important difference is the enrichment of receptors in the macrophage surface which allows them to identify and respond to various external stimuli (reviewed extensively by Taylor et al., 2005). The macrophage membrane is believed to be organised in a manner that will allow optimal response to these external cues. For instance, stimulation of a bacterial cell wall component, lipopolysaccharide (LPS), affects the critical point of phase separation between different types of lipids within the macrophage membrane by favouring the formation of lipid rafts (Cammarota et al., 2020). This subsequently leads to recruitment of receptors with lipid raft affinity such as TLR4, CXCR4 and CD14, which usually require interaction for their activation and successful transduction of extracellular signals (Triantafilou et al., 2002: Nakahira et al., 2006; Wong et al., 2009). These then ultimately result to metabolic changes in macrophages that promote a pro-inflammatory response to counter the threats of invading bacteria.

Another feature that highlights structural and functional organisation of the macrophage membrane are its diverse and numerous membrane protrusions. The best studied types are lamellipodia, filopodia, dorsal ruffles and podosomes, not only because of their unique structural properties but also because of their widespread occurrence in other cell types

such as fibroblasts, osteocytes, neurons, dendritic cells, cancerous cells and many other specialised cells (Svitkina, 2018; Matilla and Lappalainen, 2008; Stow and Condon, 2016; Labernadie et al., 2014). Lamellipodia are flat sheets of membrane extension commonly found at the leading edge of migrating cells. They propel the cell forward by generating a pushing force from a network of branched actin filaments polymerising against the membrane (Wang, 1985). Filopodia, on the other hand, are cylindrical protrusions supported by parallel bundles of actin filaments. They also participate in cell migration by promoting a cell-matrix adhesion that stabilises the advancing lamellipodium (Matilla and Lappalainen, 2008). Other roles include mechanosensory, chemosensory and cell-to-cell communication (Albuschie and Vogel, 2013; Goodman et al., 2019). Dorsal ruffles are large, sheet-like protrusions on the dorsal cell surface which are known to be induced by activation factors such as LPS, M-CSF and PMA (Patel and Harrison, 2008; Yoshida et al., 2015). They can form complex structures by circularising, fusing and collapsing back to the membrane for non-selective uptake of fluids, pathogens and receptors (Stow and Condon, 2016; Patel and Harrison, 2008). Lastly, podosomes are cone-shaped actin-rich structures surrounded by a ring of adhesion proteins integrins, vinculins and talins on the basal cell surface in contact with the substratum (Labernadie et al., 2014). They possess enzymatic activities and are shown to be important in cell migration, mechanosensing and cell fusion (Monypenny et al., 2011; Labernadie et al., 2014; Faust et al., 2019).

Recent advances in combining specimen preparation, microscopy and image analysis allowed us to examine and accurately describe the biophysical and biochemical properties of the macrophage membrane surface. These revealed many important features of macrophage biology in relation to its outermost structures. In this chapter, I will present my findings on a highly conserved membrane protrusion I discovered whilst examining the macrophage membrane using advanced microscopy techniques. Henceforth, I will refer to this structure as a membrane ridge. Its nanoscopic dimensions coupled with its localisation on the apical cell surface required customised imaging set-up and resolutions beyond the diffraction limit in order to study its architecture and dynamics. These might also be the important reasons for its recent discovery in spite of the voluminous studies on macrophage structural features dating back more than 50 years. Using different electron and superresolution microscopy techniques, I will describe the biophysical properties of membrane ridges in both *in vitro* and *in vivo* settings. I will compare its properties with other types of well-studied membrane protrusions and describe its dynamics on the surface of a macrophage. Lastly, I will present various factors that affect its expression which might provide further insights on its roles in macrophages and other phagocytes.

3.2 The different features of a macrophage's surface

Amongst the important properties of a macrophage is its ability to produce different types of membrane structures to perform migratory, sensory and phagocytic functions. The membrane surface is a dynamic yet well-organised structure that allows the cell to assume these complex roles. Initially, I was keen to describe the topographical properties of a macrophage external surface to model biophysical interaction with targets of different sizes during phagocytic uptake. To do this, I used scanning electron microscopy (SEM) and several types of *in vitro* cultures of unstimulated primary and immortalised macrophages.

SEM is a powerful technique in probing cell surfaces. It has a simple workflow, an achievable resolution of 3 nm and a wide range of viewing field which allows individual cell and cell population to be examined with high resolution (Erdman et al., 2019). However, an overwhelming challenge in probing macrophage membrane surface using SEM is preserving its native architecture and preventing its collapse and damage during specimen preparation. Hence, I tried different fixation and drying methods, and optimised a critical point drying routine (Chapter 2.3) that enabled high resolution SEM examination of macrophage membrane close to its native state.

To describe the features of macrophage external surface, a healthy culture of mouse bone marrow-derived macrophages (BMDM) *in vitro* was processed and imaged using SEM (Figure 3.1). Macrophages were commonly seen with a bright cell body (Figure 3.1 yellow arrow) and some usually less bright membrane protrusions (Figure 3.1 green arrow) extending from it. Macrophages exhibited diverse shapes: round, spindle-like, fan-like and irregular shape, which can be influenced by the type and extent of membrane protrusions they possess. These suggest remarkable mechanical properties of these cells that allow them to assume different shapes and generate different types of membrane protrusion.
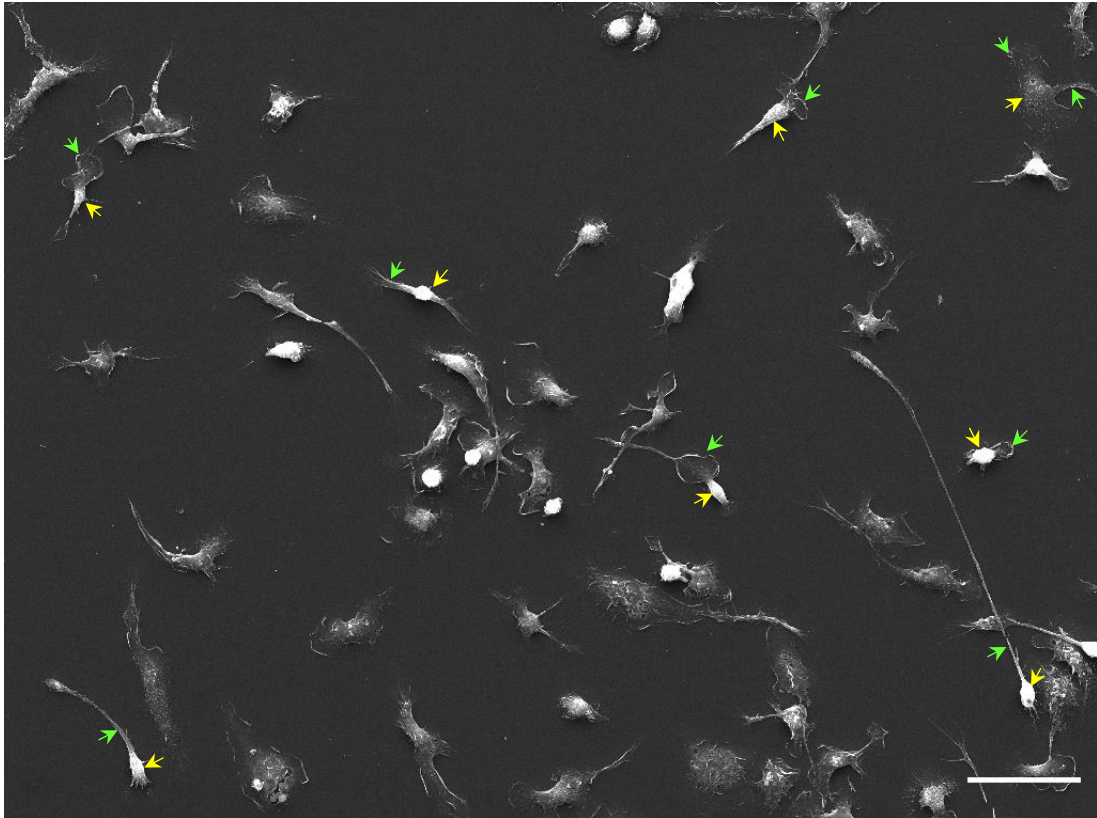
Figure 3.1 | **Scanning electron microscopy (SEM) of bone marrow-derived macrophages (BMDM) cultured *in vitro* illustrates the highly diverse morphology that macrophage populations can assume.** BMDM cells were differentiated and cultured into a 24-well plate with uncoated glass coverslips for 5-6 days. Healthy cells were then fixed and processed using an optimised SEM protocol (Chapter 2.3). Cells were imaged using a high vacuum, thermionic emission scanning electron microscope with an SE detector system and 30 kV accelerating voltage, 9 mm working distance, 63 nm spot size and 0° stage tilt. **Cell body**-yellow arrow; **Cell protrusion** - green arrow**.** Image is a representative of 9 images from 3 independent experimental repeats. Scale bar- 50 μm.

3.3 Macrophages possess different types of membrane protrusion

The diverse morphologies I observed in macrophages prompted me to examine individual cells to accurately describe the macrophage external surface. For single cell SEM imaging, I used a magnification of 10000x - 30000x due to their highly variable sizes *in vitro.* An accelerating voltage of 10 kV was used to produce a lower interaction volume and lesser penetration of the electron beam which enabled resolving the outermost features of cells being observed.

Flat, thin sheets of membrane called *lamellipodia* (Figure 3.2A) were observed extending from the macrophage cell body. These are a common feature of migratory cells such as fibroblasts, keratocytes, mesenchymal cells and cancer cells (Innocenti, 2018). In the

macrophage cell culture, these structures were frequently observed, as expected, given the mobility of these cells *in vitro*. The macrophage lamellipodia have a non-uniform border with occasional peripheral ruffles (yellow arrow) protruding from its dorsal surface (Figure 3.2A). The competing theories on the origin of these ruffles are discussed in the following subsection (3.12.1).

Macrophages were also seen to possess narrow, finger-like *filopodial* protrusions (Figure 3.2C). Filopodia were usually straight but a bent morphology was also observed (zoomed in box, yellow arrow). These properties are believed to be an inherent feature of filopodia which enables the cell to navigate through different types of extracellular matrix (Leijnse et al., 2015). In addition, macrophage filopodia were observed to originate from two different cell regions: cell body (Figure 3.2C green arrow) or lamellipodia (Figure 3.2D). These support the different theories on filopodia origin which is discussed in the succeeding subsection (3.12.1).

Quite uncommonly, I observed large sheets (>1 μm) of membrane protrusions projecting from the dorsal surface of a macrophage (Figure 3.2E). These are dorsal ruffles, which are known for their wavy borders that can circularise and fuse to form a cup-shaped membrane derivative called a macropinocytic cup (Figure 3.2F). The dorsal ruffles illustrated constitute the borders of a very large cup with an opening of about 2 um in diameter. Ruffles were observed to be rare in *in vitro* cultures of unstimulated macrophages, and were less frequently expressed than filopodia or lamellipodia by these cells.

I also noticed another type of sheet-like membrane protrusion on the dorsal macrophage surface. They were smaller, did not usually associate with macropinocytic cups and were much more common than dorsal ruffles. Because of their appearance in the cell surface in 3D (Figure 3.3C), I called them *membrane ridges*. Upon examining the available literature, I found no systematic investigation on its architecture nor its specific role in macrophages, although they were briefly mentioned in the report of Takayama et al. (1976) and described in relation to phagocytosis by Petty (1981) and co-workers. They were also seen in other immune cells such as mast cells (Burwen and Satir, 1977; Deng et al., 2009; Solsona et al., 1998) and neutrophils (Hocde et al., 2009; Jumaa et al., 2017), where they were also referred to as membrane folds, microridges or wrinkles. In neutrophil-like cells, HL-60, ridge-like features were also described (Fritz-Laylin et al., 2017) showing consistent thickness but with more than twice the thickness and forming complex pseudopodial derivatives, making it less likely to be similar to the ridge described in this thesis. Ridge fundamental properties with respect to their structure, dynamics on the membrane and functions are largely unexplored especially in the context of macrophage biology; hence, I carried on investigating these structures by first describing their geometrical properties (i.e. length, thickness, curvature and

area density) using different electron microscopy techniques and examined their internal architecture using transmission electron microscopy and airyscan superresolution microscopy.
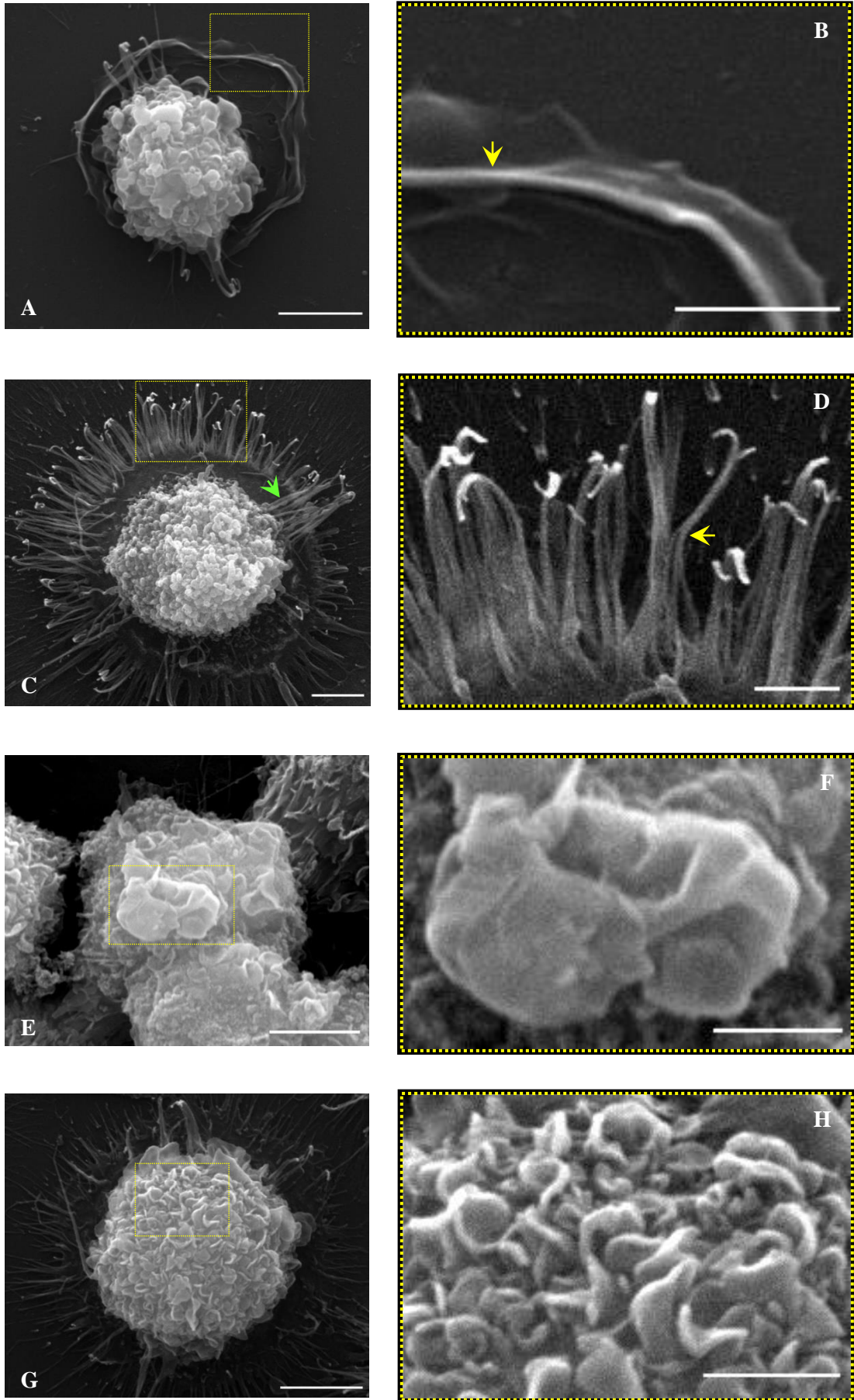
(Figure legend on the next page)

Figure 3.2 | **SEM examination of human monocyte-derived macrophages (HMDM)** *in vitro* **reveals the different types of membrane protrusion they possess.** HMDM cells were differentiated and cultured into a 24-well plate with uncoated glass coverslips for 7 days. Healthy cells were then fixed and processed using an optimised SEM protocol (Chapter 2.3). Cells were imaged using a high vacuum, thermionic emission scanning electron microscope with an SE detector system under 10 kV accelerating voltage, 9 mm working distance, 63 nm spot size and 0° stage tilt. **Left-** main panel, scale bar - 5 μm, **Right**- zoomed in section of a region (yellow box) in the left image, scale bar - 2 μm. Zoomed in images were enhanced by improving image brightness and contrast using LUTs in Fiji (Schindelin et al., 2012).

(A) An HMDM with planar and wavy sheet-like protrusions, *lamellipodia*, on its leading edge,

(B) Zoomed in region in *A* showing the wavy borders and peripheral ruffles of lamellipodia protruding dorsally,

(C) An HMDM with numerous finger-like protrusions, *filopodia*, revealing two different protrusion origins: **cell body** (green arrow) or **(D) lamellipodia** (zoomed in region of *C*) which also featured bent (yellow arrow) filopodia,

(E) An HMDM possessing large, sheet-like *dorsal ruffles* forming a macropinocytic cup,

(F) Zoomed in image of macropinocytic cup in *E* showing its ruffled border and an opening of about 2 μm in diameter,

(G) An HMDM having nanoscopic, sheet-like dorsal protrusions, *membrane ridges*,

(H) Zoomed in image of *G* showing the wavy feature and very dense expression of membrane ridges.

3.4 Membrane ridges are sheet-like protrusions with consistent thickness

To accurately describe the morphological properties of nanoscopic membrane ridges, I modified specimen preparation protocols for both transmission electron microscopy (TEM) and scanning electron microscopy (SEM), and used different image analysis scripts that automate ridge measurements. To examine specimens using TEM, I used orthogonal slicing with respect to the basal surface of embedded cells to illustrate the cross-sectional features of membrane ridges as they protrude from the macrophage dorsal surface. I used a combination of paraformaldehyde and glutaraldehyde fixatives for SEM specimen preparation, and optimised a critical point drying set up to prevent membrane collapse in high vacuum SEM. I then designed an image analysis routine based on published and custom-built image processing scripts to automate membrane ridge measurements using 2D SEM images.

To describe the geometrical properties of membrane ridges (length, width and area density), I analysed unprocessed SEM images of J774 macrophage-like cells (Hirst et al., 1971) through an image analysis script, *ridge detection* (Steger, 1999) of Fiji software (Schindelin et al., 2012). *Ridge detection* (RD) identifies each ridge as a line profile (Figure 3.3B) for its accurate and automated measurement without post processing or modifications of the raw image. I optimised image analysis workflow by setting RD parameters that accurately detect membrane ridges on each image. For a more detailed script description, the reader is referred to Steger (1999). Prior to this automated analysis, I manually measured membrane ridge thickness by drawing a line across the midsection of each ridge (Figure 3.3A-inset, orange line) using the built-in SEM analysis software (Tescan Vega3 LMU). The relative error of RD measurement (table 3.1) was then derived using the formula:

$$Relative\ error_{ridge\ detection} = \frac{|RD\ measurement - manual\ measurement|}{manual\ measurement} \tag{3.1}$$

RD mean relative error was found to be 2.22%, demonstrating a 97.78% accuracy rate of RD script to measure membrane ridge thickness. To further examine the relationship between manual and RD measurements, I used linear regression analysis (Figure 3.3D) and found a high correlation ($R^2 = 0.978$, $p < 0.0001$) between these values. Hence, I used RD as a central component of an image analysis routine to survey and measure membrane ridge properties.

SEM imaging of J774 cells demonstrated a high density of membrane ridges on their dorsal surfaces. Photometric stereo SEM allowed 3D reconstruction of the macrophage membrane surface (Figure 3.3C), and this confirmed the sheet-like property of membrane ridges. Furthermore, their variable height along their length was also noticeable (Figure 3.3C-zoomed in colour-coded depth map).

To estimate the area density of membrane ridges in J774 cells, I used the formula:

$$Ridge\ area\ density = \frac{total\ ridge\ cross-sectional\ area}{total\ cell\ cross-sectional\ area} \tag{3.2}$$

I computed ridge surface area by multiplying the length and width (thickness) of ridges from RD measurements, whilst to derive the cell surface area, I manually traced the outermost outline of each cell through their cell membrane. It should be noted that all surface area measurements referred to throughout this dissertation are cross-sectional surface area in

contrast to 3D surface area which requires voluminous image sampling by photometric stereoscopy and a script that detects and discriminates ridge contour in 3D from other types of membrane protrusion. Both of which will require a significant amount of time to carry out working protocols, hence I used cross-sectional area to approximate the density of membrane ridges and other cellular features. Computation of ridge area density (Figure 3.3G) revealed that membrane ridges constitute about 20% of the total cross-sectional surface area of J774 macrophage-like cells grown in a complete DMEM culture media.

The consistency of membrane ridge thickness along its length was a very striking feature in both raw SEM images (Figure 3.3A- inset, orange line) and 3D macrophage surface reconstruction (Figure 3.3C- zoomed in red broken lines). Hence, I analysed various macrophage SEM images and combined all thickness measurements into a single histogram (Figure 3.3E) to further examine this feature. This confirmed the highly consistent thickness of membrane ridges with a mean thickness of 142 nm (SD = 23). Its length (Figure 3.3F) however was found to be more variable having a mean measurement of 841 nm (SD = 619). Moreover, its length profile showed a positively skewed distribution (g_1 = 2.207), indicating that shorter ridges were more common than longer ones.

A

B

C

D

E

F
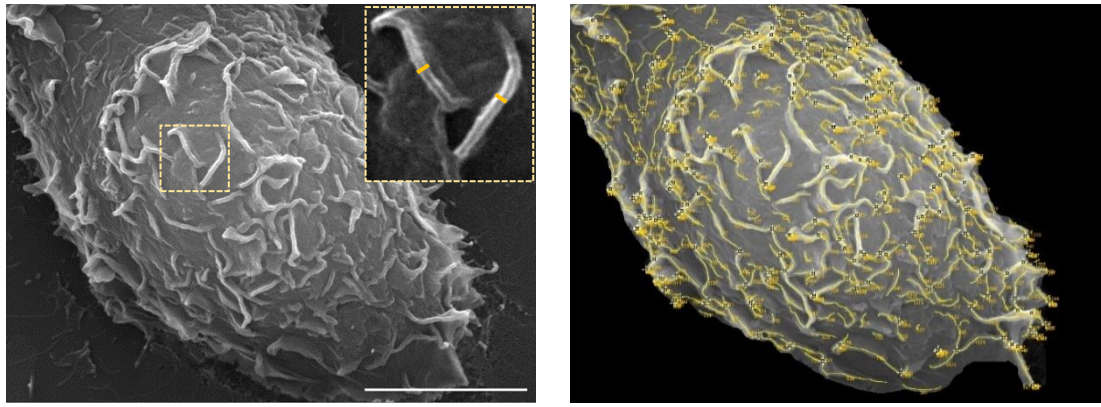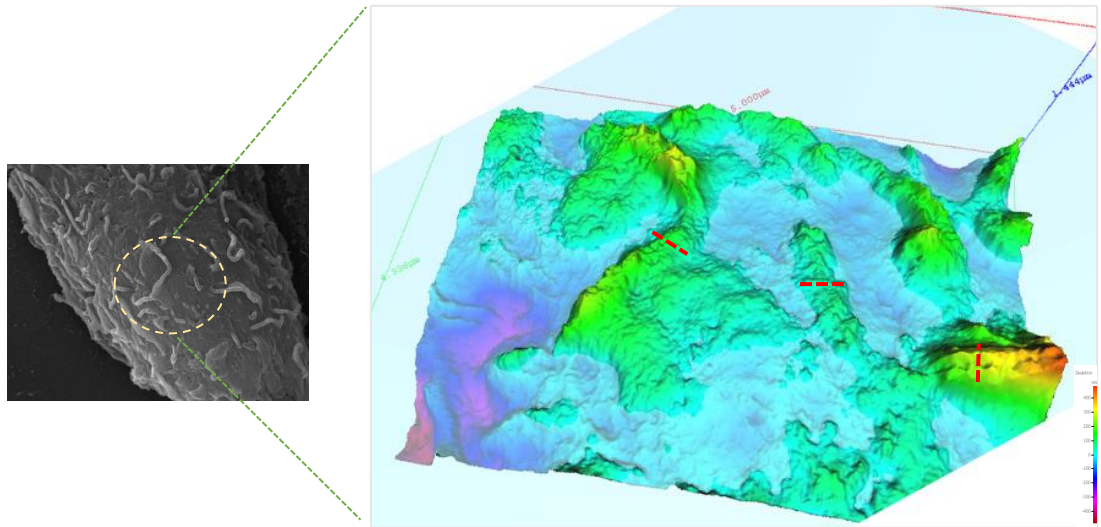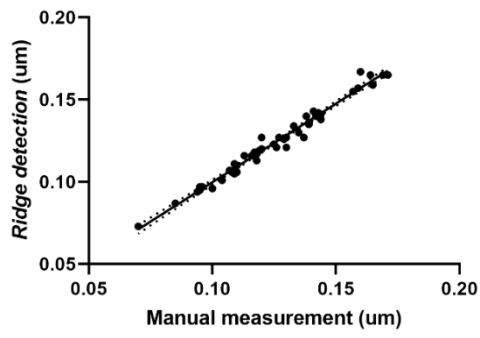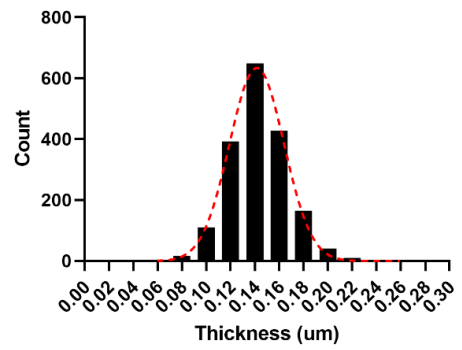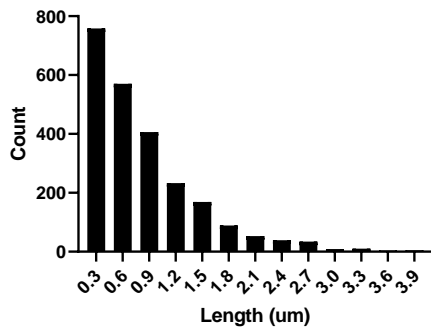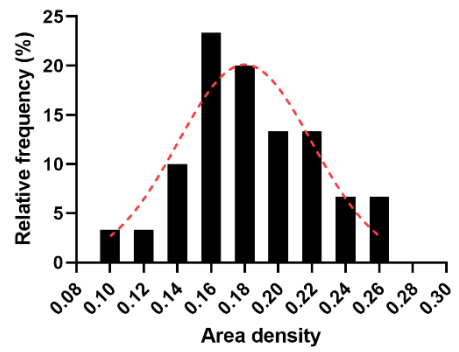
G

(Figure legend on the next page)

Figure 3.3 | Membrane ridges are nanoscopic sheet-like protrusions with consistent thickness localised on the dorsal surfaces of macrophages cultured *in vitro*. A healthy culture of J774 macrophage-like cells in complete DMEM media was plated into a 24-well with uncoated glass coverslips. After allowing to settle and acclimatise overnight, cells were then fixed and processed using an optimised SEM protocol (Chapter 2.3). Cells were imaged with a high vacuum, thermionic emission scanning electron microscope coupled with an SE detector system under 10 kV accelerating voltage, 9 mm working distance, 63 nm spot size and 0° stage tilt. 3D reconstruction was rendered using Alicona MeX software and by tilting the stage to ± 12° after an automated angular calibration focussing membrane ridges. Images are a representative of 20 cells analysed from 2 independent imaging experiments.

(A) A raw SEM image of a J774 cell, inset shows a zoomed-in section of membrane ridges and thickness annotation (orange arrow), scale bar - 5 um.

(B) Image *A* analysed by *ridge detection* (RD) script,

(C) Macrophage membrane surface and ridges viewed in 3D by photometric stereoscopy showing a colour-coded depth map (zoomed in image),

(D) Linear regression analysis between manual and RD measurements showed high measurement correlation ($R^2 = 0.978$, $p < 0.0001$),

(E) A combined histogram of membrane ridge thickness values from all J774 cells examined, red curve shows a Gaussian fit ($R^2 = 0.997$, $n = 12$ cells (1818 ridges), thickness mean (M) = 0.142, standard deviation (SD) = 0.023),

(F) A combined histogram of length measurements of membrane ridges from all J774 cells examined ($n = 12$ cells (1818 ridges), skewness (g_1) = 2.207, median = 0.670, $M = 0.841$),

(G) A combined histogram of area density of membrane ridges from all J774 cells examined, red curve is a Gaussian fit ($R^2 = 0.793$, $n = 30$ cells, $M = 0.18$, $SD = 0.04$).

Automated measurement	Manual measurement	Relative error
0.140	0.138	0.014
0.110	0.110	0.000
0.101	0.104	0.029
0.111	0.109	0.018
0.116	0.113	0.027
0.107	0.107	0.000
0.123	0.125	0.016
0.121	0.126	0.040
0.135	0.139	0.029
0.106	0.108	0.019
0.105	0.109	0.037
0.140	0.142	0.014
0.106	0.110	0.036
0.121	0.130	0.069
0.096	0.100	0.040
0.127	0.130	0.023
0.157	0.159	0.013
0.159	0.165	0.036
0.155	0.157	0.013
0.138	0.144	0.042
0.118	0.117	0.009
0.130	0.135	0.037
0.127	0.127	0.000
0.165	0.164	0.006
0.143	0.141	0.014
0.165	0.169	0.024
0.126	0.129	0.023
0.117	0.118	0.008
0.127	0.137	0.073
0.127	0.120	0.058
0.165	0.171	0.035
0.141	0.144	0.021
0.097	0.095	0.021
0.120	0.120	0.000
0.119	0.119	0.000
0.134	0.133	0.008
0.113	0.118	0.042
0.116	0.116	0.000
0.094	0.094	0.000
0.119	0.119	0.000
0.087	0.085	0.024
0.073	0.070	0.043
0.167	0.160	0.044
0.136	0.139	0.022
0.095	0.095	0.000
0.142	0.143	0.007
0.097	0.096	0.010

Table 3.1 | Comparison of automated and manual measurements of membrane ridge thickness

To illustrate the cross-sectional morphology of membrane ridges with high resolution imaging, I used transmission electron microscopy (TEM). Knowing from previous SEM experiments that membrane ridges localise on the dorsal surface of the cell in *in* vitro cultures, I oriented my samples so that a section (Figure 3.4A red box and 3.4B) passing through the tip and base of the ridge could be prepared and examined. TEM examination revealed three distinct regions of a membrane ridge (Figure 3.4C): a slightly wide **base** (green arrow and dotted line), a main **body** (orange double arrow) with highly consistent thickness and a slightly narrow and curved **tip** (red arrow). These data indicate that my previous finding of consistent membrane ridge thickness was mainly due to the thickness of its main body which makes up almost its entire architecture.
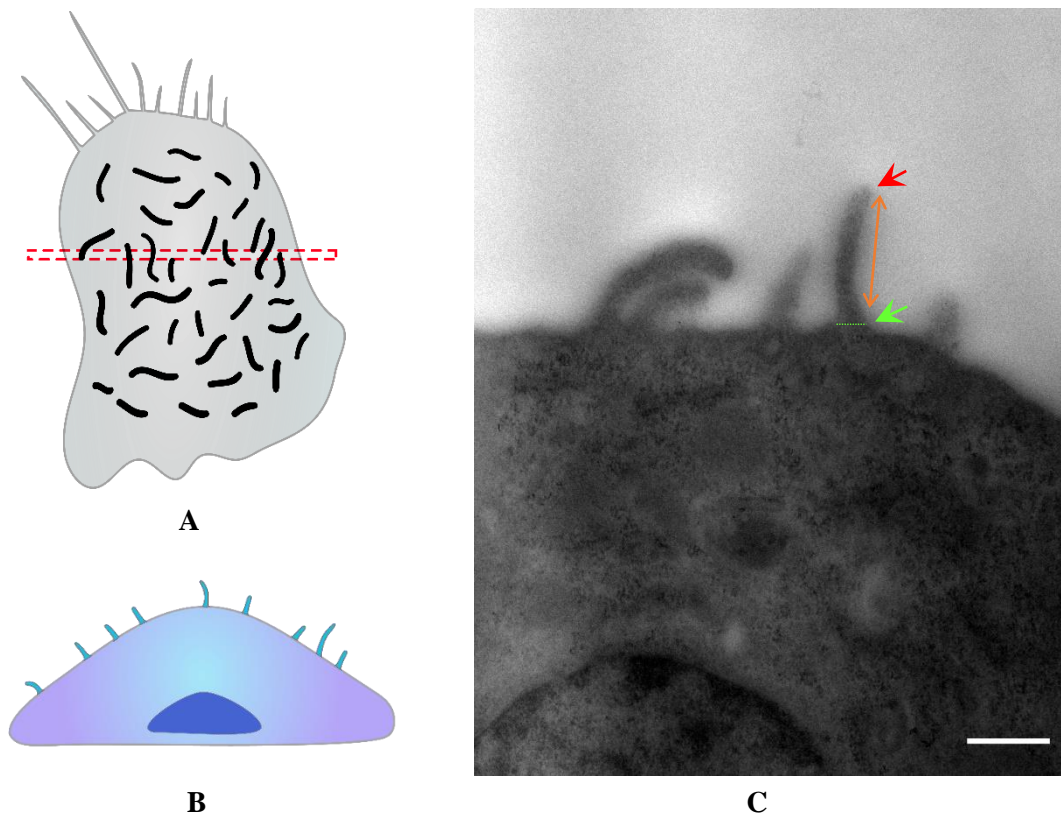
(Figure legend on next page)

Figure 3.4 | Transmission electron microscopy (TEM) of J774 macrophage-like cells reveals the consistent thickness of membrane ridges throughout its main body. A healthy culture of J774 cells was plated and acclimatised overnight into 24-well plate with uncoated glass coverslips. Cells were then fixed and processed for embedding with araldite resin. Ultrathin sections of 90 nm were prepared by cutting through the dorsoventral cell axis. Specimens were then fixed on grid and examined using a field emission transmission electron microscope at 80 kV accelerating voltage. Image is a representative of more than 20 cells analysed from three independent experimental repeats.

(A) Schematic diagram showing a macrophage top view and a slice (red box) passing through the dorsal and basal cell surfaces used to examine ridge cross-section,

 (B) A macrophage cross-section diagram representing the slice in *A*,

(C) TEM image of a macrophage cross-section showing the membrane ridge ultrastructure: **base –** green arrow, **body** - orange double arrow, **tip -** red arrow**.** Scale bar - 500 nm.

Membrane ridges also seemed to possess a characteristic wavy outline from a top view perspective (Figure 3.3A and 3.3C). Exploring this curvature property might provide additional insights on its biophysical properties, particularly on any molecular interactions leading to curvature bias. Thus, in collaboration with Dr. James Bradford of Hawkins lab in Department of Physics and Astronomy in University of Sheffield, I used a custom-built image analysis script (Appendix 1) that can profile both the magnitude and direction of membrane ridge curvature. Ridges were manually isolated from the raw SEM images (Figure 3.5A), and our custom-built curvature script was run (Figure 3.5B) after determining the line profile coordinates of membrane ridges. Results showed that whilst individual ridges might possess curvature (Figure 3.5C), the mean curvature of all membrane ridges is zero (Figure 3.5D), suggesting that the bending observed is stochastic.
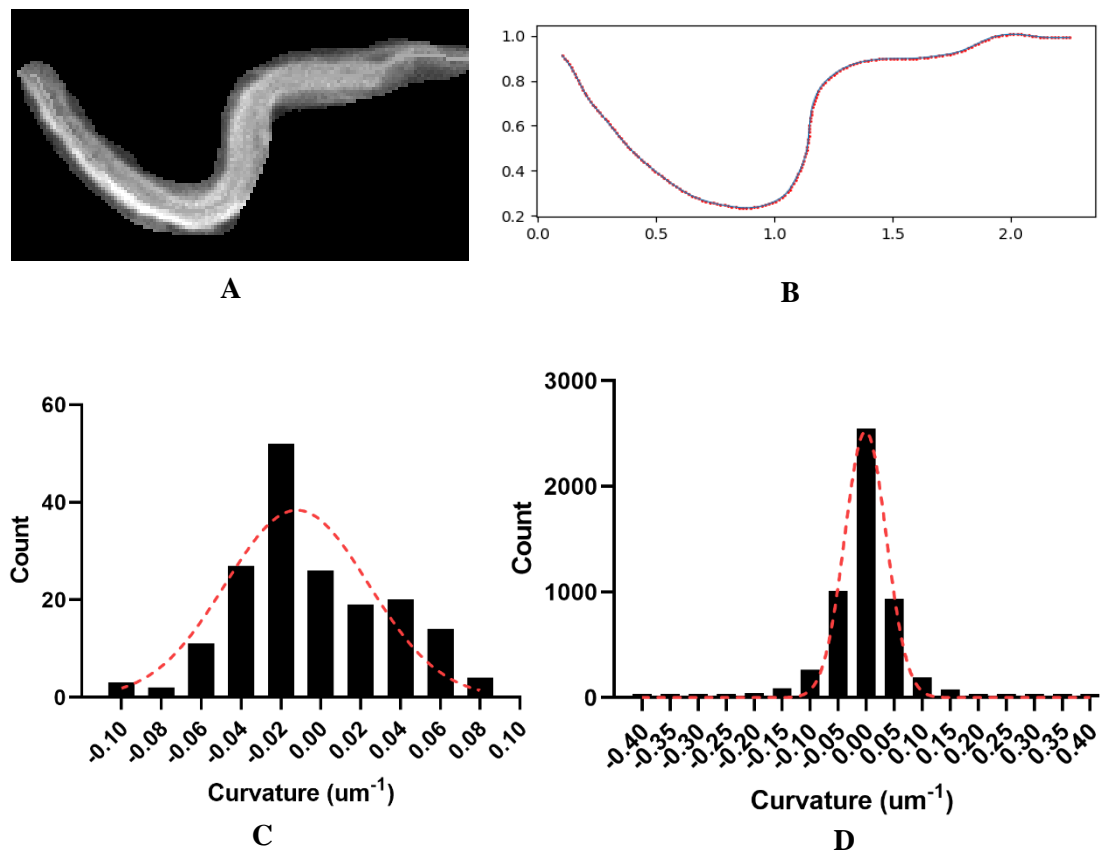
Figure 3.5 | Membrane ridges exhibit a mean curvature of zero. Raw SEM images of J774 macrophage-like cells were manually processed by isolating individual ridges. Ridge curvature was then determined using *ridge detection* (RD) and a customised script (Appendix 1). Image is a representative of 58 ridges analysed from 3 independent experimental repeats.

(A) An individual ridge extracted from a macrophage SEM image,

(B) Ridge midline of image *A* as determined by RD, red points along the midline show the coordinates used for ridge curvature analysis,

(C) Ridge curvature profile of *A* with a Gaussian fit (red, $R^2 = 0.738$) showing a slightly negative mean curvature ($M = -0.01$, $SD = 0.04$),

(D) Combined curvature histogram of all membrane ridges examined revealing a zero mean curvature ($R^2 = 0.989$, $n = 58$ ridges (5220 curvature points), $M = 0.00$, $SD = 0.06$).

3.5 Membrane ridges are actin-rich protrusions on the dorsal cell surface

Membrane protrusions are commonly supported by actin filaments whose organisation and dynamics greatly influence the physical properties of these membrane structures (Svitkina, 2018). To describe the internal architecture of membrane ridges, I

examined its actin component by fluorescence labelling and airyscan confocal superresolution microscopy.

Fluorescent phalloidin staining of macrophages demonstrated wavy, sheet-like structures on the dorsal surface, which appeared identical to the membrane ridges observed by SEM (Figure 3.6B green arrow). The lower axial surfaces also exhibited ridges (Figure 3.6C green arrow) as well as filopodia (red arrow) and cell cortex (yellow arrow), a continuous border of actin filaments contiguous to the plasma membrane. The macrophage ventral surface was devoid of any ridges but had numerous filopodia (red), with actin cortex visible (yellow) and puncta which were potentially podosomes (blue).

To further characterise the actin components of membrane ridges, I focussed on the dorsalmost sections of my whole mount images. As with SEM imaging, ridges visualised with phalloidin staining showed highly consistent thickness along their length (Figure 3.7 zoomed in images). The sheet-like property of these structures was confirmed by orthogonal examination of the actin cytoskeleton (Figure 3.7G), which also revealed that membrane ridges (red and blue arrows) are physically linked to the underlying actin cortex (yellow arrow). The actin cortex, though ideally a continuous border of actin around the cell, showed some small gaps (green arrow) in both yz and xz orthogonal sections which were not seen in raw images (Figure 3.6C and 3.6D) and thus most likely are image reconstruction artefacts when rendering these slices.

A multichannel superresolution experiment to simultaneously image macrophage plasma membrane and its actin cytoskeleton was also attempted but failed. This was assumed to be due to dye incompatibility with cell lines and fixatives (PFA or glyoxal) used in the experiment.
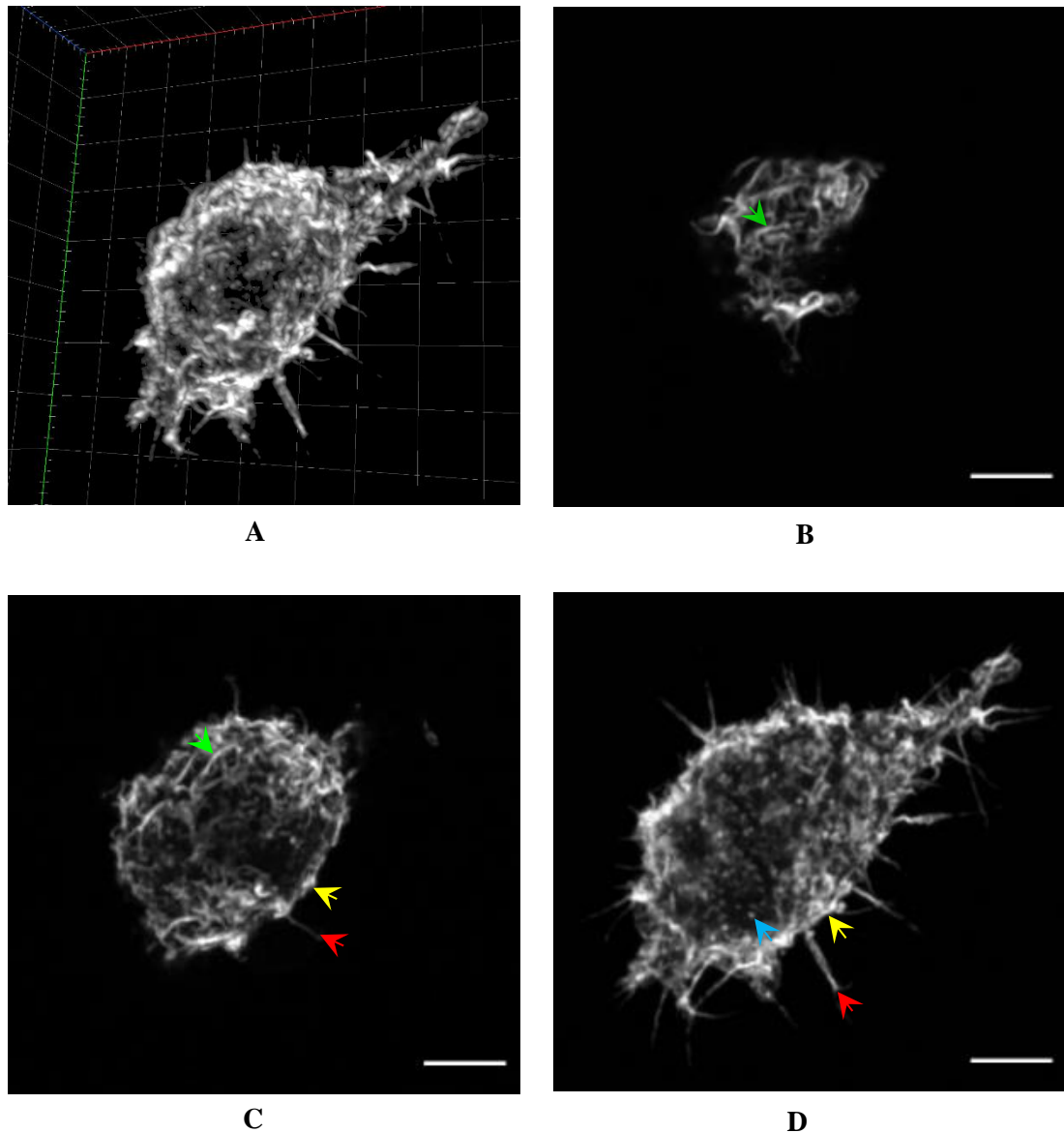
Figure 3.6 | **Airyscan superresolution imaging of actin in macrophages using phalloidin-rhodamine probe reveals the organisation of macrophage actin cytoskeleton.** A healthy culture of J774 macrophage-like cells was plated into a 24-well with uncoated glass coverslips. Cells were then fixed and labelled with phalloidin-rhodamine probe after overnight acclimatisation. Samples were imaged using an airyscan confocal laser scanning microscope with 63x oil immersion objective (1.4 NA Plan Apo) under 565/30 nm excitation and 620/60 nm emission wavelengths. Images are representative of 19 cells examined from 2 independent imaging experiments.

(A) Maximum intensity projection of a J774 actin cytoskeleton,

(B-D) Three equal z-section volumes of *(A)* split into: *(B)* upper third/dorsalmost, *(C)* middle third, and *(D)* lower third/ventralmost sections (**membrane ridges** - green arrow; **filopodia** - red arrow; **cell cortex** - yellow arrow; **podosome** - blue arrow), scale bar - 5 μm.
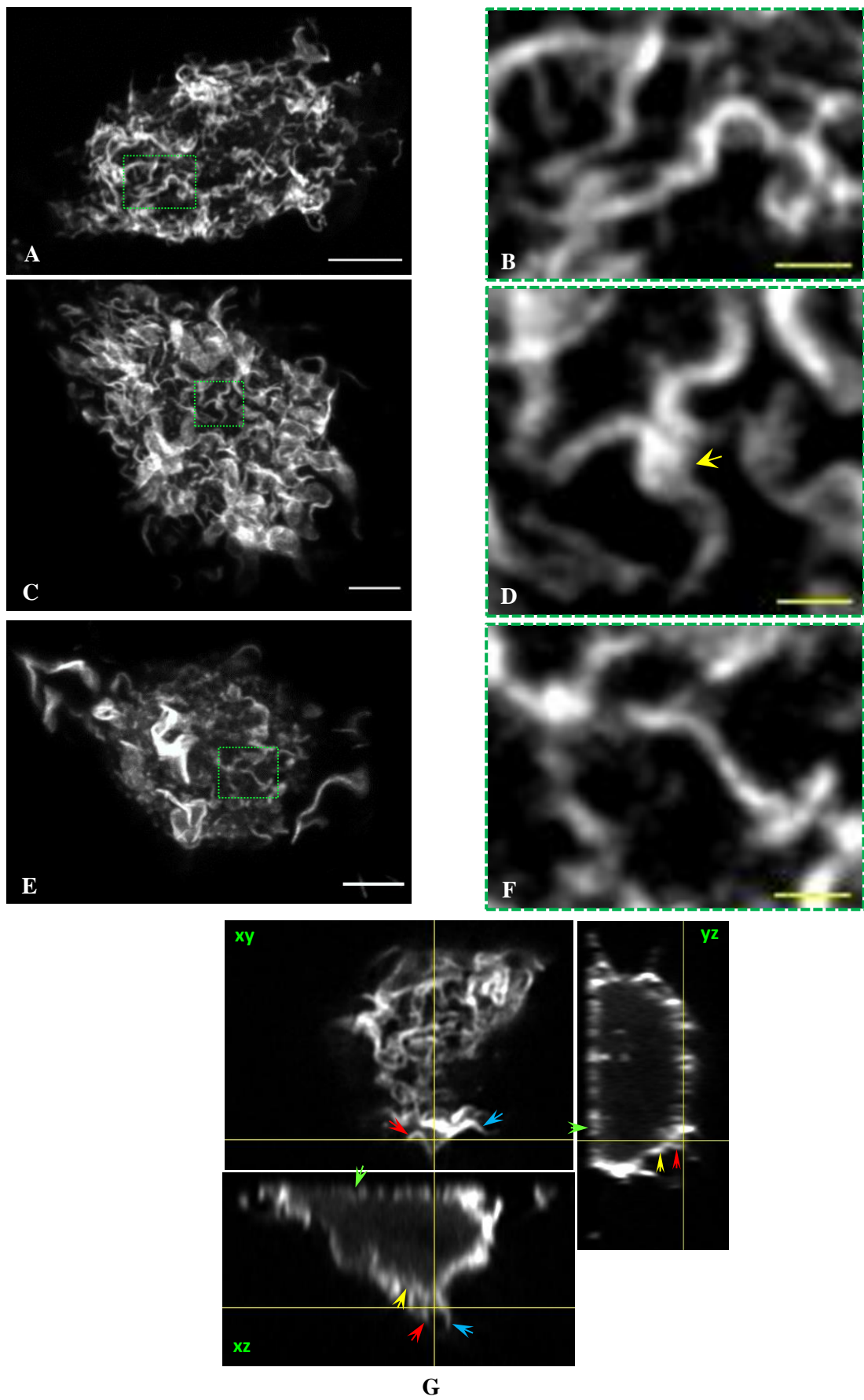
Figure 3.7 | **The actin architecture of membrane ridges has sheet-like and wavy features, similar to its properties observed using scanning electron microscopy.** Immunofluorescence images of J774 macrophage-like cells was examined. Their uppermost or dorsalmost section with 700-1400 nm thickness was inspected for the presence of membrane ridges. It was found to be the most common actin-based protrusion in this region of *in vitro* culture cells. Images are a representative of 19 cells examined from 2 independent experimental repeats.

(**A-F): Left** – main panel illustrating the uppermost macrophage actin cytoskeleton enriched with ridges, **Right** – zoomed in region (green box) of the left image. Scale bar: main - 5 μm, zoomed in - 1 μm,

(G) Orthogonal sections of a macrophage actin cytoskeleton passing through membrane ridges (red and blue arrows), their physical links to the actin cortex (yellow arrow) were revealed in both *yz* and *xz* sections.

3.6 Membrane ridge actin thickness is similar to cortical actin thickness

The biophysical properties of cellular structures provide insights on their regulations and functional implications to cellular processes. For instance, Chugh (2017) and colleagues showed that thickness of the cortical actin could inform on the existing cortical tension of the cell during mitosis. More specifically, depletion of proteins influencing actin filament length such as the capping protein CAPZB and the severing protein CFL1 was found to increase cortical thickness whilst depletion of the actin nucleator DIAPH1 led to cortical thickness reduction (Chugh et al., 2017). All of which resulted into a significant reduction of the cortical tension (Chugh et al., 2017). Cortical tension, in turn, is important in regulating cell shape (Chalut and Paluch, 2016) and performing cellular processes with pertinent mechanical attributes such as cell division (Effler et al., 2006), migration (Raab et al., 2012) and differentiation (McBeath et al., 2004). To measure actin thicknesses of lamellipodia, filopodia, membrane ridges and cell cortex of J774 cells, I designed an image processing routine that manually extracts these structures based on their physical properties (i.e. localisation and actin features), and then applied RD image analysis to automate their measurement.

Lamellipodia were seen as flat sheets extending from the main body of a macrophage (Figure 3.8A). The leading edge (zoomed in boxes) possessed a wavy outline with occasional thickened regions of actin (zoomed in box 2 green arrow). These are believed to be actin filaments that protruded upward (Figure 3.9G schematic) as a consequence of forming weak adhesion sites to the substrate (Giannone et al., 2007) or increased membrane tension (Pontes

et al., 2017). To estimate the thickness of actin filaments originating from lamellipodia, I manually isolated and measured these structures.

Actin lamellipodia (Figure 3.9E) of J774 cells was found to have a mean thickness of 311 nm ($SD = 66$). This is slightly thicker than the lamellipodia possessed by fish keratocytes (200-300 nm) as reported by Anderson (1998) and colleagues. I then compared its actin features and thickness with other types of macrophage membrane protrusion.

Filopodia (Figure 3.8B) were seen as thin, finger-like actin protrusions extending from the macrophage body. They were readily isolated using these physical properties and their usual localisation on the ventralmost region of a macrophage. The mean thickness of macrophage actin filopodia (Figure 3.9F) was found to be 294 nm ($SD = 45$ nm), which was slightly less than its lamellipodia.

As I previously determined, membrane ridges usually localise on the dorsal cell surface and are physically linked to the cell cortex through its actin component. Extracting these structures from fluorescence images therefore requires their accurate discrimination from cortical actin and other actin-based cellular structures. In each frame of a macrophage z stack image (~50 frames), I first isolated cortical actin, which as previously seen (Figure 3.6C and 3.6CD yellow arrow) forms a continuous border around the cell, by manually tracing its edges. I then identified membrane ridges in each cross-section through their short and wavy sheet-like geometry (Figure 3.7A-F) which I confirmed by rendering 3D image of the actin cytoskeleton (Figure 3.6A) and orthogonal examination (Figure 3.7G) of each image. I then reconstructed and projected in 3D all processed images to verify successful extraction of cortical actin (Movie 1) and membrane ridges (Movie 2).

After extracting the membrane ridges, I reoriented the images so that they are shown on a yz plane (Figure 3.7G). This is important to eliminate any unwanted fluorescence seen in the xy plane as a result of ridge folding (Figure 3.7D yellow arrow) which can subsequently obscure thickness measurement. I then used RD to measure them and determine membrane ridge thickness (Figure 3.9B green arrow). The thickness of cortical actin (Figure 3.9B yellow arrow) was also measured in the same orientation as the ridges.

Results (Figure 3.9G) showed that the mean thickness of membrane ridge actin was 369 nm ($SD = 86$) showing a very high consistency (i.e. similar distribution peak - 350 nm) in all cells examined. This confirms previous finding of consistent ridge thickness using electron microscopy, and suggests that a tightly regulated actin process occurs in macrophages which allows them to generate membrane ridges. However, differences in thickness values were obtained using SEM (142 nm) and Airyscan superresolution microscopy (369 nm). This is

accounted to instrumental differences having different resolution limits for these imaging equipment: SEM ~ 3nm, airyscan ~120 nm.

Meanwhile, the macrophage cortical actin also showed a consistent thickness measurement (Figure 3.9H), showing a mean measurement of 349 nm ($SD = 112$). This agrees with its known properties in the literature as an isotropic cellular structure with homogenous thickness and tension (Chugh et al., 2017; Clark et al., 2013; Svitkina, 2020; Tinevez et al., 2009).

Using data from both SEM and fluorescence images, I then compared the thicknesses of membrane protrusions found in a macrophage. Statistical analysis of actin thicknesses from airyscan superresolution images of lamellipodia ($M = 321$, $SD = 59$), filopodia ($M = 291$, $SD = 22$) and membrane ridges ($M=369$, $SD = 21$) showed significant difference using ordinary one-way ANOVA (Figure 3.9I, $F(2,23) = 16.17$, $p < 0.0001$). However, using SEM data, statistical comparison of thickness of these membrane protrusions revealed no significant difference (Figure 3.9J, $F(2,26) = 2.910$, $p = 0.072$). These conflicting results could be explained by some key steps in image processing of fluorescence images. Measuring membrane ridge thickness using airyscan data required reorientation of the images to avoid any measurement errors due to ridge folding. Differences in lateral and axial resolutions of the system (i.e. lateral ~ 0.3 axial) however might have affected reslicing and reassignment of fluorescence during image reorientation. For instance, prominent gaps were seen in the actin cortex after rendering image orthogonal sections (Figure 3.7G green arrow). Moreover, only comparisons with membrane ridge actin (table 3.2) resulted to statistically significant differences and not with lamellipodia and filopodia which were both measured without image reorientation. Meanwhile, analysis of SEM images which were also measured directly showed no statistically significant difference in the thickness of these membrane protrusions (Figure 3.9J, $p = 0.072$). It can also be observed that even though thickness measurements were different between fluorescence and SEM images, the distribution of these values appeared to be conserved (compare Figure 3.9I and Figure 3.9J), further indicating that the observed discrepancy in measurements could be due to the image processing routine applied and not on the innate physical architecture of these membrane structures.
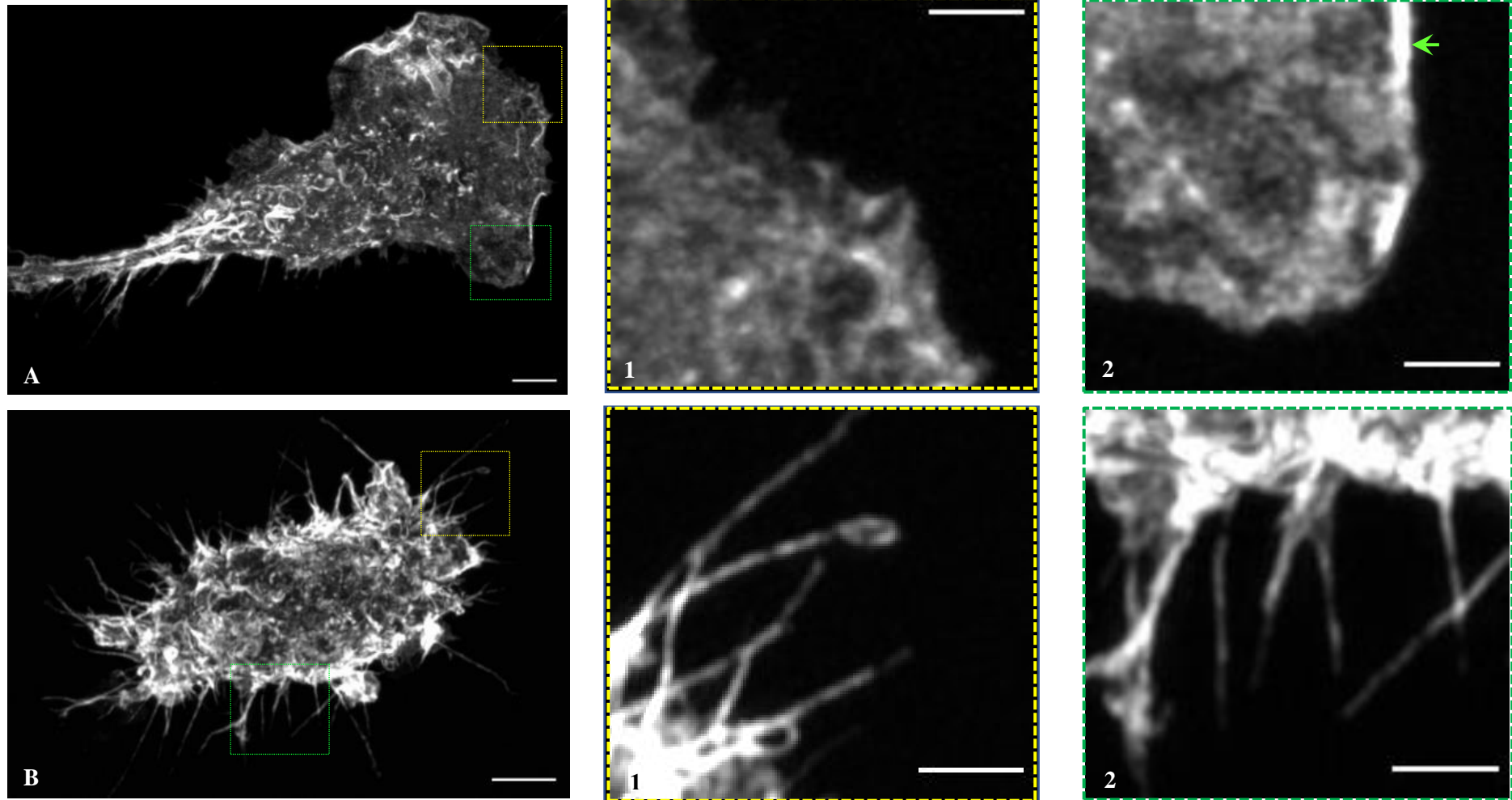
(Figure legend on next page)

Figure 3.8 │ Immunofluorescence microscopy reveals the actin morphology of macrophage membrane protrusions. J774 macrophage-like cells were seeded into 24-well plate with uncoated glass coverslips. After overnight acclimatisation, cells were fixed and labelled with phalloidin-rhodamine. Samples were imaged using an airyscan confocal laser scanning microscope with 63x oil immersion objective (1.4 NA Plan Apo) under 565/30 nm excitation and 620/60 nm emission wavelengths.

(A) Macrophage actin cytoskeleton showing prominent lamellipodia on its leading edge,

(B) Macrophage actin cytoskeleton with numerous filopodia,

(1, 2) Zoomed-in images of actin-rich protrusions in *A* and *B*. Scale bar: main image - 5 μm; zoomed in - 2 μm.
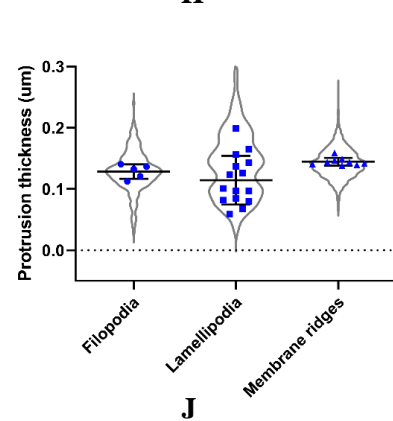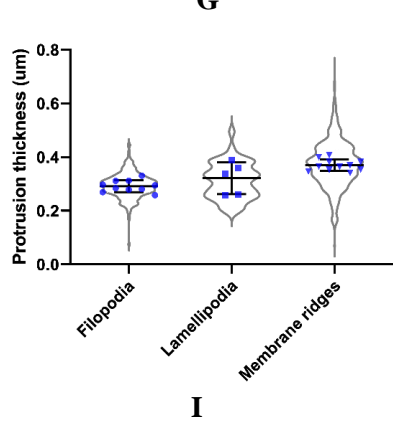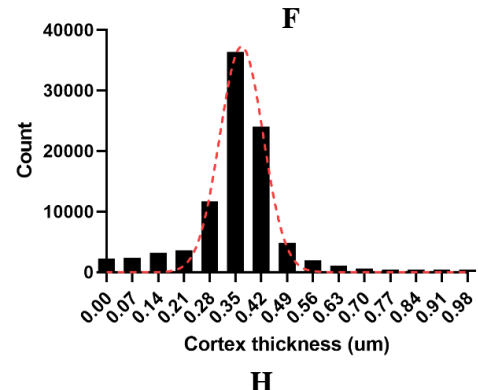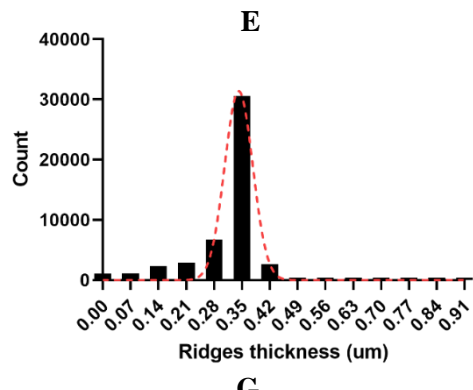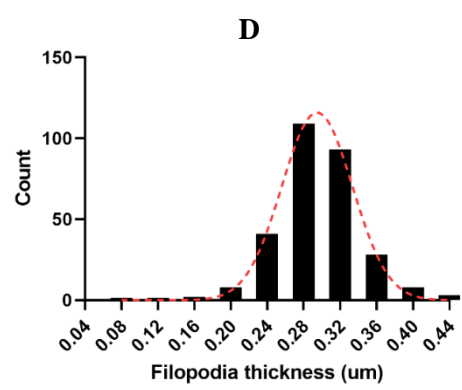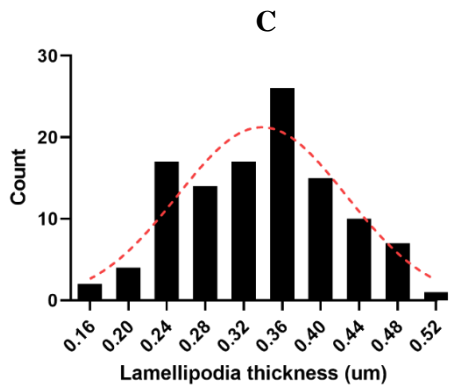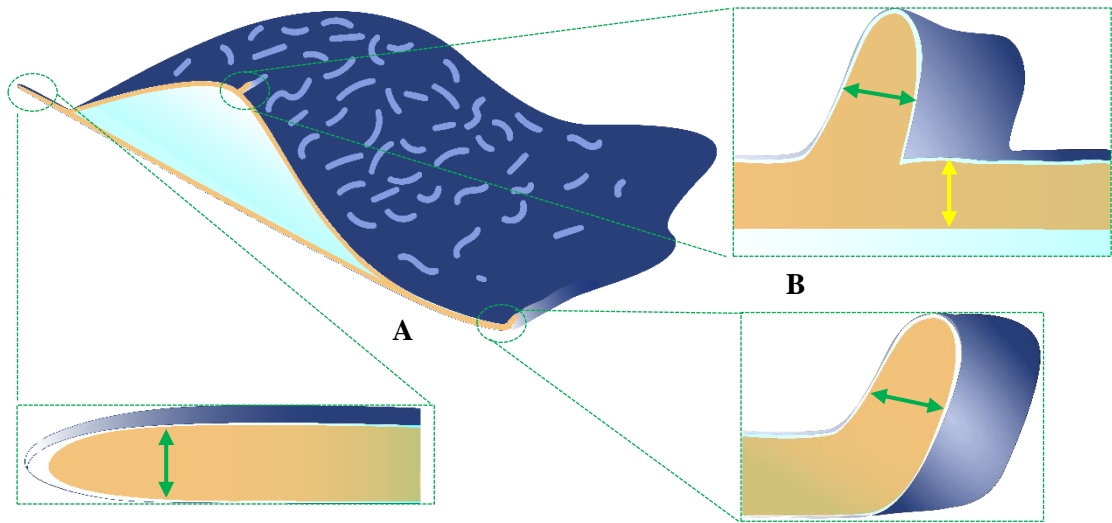
Figure 3.9 | Analysis of actin-rich macrophage features reveals the highly consistent thickness of membrane ridges that is similar to the cortical actin layer.

(A) Schematic representation of a macrophage side view section showing the different structures examined,

(B) Zoomed in region of *A* showing membrane ridge thickness (green double arrow) and cortical actin thickness (yellow double arrow),

(C) Zoomed in region of *A* showing its lamellipodia thickness (green double arrow) as seen on its dorsal protrusion,

(D) Zoomed in region of *A* showing filopodia thickness (green double arrow),

(E) Combined actin thickness histogram of J774 lamellipodia with a Gaussian fit (red curve) ($R^2 = 0.830$, $n = 5$ cells, $M = 312$, $SD = 66$),

(F) Combined actin thickness histogram of J774 filopodia with a Gaussian fit ($R^2 = 0.997$, $n = 10$ cells, $M = 294$, $SD = 46$),

(G) Combined actin thickness histogram of J774 membrane ridges with a Gaussian fit ($R^2 = 0.981$, $n = 11$ cells, $M = 369$, $SD = 86$),

(H) Combined actin thickness histogram of J774 cortical actin with Gaussian fit ($R^2 = 0.978$, $n = 11$ cells, $M = 349$, $SD = 112.6$),

(I) Ordinary one-way ANOVA using airyscan imaging data showed significant differences in the mean actin thickness of different macrophage membrane protrusions ($F(2,23)=16.17$, $p < 0.0001$), $n = 5\text{-}11$ cells, bars: $M \pm SD$, a post hoc analysis using Tukey's test (table 3.2) was done to further examine group differences, please refer to the table for statistically significant group comparisons,

(J) Ordinary one-way ANOVA using SEM imaging data did not show any significant differences in the mean thickness of macrophage membrane protrusions ($F(2,26)=2.910$, $p=0.072$), $n = 5\text{-}15$ cells, bars: $M \pm SD$.

Dependent variable: Actin thickness Alpha = 0.05				
Membrane protrusion comparison	**Mean difference**	**95% CI of difference**	**Significant?**	**Adjusted p value**
Filopodia vs. Lamellipodia	-0.02955	-0.07294 to 0.01384	No	0.2247
Filopodia vs. Membrane ridges	-0.07796	-0.1126 to -0.04335	Yes	<0.0001
Lamellipodia vs. Membrane ridges	-0.04841	-0.09114 to -0.005687	Yes	0.0244

Table 3.2 | Tukey's multiple comparisons of actin thickness of different macrophage membrane protrusions

3.7 Membrane ridges are enriched with nucleator Arp2/3 and nucleation promoting factor WASH but not with the membrane receptor TLR2

The formation of actin-rich membrane protrusions is highly dependent on the presence of different actin-binding proteins which may be directly or indirectly involved in the organisation, growth and turnover of these membrane structures (Svitkina, 2018). As my previous data revealed similarities in the thicknesses of cortical actin and membrane ridges, I then investigated if the well-known actin cortex nucleator Arp2/3 (Bovellan et al., 2014) is also responsible for the nucleation of actin ridges. I used immunofluorescence microscopy in examining the expression of Arp2/3 and Wiskott Aldrich Syndrome protein and Scar Homologue (WASH) in membrane ridges of J774 and RAW264.7 macrophage-like cells. I imaged the dorsalmost macrophage surface where ridges are usually found, and I plotted the expression profiles of Arp2/3 and WASH alongside membrane ridge actin to determine any co-localisation.

Results showed that both Arp2/3 (Figure 3.10A) and WASH (Figure 3.10B) were found in membrane ridges suggesting the presence of a branched actin network in these protrusions. However, WASH was found to colocalise not as frequent (<30% of cells examined) as Arp2/3 in both J774 and RAW264.7 cells. This suggests that it might be involved in promoting actin filament polymerisation in ridges, but is not sufficient to explain the extensive expression (>90% of cells examined) of Arp2/3 in this structure. It would be worth to examine other Arp2/3 associated factors such as WASP and Scar/WAVE and determine their relative contributions, if any, in generating membrane ridges.

Because macrophage membranes are usually decorated with phagocytic receptors which enable phagocytic uptake, I examined the potential enrichment of TLR2 in membrane ridges. TLR2 is a lipoprotein-activated receptor found to be important in the phagocytic uptake of various fungi (Underhill et al., 1999), bacteria (Anand et al., 2011; Ip et al., 2010) and

viruses (Cuevas and Ross, 2014). Using immunofluorescence and widefield microscopy, I examined its localisation and expression pattern in J774 and RAW264.7 cells. However, unlike Arp2/3 and WASH, profiling results (Figure 3.10F and I) showed only few cells (~10% of cells examined) have TLR2 enrichment in their ridges.
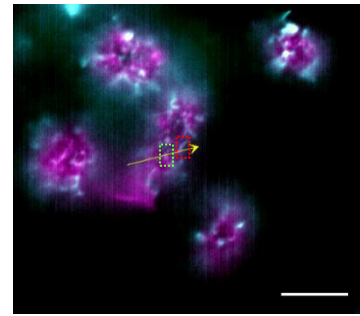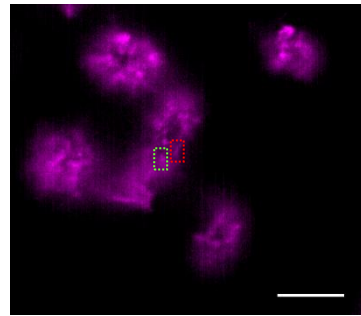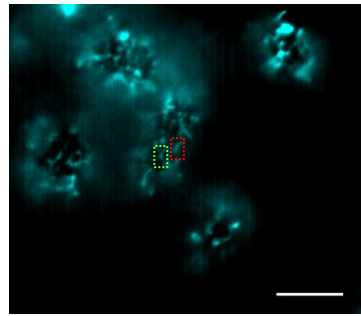
A
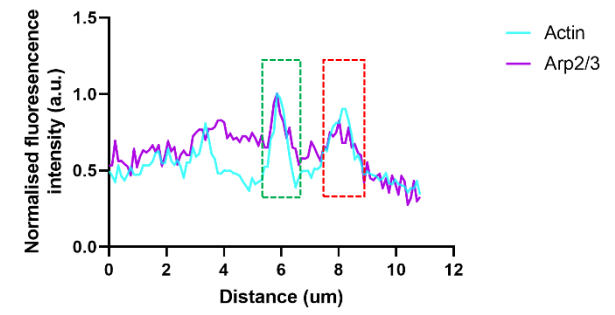
B
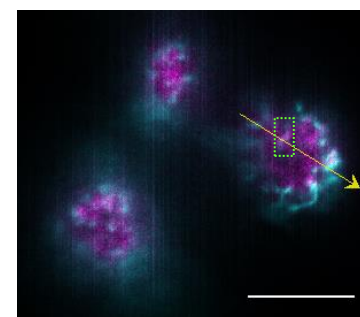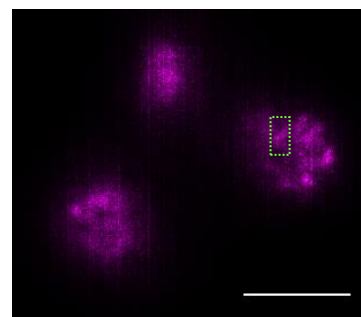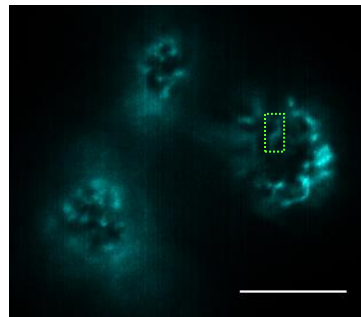
C
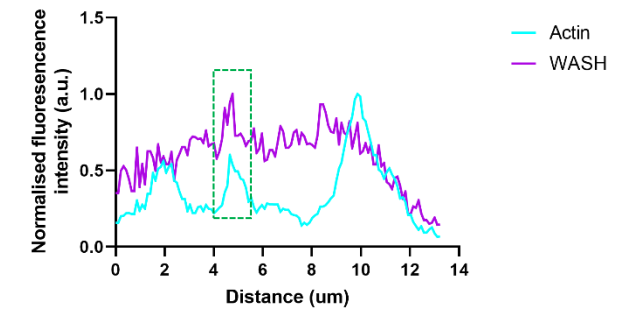
D
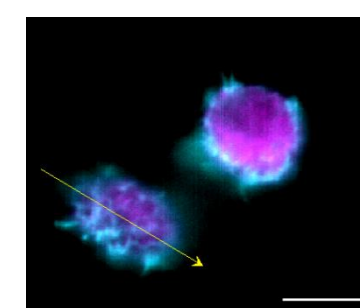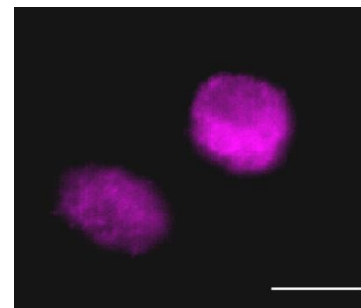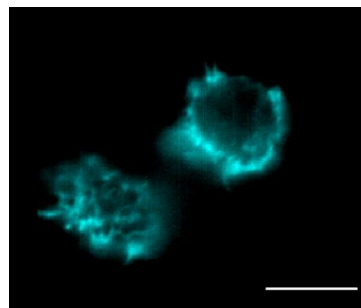
E
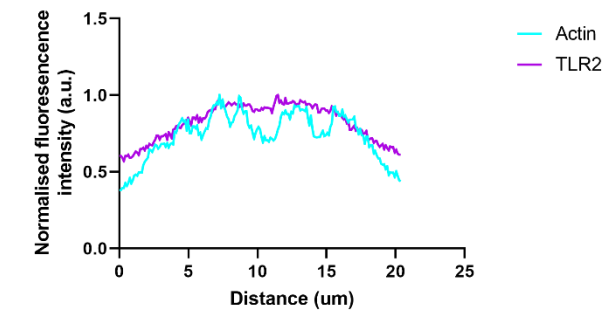
F
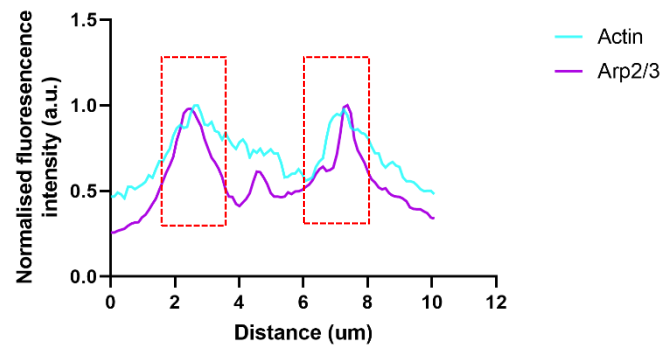
G
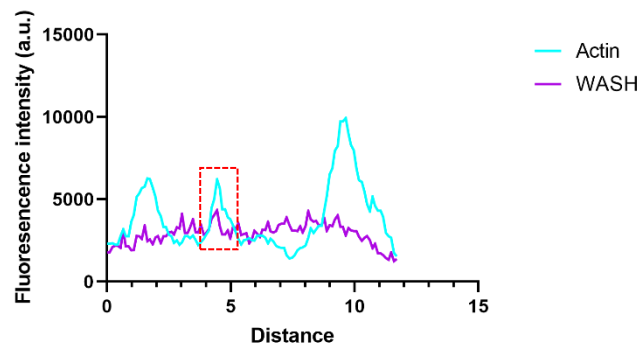
H
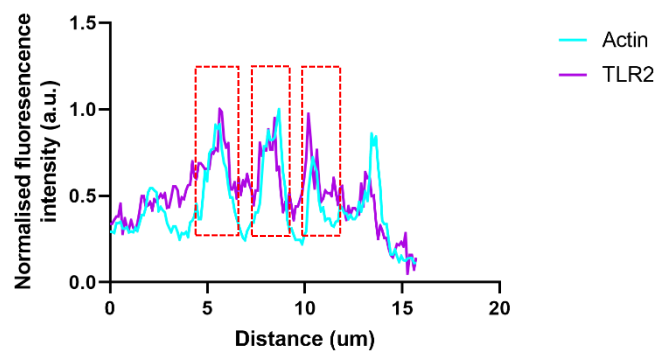
I
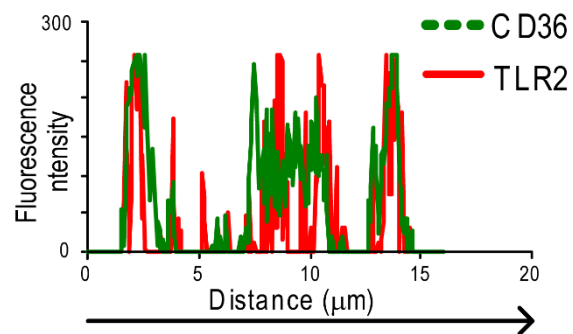
J

(Figure legend on next page)

Figure 3.10 | Both Arp2/3 and WASH are enriched in membrane ridges, however TLR2 does not show any preferential localisation in ridges using widefield fluorescence microscopy. A healthy culture of J774 and RAW264.7 macrophage-like cells was prepared for immunofluorescence microscopy as previously described. Arpc2 probe was used to tag Arp2/3 and phalloidin-TRITC for actin filament. Samples were imaged using 60x oil immersion objective lens (1.4 NA Plan Apo) in GFP (excitation: 470/40 nm, emission: 525/50 nm) and Cy3 (excitation: 545/25 nm, emission: 605/70 nm) channels of a widefield microscope. Images were blindly deconvolved using NIS Elements deconvolution software and were analysed using NIS Elements v4.11. Two independent experimental repeats were done. Images are a representative of a common expression profile in 10 cells examined per repeat. Scale bar – 10 μm.

(A) Arp2/3 was expressed and enriched in membrane ridges (red and green boxes) of J774 cells, images from left to right: actin, Arp2/3 and overlay of both images,

(B) Line scan profiles of Arp2/3 and actin passing through ridges in *A* (yellow arrow) highlighting regions of enrichment (red and green boxes),

(C) WASH was also found to be enriched in membrane ridges (green box) of J774 cells, images from left to right: actin, WASH and overlay of both images,

(D) Line scan profiles of WASH and actin passing through ridges in *C* (yellow arrow) highlighting WASH enrichment in a ridge (green box),

(E) TLR2 expression showed variable distribution patterns in membrane ridges of J774 cells, which do not typically show enrichment in ridges, images from left to right: actin, TLR2 and overlay of both images,

(F) Line scan profiles of TLR2 and actin passing through ridges (overlaid image in *E* yellow arrow).

(G) Line scan profiles of Arp2/3 with membrane ridge actin showing enrichment (red box) in RAW264.7 cells

(H) Line scan profiles of WASH and membrane ridge actin showing enrichment (red box) in RAW264.7 cells

(I) Line scan profiles of TLR2 with membrane ridge actin showing enrichment regions (red boxes) in RAW264.7 cells

(J) A published line scan profile of TLR2 in a monocytic membrane to confirm that my experimental set-up had worked (Data courtesy of Nilsen et al., 2008, see appendix 2 for reprint permission).

3.8 Membrane ridges are a dynamic structure with short lifetime

After exploring the biophysical and biochemical properties of membrane ridges, I then examined its cellular behaviour. I used both fluorescence and label-free imaging techniques to investigate its dynamics in live J774 cells. Fluorescence data were provided by collaborators from Stow's lab in University of Queensland, Australia, who were able to successfully implement superresolution live imaging of actin protrusions in macrophages; whilst, I independently carried out a label-free timelapse imaging using differential interference contrast (DIC) microscopy to complement these live imaging fluorescence data.

DIC timelapse imaging revealed the highly dynamic property of membrane protrusions in the dorsal macrophage surface (Movie 3). Most of these protrusions possessed a wavy outline with consistent thickness and therefore were identified as membrane ridges. This verified my previous finding of its high density in the dorsal region of macrophages cultured *in vitro* using scanning electron and immunofluorescence microscopy. The dynamic feature of membrane ridge showing cyclic events of emergence and collapse was observed. I tracked individual ridges to determine their lifetimes (Figure 3.12E) which I found to have a mean value of 55 seconds ($SD = 46$).

Three different origins of membrane ridges were identified by tracking individual ridges. Ridges can be produced *de novo* or without any template of pre-existing ridge (Movie 4). A membrane ridge emerges from the surface, slowly growing at its two ends (Movie 4 green arrow) and often moves laterally upon extension. Stochastic bending along its length can also be observed, which gave it a wavy appearance. Unlike membrane ruffles, membrane ridges rarely circularise or contact and fuse at its two ends before collapsing back to the membrane. Instead, they shrink along their lengths until being completely recovered in the membrane surface. *De novo* origin accounted for about 34% (16/46) of ridges examined.

Ridges were also found to be formed by coalescence of pre-existing or "mother" ridges (Figure 3.11A, Movie 5). This was observed in about 33% (15/46) of ridges tracked. Fusion usually happens along the main body of mother ridges, and prompted by their lateral outgrowths (Figure 3.11C orange arrow) which mediate their fusion and the formation of a daughter ridge. Notably, these outgrowths seem to be thicker than the mother ridge which indicates potential differences in their internal architectures.

Lastly, ridges could be generated by splitting of a mother ridge into two daughter ridges (Movie 6). Similar to coalescence, this accounted for about 33% of ridges tracked. All splitting observed were lateral and unidirectional which began from one end and continued to the opposite terminal through the ridge midline (Figure 3.11B green dotted line). It is quite remarkable that the thickness of ridges appears to be maintained throughout these events as revealed not only by DIC timelapse imaging but also by SEM examinations (Figure 3.11D-E). This suggests the critical importance of maintaining ridge thickness throughout their lifetimes.

To further explore previous observations of consistent membrane ridge thickness, I then investigated how its thickness changes throughout its lifetime. I tracked individual ridges using lattice light sheet and DIC timelapse imaging data. Lattice light sheet data were kindly provided by Professor Jennifer Stow's group from University of Queensland, Australia. We decided to collaborate with Stow's group after their successful implementation and publication (Condon et al., 2018) of live imaging of macrophage membrane protrusions using their bespoke lattice light sheet imaging system. This would have taken a significant amount of time if done independently due to the current technical requirements of both specimen preparation and live cell imaging to successfully image actin membrane ridges.

Using lattice light sheet microscopy, the dynamics of actin-rich membrane protrusions in macrophages can be illustrated (Condon et al., 2018, Movie 5). Large wavy sheet-like projections that circularised to form macropinocytic cups were observed and were identified as membrane ruffles, whilst small sheets that did not circularise and remained open, as previously described using DIC microscopy, were identified as membrane ridges. It is important to note that compared to my live cell imaging set-up using DIC, which directly imaged the macrophages in their usual culture media, Condon (2018) and co-workers preparation required an overnight activation of cells with LPS to induce membrane ruffle formation. This required me to remove giant ruffles manually on each frame to isolate and measure the membrane ridges by RD analysis (Movie 8). Finally, I also examined ridge thickness using my previously acquired DIC timelapse data to compare measurements.

Measurements of ridge thickness using lattice light sheet (Figure 3.12A) and DIC (Figure 3.12C) timelapse imaging did corroborate and confirmed the highly consistent thickness property of membrane ridges. I also tracked and recorded the thickness of individual ridges produced *de novo* from their inception until their collapse back to the membrane surface. This would allow us to illustrate how the consistent thickness of ridges is established and maintained during its lifetime. In both lattice light sheet (Figure 3.12B) and DIC (Figure 3.12D), the thickness of individual ridges was found to be highly conserved throughout their

variable lifetimes. Discrepancies in thickness measurement values can be observed between the different imaging systems used, and these were accounted to differences in their imaging resolutions. Nevertheless, these data confirm previous finding of ridge thickness consistency and strongly suggest that a very tight regulation of membrane ridge actin architecture persists throughout its lifetime on the macrophage surface. Furthermore, there was no significant difference in the lifetime of ridges produced *de novo* and via coalescence (Figure 3.12F, $p = 0.333$), suggesting that membrane ridges were maintained by a conserved set of regulatory molecules.

A

B

C　　　　　　　　**D**　　　　　　　　**E**
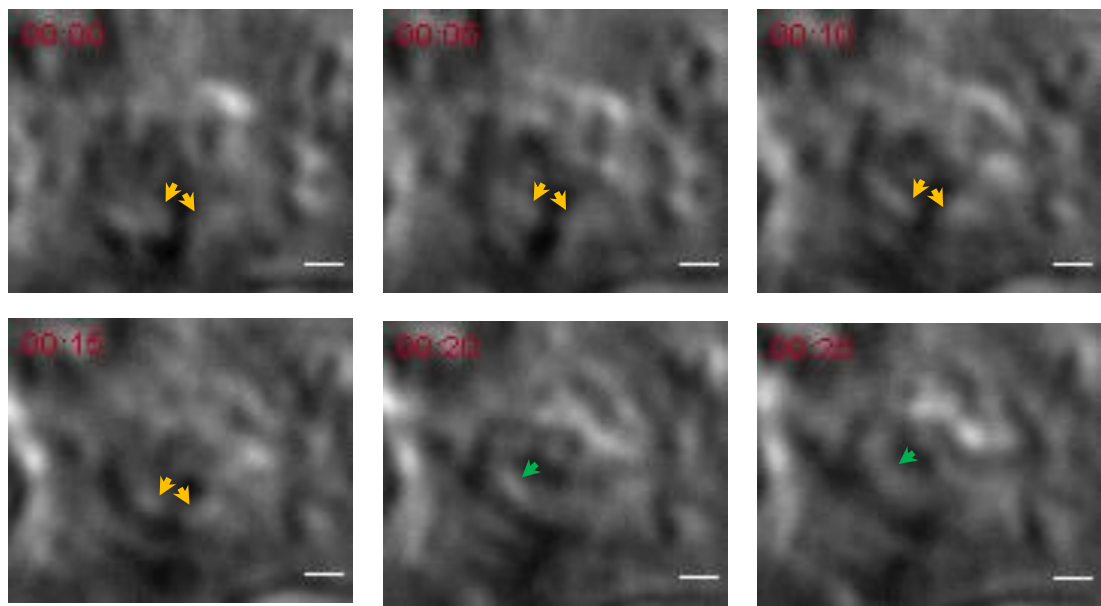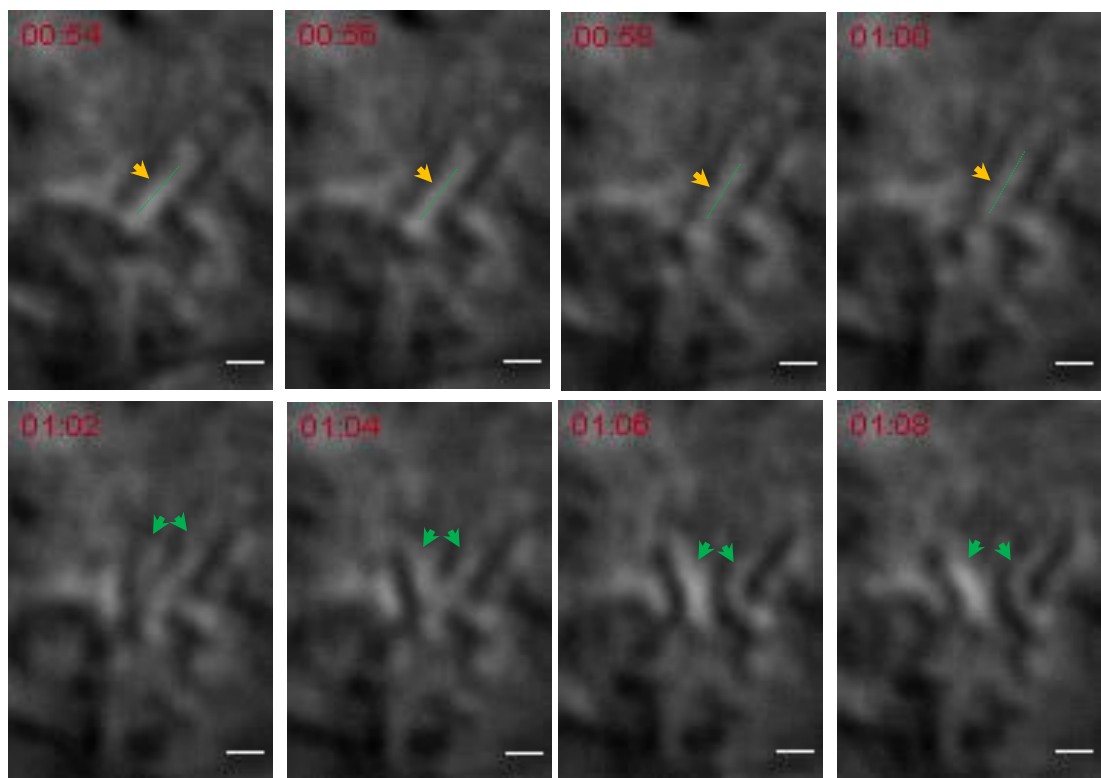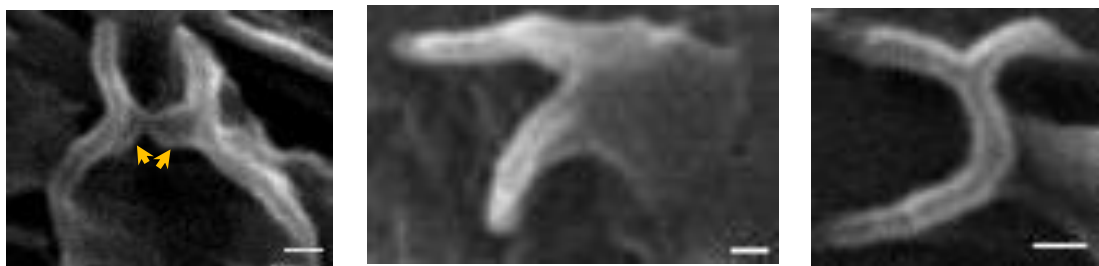
(Figure legend on next page)

Figure 3.11 | Membrane ridges are a dynamic structure that can split or fuse in the macrophage dorsal surface. A heathy culture of J774 macrophage-like cells were seeded into 96-well glass bottom plate in complete DMEM media. After overnight acclimatisation, live cells were imaged in a differential interference contrast (DIC) set-up of a widefield microscope using 60x oil immersion objective (1.4 NA Plan Apo). Images are representative of 2 cells examined in a 15-minute timelapse experiment with 1 second imaging interval. In parallel, J774 cells were prepared for SEM examination. Cells were imaged with a high vacuum, thermionic emission scanning electron microscope coupled with an SE detector system under 10 kV accelerating voltage, 9 mm working distance, 63 nm spot size and 0° stage tilt. DIC images are a representative of 46 ridges examined.

(A) Montage from DIC timelapse imaging showing **fusion** of membrane ridges (orange arrow),

(B) Montage from DIC timelapse imaging showing **splitting** of a membrane ridge (orange arrow),

(C) SEM image of membrane ridges which were about to fuse through their lateral outgrowths (orange arrow),

(D-E) SEM images of membrane ridge splitting laterally showing the highly consistent thickness of its daughter ridges. Scale bar: DIC images -1 μm; SEM images - 200 nm.

A

B

C

D

E

F
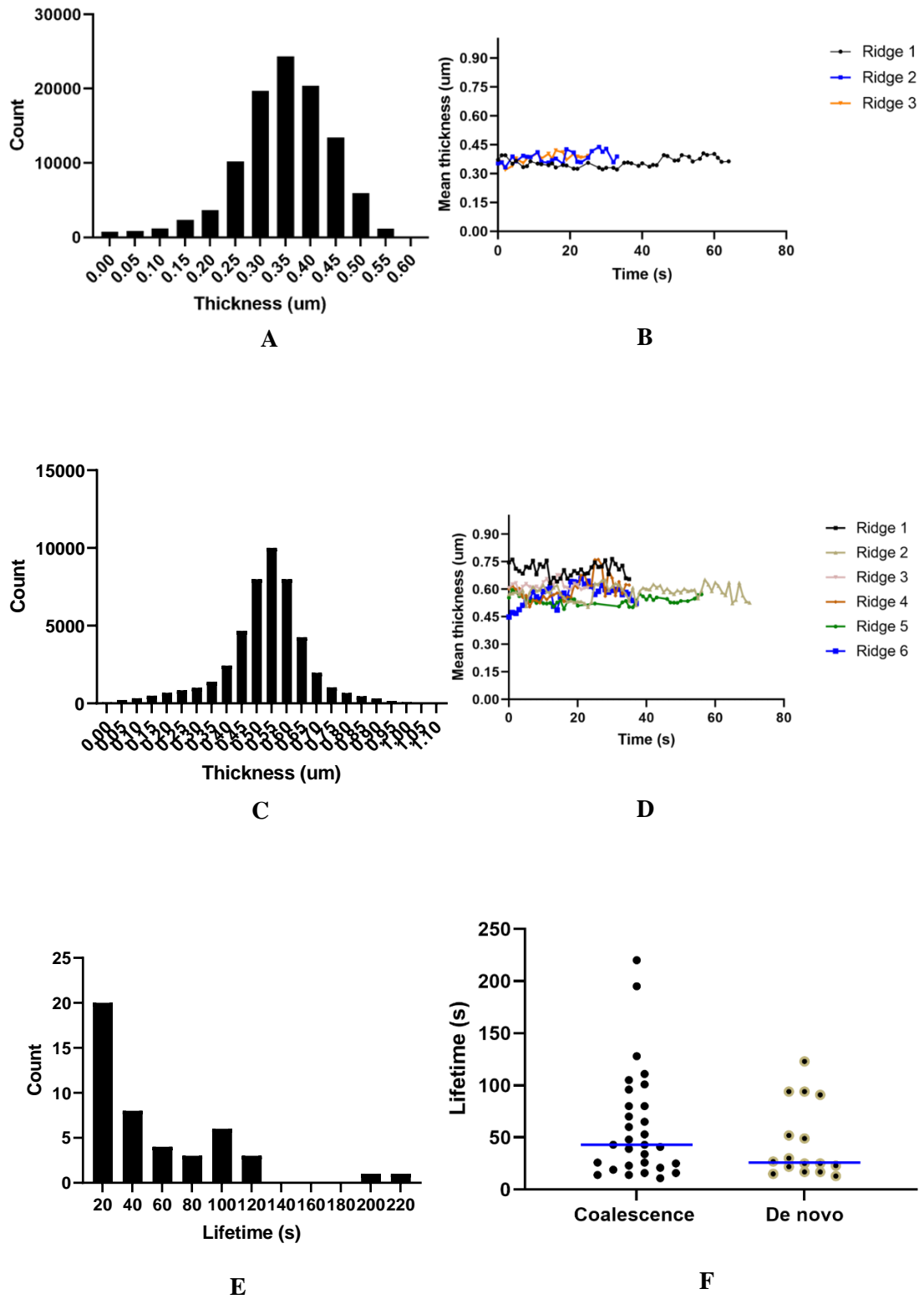
(Figure legend on next page)

Figure 3.12 | Membrane ridges have a mean lifetime of 55 seconds and possess a consistent thickness throughout its lifetime.

(A) Combined thickness histogram of all membrane ridges imaged with lattice light sheet (LLS) for 30 minutes (n = 3 cells (103,982 values), M = 346, SD = 94),

(B) Thickness of individual ridges tracked throughout their lifetimes using LLS,

(C) Combined thickness histogram of all ridges imaged by differential interference contrast (DIC) microscopy for 15 minutes (n = 2 cells (47,052 values), M = 530, SD = 139),

(D) Thickness of individual ridges tracked throughout their lifetimes using DIC,

(E) A histogram of the lifetime of membrane ridges as revealed by DIC timelapse imaging (*n*= 2 cells (46 ridges), M = 55, *SD* = 46),

(F) Comparing lifetimes of ridges produced by coalescence/fusion (Median = 43) and *de novo* (Median = 26) did not show any statistically significant difference using Mann-Whitney test (n = 16-30 ridges, p = 0.333), bar: median.

3.9 Membrane ridges are a common feature of phagocytic cells but are expressed at different densities

After investigating membrane ridges in J774 cells, I then examined its expression in other types of phagocytic cells. I surveyed *in* vitro samples of mouse bone marrow-derived macrophages (BMDM), mouse immortalised BMDM (iBMDM), human monocyte-derived macrophages (MDM), human neutrophils, human THP1, mouse RAW264.7 and the amoeba *Dictyostelium discoideum*. I also used mouse lung and liver samples to illustrate a phagocyte membrane surface in its natural environment.

SEM examination of different types of phagocytes in both *in vitro* (Figure 3.13) and *in vivo* (Figure 3.15) settings revealed their conserved property of producing membrane ridges. Other membrane structures such as lamellipodia and filopodia were also observed. However, in almost all phagocytes examined membrane ridges were the most commonly expressed protrusion in their surfaces *in vitro*, suggesting its fundamental importance in phagocyte morphology. Furthermore, SEM examinations revealed that prior to differentiation into a mature phagocyte (Figure 3.13H) by THP1, its undifferentiated precursor cell (Figure 3.13G) possessed a relatively smooth surface that was devoid of any ridges. This further highlights the structural importance of membrane ridges amongst phagocytes, and, potentially, in the phagocytic role of these cells (explored in chapter 5).

A

B

C

D

E

F

G

H
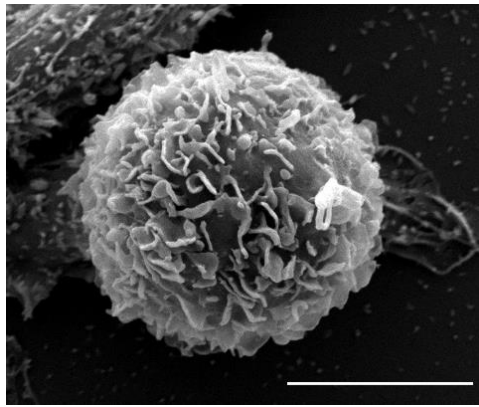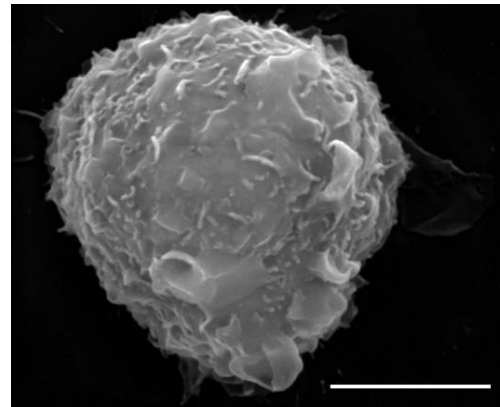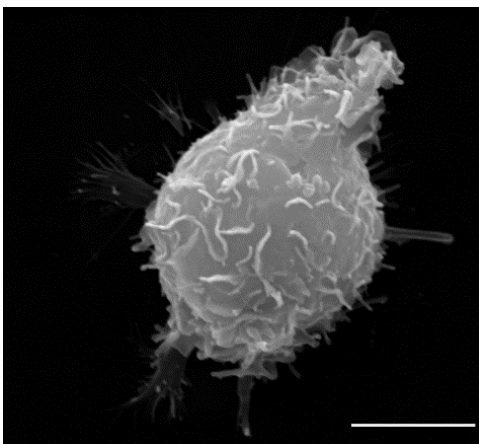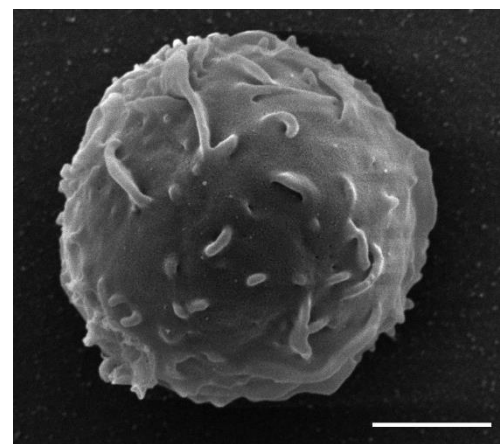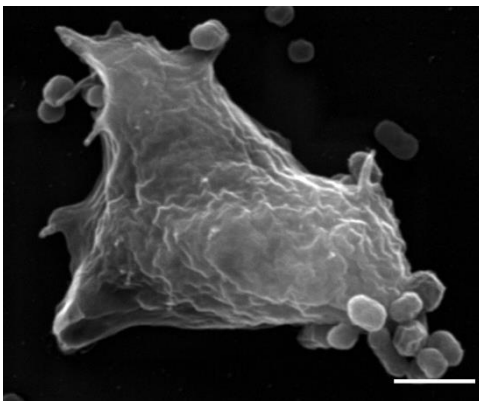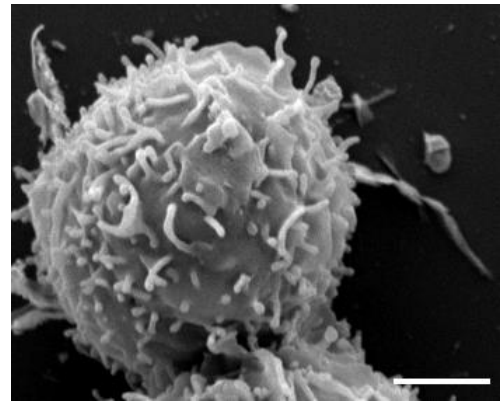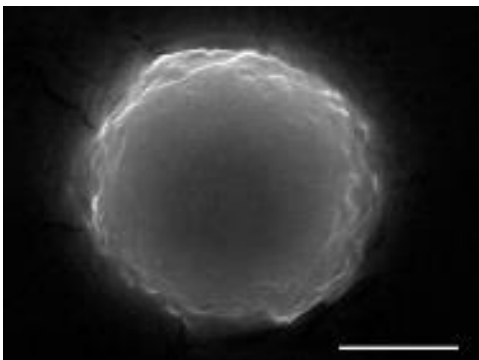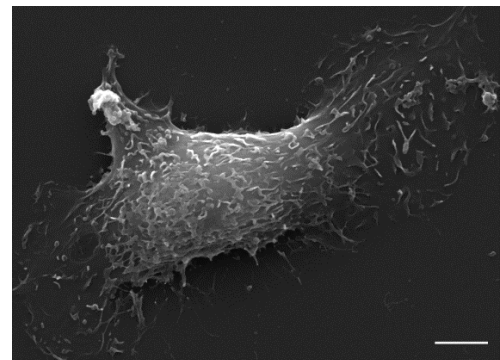
(Figure legend on next page)

Figure 3.13 | SEM imaging revealed that membrane ridges are a conserved feature of phagocytic cells *in vitro*. Different types of phagocytic cells were plated into a 24-well with uncoated glass coverslips. After allowing to settle, cells were then fixed and processed for SEM. Cells were imaged with a high vacuum, thermionic emission scanning electron microscope with an SE detector system, 10 kV accelerating voltage, 9 mm working distance, 63 nm spot size and 0° stage tilt. Images are a representative of more than 20 single cell SEM imaging data for each cell type from 2-4 independent experiments.

(A) SEM photomicrographs of external surfaces of mouse bone marrow-derive macrophage (BMDM), **(B)** mouse immortalised BMDM, **(C)** human monocyte-derive macrophage, **(D)** human neutrophil, **(E)** *Dictyostelium discoideum*, **(F)** mouse RAW264.7, **(G)** *undifferentiated* THP1 and **(H)** *differentiated* THP1. Scale bars: **A, B, C, G, H** - 5 μm; **D, E, F** - 2 μm.

The biophysical properties (i.e. thickness and area density) of membrane ridges possessed by these phagocytic cells *in vitro* were also examined using the RD image analysis previously described (section 3.4). As in J774 cells (Figure 3.14A), membrane ridges of these phagocytes showed a remarkable thickness consistency (Figure 3.14B-D). Their profiles were almost similar and peaked at about 140 nm. Taken together, these imply a conserved actin architecture with regular thickness amongst phagocytic cells that is manifested in the form of membrane ridges.

I next compared the density of membrane ridges across different types of phagocytes. Using the RAD formula (equation 3.2), I computed the amount of ridges possessed by each type of phagocyte grown in their usual culture media. Results (Figure 3.14E) showed that ridge area density varies across different phagocytic cells ($F(5,75) = 26.99$, $p < 0.0001$). The amoeba *D. discoideum* was found to have the least amount of ridges per cell unit area (3.8%) whilst mouse BMDM possessed the most (20.6%). This shows that different types of phagocytes could have variable expression of membrane ridges on their surfaces. Furthermore, it was also found that the size of phagocytes varied across different cell types (Figure 3.16E, table 3.4). Human monocyte-derived macrophages (HMDM) had the largest surface area ($M = 529$ μm^2, $SD = 317$) whilst *D. dictyostelium* ($M = 47$ μm^2, $SD = 15$) and human neutrophils ($M = 48$ μm^2, $SD = 18$) were amongst the smallest phagocytes examined. Although human neutrophils were found to be more than 10x smaller than HMDM, they possessed almost twice as much ridges as HMDM with respect to computed RAD. This suggests that the capacity of phagocytic cells to produce membrane ridges might be independent of cell size.

A

B

C

D

E

F
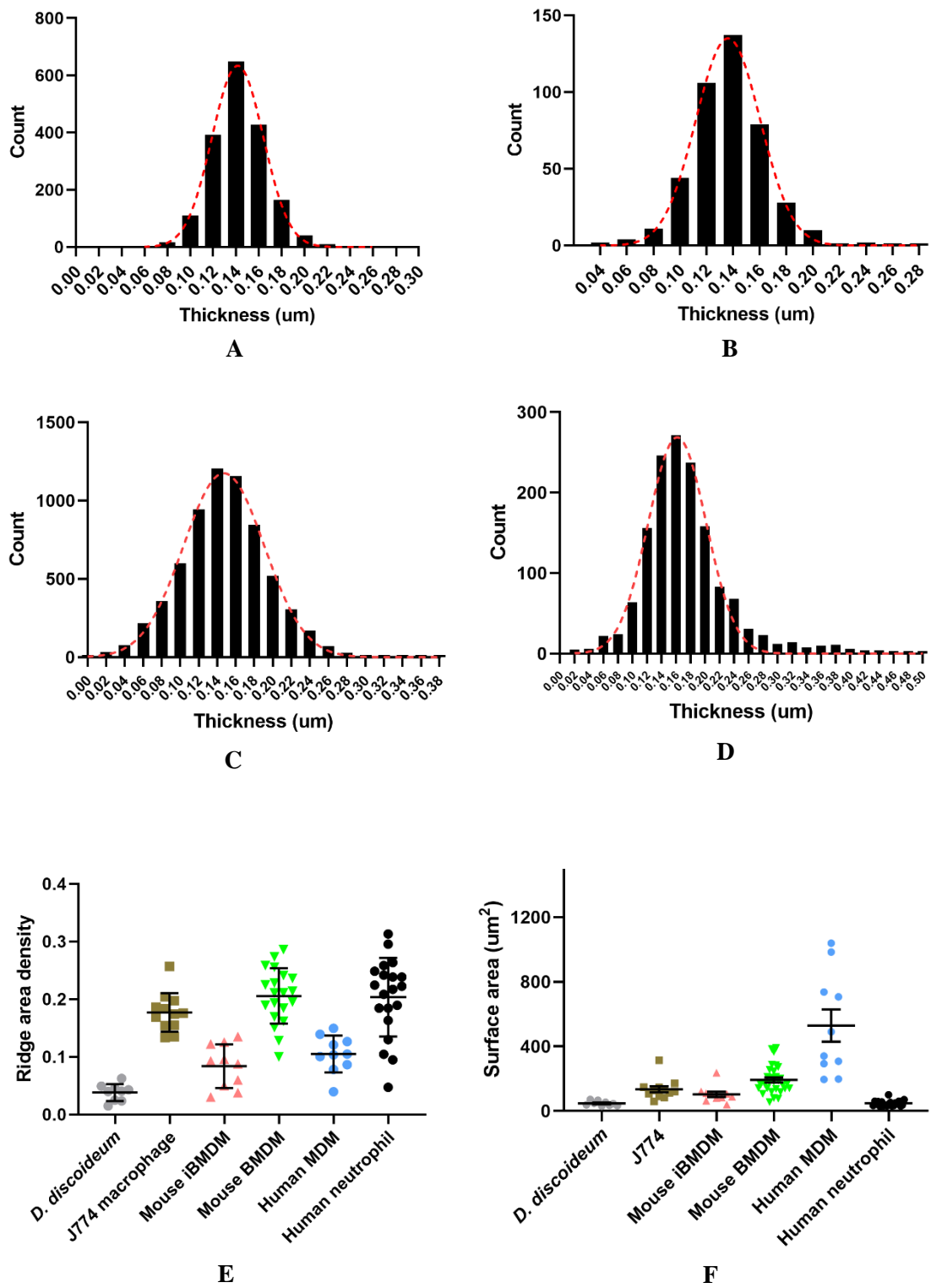
(Figure legend on next page)

Figure 3.14 | Membrane ridges are a highly conserved feature amongst phagocytes, however its area density varies across phagocytic cell types. SEM images of different phagocytes were used to survey cell surface area, ridge area density and thickness for each type of cell. Results were then plotted and anlysed for statistical significance.

(A) Combined thickness histogram of all membrane ridges of J774 macrophage-like cells examined shown with a Gaussian fit (red curve) ($R^2 = 0.997$, $n = 12$ cells (1818 ridges), M=142, $SD = 24$),

(B) Combined thickness histogram of mouse BMDM membrane ridges ($R^2 = 0.996$, $n = 4$ cells (425 ridges), $M = 137$, $SD = 28$),

(C) Combined thickness histogram of human MDM membrane ridges ($R^2 = 0.994$, $n = 9$ cells (6555 ridges), $M= 147$, SD $= 47$),

(D) Combined thickness histogram of human neutrophil membrane ridges ($R^2 = 0.981$, $n = 11$ cells (1467 ridges), $M = 174$, SD $= 62$),

(E) There was statistically significant difference in the ridge area density of different phagocytic cells examined *in vitro* as shown by ordinary one-way ANOVA ($F(5,75) = 26.99$, $p < 0.0001$), $n = 9$-20 cells, bars: $M \pm SD$, a post hoc analysis using Tukey's test (table 3.3) was used to analyse differences between groups, please refer to the table for statistically significant group comparisons,

(F) There was statistically significant difference in cell surface area of different phagocytes examined *in vitro* as confirmed by ordinary one-way ANOVA of log-transformed data ($F(5,85) = 50.69$, $p<0.0001$), , $n = 9$-31 cells, bars: $M \pm SD$, a post hoc analysis using Tukey's test (table 3.4) was used to analyse group differences, please refer to the table for statistically significant group comparisons.

Dependent variable: Ridge area density Alpha = 0.05				
Cell type comparison	**Mean difference**	**95% CI of difference**	**Significant?**	**Adjusted p value**
Dictyostelium discoideum vs. J774 macrophage	-0.1388	-0.1999 to -0.07772	Yes	<0.0001
D. discoideum vs. Mouse immortalised BMDM	-0.04552	-0.1092 to 0.01815	No	0.3032
D. discoideum vs. Mouse BMDM	-0.1675	-0.2231 to -0.1119	Yes	<0.0001
D. discoideum vs. Human MDM	-0.06674	-0.1304 to -0.003071	Yes	0.0344
D. discoideum vs. Human neutrophil	-0.1653	-0.2209 to -0.1097	Yes	<0.0001
J774 macrophage vs. Mouse iBMDM	0.09330	0.03397 to 0.1526	Yes	0.0002
J774 macrophage vs. Mouse BMDM	-0.02867	-0.07926 to 0.02193	No	0.5640
J774 macrophage vs. Human MDM	0.07208	0.01275 to 0.1314	Yes	0.0084
J774 macrophage vs. Human neutrophil	-0.02646	-0.07706 to 0.02413	No	0.6464
Mouse iBMDM vs. Mouse BMDM	-0.1220	-0.1756 to -0.06830	Yes	<0.0001
Mouse iBMDM vs. Human MDM	-0.02122	-0.08319 to 0.04075	No	0.9160
Mouse iBMDM vs. Human neutrophil	-0.1198	-0.1734 to -0.06610	Yes	<0.0001
Mouse BMDM vs. Human MDM	0.1007	0.04708 to 0.1544	Yes	<0.0001
Mouse BMDM vs. Human neutrophil	0.002205	-0.04161 to 0.04602	No	>0.9999
Human MDM vs. Human neutrophil	-0.09854	-0.1522 to -0.04488	Yes	<0.0001

Table 3.3 Tukey's multiple comparisons of ridge area density of different types of phagocytes

Dependent variable: Cell surface area Alpha = 0.05				
Cell type comparison	**Mean difference**	**95% CI of difference**	**Significant?**	**Adjusted p value**
Dictyostelium discoideum vs. J774 macrophage	-0.4373	-0.6838 to -0.1907	Yes	<0.0001
D. discoideum vs. Mouse immortalised BMDM	-0.3155	-0.5724 to -0.05860	Yes	0.0073
D. discoideum vs. Mouse BMDM	-0.5867	-0.7992 to -0.3742	Yes	<0.0001
D. discoideum vs. Human MDM	-0.9944	-1.251 to -0.7376	Yes	<0.0001
D. discoideum vs. Human neutrophil	0.0008788	-0.2235 to 0.2253	No	>0.9999
J774 macrophage vs. Mouse iBMDM	0.1218	-0.1176 to 0.3612	No	0.6758
J774 macrophage vs. Mouse BMDM	-0.1494	-0.3404 to 0.04155	No	0.2132
J774 macrophage vs. Human MDM	-0.5572	-0.7966 to -0.3178	Yes	<0.0001
J774 macrophage vs. Human neutrophil	0.4382	0.2340 to 0.6423	Yes	<0.0001
Mouse iBMDM vs. Mouse BMDM	-0.2712	-0.4754 to -0.06704	Yes	0.0028
Mouse iBMDM vs. Human MDM	-0.6789	-0.9290 to -0.4289	Yes	<0.0001
Mouse iBMDM vs. Human neutrophil	0.3164	0.09983 to 0.5329	Yes	0.0007
Mouse BMDM vs. Human MDM	-0.4077	-0.6119 to -0.2036	Yes	<0.0001
Mouse BMDM vs. Human neutrophil	0.5876	0.4262 to 0.7490	Yes	<0.0001
Human MDM vs. Human neutrophil	0.9953	0.7788 to 1.212	Yes	<0.0001

Table 3.4 Tukey's multiple comparisons of cross-sectional surface area of different types of phagocytes

In collaboration with Ms. Mahrukh Shameem in our lab, we examined the membrane surface of tissue resident phagocytes in their natural environment. Using a precision cut slicing technique, mouse lung and liver sections were prepared for SEM examination to illustrate the surfaces of their resident macrophages, alveolar macrophages and Kupffer cells, respectively. Results (Figure 3.15) showed a more variable and more complex surface features of phagocytes in their natural environment. Alveolar macrophages (Figure 3.15A-C) possessed dense mushroom-like protrusions (red box) in their surfaces alongside ruffles (green box) and ridges (yellow box). Interestingly, when these cells were retrieved from mouse lungs and allowed to settle in a 24-well plate overnight (Figure 3.16), their surfaces became more similar with respect to the type of membrane protrusions they possess characterised by high ridge

density. These differences might be due to a more heterogenous physical and chemical environment *in vivo* than *in vitro*, suggesting that ridges are sensitive to changes in phagocyte's external environment (explored further in section 3.10). On the other hand, Kupffer cells (Figure 3.14D-F) of the liver were seen to possess nanoscopic membrane protrusions that did not show any sheet-like property as membrane ridges. These microvillus-like structures (red box) were the most common type of protrusion on their surfaces. However, in most instances, Kupffer cells displayed an almost smooth surface feature (Figure 3.14E); ridges were very rarely seen (Figure 3.14F yellow box) and, when present, were in very low density.

A

B

C

D

E

F
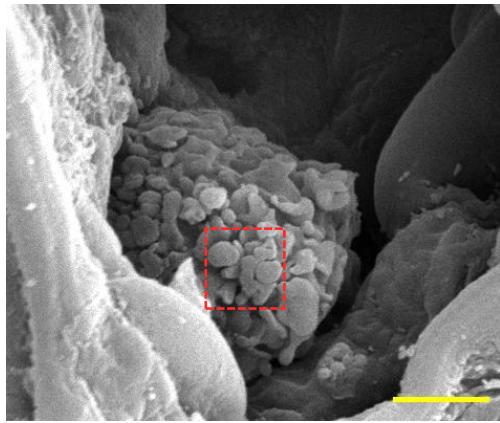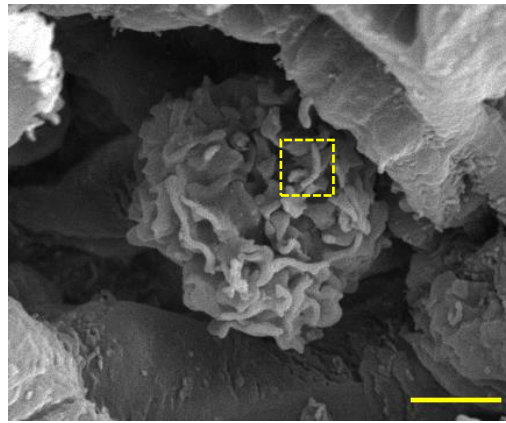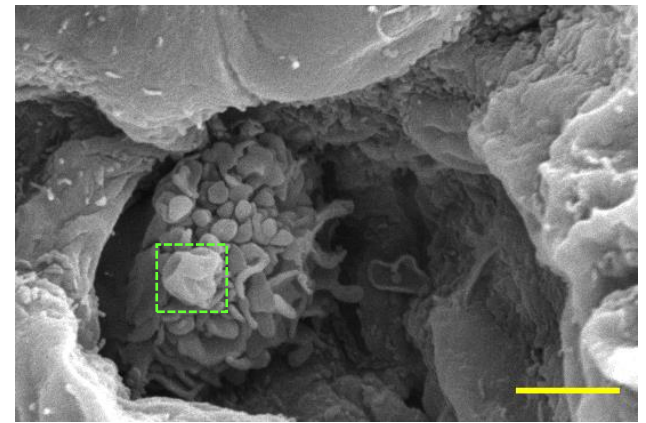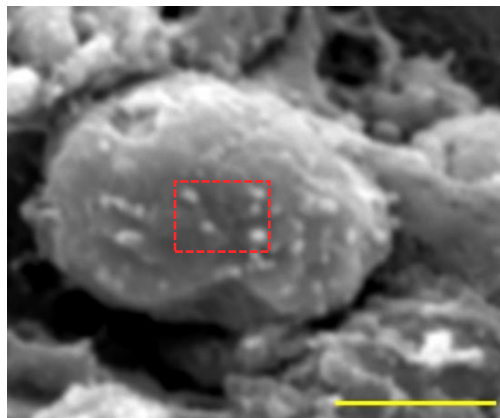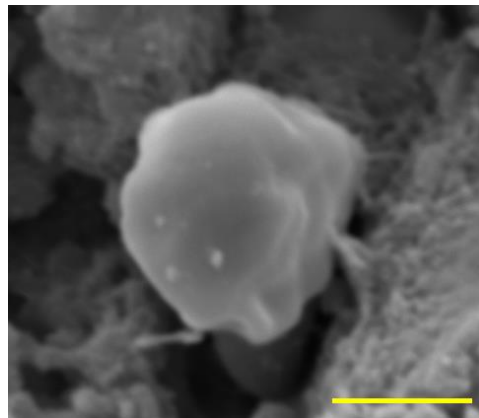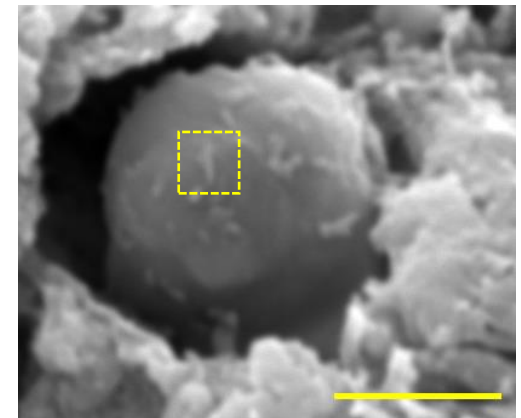
(Figure legend on next page)

Figure 3.15 | Membrane ridges are also expressed by macrophages *in vivo*. Lung and liver samples were recovered from euthanised mouse. Sections of 100 μm thickness passing through the frontal plane were prepared using precision cut slicing method, and processed for SEM examination. Samples were imaged using a high vacuum, thermionic emission scanning electron microscope with an SE detector system and 10 kV accelerating voltage. Images are a representative of 2 independent imaging experiments.

(A-C) The resident alveolar macrophages of mouse lung showing their different membrane protrusions *in vivo*: mushroom-like protrusions (red box), ridges (yellow box) and ruffles (green box),

(D-E) The resident Kupffer cells of mouse liver showing microvillus-like protrusion (red box) and ridges (yellow box). Scale bar in all images - 2 μm.

A **B**
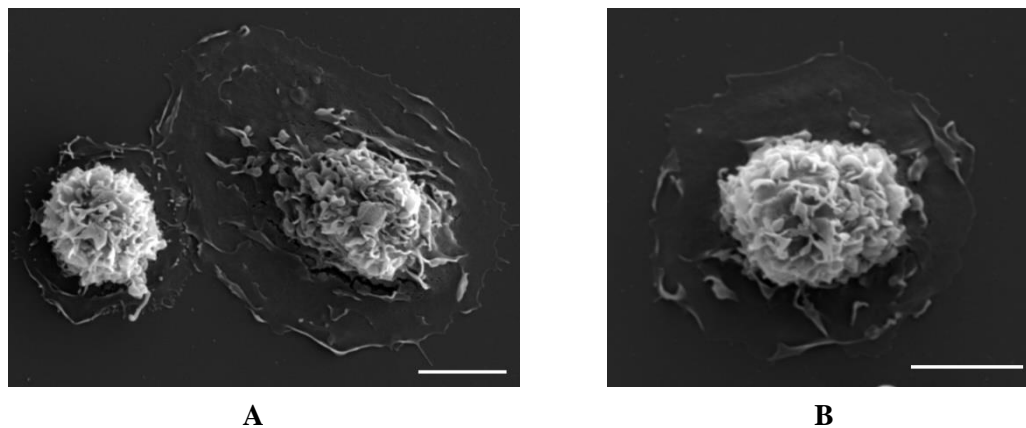
Figure 3.16 | Alveolar macrophages examined *in vitro* have a more consistent surface feature predominated by membrane ridges than their *in vivo* (figure 3.15A-C) counterparts. Alveolar macrophages were recovered from mouse lungs through bronchoalveolar lavage. They were then plated into 24 well plate with uncoated glass coverslip and comp DMEM media. After overnight acclimatisation, they were processed for SEM and imaged using a high vacuum, thermionic emission scanning electron microscope with an SE detector system under 10 kV accelerating voltage, 9 mm working distance, 63 nm spot size and 0° stage tilt. Images are a representative of 3 independent imaging experiments.

(**A** and **B**) *In vitro* SEM images of mouse alveolar macrophages. Scale bar – 5 μm.

3.10 Effect of cell activation, genetic manipulation, osmosis and disease phenotype on membrane ridges

After exploring the architecture and dynamics of membrane ridges, I then looked at factors which might affect its expression in the macrophage surface. I used these factors as they were reported to have profound effects in macrophage morphology and function, which might provide important insights on the role of membrane ridges.

3.10.1 Activation of macrophages

Macrophages are well known to be sensitive to external stimuli for their functions; they can be classically activated into a pro-inflammatory (M1) phenotype or alternatively activated into an anti-inflammatory (M2) phenotype. M1 macrophages respond to tissue injury or infection by secreting pro-inflammatory cytokines, reactive oxygen species and nitrogen intermediates to neutralise microbes causing infection (Murray and Wynn, 2011). They are also known for their high phagocytic activity and are reported to display a rounder shape than unstimulated (M0) and M2 macrophages (McWhorter et al., 2013). On the other hand, M2 macrophages promote wound healing and secrete growth factors that stimulate the recruitment and development of cellular components essential for tissue repair (Wynn et al, 2011). These cells are characterised by a more elongated shape compared to M0 and M1 macrophages (McWhorter et al., 2013).

Using *in vitro* cultures of human monocyte-derived macrophages donated by Dr. Chiara Niespolo of Kiss-Toth lab in University of Sheffield Medical School, I examined the effect of M1 (LPS/IFNγ) and M2 (IL-10 or IL-4) stimulation on membrane ridge expression. HMDM samples were processed for SEM examination, and the expression of membrane ridges were estimated through their area density (equation 3.2) and RD analysis routine (section 3.4).

Results (Figure 3.17E) revealed that cell activation did not significantly affect the density of membrane ridges on macrophage surfaces except after IL-10 stimulation ($F(5,4) = 16.04$, $p = 0.011$). Strikingly, membrane ridges were almost completely inhibited following exposure to IL-10. The macrophage surface was transformed into a rough, raspberry-like phenotype with some unidentified minute protrusions (Figure 3.17D yellow arrow). This phenotype is similar to the cellular feature reported by Burwen and Satir (1977) in mast cells, which was found to have reduced secretory capacity and resistance to stimulation. I was not able to confirm if this is also true for macrophages; however, these results provide compelling evidence of the strong inhibitory effect of IL-10 to membrane ridge expression.

On the other hand, the maintenance of membrane ridges following LPS/IFNγ and IL-4 activation suggests that these structures are important in macrophage functions promoted by these cytokines. One of the most likely events is during antigen presentation (Hart et al., 1996) that requires physical interaction of macrophages with other immune cells (discussed in 3.12.5.1).

A

B

C

D

E
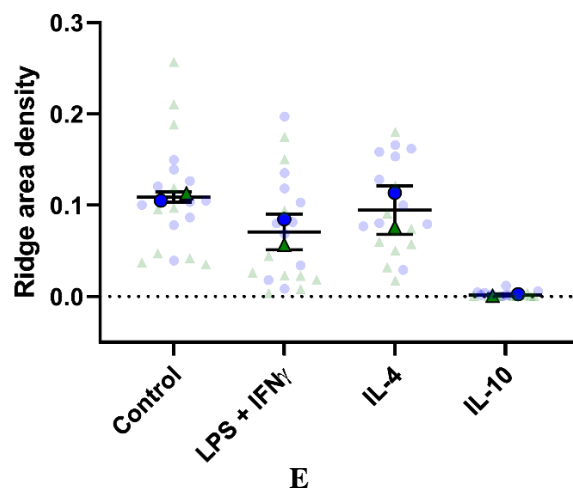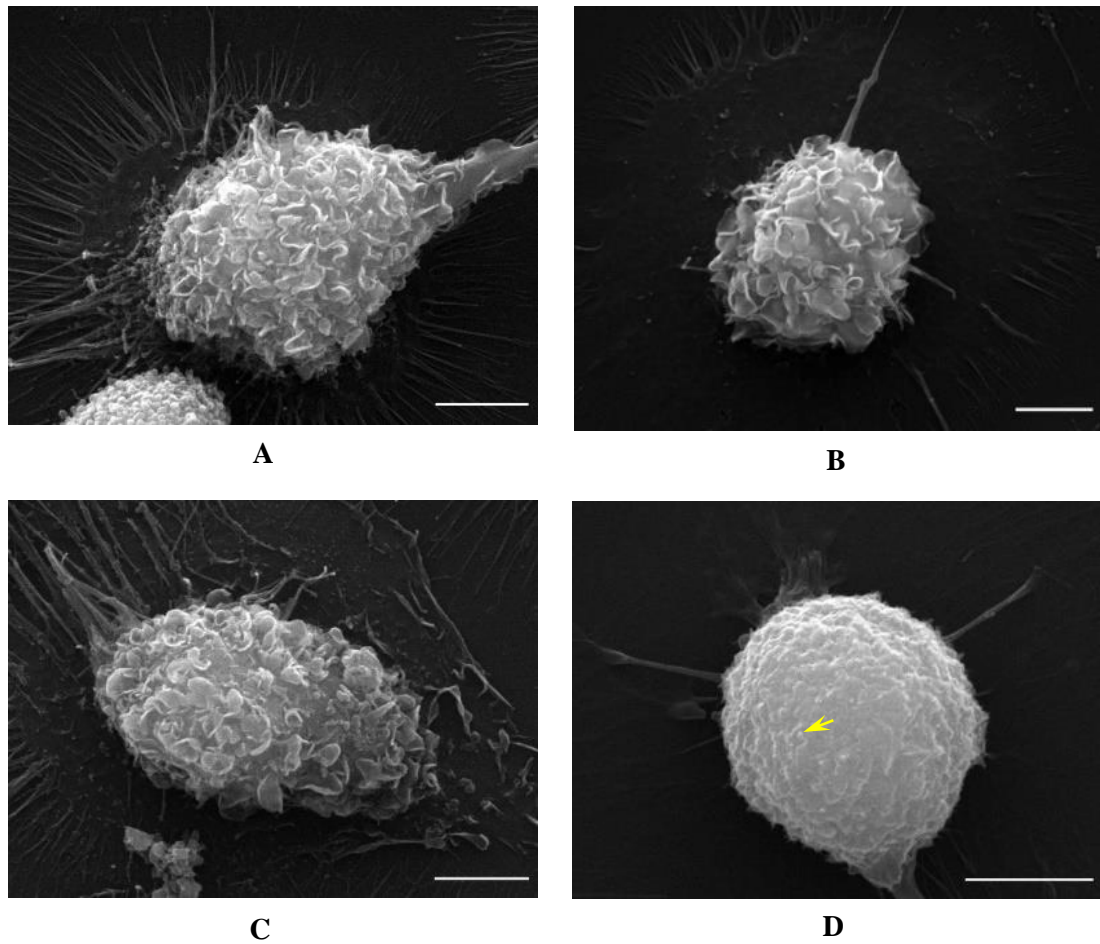
(Figure legend on next page)

Figure 3.17 | IL-10 activation represses membrane ridge expression in human monocyte-derived macrophages (HMDM). HMDM were seeded and differentiated into a 24-well plate with uncoated glass cover slip. Cells were then stimulated using LPS/IFNγ, IL-4 or IL-10, and processed for SEM examinations. Samples were imaged using a high vacuum, thermionic emission scanning electron microscope with an SE detector system, 10 kV accelerating voltage, 9 mm working distance, 63 nm spot size and 0° stage tilt. Images are a representative of 20 single cell SEM imaging data from 2 independent experimental repeats.

(A) Representative SEM images of unstimulated (control) HMDM, **(B)** LPS/IFNγ- activated HMDM, **(C)** IL-4- activated HMDM and **(D)** IL-10- activated HMDM from 10 cells examined per repeat, scale bar - 5 μm,

(E) Comparison of HMDM membrane ridge area density at different activation states revealed statistically significant difference using ordinary one-way ANOVA ($F(5,4) = 16.04$, $*p=0.011$), $n = 2$ (10 cells per repeat), bars: mean ± standard deviation, a post hoc analysis using Tukey's test (table 3.5) was done to further examine group differences, please refer to the table for statistically significant group comparisons.

Dependent variable: Ridge area density Alpha = 0.05				
Activation state comparison	**Mean Difference**	**95% CI of Difference**	**Significant?**	**Adjusted p value**
Control vs. LPS + IFNγ	0.03832	-0.03008 to 0.1067	No	0.2455
Control vs. IL-4	0.01436	-0.05404 to 0.08277	No	0.8275
Control vs. IL-10	0.1073	0.03893 to 0.1757	Yes	0.0106
LPS + IFNγ VS. IL-4	-0.02395	-0.09236 to 0.04445	No	0.5475
LPS + IFNγ VS. IL-10	0.06902	0.0006154 to 0.1374	Yes	0.0486
IL-4 VS. IL-10	0.09297	0.02457 to 0.1614	Yes	0.0177

Table 3.5 Tukey's multiple comparisons of ridge area density of HMDM at different activation states

I next examined whether macrophage activation affects cell surface area and elongation property of the cells. I implemented an image segmentation method by thresholding to measure these parameters in macrophages. Briefly, a threshold was assigned to each SEM image (Figure 3.18A) to detect macrophage cell borders. Each cell was then visually examined to verify that cell borders were correctly identified without overlapping with adjacent cells or extracellular debris before measuring its surface area and aspect ratio by shape descriptor of Fiji software (Schindelin et al., 2012).

Results showed that neither M1 (LPS/IFNγ) nor M2 (IL-10, IL-4) activation of HMDM had any significant effect on their cell surface area ($F(3,4) =0. 469$, $p = 0.72$) and cell elongation or aspect ratio ($F(3,4) = 2.719$, $p = 0.179$). These suggest that cell surface area and elongation properties of macrophages are tightly monitored and conserved across different functional phenotypes. However, this slightly contradicts a previous report by McWhorter (2013) and colleagues. Their results showed that M2 activation results in a more elongated (higher aspect ratio) macrophage phenotype. Hence, I examined their data and accounted these opposing results to some key differences in experimental set-up and data analysis. The modality used for cell imaging will greatly affect how cell structures will register in the final image given the differences in system resolution. McWhorter and colleagues (2013) used light microscopy to examine activated macrophages which might not have accurately captured the round nanometric size lamellipodia bordering the cells, thus making them appear more elongated. Another plausible reason is that the wider spread of aspect ratio values in M2 macrophages compare to M1 and unstimulated cells (Figure 3.18F) would make measurements susceptible to biases especially when measuring a small population size (i.e.<100 cells). Data of McWhorter (2013) and co-workers unfortunately were presented in a bar graph, hence the distribution of data cannot be examined. Finally, the different cell types (BMDM – McWhorter vs HMDM – my experiment) and activation factors used (IL-13 – McWhorter vs IL-4 and IL-10 – this experiment) might have variable effects when examining macrophage cell morphology and assigning an M2 phenotype. Thus, an experiment using the same experimental set-up by McWhorter (2013) and colleagues but using SEM imaging could help resolve these issues.

A

B

C

D

E

F
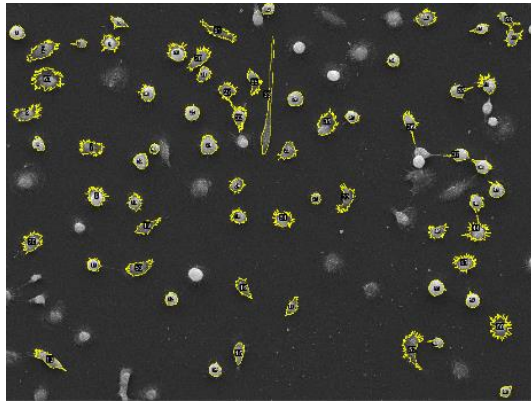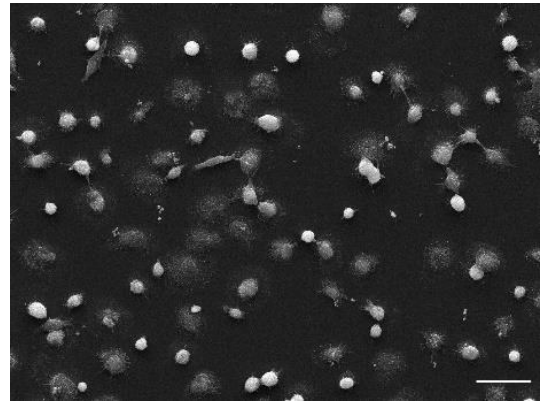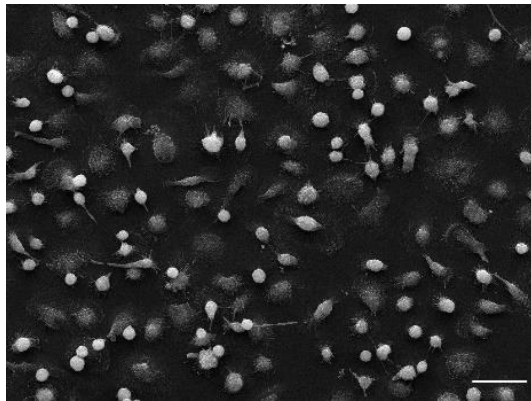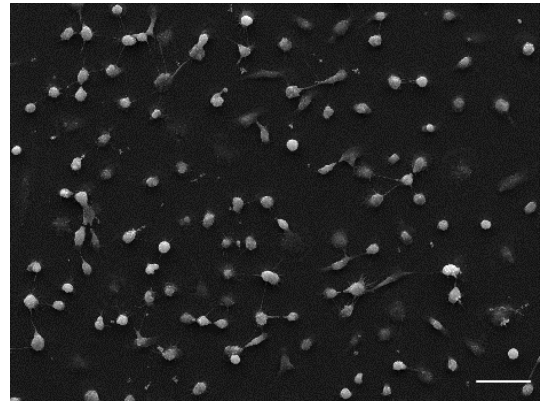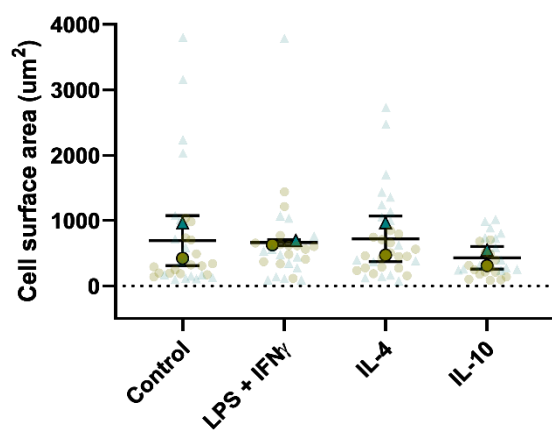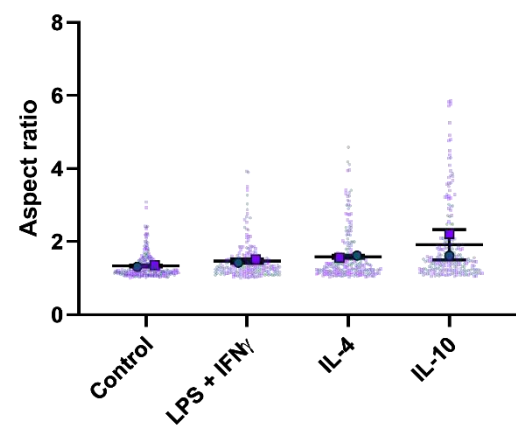
(Figure legend on next page)

Figure 3.18 | Activation of human monocyte-derived macrophages (HMDM) does not alter their cross-sectional surface area nor cell shape with respect to aspect ratio. HMDM were seeded and differentiated into a 24-well plate with uncoated glass cover slip. Cells were then stimulated with LPS/IFNγ (M1), IL-4 (M2), or IL-10 (M2), processed for SEM and imaged using a high vacuum, thermionic emission scanning electron microscope with an SE detector system under 10 kV accelerating voltage, 9 mm working distance, 63 nm spot size and 0° stage tilt. Images are a representative of 6 imaging frames from 2 independent experimental repeats.

(A) SEM images of unstimulated (control) macrophages showing the cell borders as determined by image segmentation via thresholding, **(B)** LPS/IFNγ- activated HMDM, **(C)** IL-4- activated HMDM and **(D)** IL-10- activated HMDM, scale bar in all images - 50 μm,

(E) No statistically significant difference in cell surface area of differentially activated HMDM was found using ordinary one-way ANOVA ($F(3,4) = 0.469$, $p = 0.72$), $n = 2$ (14-17 cells per repeat), bars: mean (*M*) ± standard deviation (*SD*),

(F) No statistically significant difference in aspect ratio of differentially activated HMDM was found using ordinary one-way ANOVA ($F(3,4) = 2.719$, $p = 0.179$), $n = 2$ (96-140 cells per repeat), bars: $M \pm SD$.

3.10.2 Genetic manipulation of *trib1* and *trib3*

Gene regulation is an important feature of macrophages to fine tune their functional properties to changing extracellular conditions and physiological requirements (Jantsch et al., 2014). Critical genes that regulate macrophage metabolism and functions are often involved in their activation as well. Hence, it is not surprising that these genes are often associated with pro-inflammatory and anti-inflammatory macrophage phenotypes. To examine any effect of macrophage regulatory genes on membrane ridge expression and other biophysical properties of macrophages, I used *trib1* knockdown and *trib3* knockout macrophage models.

Tribbles homolog 1 (*trib1*) is a pleiotropic gene influencing cell differentiation, proliferation and metabolism (Kraja et al., 2011). Additionally, it was recently reported to regulate M1/M2 macrophage polarisation via JAK/STAT signalling pathway (Arndt et al., 2018). Thus, using donated samples of *trib1* knockdown (KD) human monocyte-derived macrophages (HMDM) from Dr. Chiara Niespolo, I examined its effect on membrane ridge expression, cell surface area and cell elongation. I used the previously described routines to estimate membrane ridge area density (section 3.4), cell surface area and aspect ratio/cell elongation (section 3.10.1) of *trib1* KD HMDM.

Results (Figure 3.19C) revealed that membrane ridges are reduced by more than 50% in macrophages following *trib1* KD ($t(2) = 8.42$, $p = 0.014$). I carried out four independent experiment repeats but due to the collapse of the membrane in half of the repeats, which were chemically dried, I was only able to analyse two repeats. Nonetheless, I did statistical analysis for each repeat to verify significant findings in the combined data. In both repeats (Figure 3.19C - R1 and R2), the reduction in density of membrane ridges after *trib1* KD was consistent (R1- $t(22) = 2.55$, $p = 0.018$, R2 - $t(18) = 2.28$, $p = 0.035$). Collectively, these suggest a very likely role of *trib1* in regulating membrane ridge expression in macrophages. Meanwhile, there were no statistically significant changes in cell surface area (Figure 3.19D) and aspect ratio or cell elongation (Figure 3.19E) following *trib1* KD, indicating that *trib1* might not be involved in regulating these biophysical properties in HMDM.

A

B

R1

R2

C

D

E
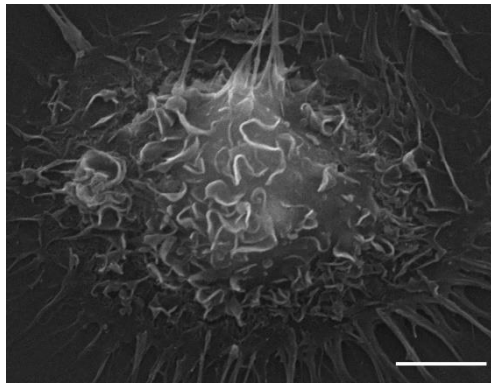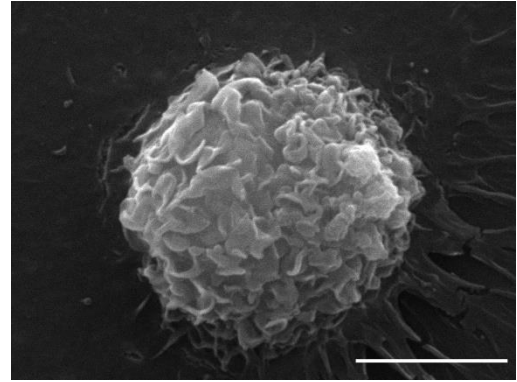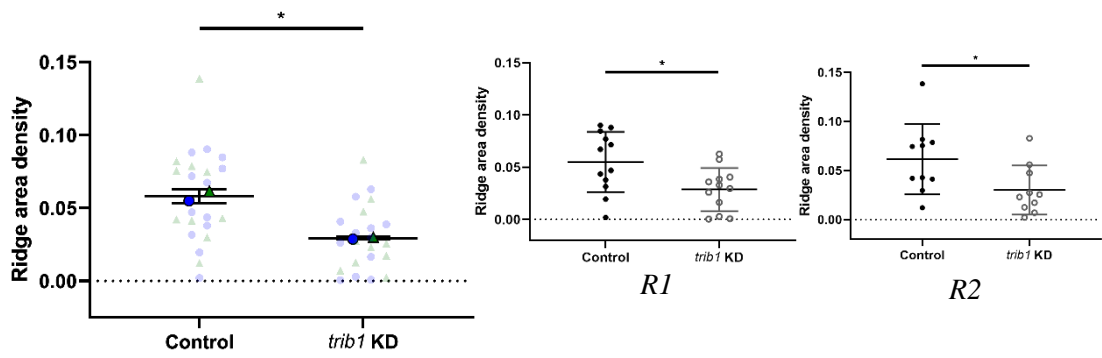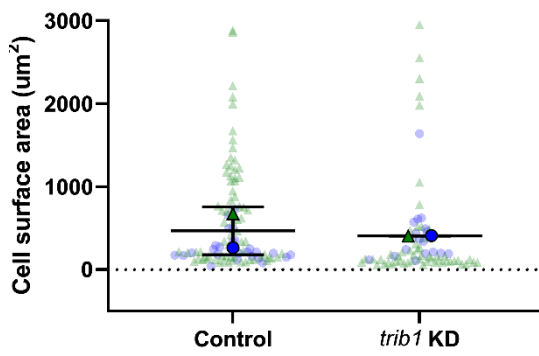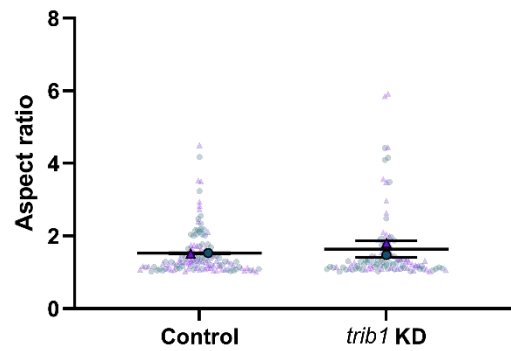
(Figure legend on next page)

Figure 3.19 | Knockdown (KD) of *trib1* in human monocyte-derived macrophages (HMDM) leads to reduction in their membrane ridge area density but does not alter their surface area nor their cell shape. HMDM were seeded and differentiated into a 24-well plate with uncoated glass cover slip. Cells were then incubated with *trib1* scramble (negative control) or *trib1* siRNA. Confirmatory test on *trib1* knockdown was done using RT-qPCR, and samples were then processed for SEM analysis. SEM imaging was performed using a high vacuum, thermionic emission scanning electron microscope with an SE detector system under 10 kV accelerating voltage, 9 mm working distance, 63 nm spot size and 0° stage tilt. Images are a representative of 20 cells from 2 independent experimental repeats.

(A) SEM images of *trib1* scramble HMDM and **(B)** *trib1* KD HMDM, scale bar - 5 μm,

(C) There was a statistically significant reduction in membrane ridge density of HMDM (M=0.058, $SD = 0.005$) after *trib1* KD ($M = 0.029$, $SD = 0.001$) as revealed by unpaired t-test ($t(2) = 8.42$, $*p = 0.014$), $n = 2$ (10-12 cells per repeat), bars: mean (M) ± standard deviation (SD), R1- repeat 1 unpaired t-test ($t(22) = 2.56$, $*p = 0.018$), $n = 12$ cells, bars: $M ± SD$), R2 - repeat 2 unpaired t-test ($t(18) = 2.28$, $*p = 0.035$), $n = 10$ cells, bars: $M ± SD$,

(D) No statistically significant change in surface area of HMDM ($M = 466$, $SD = 288$) after *trib1* KD ($M = 406$, $SD = 4$) was found using unpaired t-test ($t(2) = 0.295$, $p = 0.796$), $n = 2$ (18-72 cells per repeat), bars: $M ± SD$,

(E) No statistically significant change in aspect ratio/elongation of HMDM ($M = 1.520$, SD=0.018) after *trib1* KD ($M = 1.639$, $SD = 0.228$) was observed using unpaired t-test ($t(2) = 0.737$, $p = 0.538$), $n = 2$ (43-64 cells per repeat), bars: $M ± SD$.

I next examined the role of another macrophage regulatory gene, *trib3,* in membrane ridge expression and other biophysical properties of macrophages. The *trib3* gene like *trib1* is well-known to participate in a wide range of metabolic processes from insulin signalling to cell growth and survival (Mondal et al., 2016; Butcher et al., 2017). Recently, it was described in macrophages as a potent pro-inflammatory mediator using gene expression analysis and polarisation markers (Campesino et al., 2018). As membrane ridges were previously seen to be maintained in macrophages expressing a pro-inflammatory phenotype (Figure 3.17-LPS/IFNγ), it is worth examining how *trib3* manipulation will affect its expression.

Wild type and *trib3* knockout mouse bone-marrow derived macrophages (BMDM) cultured *in vitro* were donated by Dr. Laura Martinez-Campesino of Wilson lab in University of Sheffield Medical School. I then processed them for SEM examination and analysed them using the previously described methods for ridge area density (section 3.4), cell surface area and cell elongation (section 3.10.1).

Results (Figure 3.20C) showed that *trib3* knockout BMDM had more than 10% reduction in membrane ridge area density ($t(4) = 3.474$, $p = 0.026$), which further underscores potential role of membrane ridges in pro-inflammatory response of macrophages. Compare to *trib1* however*, trib3* had also notable effect on macrophage size, whereby its knockout resulted to more than 50% increase in cell surface area (Figure 3.20D, $t(4) = 4.057$, $p = 0.015$). This reiterates the pleiotropic nature of *trib3* gene in affecting multiple cellular processes. Meanwhile, as in previous analyses, there was no statistically significant change in cell elongation (aspect ratio) following *trib3* KO (Figure 3.20E).

Concomitant with ridge density reduction, it is interesting to note that our collaborators had also found a statistically significant decrease in the expression of actin nucleator Spire1 (Figure 3.20F $t(9) = 3.289$, $p = 0.009$) in *trib3* KO BMDM. This suggests that membrane ridge actin could be potentially regulated by Spire1, which is yet to be confirmed. On the other hand, the expression of β-actin mRNA was found to be increased by about 45% in these cells (Figure 3.20G, $t(22) = 2.576$, $p = 0.017$), presumably necessary to support the increase in cell size that is observed following *trib3* KO.

A

B

C

D

E

F

G
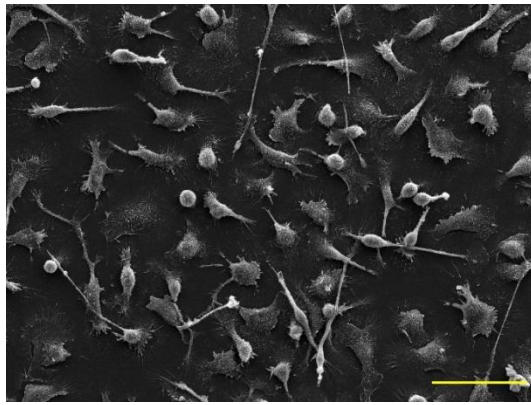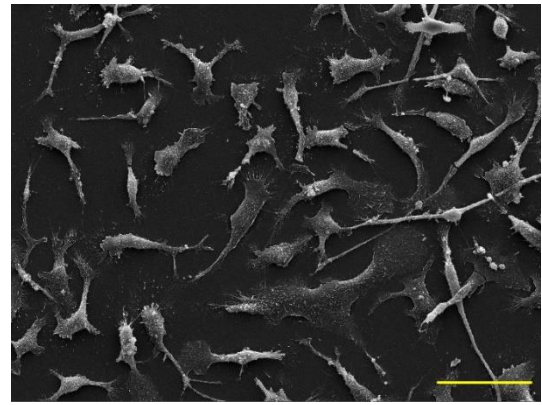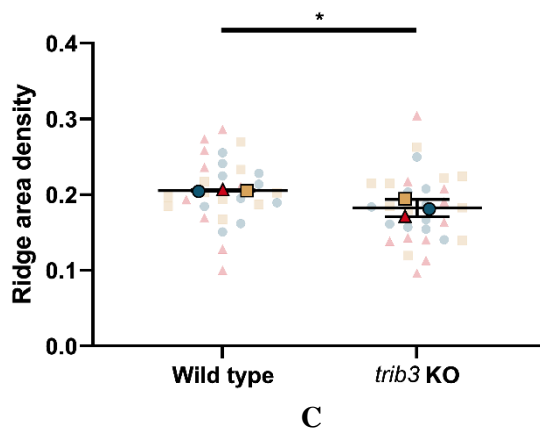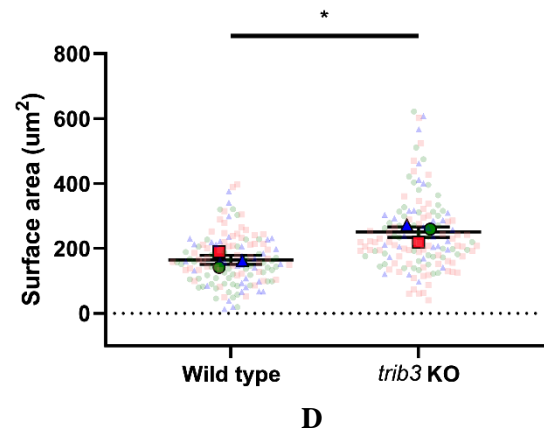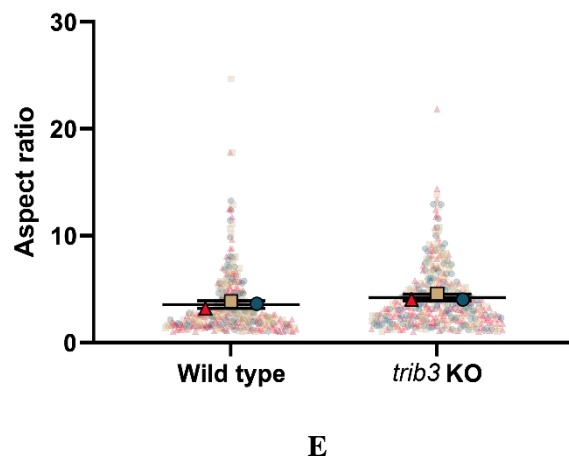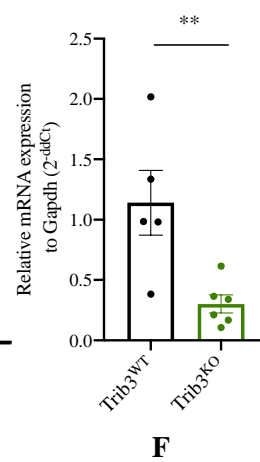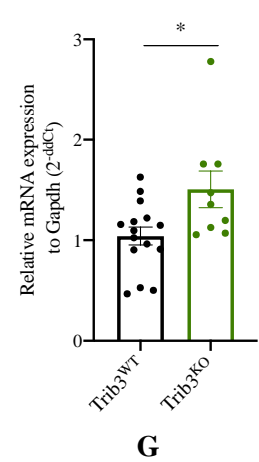
(Figure legend on next page)

Figure 3.20 | *Trib3* knockout (KO) in mouse bone marrow-derived macrophages (BMDM) leads to reduction in membrane ridge density and increase in cell surface area. Wild and *trib3* KO BMDMs were seeded and differentiated into a 24-well plate with uncoated glass cover slip. Cells were then processed for SEM and imaged using a high vacuum, thermionic emission scanning electron microscope with an SE detector system under 10 kV accelerating voltage, 9 mm working distance, 63 nm spot size and 0° stage tilt. Three independent experimental repeats were done acquiring 3 images per condition in each repeat for surface area analysis and 10 single cell images per condition for ridge area density examination.

(A) SEM images of mouse wild type BMDM and **(B)** *trib3* KO BMDM, scale bar - 50 μm,

(C) There was statistically significant reduction in ridge area density of mouse BMDM (M=0.2056, SD = 0.0012) after *trib3* KO (M = 0.1825, SD = 0.0115) as confirmed by unpaired t-test analysis ($t(4)$ = 3.474, *p = 0.026), n = 3 (10 cells per repeat), bars: $M \pm SD$,

(D) There was statistically significant increase in cell size of mouse BMDM (M = 165, SD=24) following *trib3* KO (M = 250, SD = 28) as shown by unpaired t-test ($t(4)$ = 4.06, *p = 0.02), n = 3 (30-60 cells per repeat), bars: $M \pm SD$,

(E) No statistically significant change in aspect ratio/cell elongation of mouse BMDM (M = 3.537, SD = 0.345) after *trib3* KO (M = 4.198, SD = 0.321) was found as confirmed by unpaired t-test ($t(4)$ = 2.429, p = 0.072), n = 3 (95-148 cells per repeat), bars: $M \pm SD$,

(F) *trib3* KO mouse BMDM had statistically significant reduction in mRNA expression of Spire1 as determined by unpaired t-test ($t(9)$ = 3.289, **p = 0.009), n = 5-6 mice, bars: $\pm SD$,

(G) β-actin mRNA expression was significantly reduced in mouse BMDM following *trib3* KO as confirmed by unpaired t-test ($t(22)$ = 2.576, *p = 0.017), n = 9-15 mice, bars: $\pm SD$.

Data in *F* and *G* courtesy of Dr. Laura Martinez-Campesino.

3.10.3 Osmosis

Biophysical factors such as cell volume, cytoplasmic viscosity, membrane tension and cortical tension are known to affect the expression of different membrane features including blebs (Tinevez et al., 2009) and pseudopodial extensions (Heinrich, 2015). These highlight the biophysical regulations of these membrane structures. To explore the effect of membrane tension force on membrane ridges, I subjected macrophages to different media of varying osmolarities and hypothesised that an increase in osmotic pressure or membrane tension force would lead to reduction in membrane ridge density.

Membrane tension and cell surface area are known to be affected by osmosis or the movement of water across a membrane (Graham, 1854). Lower osmotic (hypoosmotic) pressure normally results in a net movement of water into the cell which subsequently increases membrane tension force and cell surface area (Groulx et al., 2006; Pontes et al., 2017). Using this principle, I subjected macrophages into media with different osmolarities by varying NaCl concentrations, which were classified as hypoosmotic (0.2% and 0.5%), isosmotic (0.9%) and hyperosmotic (1.5% and 2.5%). I then used fluorescence and SEM imaging to describe and measure any changes in membrane ridges, filopodia and cell surface area.

Macrophages showed striking physical changes after exposure to different osmotic conditions. Cells in hypoosmotic media usually appeared flat (Figure 3.21A and 3.21C) with membrane folds (Figure 3.21A yellow arrow) that became very prominent in cells exposed to extremely hypoosmotic condition (0.2% NaCl). Their actin cortex was not noticeable compare to cells in isosmotic (Figure 3.21L green arrow) and hyperosmotic (Figure 3.21H and 3.21J green arrow) media, suggesting a change in its architecture which most likely caused the observed changes in cell shape. Membrane ridges were also very rarely seen in these cells. Finally, these cells were seen to commonly expressed filopodial protrusions (Figure 3.21A and 3.21B green arrow) and some unidentified actin puncta (Figure 3.21B blue arrow).

On the other hand, even though cells in hyperosmotic media maintained their spherical shape, its actin cortex was observed to become thinner with increasing osmolarity (compare Figure 3.21H and 3.21J). This was however not quantified due to time constraint, but visual examination showed very distinct changes in cortical actin fluorescence and its thickness in both J774 and RAW264.7 cells (data not shown). These suggest structural changes in the cortical actin that is not manifested in cell shape. Their surfaces however maintained expression of membrane ridges (Figure 3.21G and 3.21I yellow arrow) similar to those cells in isosmotic media (Figure 3.21E and 3.21K yellow arrow) which occasionally featured some membrane ruffles as well (Figure 3.21E green arrow).

A   B   C   D

E   F   G   H

I   J   K   L
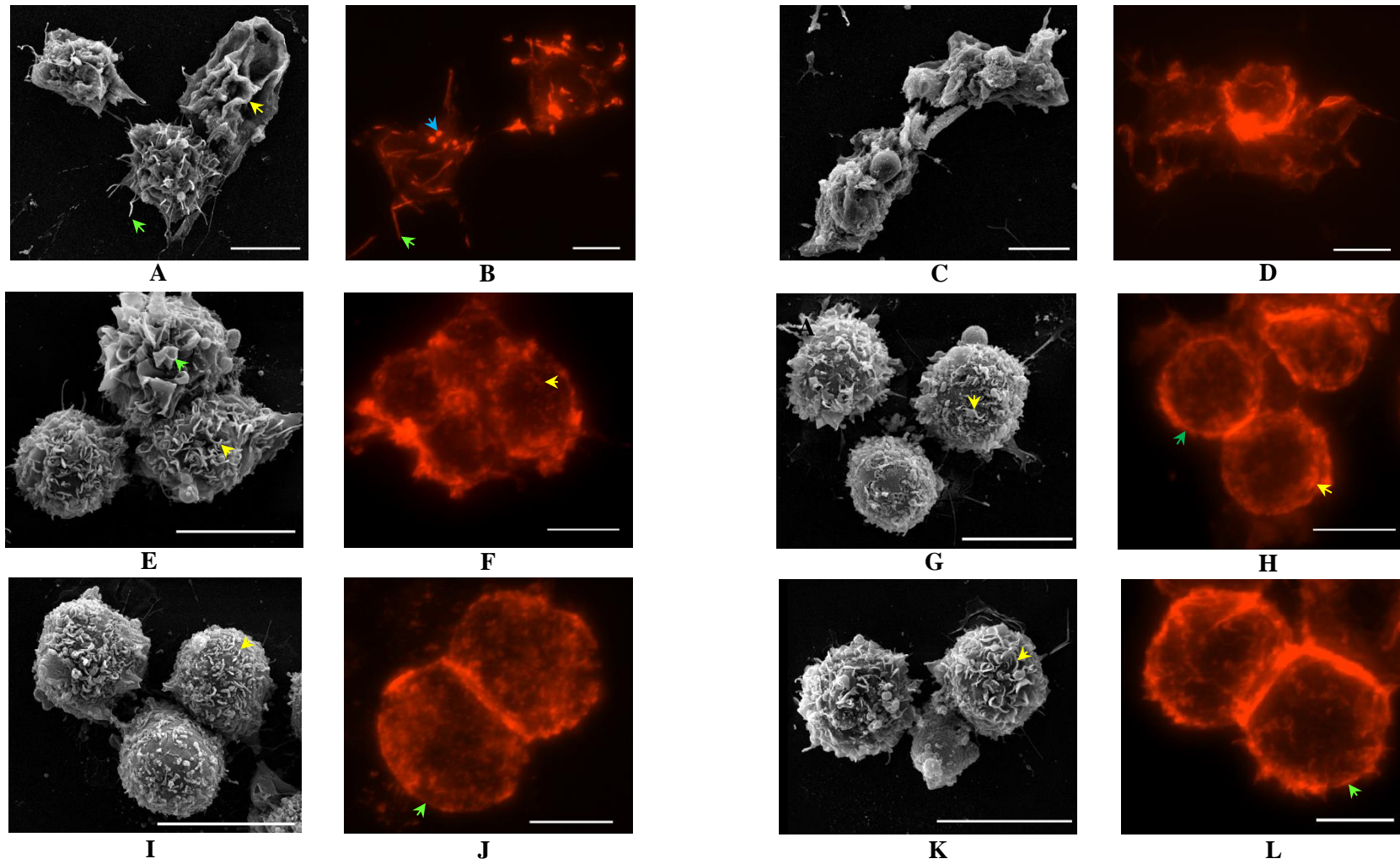
(Figure legend on next page)

Figure 3.21 | SEM and fluorescence microscopy reveal changes in membrane ridges, cell surface area and cell shape of macrophages exposed to different osmotic pressures. A heathy culture of J774 macrophage-like cells was seeded into 24-well plate with uncoated glass coverslips. After overnight acclimatisation, cells were then exposed for 30 minutes to different media: distilled water, 0.2% NaCl, 0.5% NaCl, 0.9% NaCl, 1.5% NaCl, 2.5% NaCl and complete DMEM. After the assay, cells were immediately fixed and processed for SEM and fluorescence microscopy separately. For SEM, cells were imaged with a high vacuum, thermionic emission scanning electron microscope coupled with an SE detector system using 10 kV accelerating voltage. For fluorescence imaging, fixed cells labelled with phalloidin-TRITC to reveal its actin were imaged using a 60x oil immersion objective (1.4 NA Plan Apo) in Cy3 (excitation: 545/25 nm, emission: 605/70 nm) channel of a widefield microscope. **Left**-SEM image, **Right**- maximum intensity image projection of cellular actin fluorescence with the same osmotic condition to its left but showing different cells. Images are a representative of 15-30 imaging frames from 3 independent experimental repeats.

(A) Cells subjected to extremely hypoosmotic (0.2% NaCl) media displaying irregular shapes, almost no membrane ridges, frequent membrane folds (yellow arrow) and numerous filopodia (green arrow),

(B) Actin cytoskeleton of cells exposed to 0.2% NaCl revealing its filopodia (green arrow), commonly observed but unidentified actin puncta (blue arrow) and indistinguishable actin cortex,

(C, D) Cells subjected to mildly hypoosmotic 0.5% NaCl,

(E, F) Cells in isosmotic 0.9% NaCl showing high density of ridges (yellow arrow),

(G, H) Cells in mildly hypertonic 1.5% NaCl displaying very distinct actin cortices (green arrow),

(I, J) Cells in extremely hypertonic 2.5% NaCl with numerous but short ridges (yellow arrow) and its actin cortex (green arrow),

(K, L) Cells in complete DMEM showing its ridges (yellow arrow) and actin cortex (green arrow). Scale bar in all images – 10 μm.

Because changes in cell surface area is a key feature of any osmosis experiment on mammalian cells (Sach and Sivaselvan, 2015), I used the previously described image analysis routine (section 3.10.1) to measure and compare the surface area of macrophages following the osmosis assay. It should be noted that a distilled water media or 0% NaCl was also used, but due to the very limited number of cells survived, it was not included in the analysis.

Results (Figure 3.22A) confirmed the significant effect of media osmolarity to cell surface area ($F(5,12) = 9.262$, $p = 0.001$). A post hoc analysis (table 3.6) was done and further revealed that macrophages subjected to hypoosmotic conditions (0.2% and 0.5% NaCl) had significantly larger surface area than those in hyperosmotic media (1.5% and 2.5% NaCl). Interestingly, no statistically significant difference was found between any of the isosmotic conditions (0.9% NaCl and comp DMEM) and the extreme media osmolarities (0.2%, 0.5%, 1.5%, 2.5% NaCl). Hence, I further examined the surface area distributions of these cells to possibly explain this observation.

Results (Figure 3.22B-G) showed that cell surface area of macrophages in different osmotic media had a positively skewed distribution in general (table 3.7-skewness). In osmotic conditions (Figure 3.22B and 3.22G), surface area peaks at 80 μm^2 that is slightly shifted to the right in hypoosmotic conditions (Figure 3.22C and 3.22D) but is maintained in hyperosmotic ones (Figure 3.22E and 3.22F). These suggest tolerance to osmotic stress, which is believed to be due to the critical role of cytoskeleton in mammalian cells by increasing cross-linked polymers (Sach and Sivaselvan, 2015; Spagnoli et al., 2008).

A

B

C

D

E

F

G
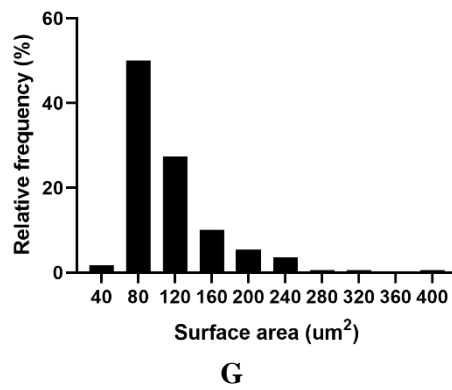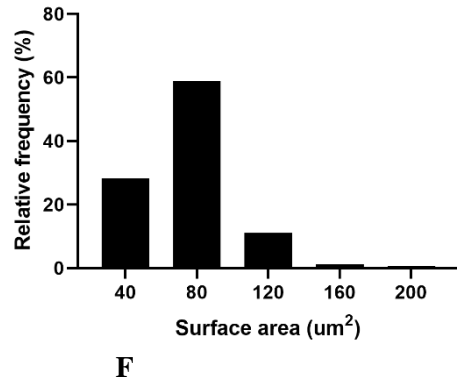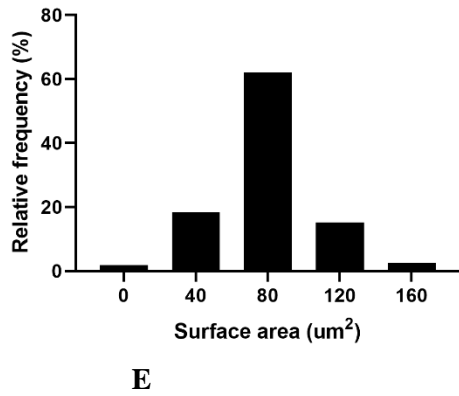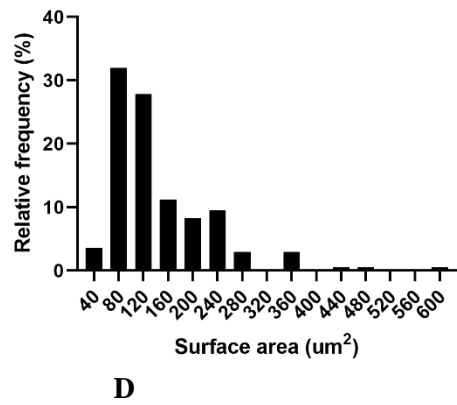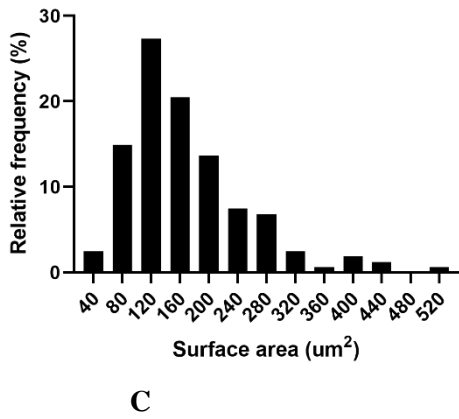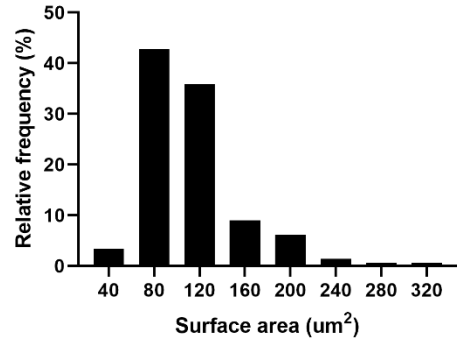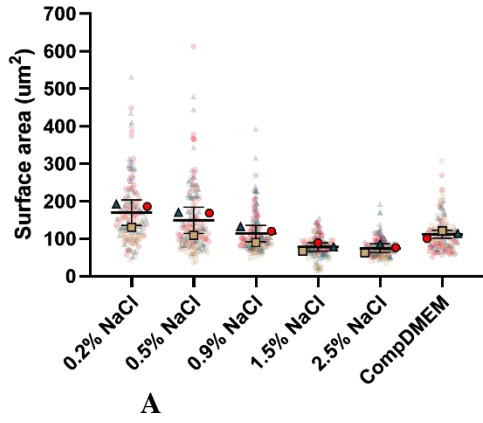
(Figure legend on next page)

Figure 3.22 | Media osmolarity affects the surface area of J774 macrophage-like cells. SEM images of cells from osmosis assay were analysed using image segmentation by thresholding (section 3.10.1) to obtain cell surface area. All values were then combined into a single histogram for each condition for further analysis.

(A) There was statistically significant difference in the surface area of macrophages exposed to different media of varying osmolarities as revealed by ordinary one-way ANOVA of log transformed data ($F(5,12) = 9.262$, $p = 0.001$), $n = 3$ (40-60 cells per repeat), bars: mean ± standard deviation, refer to table 3.6 for statistically significant group comparisons,

 (B-G) Cell surface area histogram of cells subjected to different media: usual culture media complete DMEM (*B*), 0.2 % NaCl (*C*), 0.5% NaCl (*D*), 1.5% NaCl (*E*), 2.5% NaCl (*F*), 0.9% NaCl (*G*)**.** Statistical details of these histograms were summarised in table 3.7

Dependent variable: Cell surface area Alpha = 0.05				
Media comparison	**Mean Difference**	**95.00% CI of difference**	**Significant**	**Adjusted p value**
0.2% NaCl vs. 0.5% NaCl	0.05877	-0.1628 to 0.2803	No	0.9416
0.2% NaCl vs. 0.9% NaCl	0.1717	-0.04984 to 0.3933	No	0.1698
0.2% NaCl vs. 1.5% NaCl	0.3331	0.1115 to 0.5546	Yes	0.0030
0.2% NaCl vs. 2.5% NaCl	0.3537	0.1321 to 0.5752	Yes	0.0018
0.2% NaCl vs. comp DMEM	0.1753	-0.04621 to 0.3969	No	0.1560
0.5% NaCl vs. 0.9% NaCl	0.1129	-0.1086 to 0.3345	No	0.5491
0.5% NaCl vs. 1.5% NaCl	0.2743	0.05273 to 0.4958	Yes	0.0130
0.5% NaCl vs. 2.5% NaCl	0.2949	0.07333 to 0.5164	Yes	0.0077
0.5% NaCl vs. comp DMEM	0.1166	-0.1050 to 0.3381	No	0.5182
0.9% NaCl vs. 1.5% NaCl	0.1613	-0.06022 to 0.3829	No	0.2151
0.9% NaCl vs. 2.5% NaCl	0.1819	-0.03962 to 0.4035	No	0.1334
0.9% NaCl vs. comp DMEM	0.003631	-0.2179 to 0.2252	No	>0.9999
1.5% NaCl vs. 2.5% NaCl	0.02061	-0.2010 to 0.2422	No	0.9995
1.5% NaCl vs. comp DMEM	-0.1577	-0.3793 to 0.06385	No	0.2331
2.5% NaCl vs. comp DMEM	-0.1783	-0.3999 to 0.04325	No	0.1455

Table 3.6 Tukey's multiple comparisons of cell surface area of J774 macrophage-like cells subjected to different media osmolarities

	0.2% NaCl	0.5% NaCl	0.9% NaCl	1.5% NaCl	2.5% NaCl	Comp DMEM
Number of values	161	169	168	158	163	145
Minimum	44.21	35.66	48.72	15.06	33.90	51.15
25% Percentile	113.8	91.19	79.86	64.64	58.82	79.27
Median	150.8	121.6	99.17	75.14	70.15	103.2
75% Percentile	201.7	190.7	130.9	89.16	87.39	127.6
Maximum	531.9	611.4	392.5	154.0	192.9	308.2
Range	487.7	575.8	343.8	139.0	159.0	257.1
Mean	169.7	147.6	114.2	77.88	75.34	111.5
Std. Deviation	83.41	86.46	51.18	27.05	24.29	43.93
Std. Error of Mean	6.574	6.651	3.948	2.152	1.903	3.649
Skewness	1.477	2.028	2.057	0.1952	1.725	1.534

Table 3.7 Descriptive statistics of cell surface area histograms (figure 22) of J774 macrophage-like cells in different media osmolarities.

I next examined any changes in the density of membrane ridges and filopodia. Visual inspection of images showed that filopodia expression seemed to be enhanced in hypoosmotic conditions thus I included it in my image analysis. However, results (Figure 3.23) revealed that only membrane ridges were significantly affected with respect to their count ($F(5,12) = 7.784, p = 0.002$) and their area density ($F(5,12) = 17.74, p < 0.0001$) after exposure to variable osmotic conditions. Further analysis using Tukey's test (table 3.8) revealed that cells in extremely hypoosmotic media (0.2% NaCl) had significantly reduced membrane ridge count compare to those in isosmotic (0.9% NaCl) and hyperosmotic (1.5% and 2.5% NaCl) media.

Meanwhile, a post hoc analysis of membrane ridge area density (table 3.9) further highlighted the negative effect of hypoosmotic condition/increase in membrane tension force to ridge expression. Cells in both hypoosmotic conditions (0.2% and 0.5% NaCl) had significantly lower ridge area density than those in isosmotic (0.9% NaCl and comp DMEM) and hyperosmotic (1.5% and 2.5% NaCl) media. Taken together, these results indicate that membrane ridge expression in different osmotic conditions is more sensitive than filopodia with respect to count and area density of these protrusions. Furthermore, membrane ridges were shown to be negatively regulated by osmotic pressure which was not observed for filopodia.
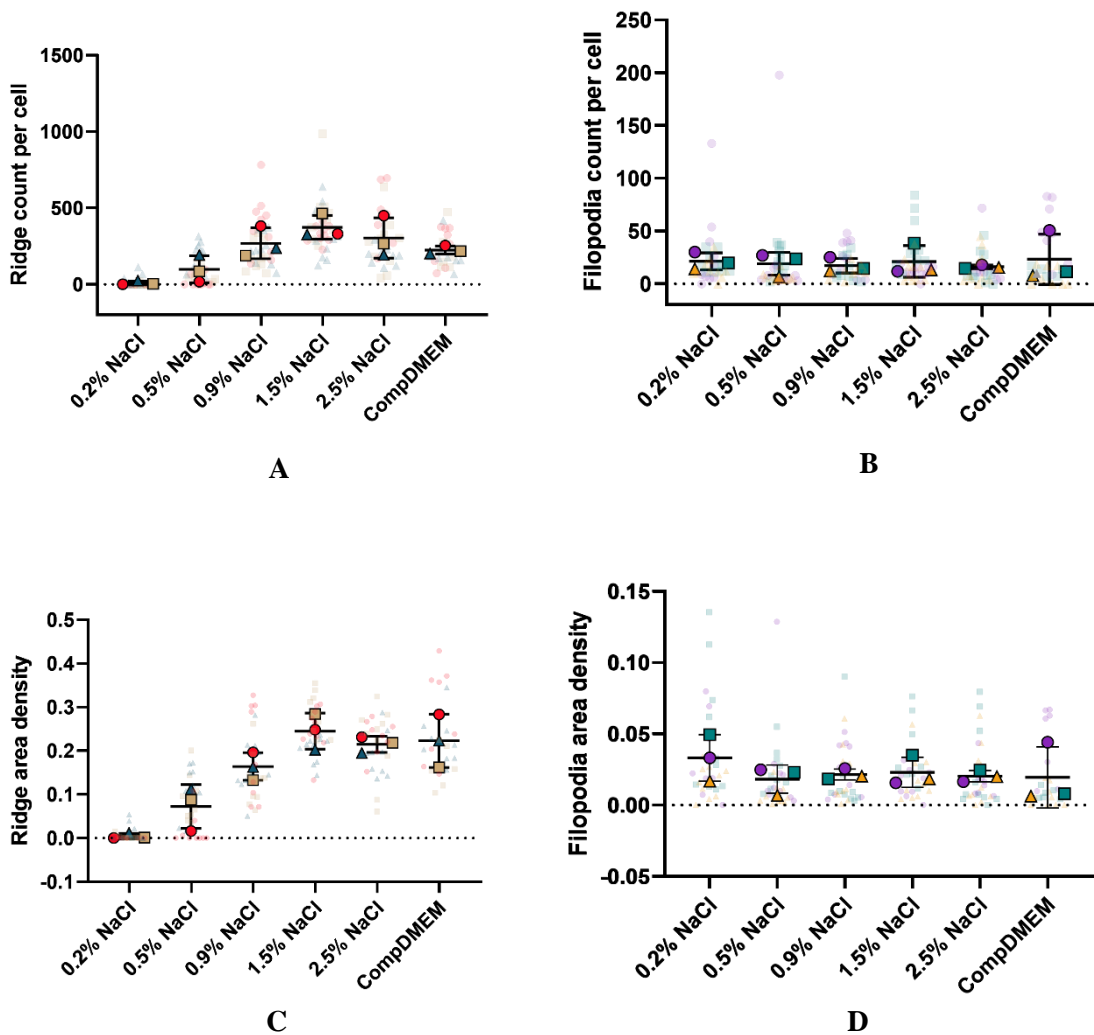
Figure 3.23 | Osmotic pressure affects both the number and surface area density of membrane ridges but not filopodia of J774 macrophage-like cells. SEM images of cells obtained from osmosis assay were analysed using RD analysis (section 3.4). Membrane ridge and filopodia count were recorded on each cell alongside their area densities to profile their expression at different media osmolarities.

(A) There was statistically significant difference in ridge count per cell of macrophages exposed to different osmotic conditions as revealed by ordinary one-way ANOVA ($F(5,12) = 7.784$, $p = 0.002$), $n = 3$ (6-10 cells per repeat), bars: mean (M) ± standard deviation (SD), a post hoc analysis using Tukey's test (table 3.8) was done to further examine the differences between groups, please refer to the table for statistically significant group comparisons.

(B) No statistically significant difference in filopodia count per cell of macrophages exposed to different media osmolarities was found using ordinary one-way ANOVA ($F(5,12) = 0.132$, $p = 0.982$), $n = 3$ (6-10 cells per repeat), bars: $M ± SD$,

(C) There was statistically significant difference in ridge area density of macrophages exposed to different media osmolarities as confirmed by ordinary one-way ANOVA ($F(5,12) = 17.74$, $p < 0.0001$), $n = 3$ (6-10 cells per repeat), bars: $M \pm SD$, post hoc analysis using Tukey's test (table 3.9) was done to further examine group differences, please refer to the table for statistically significant group comparisons,

(D) No statistically significant difference in filopodia area density of macrophages exposed to different media osmolarities was found using ordinary one-way ANOVA ($F(5,12) = 0.548$, $p = 0.737$), $n = 3$ (6-10 cells per repeat), bars: $M \pm SD$.

Dependent variable: Ridge count Alpha = 0.05				
Media comparison	**Mean Difference**	**95.00% CI of difference**	**Significant**	**Adjusted p value**
0.2% NaCl vs. 0.5% NaCl	-89.00	-319.6 to 141.6	No	0.7818
0.2% NaCl vs. 0.9% NaCl	-259.3	-489.9 to -28.72	Yes	0.0247
0.2% NaCl vs. 1.5% NaCl	-363.9	-594.5 to -133.3	Yes	0.0020
0.2% NaCl vs. 2.5% NaCl	-294.1	-524.7 to -63.47	Yes	0.0105
0.2% NaCl vs. comp DMEM	-215.5	-446.1 to 15.07	No	0.0720
0.5% NaCl vs. 0.9% NaCl	-170.3	-400.9 to 60.28	No	0.2042
0.5% NaCl vs. 1.5% NaCl	-274.9	-505.5 to -44.32	Yes	0.0168
0.5% NaCl vs. 2.5% NaCl	-205.1	-435.7 to 25.53	No	0.0925
0.5% NaCl vs. comp DMEM	-126.5	-357.1 to 104.1	No	0.4766
0.9% NaCl vs. 1.5% NaCl	-104.6	-335.2 to 126.0	No	0.6573
0.9% NaCl vs. 2.5% NaCl	-34.74	-265.4 to 195.9	No	0.9949
0.9% NaCl vs. comp DMEM	43.80	-186.8 to 274.4	No	0.9856
1.5% NaCl vs. 2.5% NaCl	69.86	-160.8 to 300.5	No	0.9033
1.5% NaCl vs. comp DMEM	148.4	-82.21 to 379.0	No	0.3211
2.5% NaCl vs. comp DMEM	78.54	-152.1 to 309.1	No	0.8539

Table 3.8 Tukey's multiple comparisons of ridge count per cell of J774 macrophage-like cells subjected to media of different osmolarities

| | Mean | 95.00% CI of | | Adjusted |
| Dependent variable: Ridge area density
Alpha = 0.05 | | | | |
Media comparison	Mean Difference	95.00% CI of difference	Significant	Adjusted p value
0.2% NaCl vs. 0.5% NaCl	-0.06760	-0.1756 to 0.04038	No	0.3469
0.2% NaCl vs. 0.9% NaCl	-0.1594	-0.2674 to -0.05139	Yes	0.0035
0.2% NaCl vs. 1.5% NaCl	-0.2404	-0.3484 to -0.1324	Yes	<0.0001
0.2% NaCl vs. 2.5% NaCl	-0.2103	-0.3182 to -0.1023	Yes	0.0003
0.2% NaCl vs. comp DMEM	-0.2182	-0.3262 to -0.1102	Yes	0.0002
0.5% NaCl vs. 0.9% NaCl	-0.09177	-0.1998 to 0.01621	No	0.1145
0.5% NaCl vs. 1.5% NaCl	-0.1728	-0.2808 to -0.06480	Yes	0.0018
0.5% NaCl vs. 2.5% NaCl	-0.1427	-0.2506 to -0.03467	Yes	0.0081
0.5% NaCl vs. comp DMEM	-0.1506	-0.2586 to -0.04264	Yes	0.0054
0.9% NaCl vs. 1.5% NaCl	-0.08101	-0.1890 to 0.02698	No	0.1927
0.9% NaCl vs. 2.5% NaCl	-0.05088	-0.1589 to 0.05711	No	0.6234
0.9% NaCl vs. comp DMEM	-0.05885	-0.1668 to 0.04913	No	0.4834
1.5% NaCl vs. 2.5% NaCl	0.03013	-0.07786 to 0.1381	No	0.9289
1.5% NaCl vs. comp DMEM	0.02216	-0.08583 to 0.1301	No	0.9798
2.5% NaCl vs. comp DMEM	-0.007973	-0.1160 to 0.1000	No	0.9998

Table 3.9 Tukey's multiple comparisons of ridge area density of J774 macrophage-like cells subjected to media of different osmolarities

To further investigate the effect of osmotic pressure on the production of macrophage filopodia and membrane ridges, I did a correlation analysis of cell size to count and area density of each protrusion. It is commonly believed that osmotic pressure negatively regulates formation of local protrusions (Sitarska and Diz-Muñoz, 2020; Heinrich, 2015). Thus, an increase in cell surface area due to increase in osmotic pressure should lead to a decrease in both filopodia and membrane ridge expression. However, upon examining filopodia and membrane ridges in J774 macrophage-like cells grown *in vitro*, results showed very poor correlation of count and area density of these protrusions to cell surface area (Figure 3.24). An increase in sample size and a more accurate method to quantify cell features such as 3D surface area might improve these analyses. In spite of these limitations, membrane ridge area density was found to have statistically significant negative correlation with cell surface area (Figure 3.24B, $R^2 = 0.214$, $p = 0.026$), suggesting that membrane ridges are more sensitive than filopodia to changes in cell surface area due to increase in osmotic pressure and thus might be useful in assessing macrophage response to osmotic stress.
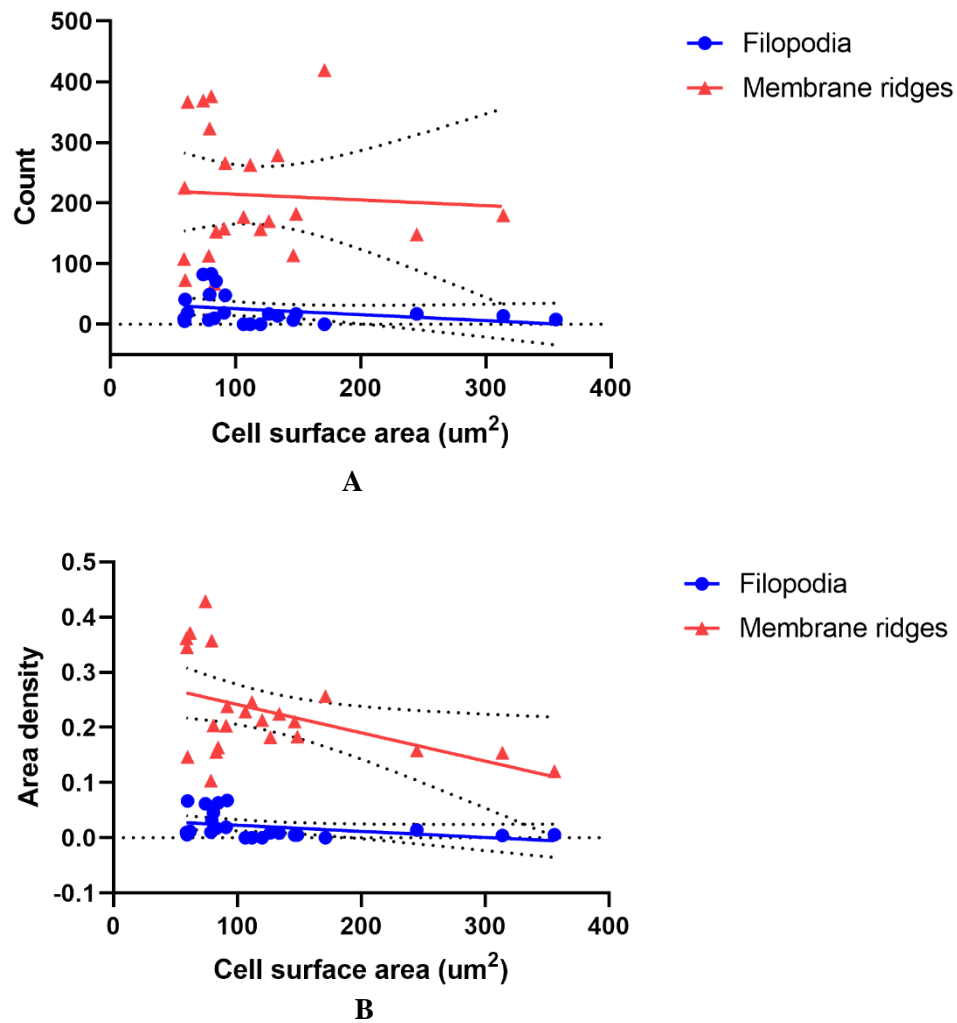
Figure 3.24 | The number and area density of filopodia and membrane ridges are poorly correlated to cell surface area in J774 macrophage-like cells. Using SEM images of J774 macrophage-like cells, the number and area density of membrane ridges and filopodia were derived by RD analysis. Cell surface area, on the other hand, was manually measured by tracing the outermost cell membrane outline of each cell.

(A) There was poor correlation between cell surface area and number of filopodia ($R^2 = 0.091$, $p = 0.162$, y = -0.09869x + 35.73, $n = 23$) and, likewise, between cell surface area and number of membrane ridges ($R^2 = 0.003$, $p = 0.803$, y = -0.09393x + 223.8, $n = 23$) in macrophages grown in comp DMEM,

(B) A poor correlation between cell surface area and filopodia area density ($R^2 = 0.141$, $p = 0.078$, y = -0.0001107x + 0.03398, $n = 23$) was also found, however there was statistically significant negative correlation between cell surface area and membrane ridge area density ($R^2 = 0.214$, $p = 0.026$, y = -0.0005118x + 0.2928, $n = 23$).

By visually examining SEM images of macrophages exposed to different media osmolarities (Figure 3.21), I noticed changes in the length of their membrane protrusions, filopodia and ridges, hence I further analysed these measurements. Results (Figure 3.25A) revealed a significant effect of media osmolarity to filopodia length using ordinary one-way ANOVA ($F(5,48) = 2.849$, $p = 0.025$), thus I did a post hoc test to further examine specific group differences. Tukey's test (table 3.10) showed that cells in hypoosmotic conditions (0.2% and 0.5% NaCl) had significantly longer filopodia than those grown in usual culture media (comp DMEM). Combined histogram of all filopodia (Figure 3.25B-F) measured for each condition revealed a dramatic shift in filopodia peak length after cells were exposed to very hypoosmotic media (Figure 3.25C). Results showed that the usual 0.2 μm peak length in cell culture media (Figure 3.25B) had increased by 0.6 μm after exposure to 0.2% NaCl. However, its positively skewed distribution (table 3.11 skewness) was conserved, suggesting no fundamental change in the mechanism of filopodia elongation. This could be potentially explained by a subsequent promotion of filopodia growth upon los of membrane ridges by exploiting the available actin and membrane components. Taken together, these results indicate that hypoosmotic condition promotes filopodia growth, which agrees with the model proposed by Karlsson (2013) and co-workers (discussed in 3.11.6.9).

A

B

C

D

E

F
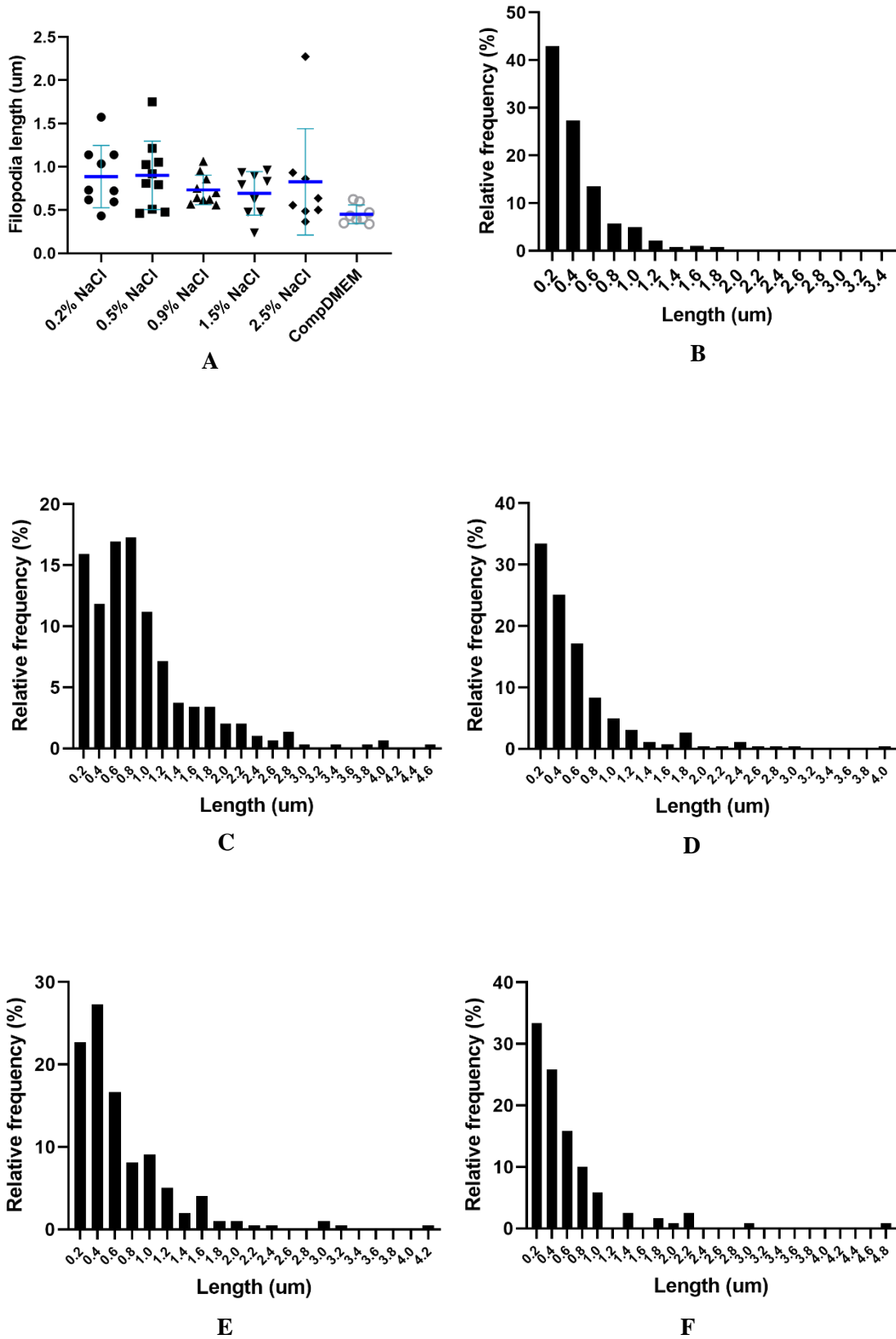
(Figure legend on next page)

Figure 3.25 | Filopodia length is increased in J774 macrophage-like cells exposed to hypotonic solution. SEM images of cells from osmosis experiment were analysed using RD (section 3.4) to determine the length of each filopodium. Mean length of filopodia per cell was then computed, plotted and analysed for statistical significance.

(A) There was statistically significant difference in mean filopodia length of cells exposed to different media osmolarities as revealed by ordinary one-way ANOVA of log-transformed data ($F(5,48) = 2.849$, $p = 0.025$), $n = 8$-10 cells, bars: mean ± standard deviation, post hoc analysis using Tukey's test (table 3.10) was done to further examine group differences, please refer to the table for statistically significant group comparisons,

(B-E) Combined histograms of individual filopodia lengths in cells exposed to complete DMEM *(B)*, 0.2% NaCl *(C)*, 0.5% NaCl *(D)*, 0.9% NaCl *(E)*, and 2.5% NaCl *(F)*. Descriptive statistics of each histogram were summarised in table 3.11.

Dependent variable: Filopodia length Alpha = 0.05				
Media comparison	**Mean Difference**	**95.00% CI of difference**	**Significant?**	**Adjusted p value**
0.2% NaCl vs. 0.5% NaCl	-0.001770	-0.2402 to 0.2366	No	>0.9999
0.2% NaCl vs. 0.9% NaCl	0.06132	-0.1771 to 0.2997	No	0.9723
0.2% NaCl vs. 1.5% NaCl	0.1109	-0.1337 to 0.3555	No	0.7585
0.2% NaCl vs. 2.5% NaCl	0.07122	-0.1809 to 0.3234	No	0.9587
0.2% NaCl vs. comp DMEM	0.2731	0.02095 to 0.5252	Yes	0.0267
0.5% NaCl vs. 0.9% NaCl	0.06309	-0.1690 to 0.2951	No	0.9649
0.5% NaCl vs. 1.5% NaCl	0.1126	-0.1258 to 0.3510	No	0.7255
0.5% NaCl vs. 2.5% NaCl	0.07299	-0.1731 to 0.3191	No	0.9495
0.5% NaCl vs. comp DMEM	0.2748	0.02872 to 0.5210	Yes	0.0205
0.9% NaCl vs. 1.5% NaCl	0.04954	-0.1889 to 0.2879	No	0.9893
0.9% NaCl vs. 2.5% NaCl	0.009902	-0.2362 to 0.2560	No	>0.9999
0.9% NaCl vs. comp DMEM	0.2118	-0.03437 to 0.4579	No	0.1292
1.5% NaCl vs. 2.5% NaCl	-0.03964	-0.2918 to 0.2125	No	0.9971
1.5% NaCl vs. comp DMEM	0.1622	-0.08991 to 0.4143	No	0.4091
2.5% NaCl vs. comp DMEM	0.2019	-0.05759 to 0.4613	No	0.2105

Table 3.10 Tukey's multiple comparisons of mean filopodia length of J774 macrophage-like cells subjected to different media osmolarities

	0.2% NaCl	0.5% NaCl	0.9% NaCl	1.5% NaCl	2.5% NaCl	Comp DMEM
Number of values	295	263	198	106	120	384
Minimum	0.1010	0.1500	0.1350	0.1410	0.1420	0.1010
25% Percentile	0.4500	0.2560	0.3108	0.2493	0.2313	0.2145
Median	0.7470	0.4190	0.4960	0.3995	0.4185	0.3365
75% Percentile	1.162	0.6960	0.9025	0.8470	0.6963	0.5720
Maximum	4.573	4.005	4.227	5.317	4.781	3.408
Range	4.472	3.855	4.092	5.176	4.639	3.307
Mean	0.9251	0.5868	0.6907	0.6868	0.6020	0.4536
Std. Deviation	0.7150	0.5352	0.5880	0.7468	0.6306	0.3784
Std. Error of Mean	0.04163	0.03300	0.04179	0.07254	0.05756	0.01931
Skewness	1.882	2.740	2.573	3.573	3.554	2.751

Table 3.11 Descriptive statistics of filopodia length histograms shown in figure 3.25

On the other hand, I observed that membrane ridge growth was also affected by media osmolarity. Results (Figure 3.26A, table 3.12) showed a statistically significant decrease in length of membrane ridges at increasing osmolarity (Figure 3.26A, $F(4,96) = 22.42$, $p < 0.0001$). Like filopodia, the distributions of membrane ridge length across different osmotic conditions (Figure 3.26B-F) appear to be conserved, suggesting no fundamental change in the mechanism of ridge elongation but potentially on physical properties that can suppress ridge elongation such as very high viscosity. It should be noted that ridge length values of cells exposed to 0.2% NaCl were not plotted as ridges were rarely found in these cells.
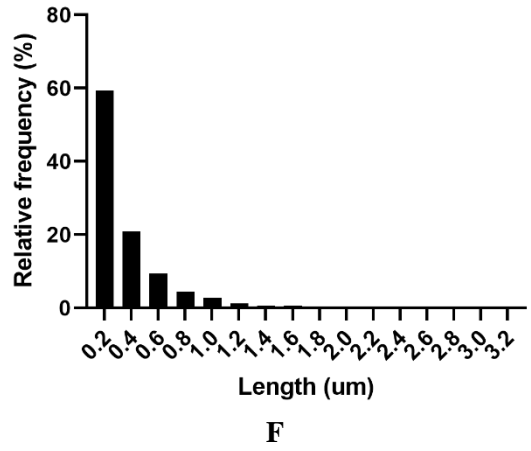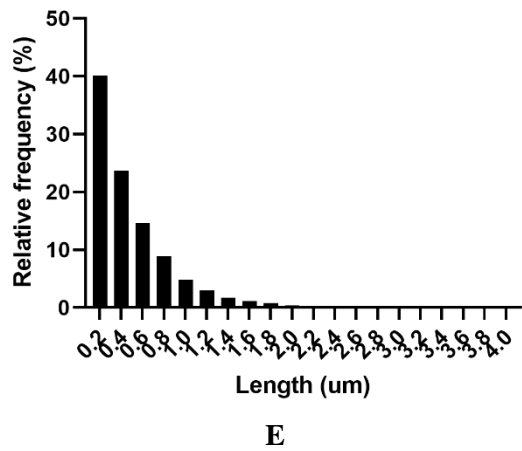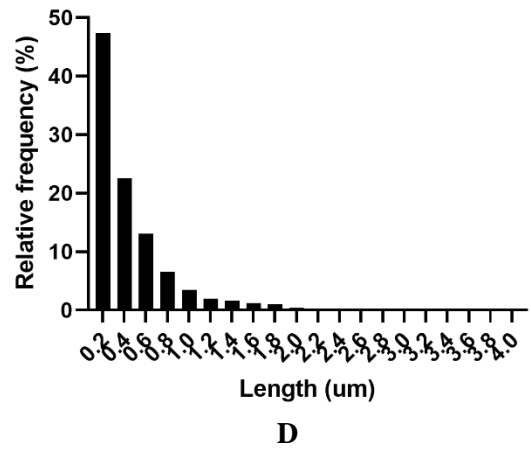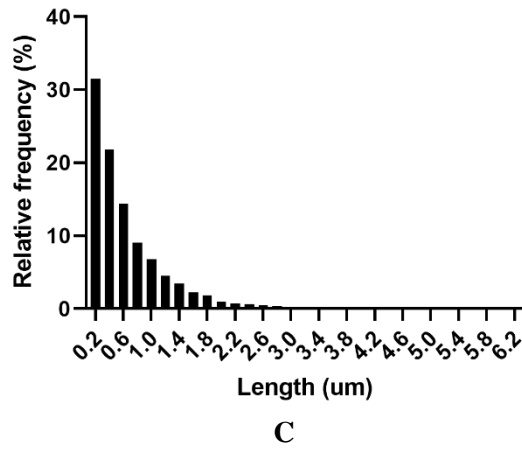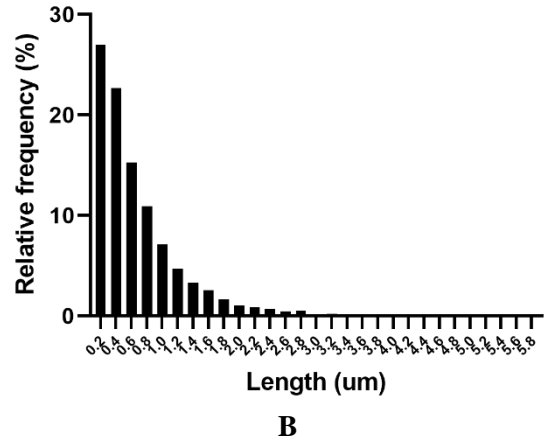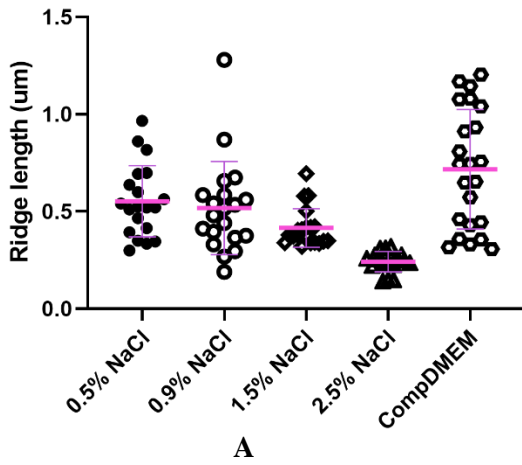
(Figure legend on next page)

Figure 3.26 | Ridge length is reduced in J774 macrophage-like cells exposed to isotonic and hypertonic solutions. SEM images of cells from osmosis assay were analysed using RD analysis (section 3.4) to determine the length of each ridge. Mean ridge length per cell was then computed, plotted and analysed for statistical significance.

(A) There was statistically significant difference in mean ridge length of cells exposed to different media osmolarities as revealed by ordinary one-way ANOVA of log-transformed data ($F(4,96) = 22.42$, $p < 0.0001$), $n = 18\text{-}23$ cells, bars: mean $\pm$ standard deviation, post hoc analysis using Tukey's test (table 3.12) was done to further examine differences between groups, please refer to the table for statistically significant group comparisons,

(B-F) Combined histograms of individual ridge lengths of cells exposed to complete DMEM *(B)*, 0.5% NaCl *(C),* 0.9% NaCl *(D)*, 1.5% NaCl *(E),* and 2.5% NaCl *(F)*. Descriptive statistics for each histogram are summarised in table 3.13

Dependent variable: Ridge length Alpha = 0.05				
Media comparison	**Mean Difference**	**95.00% CI of difference**	**Significant?**	**Adjusted p value**
0.5% NaCl vs. 0.9% NaCl	0.04425	-0.09188 to 0.1804	No	0.8948
0.5% NaCl vs. 1.5% NaCl	0.1121	-0.02401 to 0.2483	No	0.1571
0.5% NaCl vs. 2.5% NaCl	0.3488	0.2089 to 0.4887	Yes	<0.0001
0.5% NaCl vs. comp DMEM	-0.09215	-0.2238 to 0.03947	No	0.3003
0.9% NaCl vs. 1.5% NaCl	0.06787	-0.06826 to 0.2040	No	0.6380
0.9% NaCl vs. 2.5% NaCl	0.3046	0.1647 to 0.4444	Yes	<0.0001
0.9% NaCl vs. comp DMEM	-0.1364	-0.2680 to -0.004780	Yes	0.0384
1.5% NaCl vs. 2.5% NaCl	0.2367	0.09682 to 0.3765	Yes	<0.0001
1.5% NaCl vs. comp DMEM	-0.2043	-0.3359 to -0.07265	Yes	0.0004
2.5% NaCl vs. comp DMEM	-0.4410	-0.5764 to -0.3055	Yes	<0.0001

Table 3.12 Tukey's multiple comparisons of ridge length of J774 macrophage-like cells subjected to different media osmolarities

	0.5% NaCl	*0.9% NaCl*	*1.5% NaCl*	*2.5% NaCl*	*Comp DMEM*
Number of values	3203	3092	2490	1873	4935
Minimum	0.1000	0.1000	0.1000	0.1000	0.1000
25% Percentile	0.2500	0.1780	0.2010	0.1570	0.2860
Median	0.4560	0.3205	0.3680	0.2500	0.5040
75% Percentile	0.8560	0.5598	0.6353	0.4250	0.8880
Maximum	6.229	3.943	3.988	3.197	5.798
Range	6.129	3.843	3.888	3.097	5.698
Mean	0.6583	0.4482	0.4895	0.3522	0.6887
Std. Deviation	0.6201	0.4024	0.4054	0.3076	0.6059
Std. Error of Mean	0.01096	0.007236	0.008124	0.007108	0.008625
Skewness	2.603	2.502	2.189	2.926	2.447

Table 3.13 Descriptive statistics of ridge length histograms in figure 3.26

3.10.4 Disease phenotype

Macrophages are known to regulate many important processes in the body including tissue homeostasis. Pulmonary arterial hypertension (PAH) is a rare, progressive disorder characterised by increased vascular remodelling leading to right ventricular failure and ultimately death (Kiely et al., 2013). Previous reports described macrophage infiltration in both experimental and clinical PAH (Savai et al., 2012), however their exact role in the disease is currently unclear and is an active area of research (Pugliese et al., 2015; Zawia et al., 2021). Thus, in collaboration with Dr. Amira Zawia of the Lawrie lab in University of Sheffield Medical School, we examined the morphology of macrophages obtained from a PAH patient using high resolution SEM imaging. This might reveal important changes in macrophage during PAH which can be further explored to shed light on this disease. Some of the succeeding data can be found in our published work (Zawia et al. 2021).

Human monocyte-derived macrophages obtained from a PAH patient (PAH-MDM) donor were cultured and differentiated *in vitro* to examine their biophysical properties. Macrophages were activated into an M1 phenotype using LPS and IFNγ or an M2 phenotype through IL-4, and were subsequently processed for SEM examination. Images were analysed using the previously described RD analysis (section 3.4) and image segmentation via thresholding (section 3.10.1) to profile ridge area density, cell surface area and aspect ratio (cell elongation) of these cells. It should be reiterated that only a single repeat was done for this experiment due to scarcity of donor and time constraints brought by lockdowns during COVID-19 pandemic.

Results (Figure 3.27A-C) showed that the membrane surface of PAH-MDM was remarkably transformed after activation. Large ruffles forming macropinocytic cups (Figure 3.27B and 3.27C yellow arrow) were observed to become very prevalent in both M1 and M2 activated cells. Meanwhile, a significant change in the density of their membrane ridges was also found following activation ($F(2,27) = 5.845$, $p = 0.0078$). Tukey's test (table 3.14) confirmed the significant reduction in ridge area density of both M1 and M2 activated cells. In contrast, no statistically significant changes were seen in HMDM of non-PAH donors (Figure 3.17E) following the same activation.

Another striking PAH-MDM feature observed was the significant change in their cell surface area after activation (Figure 3.27E, $F(2,193) = 27.77$, $p < 0.0001$). Results (table 3.15) showed significant reduction in cell surface area of both M1 and M2 activated cells, which was also not observed in non-PAH donors (Figure 3.18E). Taken together, these suggest profound changes in the cytoskeletal and mechanical properties of PAH-MDM which could be later on explored to further understand PAH pathophysiology.

Meanwhile, cell elongation of PAH-MDM upon activation was also examined, and no statistically significant difference was found ($F(2,163) = 0.1637$, $p = 0.8492$) as in previous experiment with non PAH donors (Figure 3.18F).

A

B

C

D

E

F
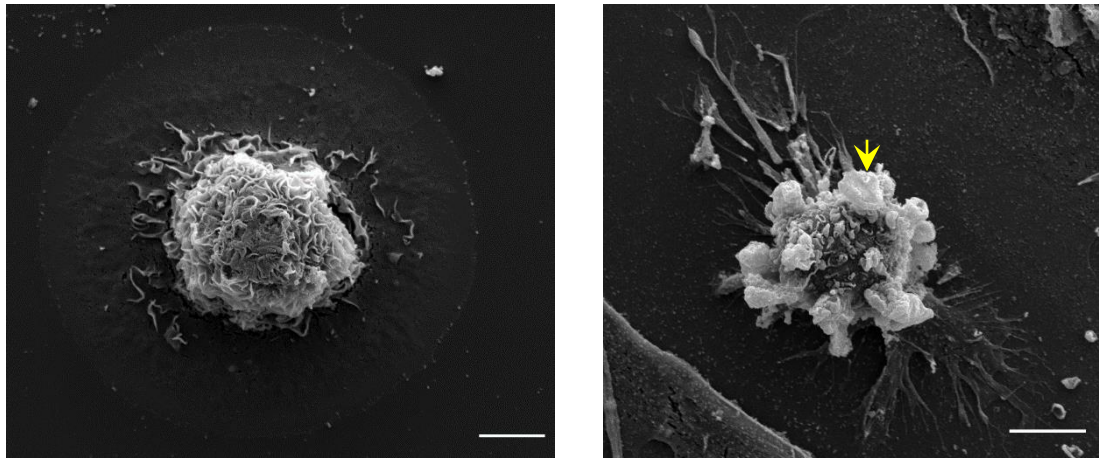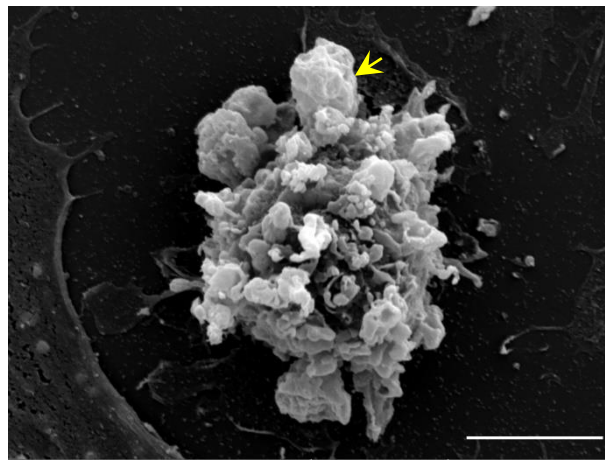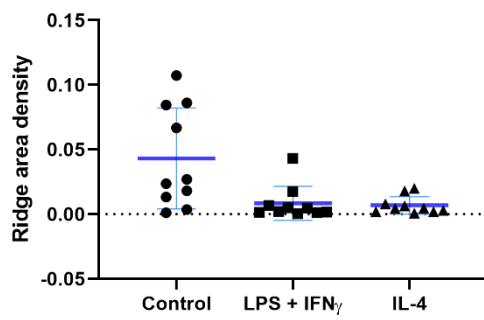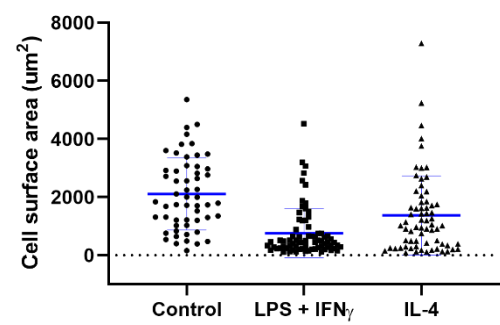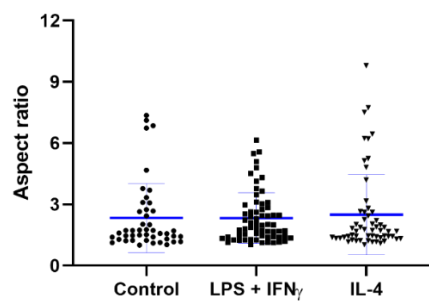
(Figure legend on next page)

Figure 3.27 | Membrane ridges are reduced in both LPS/IFNγ–activated and IL-4-activated human monocyte-derived macrophages (HMDM) from PAH patient. HMDM derived from patients with pulmonary arterial hypertension were seeded and differentiated into a 24-well plate with uncoated glass cover slip. Cells were then stimulated with either LPS/IFNγ (M1) or IL-4 (M2) cytokines. After overnight activation, cells were processed for scanning electron microscopy. Cells were imaged using a high vacuum, thermionic emission scanning electron microscope with an SE detector system, 10 kV accelerating voltage, 9 mm working distance, 63 nm spot size and 0° stage tilt. Images are a representative of 10 images from a single experimental repeat.

(A) SEM images of unstimulated (control) HMDM,

(B) LPS and IFNγ–activated (M1) HMDM,

(C) IL-4-activated (M2) HMDM, scale bar – 5 μm,

(D) There was statistically significant difference in ridge area density of PAH-derived HMDM after M1 and M2 activation as revealed by ordinary one-way ANOVA of log-transformed data $(F(2,27) = 5.845, p = 0.008)$, $n = 10$ cells, bars: $M \pm SD$, post hoc analysis using Tukey's test (table 3.14) was done to further examine differences between groups, please refer to the table for statistically significant group comparisons,

(E) There was statistically significant difference in cross-sectional cell surface area of PAH-derived HMDM following M1 and M2 activation as confirmed by ordinary one-way ANOVA of log-transformed data $(F(2,193) = 27.77, p < 0.0001)$, $n = 1$ (55-74 cells), bars: $M \pm SD$, post hoc analysis using Tukey's test (table 3.15) was done to further analyse differences between groups, please refer to the table for statistically significant group comparisons,

(F) No statistically significant difference in cell aspect ratio/cell elongation of PAH-derived HMDM was found after activation as confirmed by ordinary one-way ANOVA of log-transformed data $(F(2,163) = 0.1637, p = 0.849)$, n = 1 (45-64 cells), bars: $M \pm SD$.

Dependent variable: Ridge area density Alpha = 0.05				
Activation state comparison	**Mean Difference**	**95% CI of Difference**	**Significant?**	**Adjusted p value**
Control vs. LPS + IFNγ	0.03474	0.008002 to 0.06148	Yes	0.0090
Control vs. IL-4	0.03621	0.009467 to 0.06295	Yes	0.0064
LPS + IFNγ vs. IL-4	0.001465	-0.02528 to 0.02820	No	0.9899

Table 3.14 Tukey's multiple comparisons of ridge area density of HMDM derived from PAH patients at different activation states

Dependent variable: Cell surface area Alpha = 0.05				
Activation state comparison	**Mean Difference**	**95% CI of Difference**	**Significant?**	**Adjusted p value**
Control vs. LPS + IFNγ	0.5391	0.3683 to 0.7100	Yes	<0.0001
Control vs. IL-4	0.3129	0.1383 to 0.4875	Yes	0.0001
LPS + IFNγ vs. IL-4	-0.2262	-0.3881 to -0.06438	Yes	0.0033

Table 3.15. Tukey's multiple comparisons of cell surface area of HMDM derived from PAH patients at different activation states

3.11 General Discussion

With the goal of describing macrophage surface topography to investigate phagocytosis, the remarkable external features of macrophages were illustrated in this study. Using current advanced imaging techniques, the presence of a highly conserved membrane structure called membrane ridges was identified. These structures were seen to be highly dynamic, capable of splitting and fusing, yet were able to maintain a highly consistent thickness architecture. Their very consistent thickness within a phagocyte population and across different types of phagocytes suggests an uncharacterised, highly conserved actin structure with very tight regulation.

The similarity of membrane ridges with other actin-based cell structures particularly the actin cortex was observed. They consisted of Arp2/3, an important nucleator of cortical actin, indicating the presence of a branched actin network in membrane ridges. The expression of nucleation promoting factor WASH in ridges was also determined suggesting its potential role in generating membrane ridges alongside Arp2/3.

Membrane ridge architecture and expression were found to be sensitive to different well-known factors that affect physical, metabolic and functional properties of macrophages. IL-10 activation which results in an anti-inflammatory phenotype was observed to strongly inhibit ridge expression. LPS/IFNγ and IL-4 activation, on the other hand, were seen to sustain them suggesting their important role during these activation states. Two very likely functions are during phagocytosis (explored in chapter 5) and antigen presentation.

Genes that are known to regulate macrophage polarisation were also seen to affect membrane ridge expression. Supressing *trib1* and *trib3*, which both mediate a pro-inflammatory macrophage phenotype, were seen to significantly reduce ridge production. This further underscores the potential role of membrane ridges in inflammatory response.

Compared to filopodia, membrane ridges were found to be sensitive to changes in osmotic conditions. They were observed to be almost completely inhibited in hypoosmotic media given the increase in membrane tension force in these cells. Macrophages are known to be sensitive to physiological changes in the body including salt and water balance (Jantsch et al., 2014). The striking changes in their morphology in different osmotic conditions therefore demonstrate their regulatory responses towards osmotic stress. Amongst the morphological changes identified here is the decrease in membrane ridge density and its shortening during hypoosmotic and hyperosmotic stresses, respectively. These suggest that membrane ridges are features sensitive to osmotic stress and could be used to describe important physiological changes amongst macrophages.

Finally, membrane ridge expression was also seen to be affected by impaired macrophage polarisation in PAH disease. The profound changes in cell size and ridge density of activated macrophages in this disease indicate that ridges are highly sensitive to alterations in macrophage behaviour and function.

3.12 Specific Discussions

In this chapter, different advanced microscopy techniques were used to interrogate the surface properties of macrophages. Describing the macrophage surface provides a wealth of knowledge on its physical interaction with other cells, particles and its extracellular environment. Furthermore, this allows us to understand any changes on macrophage biology brought by internal and external factors. Using scanning electron microscopy (SEM), I characterised the physical properties of macrophage external surface. They were found to assume various shapes *in vitro* and to produce different types of membrane protrusions, indicating their highly mechanical and dynamic internal architecture.

3.12.1 The macrophage membrane protrusions

Single cell SEM examination of macrophages revealed the organisation of their external membrane surface. Four distinct common types of membrane protrusions were identified: lamellipodia, filopodia, dorsal ruffles, and membrane ridges. These structures generally differ in their shapes, sizes and localisation in the macrophage body, suggesting their specialised roles.

Lamellipodia were seen as large, flat sheets of membrane on the dorsal surface of macrophages. They were also found to possess peripheral ruffles (Figure 3.2B yellow arrow). Giannone (2007) and colleagues proposed that these are produced by myosin-mediated contraction of lamellipodia actin filaments upon formation of weak adhesion sites to the underlying substrate. However, this was challenged by Pontes (2017) and his collaborators,

proposing that an increase in membrane tension in a myosin-II independent manner is responsible for buckling of actin filaments in lamellipodial periphery. This suggests that mechanical signals such as membrane tension can regulate the morphological properties of lamellipodia. Regardless of its origin, this was found to be useful in estimating lamellipodia thickness to make important structural comparisons with other types of membrane protrusion.

Macrophages were also observed to produce narrow finger-like protrusions called filopodia. Single cell SEM imaging revealed that filopodia of macrophages can originate from either cell body (Figure 2C green arrow) or lamellipodia (Figure 2D). These observations provide evidence for the two proposed models of filopodia formation: *de novo* actin nucleation hypothesis and convergent elongation model. Macrophage filopodia originating from the cell body agrees with *de novo* formation hypothesis which argues that filopodia are synthesised without pre-existing lamellipodium via available formins; whilst those originating from lamellipodia provides evidence for convergent elongation hypothesis, which describes lamellipodia as a source of actin filaments during filopodia formation and therefore critical for its inception (Mattila and Lappalainen, 2008). Taken together, these suggest that both models might be true when describing the origin of filopodia in macrophages.

SEM imaging also revealed that macrophage filopodia were capable of bending (Figure 3.2D yellow arrow). This feature is not exclusive to macrophages and is also observed in other cell types such as HEK293T cells and neurons (Leijnse et al., 2015). Alongside coiling and buckling, bending is believed to be a result of the dynamic behaviour of actomyosin complex supporting filopodia which allows cells to explore its immediate environment and probe its physical makeup (Leijnse et al., 2015).

Finally, large, sheet-like dorsal ruffles were seen to be occasionally present in unstimulated macrophages cultured *in vitro*. These are sometimes called circular dorsal ruffles to differentiate them from peripheral ruffles of lamellipodia and to describe their distinct property of fusing at their opposite ends (circularise) to form a macropinocytic cup. Their fusion is believed to be mediated by tent poles stabilising their extreme ends (Condon et al., 2018). This complex macropinocytic cup derivative is later on used for non-selective uptake of particles and recycling of membrane receptors (Stow and Condon, 2016).

3.12.2 Morphological properties of membrane ridges

Through single cell SEM imaging, another type of membrane protrusion that showed very high density, shorter length and more common expression than dorsal ruffles and other types of membrane protrusion in macrophage surface was identified. These were called membrane ridges due to their appearance in macrophage surface using 3D reconstruction

microscopy. They were found to be poorly characterised, hence different advanced microscopy techniques were used to describe their biophysical properties.

SEM examination and 3D surface reconstruction through a photometric stereo technique revealed the sheet-like and consistent thickness of membrane ridges. An unbiased and robust image analysis routine was designed based on *ridge detection* (RD) script (Steger,1999) to measure the length and width (thickness) of these structures from a top view perspective. These confirmed the highly consistent thickness of membrane ridges observed in 3D macrophage surface reconstruction. Their length however showed a positively skewed distribution with more variable (higher SD) measurements.

I further examined the architecture of membrane ridges using transmission electron microscope (TEM). Results confirmed their highly consistent thickness from a dorsoventral cross-sectional view. Moreover, this demonstrated that different regions of a membrane ridge could be described according to its proximity to the macrophage main body: a slightly wide *base*, a long *body* with consistent thickness and a slightly narrow and curved *tip*. Taken together, these results suggest that its main body, which spans almost its entire architecture, is responsible for its highly consistent thickness property.

The curvature of membrane ridges was also examined by combining single cell SEM imaging, RD analysis and our custom-built image analysis script that can profile both magnitude and direction of a curvature. Describing this property could give us important insights on the behaviour of its actin component and its actin-associated molecular interactions. Results showed that membrane ridges do not possess any mean curvature with equally distributed positive and negative curvatures indicating that there is no bias in the direction of ridge bending on the macrophage surface.

3.12.3 The actin architecture of membrane ridges and its dynamics

Actin acts as the main structural component of most membrane protrusions (Svitkina 2020). Their interaction with other molecules, organisation and dynamics greatly affect the morphological and functional properties of cellular protrusions. Through airyscan superresolution microscopy, the actin cytoskeleton of macrophages was examined. They formed highly complex structures of distinct morphology and logical spatial arrangement such that those involved in substrate adhesion and migration (e.g. lamellipodia and filopodia) were normally found on the ventral cell region. These enabled easy identification and isolation of these structures for their analysis.

Membrane ridge actin was usually found in the upper third z section of a macrophage body. Visual examination of their actin thickness indicated an end-to-end consistency. Their sheet-like property was confirmed by rendering 3D projections of actin fluorescence images.

Moreover, examining image orthogonal slices revealed that membrane ridges were continuous with the cell cortex through their actin component. Taken together, these revealed that actin is a primary constituent of membrane ridges which provides them with their morphological properties as in other well-known membrane protrusions.

By following the physical features of actin-based lamellipodia, filopodia, membrane ridge and actin cortex in macrophages, they were successfully extracted from fluorescence images and analysed. This enabled structural comparisons of these features and validation of my previous finding of membrane ridge thickness consistency. Results reaffirmed the highly consistent thickness of membrane ridges and additionally revealed its actin thickness similarity to cortical actin. This underscores the well-described property of actin cortex in the literature as an isotropic structure with homogenous thickness and tension (Clark et al., 2013; Svitkina, 2020; Tinevez et al., 2009)

The striking thickness similarity between actin components of membrane ridges and macrophage cortex indicates potential similarities in their architecture. Thus, I examined if Arp2/3, a well-established nucleator of cortical actin (Bovellan et al., 2014), is also found in membrane ridges. By doing so, this could provide important insights on key membrane ridge actin regulatory proteins such as GTP-binding proteins GTPases, guanine nucleotide exchange factors (GEFs) and GTPase-activating proteins (GAPs) which could later on be exploited to modulate their expression. Results showed that membrane ridges were indeed extensively enriched (>90%) with Arp2/3, which further implies that a branched actin network is present in these structures and a very likely similarity with cortical actin with respect to actin regulators. Membrane ridge proximity to the cortical actin and its dense expression in the macrophage surface suggest that similar regulation with that of cortical actin seems highly likely.

Amongst the known regulators of Arp2/3 is the nucleation promoting factor WASH (Liu et al., 2009; Wang et al., 2014). Hence, I examined if WASH is also expressed in membrane ridges. Results showed that they were also enriched in membrane ridges; however, their expression was not as common as Arp2/3 in both J774 and RAW264.7 cells. These show that WASH potentially regulates Arp2/3 in ridges but is not sufficient to explain the extensive Arp2/3 enrichment in this structure. It would be worth investigating if the other Arp2/3 regulatory molecules, Scar/WAVE and WASP (Stradal et al, 2004), are involved in Arp2/3 localisation in membrane ridges.

WAVE and WASP are important nucleation promoting factors that act as protein scaffolds (Insall and Machesky, 2009) to mediate Arp2/3 activation through Rac and Cdc42, respectively (Stradal et al., 2004). They are implicated in formation of cellular protrusion such that Scar/WAVE is believed to be the key activator of lamellipodia and pseudopodia (Buracco et al., 2019). On the other hand, WASP was shown to be important in initiation and stability

of podosomes in myeloid cells (Monypenny et al., 2011). Finally, WASH regulation of cellular protrusions is rather rare and is thought to mainly have endocytic roles (Buracco et al., 2019). However, a previous report showed that WASH can link linear and branched actin formation by acting downstream of Rho to participate in actin and microtubule dynamics in *Drosophila* oogenesis (Liu et al., 2009). Overall, these demonstrate the highly complex mechanisms by which intracellular actin is regulated to produce critical cellular structures. It is therefore not surprising if membrane ridges are influenced by these factors and regulate its dynamic behaviour.

Because the phagocytic cell membrane is commonly enriched with receptors that promote phagocytosis (Taylor et al, 2005), I next examined if the TLR2 receptor preferentially localises in membrane ridges. Results however showed no enrichment pattern, but it should be noted that the technique used here was based on immunofluorescence widefield microscopy which has significantly lower spatial resolution than superresolution techniques. It would be interesting to profile their distribution using 3D superresolution approaches such as in that elegant experiment of Jung (2016) and colleagues which demonstrated the localisation of T-cell receptors in microvilli of T cell lymphocytes.

The dynamics of membrane ridges on the macrophage surface was also examined. They were found to have a short lifetime of under one minute and are formed through different processes: *de novo*, splitting or fusion of pre-existing ridges. They were also found to collapse back to the cell surface without circularisation which differentiates them from dorsal ruffles. Moreover, dorsal ruffles were reported to have a mean lifetime of 176 seconds (Condon et al., 2018) compare to 55 seconds of membrane ridges. This is highly expected as dorsal ruffles have more complex behaviour which includes cup formation, sinking and constriction before collapsing back to the membrane surface (Condon et al., 2018). It is noteworthy that in spite of the different processes describing ridge dynamics (i.e. splitting, fusion etc.), their thickness appears to be highly maintained throughout their lifetime. These suggest that a highly conserved actin structure underpins their expression and maintaining their thickness property is essential for their putative role on a macrophage surface.

3.12.4 Membrane ridges as a universal feature of phagocytic cells

By SEM examination of various phagocytes, membrane ridges were found to be their common feature. The highly consistent thickness of this structure was also observed across different phagocytic cells. Their density in a phagocytic membrane however varies depending on cell type. The absence of membrane ridges in precursor cells or undifferentiated phagocytes strongly suggests their potential role in phagocytosis (explored in chapter 5).

Membrane ridges were observed not only in phagocytes *in vitro* but also *in vivo* whereby macrophages reside in various tissues and organs of different architecture and physiology. SEM examination of lung and liver samples revealed that their resident macrophages, alveolar macrophages and Kupffer cells, respectively, possessed membrane ridges. However, unlike cells *in vitro*, they were seen to have a more heterogenous surface property and appeared to have lower ridge densities. The differences in macrophage phenotype and response in *in vitro* and *in vivo* environments had been well documented (Morlan and Kaplan, 1977; Schmid et al., 2009; McNeill et al., 2014). The more variable biochemistry of *in vivo* setting and its fundamentally different architecture had most likely caused the highly heterogenous surface characteristics of macrophages *in vivo*.

Phagocytes are well known to be highly dynamic cells that perform various tasks in cell-to-cell communication (Goodman et al., 2019), migration (Gautier et al., 2009), extracellular transport of cellular products (He et al., 2018), fluid uptake and phagocytosis (Bohdanowicz and Grinstein, 2013). These physical activities usually involve the cell membrane and its underlying actin architecture. Thus, an organised membrane that does not compromise its dynamic property would be advantageous to perform a set of highly complex tasks and to efficiently carry out cellular responses. Amongst the macrophage surface features that highlight this remarkable organisation and dynamic properties is the highly conserved membrane ridges, and therefore it would not be surprising if it is involved in different aspects of macrophage biology.

3.12.5 Factors affecting membrane ridge expression

3.12.5.1 Macrophage activation

The biophysical and functional features of macrophages are known to be affected by chemical signals from their extracellular environment as well as mechanical stimuli. Using current knowledge on macrophage activation and function, I examined the effects of M1 (LPS/IFNγ) and M2 (IL-4, IL-10) activation to membrane ridge expression.

A striking change in macrophage surface with almost complete inhibition of membrane ridges was found following IL-10 activation. This suggests a profound effect of IL-10 in macrophage cytoskeleton by negatively regulating actin-related pathways involved in ridge production which is yet to be explored. Amongst the well-established functions of IL-10 is its ability to supress immune response to pathogens by inhibiting the release of pro-inflammatory mediators (Iyer and Cheng, 2012), downregulation of co-stimulants during antigen presentation (Knolle et al., 1998; Mittal and Roche, 2015) and dampening of phagocytic activities (Couper et al., 2008). Thus, these suggest a highly likely role of membrane ridges in inflammatory response. Interestingly, IL-10 is a well-described cytokine

that is widely expressed in the liver (Ali et al., 2019; Stijlemans et al., 2020) to inhibit any unnecessary inflammatory response from dietary metabolites (Robinson et al., 2016). *In vivo* examination of liver resident macrophages, Kupffer cells, showed very rare expression of membrane ridges on their surfaces and this could be potentially due to the non-inflammatory liver environment under homeostatic state (Wohlleber and Knolle, 2016) but this is yet to be examined.

The conservation of membrane ridges in M1-activated and IL-4 activated cells suggest that they are required in performing roles seen in both activation states. Amongst these events is the antigen presentation of macrophages to T cells via major histocompatibility complex II (MHC-II). Hart (1996) and colleagues showed that both IFNγ and IL-4 upregulate MHC-II expression in human monocyte-derived macrophages *in vitro*. This seems reasonable with respect to membrane ridges as macrophages can contact T cells more efficiently with the increase in cell surface area brought by these protrusions, which would subsequently increase the likelihood of presenting antigens to T cells.

Meanwhile, the density of membrane ridges in both IFNγ and IL-4 activated human monocyte-derived macrophages did not show any further increase. This suggests a peak density of membrane ridges in the cell surface owing potentially to a limited supply of actin monomers in these cells (Koestler et al., 2009). Succeeding experiments on osmosis using J774 cells further supports this idea as no further increase in ridge density was found in cells exposed to hyperosmotic media which do not inhibit ridge expression compared to hypoosmotic media.

3.12.5.2 trib1 and trib3 genes

To further investigate the role of membrane ridges in macrophages, I then looked at the effects of genes with known regulatory roles on macrophages. The *trib1* gene is known to be upregulated during M1/M2 macrophage polarisation (Arndt et al., 2018). Its absence leads to reduced secretion of both pro-inflammatory (IL-6, TNFα, IL-1β, and CXCL1) and anti-inflammatory cytokines (IL-4 and TGFβ) following LPS/IFNγ and IL-4 stimulation, respectively (Arndt et al., 2018).

The expression of membrane ridges appears to be conserved upon stimulation with LPS/IFNγ or IL-4, suggesting their importance in these activation states. Thus, it was not surprising that *trib1* knockdown led to a reduction in membrane ridge density by more than 50%. Taken together, these data suggest that membrane ridges play an important role in macrophage polarisation potentially in mediating physical events after LPS/IFNγ and IL-4 activation.

To further explore the relationship between macrophage regulatory genes and membrane ridge expression, I examined the effect of knocking out *trib3* in mouse bone marrow-derived macrophages. The *trib3* gene is believed to mediate a pro-inflammatory response of macrophages through upregulation of iNOS and CD11c (Martinez-Campesino et al., 2018). Results revealed a significant reduction in membrane ridge density of *trib3* knockout (KO) macrophages compared with wild type. There was also significant reduction in cell size of *trib3* KO macrophages, reiterating the pleiotropic nature of this gene. *β-actin* expression was seen to be upregulated in these cells, potentially important to support their increase in size. Finally, the actin nucleator Spire1 was observed to be downregulated in *trib3* KO cells suggesting a potential role in nucleation of actin filaments in membrane ridges which is yet to be explored.

3.12.5.3 Osmotic pressure

Macrophages are highly mechanical cells capable of cellular deformation and production of membrane protrusions to perform migratory and phagocytic roles (Lam et al., 2009). It was previously reported that membrane structures such as blebs (Tinevez et al., 2009), filopodia (Liejnse et al., 2015) and lamellipodia (Pontes et al., 2017; Raucher and Sheetz, 2000) were intrinsically regulated by mechanical cellular parameters such as cytoplasmic pressure, viscosity and membrane tension. I therefore examined how modulation of membrane tension force by osmosis affects the expression and morphology of membrane ridges and filopodia in macrophages.

Membrane ridges were found to be inhibited in hypoosmotic conditions. This supports the widely accepted notion that cellular protrusions are negatively regulated by osmotic pressure (Sitarska and Diz-Muñoz, 2020; Heinrich, 2015). Moreover, Houk (2012) and collaborators demonstrated that actin assembly and Rac activation were both affected by inhibitory and global effects of membrane tension force, providing a plausible explanation of membrane ridge suppression in hypoosmotic condition.

Conversely, there was no significant change found in filopodia density in all osmotic conditions. It was rather observed to increase in length at extremely hypoosmotic condition (0.2% NaCl). A more likely explanation to this is based on the filopodia growth model proposed by Karlsson (2013) and collaborators. In this model, the confinement of aquaporin channels, which regulate the entry and exit of water molecules into the cell, results to a localised and very high hydrostatic pressure that can push the membrane upward and create spaces between the membrane and cortex. These spaces are subsequently exploited for actin polymerisation to induce filopodial growth (Karlsson et al., 2013). This mechanism was verified by overexpressing aquaporin channels on surfaces of fibroblasts, neutrophils (Loitto

et al., 2007) and HEK cells (Karlsson et al., 2013) which resulted to a highly robust filopodia phenotype.

I also observed cell shape changes after exposing macrophages to different osmotic conditions. In particular, a very striking change was seen in cells exposed to extremely hypoosmotic media (0.2% NaCl). These cells became very flat with numerous membrane folds. This is in contrast to the well-known swelling effect of hypoosmotic media to mammalian cells (Borle et al., 1986; Hammami et al., 2007; Sach and Sivaselvan, 2015). However, in immune cells, it was reported that a regulatory volume decrease (RVD) serves as a mechanism to counter the rapid flow of water into the cell during hypoosmotic shock (Grinstein et al., 1984). During RVD, ion transport-dependent processes return the cytosol to its native tonicity and cell volume shrinks (Grinstein et al., 1984). Thus, this might have caused the prominent membrane folds seen on the macrophage surface potentially due to the excess membranes during rapid expansion.

It is also noteworthy that cortical actin of cells exposed to extremely hypoosmotic condition was barely noticeable compare to other media conditions. This highly suggests a fundamental change in the architecture of their cortical actin which led to the characteristic cell shape changes portrayed in a flattened morphology. Cell shape is a product of both physical interaction with the environment and mechanical properties of the cell itself (Chalut and Paluch, 2016). A key component that determines changes in the physical property the cell surface and subsequently cellular shape is the cortical actin (Chugh and Paluch, 2018). Therefore, it is not surprising that cell shape changes caused by hypoosmotic media also resulted to an indistinct and very likely reorganisation of cortical actin. However, the mechanism by which cortical actin is remodelled during cellular perturbations that leads to changes in its nanoscale organisation and mechanical properties is not well understood. Levayer and Lecuit (2012) proposed that gradients in cortical tension drives changes in shape during cell migration, cell division and tissue morphogenesis. How this could implicate the observed changes in macrophage shape during osmotic stress is yet to be described.

On the other hand, macrophages subjected to hyperosmotic condition did not show any apparent change in cell shape and membrane ridge density, suggesting a maximum amount of ridges produced by macrophages presumably due to the limited pool of actin monomers in the cell (Koestler et al., 2009). Interestingly, their ridges were found to shorten at increasing osmolarity, and their actin cortices appeared thinner than those in isosmotic media suggesting structural changes in the cortical actin that was not manifested in cell shape. It was previously shown that hyperosmolarity induces the activities of Arp2/3, Cdc42 and Rac (Ciano et al., 2002), and could therefore maintain the structural properties of ridge and cortical actin observed in isosmotic condition. However, the dynamic properties of these structures at

varying osmolarities were not assessed in this study, which might help us reconcile these observations.

3.12.5.4 Disease phenotype

Lastly, the morphology of macrophage in pulmonary arterial hypertension (PAH) disease was examined. Macrophages participate in many events in the body including homeostasis (Wynn et al., 2013), hence any profound changes on their functions can lead to serious physiological consequences. In collaboration with Lawrie's group in University of Sheffield Medical School, we showed that macrophages from both mouse PAH model (MacLow) and human PAH patients have impaired M1/M2 polarisation (Zawia et al., 2020). Its possible correlation to PAH pathogenesis is that the favoured polarisation state, M2 phenotype, leads to upregulation of IL-6 which subsequently induces proliferation of pulmonary artery smooth muscle cells that promotes vascular remodelling (Zawia et al., 2020).

With respect to membrane ridge expression, it was shown that both LPS/IFNγ and IL-4 activated macrophages from PAH patient had reduced membrane ridge density compare to their unstimulated counterpart. This is in contrast to macrophages from non-PAH patient showing no changes in membrane ridge expression following activation with the same set of cytokines. Moreover, activated cells of PAH patient frequently showed macropinocytic cups which seemed to replace ridges on their surfaces.

Another morphological difference found between PAH and non-PAH macrophages was the very striking reduction in cell surface area after activation. This suggests a fundamental change in their actin cytoskeleton as it determines their ability to spread and generate important cellular protrusions (Figard and Sokac, 2014). Different studies have shown that proper reorganisation of the cytoskeleton during immune cell activation is critical to efficiently carry out essential cellular functions. This was illustrated in mast cells (Colin-York et al., 2019) and T cell lymphocytes (Fritzsche et al., 2017; Yu et al., 2013) using superresolution microscopy techniques which revealed extensive reorganisation of the cortical actin and symmetry breaking in these cells leading to distinct patterns of actin following activation. These profound cytoskeletal changes are then believe to be important in performing different roles of these cells such as granule exocytosis (Colin-York et al., 2019), adhesion and formation of immunological synapses (Fritzsche et al., 2017). In macrophages the exact role of cytoskeleton following activation remains unclear. Changes in the cytoskeleton after LPS activation was reported (Eswarappa et al., 2008; Bian et al., 2017), and a subsequent reduction in inducible nitric oxide synthase (iNOS) was observed after disrupting the cytoskeleton of LPS-activated cells (Eswarappa et al., 2008). However, the exact mechanism

on how these physical changes in macrophage cytoskeleton lead to iNOS downregulation is unknown (Eswarappa et al., 2008). These results nevertheless underscore the importance of a properly functioning cytoskeleton for macrophage activation and function. Thus, it will not be surprising if the altered phenotype of macrophages in PAH disease that we recently determined (Zawia et al., 2018) stems from an inherent defect in the cytoskeleton of these cells. This is yet to be confirmed but shows a very promising aspect of macrophage biology that we can investigate to further understand their roles in PAH and other diseases.

3.13 Conclusions and future work

The investigation carried out in here revealed a highly conserved membrane feature amongst phagocytes that was previously uncharacterised and thus underappreciated. The remarkable consistency of its architecture, its conserved expression in a phagocytic membrane and its sensitivity to various external and internal cellular factors highlight its importance in understanding phagocyte biology. Different advanced imaging methods used here showed that membrane ridges possess a highly conserved thickness brought about by its underlying actin architecture.

The similarities between membrane ridge and cortical actin were also identified. The consistency in thickness of cortical actin is very striking which agrees with its known properties from the literature. Immunofluorescence microscopy revealed that Arp2/3, an important cortical actin nucleator (Bovellan et al., 2014), would also localise in membrane ridges. The extensive expression of Arp2/3 in membrane ridges is highly indicative of a branched actin network architecture. In other well-studied membrane protrusions such as lamellipodia, this is associated with regions of high capping rate as the cell needs to produce more new filament tips to compensate for the loss of old ones brought by capping (Schaub et al., 2007). This is yet to be seen in membrane ridges, but this would provide an important insight on the plausible mechanism of maintaining thickness in membrane ridges. The contrasting roles of these key molecules, Arp2/3 and capping protein, on actin growth would suggest that a fine balance between their activities must exist to generate a protrusion with consistent thickness.

Other actin and membrane associated molecules were also examined to describe the structure of membrane ridges. The TLR2 receptor does not seem to be regularly enriched in membrane ridges. Potential distribution of other important phagocytic receptors such as Fc receptors and complementary receptors in membrane ridges is worth exploring. As equally important is to identify if the major histocompatibility complex II is enriched in membrane ridges as my data suggest conservation of this structure in macrophages activation states characterised by antigen presentation. This could provide further insights on the dynamics of

antigen presentation and how they are stabilised in macrophages during certain activation states. Lastly, it would also be useful to identify the expression of another important cortical actin nucleator mDia1 (Bovellan et al., 2014) and its associated proteins in membrane ridges. Simultaneous imaging of these proteins with Arp2/3 will help uncover their relative contributions, if any, in producing membrane ridges.

Finally, understanding how macrophages integrate a diverse set of chemical and physical signals from their environment is an exciting avenue of research. Our data reveal important changes in macrophages with respect to their ridge density during IL-10 activation and hypoosmotic stress, which likely suggest changes in the cytoskeletal properties in macrophages during these conditions. This is a very important knowledge gap to be addressed as most researches focussed on enumerating the resulting macrophage phenotypes caused by certain factors rather than unravelling the mechanisms leading to such phenotype. This is rather easier said than done, but recent advances in microscopy, genetic manipulation and cell culture techniques would be indispensable tools to realise these goals and further understand the highly complex yet profoundly elegant macrophage biology.

CHAPTER 4

The roles of target size and surface chemistry in the phagocytic uptake of spherical targets

4.1 Introduction

Internalisation of particles is an important event that allows cells to take up nutrients, communicate with their surroundings and respond to changes in their external environment (Alberts et al., 2015). In macrophages and other phagocytes, this process had evolved to accommodate large particles ($\geq$ 0.5 μm), such as bacteria and fungi, for intracellular processing in a mechanism called phagocytosis. Phagocytosis is a biochemically complex event that makes use of the force of actin polymerisation against the host cell membrane to internalise particles. It proceeds with a series of well-orchestrated steps from actin-mediated shaping of the phagocyte membrane that produces a phagosome containing the target to its ultimate transport and processing within the host cell. These highlight the remarkable mechanical properties of phagocytes which are able to exploit their biochemical components to generate the forces for target internalisation.

Different variables are known to influence phagocytic uptake by immune cells. Host cell properties such as type and density of phagocytic receptors (Hed and Stendahl 1982; Williams et al., 2000), amount of membrane reserve (Heinrich, 2015) and cortical tension (Lam et al., 2009; Herant et al., 2005) are believed to determine the phagocytic capacity of immune cells. On the other hand, there is an overwhelming evidence that biochemical and biophysical properties of the phagocytic target also play important roles during phagocytosis. Surface chemistry (Pacheco et al., 2013), size (Champion et al., 2008), shape (Champion and Mitragotri, 2006; Richards and Endres, 2016) and stiffness (Sosale et al., 2015; Beningo and Wang, 2002) of the target were all shown to influence phagocytic uptake by immune cells. However, most of these studies investigated the mechanics of phagocytosis using inorganic beads; our knowledge on how complex biophysical properties of a pathogen could determine its phagocytic fate remains cursory. In this chapter, I will present my experimental work to address this gap in knowledge. I will describe the different optical imaging set-ups I used to illustrate and quantitate the interaction between macrophages and spherical phagocytic targets. Different variants of the fungal pathogen *Cryptococcus neoformans* and different sizes of polystyrene beads were used to determine the roles of surface chemistry and target size in phagocytic uptake of spherical particles. Finally, I will compare my results with the

simulations done by our physicist collaborators in illustrating the dynamic role of actin in phagocytosis and how it might explain the size-dependent property of phagocytic process.

4.2 A combination of transillumination microscopy and epifluorescence microscopy allows investigation of bead phagocytosis by macrophages

The phagocytosis assay I used was based on incubation of macrophages (MΦ) with beads of different sizes: 0.25 μm, 0.5 μm, 1.0 μm, 1.5 μm and 3.0 μm in radius, in a 24-well plate for 30 minutes. Thirty minutes was found to be a sufficient time to allow beads to settle and be taken up by macrophages without losing their fluorescence. Samples were fixed thereafter and mounted onto glass slides for light microscopy examination. To illustrate the interaction of macrophages with spherical beads, I used an imaging approach that combined transmitted illumination and fluorescence microscopy. The transillumination setup I used was a modified form of differential interference contrast (DIC) microscopy which makes use of all its components apart from the polariser. This was observed to capture lesser intracellular materials (data not shown) compare with full DIC, which enabled easier identification of small (≤ 1μm) bead particles. In addition, the elimination of the polariser still provided sufficient contrast to manually detect all bead sizes used in the experiment.

To score macrophages for phagocytic uptake, it is important to identify the exact location of the bead target, whether they are inside or outside the macrophage or host cell. To do this, I examined the cell membrane features of macrophages with respect to the axial position of the bead in the modified DIC set-up I previously described. Beads that were bounded by the cell membrane and were in focus with the macrophage body (Figure 4.1A green arrow) were considered internalised. On the other hand, beads that were not bounded by the cell membrane (Figure 4.1B yellow arrow) or within the intracellular space but were out of focus (red arrow) were deemed uninternalized. The extracellular localisation of these out of focus beads was verified by scanning across different axial regions and confirming bead position (Figure 4.1C red arrow) outside the cell in reference to external features of macrophages such as membrane ridges (green arrow). In my modified DIC set-up, the dorsal surface of macrophages was found to have a rough and wavy appearance (Figure 4.1D green arrow), which is most likely due to the high density of membrane ridges in this region as illustrated in the previous chapter (3). In addition, an imaging artefact called a "halo" (Figure 4.1D yellow arrow) around the cell was also found to intensify when focussing away from the cell body, which provides a useful reference in imaging the membrane surface. This artefact could then be rectified by returning the focus back to the macrophage main body (Figure 4.1A and 4.1B).
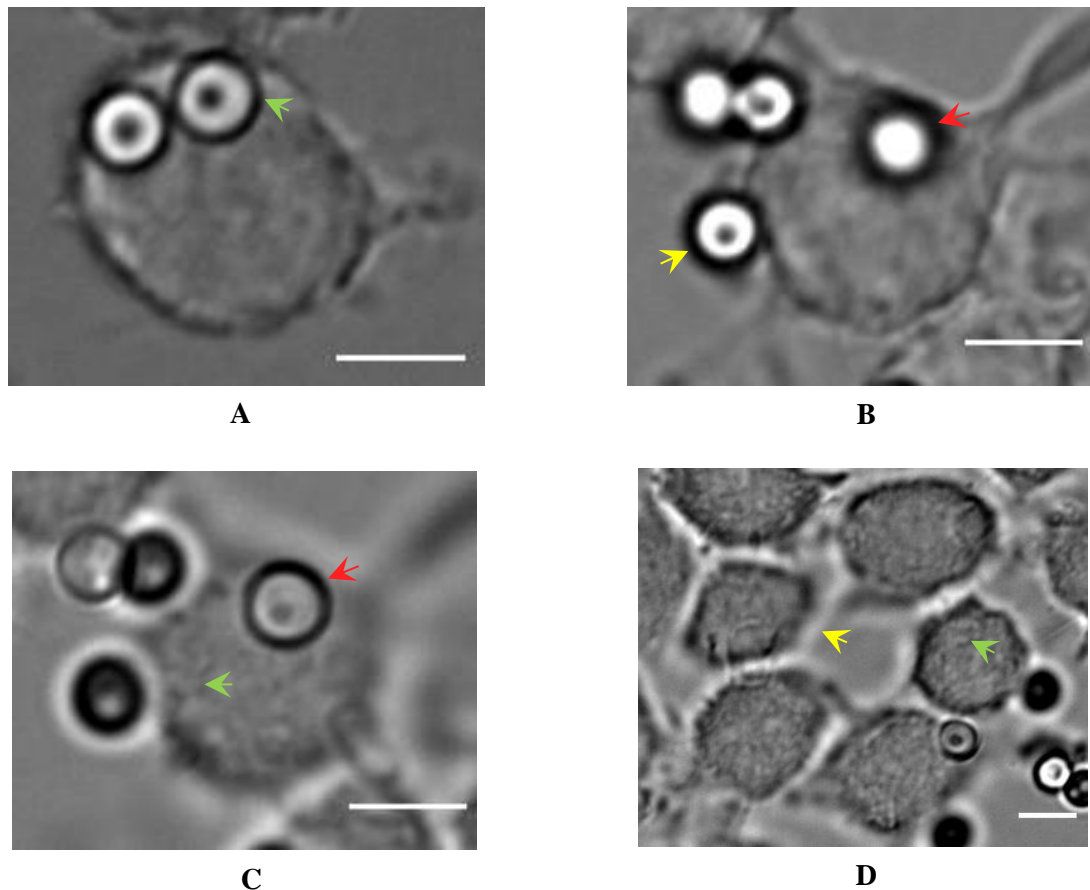
Figure 4.1 | Using a modified DIC imaging set-up, the localisation of beads with respect to MΦ could be determined using the cell membrane features of MΦ. J774 macrophages plated in a 24-well plate were incubated with 1.5 μm (radius) beads for 30 minutes. Samples were then mounted onto glass slides and imaged using a 60x oil immersion objective lens (1.4 NA Plan-Apo). A transillumination setup using DIC but excluding its polariser was used to capture images in z stack, and describe bead localisation.

(A) A macrophage with internalised beads (green arrow),

(B) A macrophage with uninternalised beads (outside/not bounded the cell membrane - yellow arrow, bounded but out of focus – red arrow),

(C) Verifying the extracellular position of bead (red arrow) in image *B* by showing the optical section where the bead is in focus alongside features of the dorsal macrophage surface such as membrane ridges (green arrow),

(D) Zoomed out image showing the characteristic rough and wavy features of the dorsal macrophage surface due to ridges (green arrow) in the modified DIC set-up. Scale bar in all images - 5 μm.

Another challenge in accurately profiling internalised beads by macrophages using this set-up is to discriminate small (≤ 0.5 μm radius) beads from bead-like structures within the intracellular space. Spherical structures within the cell such as vesicles can confound scoring of small beads because of their very similar sizes and appearances in the modified DIC channel (Figure 4.2A, bead-like: red vs true beads: green). Hence, I used the bead fluorescence to differentiate them from non-fluorescent intracellular vesicles and other bead-like structures. However, fluorescence intensity of small beads is greatly reduced along the optical path (Figure 4.2 right images) because of its positive correlation to the volume of spherical object (Kunding et al., 2008). Furthermore, an optical section of at least 5 μm is usually required to completely scan the entire body of a macrophage. To address these issues, I used multiple z-sections that accurately illustrate bead localisation on each imaging plane and a z-interval slightly larger than the bead diameter to avoid any counting repetition during image scoring. I also used an optical imaging thickness of 15 μm to ensure that a complete scan of the macrophage body is achieved regardless of their variable thickness and position in an 833 x 703 μm imaging frame.

A

B

C

D

E

F
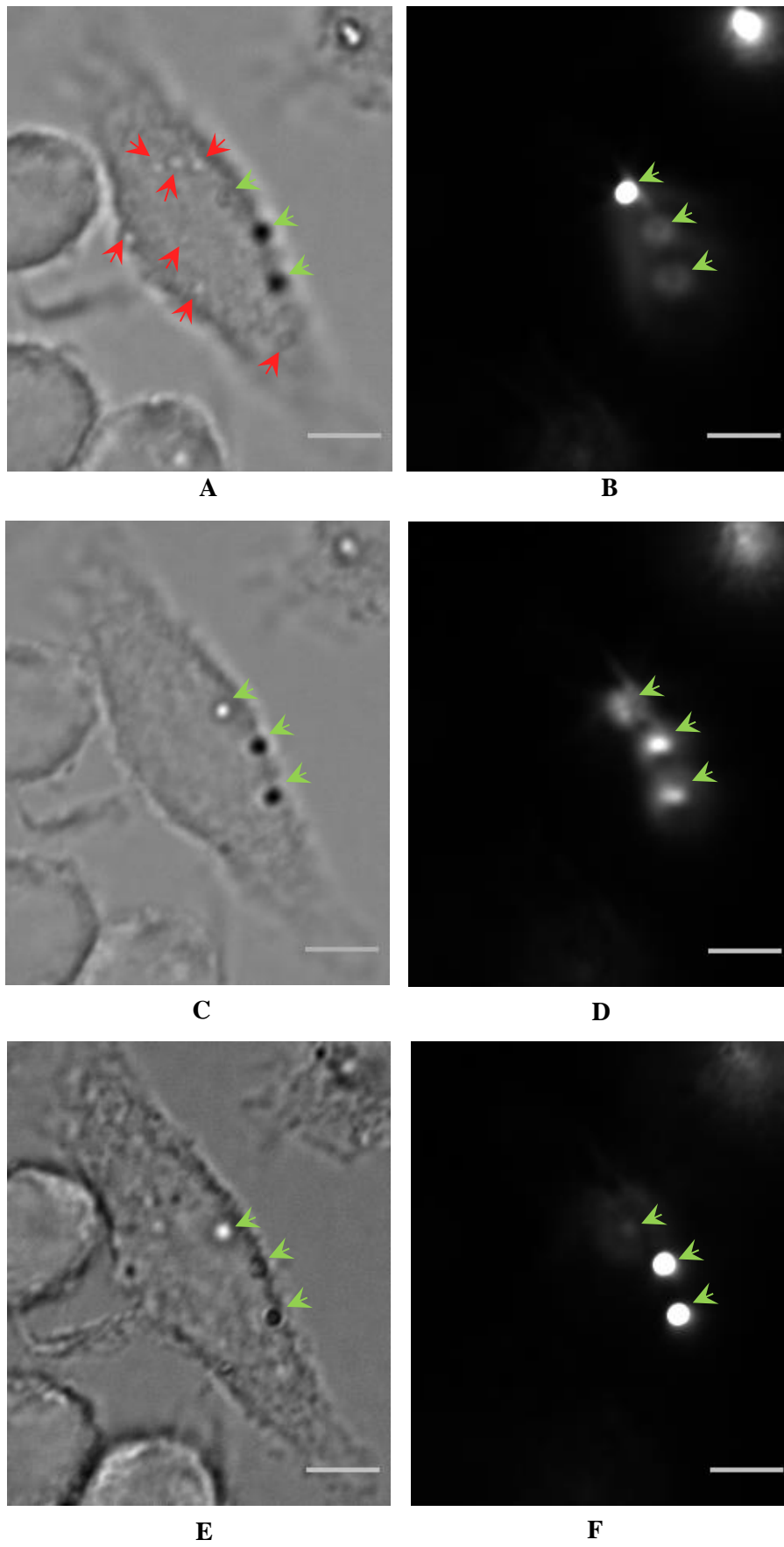
(Figure legend on next page)

Figure 4.2 | Small (≤ 0.5 μm radius) beads can be differentiated from bead-like, intracellular vesicles by their fluorescence, whilst their localisation with respect to MΦ can be determined using optical sectioning. J774 macrophage-like cells plated on a 24-well plate overnight were incubated with beads of 0.5 μm radius for 30 minutes. Samples were then mounted onto glass slides and imaged using a 60x oil immersion objective lens (1.4 NA Plan-Apo). A combination of modified DIC excluding its polariser and GFP channel (excitation: 470/40 nm, emission: 525/50 nm) of a widefield microscope was used to image the specimen in multiple z-sections. **Left:** transillumination image, **Right:** fluorescence image of the same section to its left. All images are of the same cell at different optical sections.

(A) An upper z-section showing internalised beads (green arrow) and bead-like structures (red arrow) of a MΦ in transillumination channel,

(B) Showing bead fluorescence in the upper z-section,

(C) A mid z-section in transillumination channel,

(D) Showing mid z-section fluorescence and its variable intensities from upper section *B*,

(E) A lower z-section in transillumination channel,

(F) Showing lower z-section fluorescence and its variable intensities from the upper section *B* and mid-section *D*. Scale bar in all images – 5 μm.

4.3 Size affects settling of spherical beads in a 24-well plate

Size of the particle was reported to affect its settling in suspension (Gibbs et al., 1971). As a consequence, this could affect the actual number of beads available for uptake by macrophages during *in vitro* phagocytosis assay where settled macrophages on a plate are incubated with beads suspended in a serum-free media. Hence, I examined any differences in settling of different beads used in the assay before the actual phagocytosis experiment.

Naked or unopsonised beads of different sizes: 0.25 µm, 0.5 µm, 1.0 µm, 1.5 µm and 3.0 µm in radius, were prepared separately in a serum-free media at equal concentrations ($1x10^6$ beads/ml). The concentration of each bead size was estimated using a haemocytometer and fluorescence microscopy to count the number of beads on each grid of known volume. Each bead suspension was vortex mixed for 5 minutes before seeding into a 24-well plate in triplicates and incubating for 30 minutes. An image of the bottom central region of each well was then taken using GFP channel of a widefield microscope, and the amount of beads settled was estimated using *particle analysis* (PA) of the open-source Fiji software (Schindelin et al., 2012). *Watershed* segmentation was used to separate beads in close contact and minimise counting errors. Finally, the accuracy of this routine in counting beads settled *in vitro* was evaluated using the formula:

$$Relative\ error_{particle\ analysis} = \frac{|PA\ count - manual\ count|}{manual\ count} \qquad (4.1).$$

I also did manual counting of beads (table 4.2) in each image and compared the results with that of automated (PA) counting. The mean relative error of PA was found to be 0.2%, revealing a very high accuracy rate (99.8%) of this method to estimate bead settling *in vitro*. To further illustrate the accuracy of PA, I compared manual and PA counts using linear regression. A very high correlation between these results was found (Figure 4.3G, $R^2 = 0.999$, $p < 0.0001$), reiterating the high accuracy rate of PA to quantitate settling of bead particles. This could be accounted to the very bright and stable fluorescence of the beads, well-dispersed particles in the well and an optimised imaging setup to produce high signal to noise ratio (SNR) images used for automated particle counting.

Figure 4.3A to 4.3E show fluorescence images of different sizes of beads settled in the well after incubation. The smallest bead size used (0.25 µm radius, Figure 4.3A) could be readily observed to have the least particles settled after 30 minutes. Aside from estimating the number of particles settled in the well, this approach also allows checking of any physical interaction between beads, such as clustering, which could affect their phagocytic interaction

with macrophages. Ideally, there should be one to one interaction between beads and macrophages for a reliable data analysis and comparison with simulations done by our physicist collaborators (described in section 4.6). Hence, bead clustering was discouraged by vortex mixing each sample for at least 2 minutes before incubating with macrophages. Upon checking, each bead size was found to settle individually and rarely clustered (Figure 4.3A - 4.3E). Bead settling from three independent repeats were recorded, and data were analysed using ordinary one-way ANOVA (Figure 4.3H). Results showed a statistically significant effect of size in settling of bead particles *in vitro* ($F(4,10) = 30.81$, $p < 0.0001$). A post hoc analysis was then done using Tukey's multiple comparisons test (table 4.2) to further examine settling differences between bead sizes.

The smallest bead used (0.25 μm) was found to settle the least after 30 minutes (Figure 4.3H). Furthermore, its settling was found to be significantly different from the rest of bead sizes used in the experiment (table 4.2). Settling drastically increases between 0.25 μm and 0.5 μm, and from 0.5 μm up to the largest bead used (3.0 μm), settling was fairly similar. These data highlight the importance of examining any differences in settling of suspended spherical particles in carrying out *in vitro* experiments that probe physical interactions with specimens settled at the bottom of the dish such as, in this case, phagocytosis.

A

B

C

D

E

F

G

H
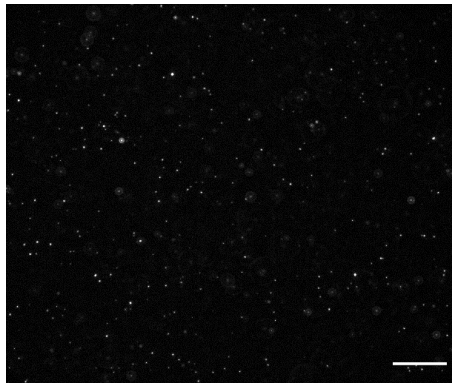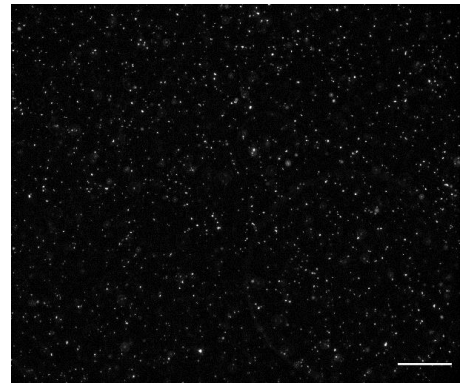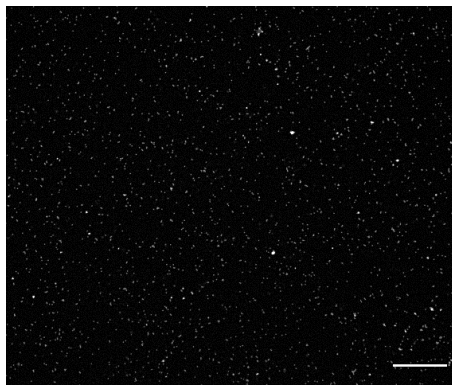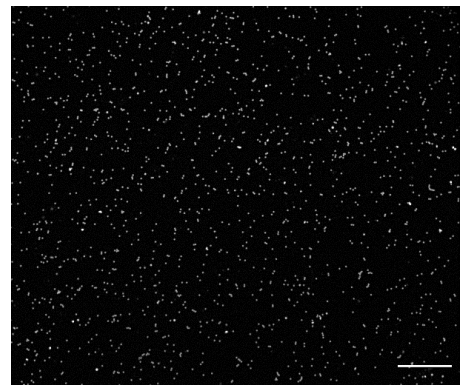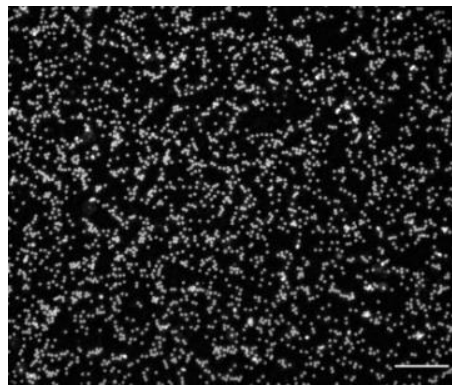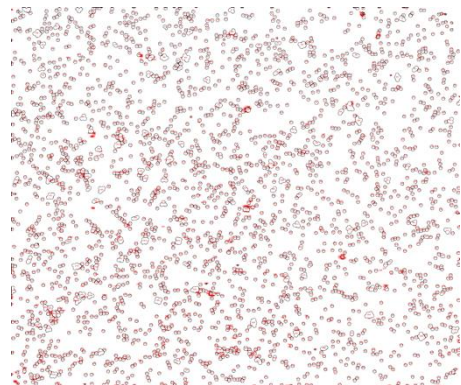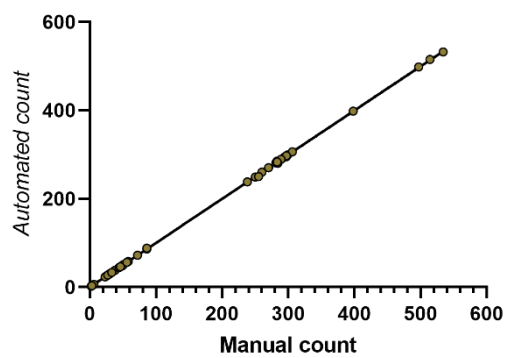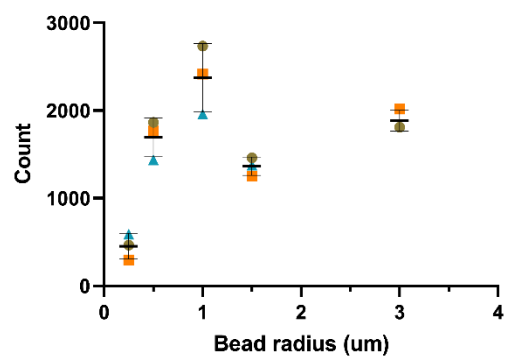
(Figure legend on next page)

Figure 4.3 | Size of unopsonised spherical beads affects their settling in a 24-well plate.
Beads of different sizes (radius): 0.25 μm, 0.5 μm, 1.0 μm, 1.5 μm and 3.0 μm, were allowed to settle in each well of a 24-well plate with 1 x 10^6 particles/ml concentration in triplicate. An image of the central bottom area of each well was then taken after 30 minutes using a 20x objective lens (0.45 NA S Plan-Flour) in GFP channel (excitation: 470/40 nm, emission: 525/50 nm). Particles were counted by applying *particle analysis* (PA) of Fiji software on each image and the total number of beads was computed. Beads were also counted manually to compare results with PA and determine its accuracy. Three independent experimental repeats were done.

(A-E) GFP fluorescence images of settled beads with different radii 0.25 μm (*A*), 0.5 μm (*B*), 1.0 μm (*C*), 1.5 μm (*D*) and 3.0 μm (*E*), scale bar in all images - 100 μm,

(F) Image analysis of *E* using PA,

(G) Linear regression analysis between manual and PA (automated) counting of settled beads showed high correlation ($R^2 = 0.999$, $p < 0.0001$, y = 0.9992x - 0.01251),

(H) There was statistically significant difference in settling of unopsonised beads *in vitro* as confirmed by ordinary one-way ANOVA ($F(4,10) = 30.81$, $p < 0.0001$), $n = 3$ (total particle count in 3 imaging frames per repeat), bars: mean ± standard deviation, a post hoc analysis (table 4.1) using Tukey's test was used to further examine settling differences between bead sizes and determine statistically significant comparisons.

Dependent variable: Particle count Alpha = 0.05				
Bead size (um) comparison	**Mean Difference**	**95% CI of difference**	**Significant?**	**Adjusted p value**
0.25 vs. 0.5	-3724	-5523 to -1925	Yes	0.0003
0.25 vs. 1.0	-5758	-7557 to -3959	Yes	<0.0001
0.25 vs. 1.5	-2740	-4539 to -940.7	Yes	0.0037
0.25 vs. 3.0	-4295	-6094 to -2496	Yes	0.0001
0.5 vs. 1.0	-2034	-3833 to -234.7	Yes	0.0257
0.5 vs. 1.5	984.3	-814.7 to 2783	No	0.4235
0.5 vs. 3.0	-570.7	-2370 to 1228	No	0.8298
1 vs. 1.5	3018	1219 to 4817	Yes	0.0018
1 vs. 3.0	1463	-336.0 to 3262	No	0.1282
1.5 vs. 3.0	-1555	-3354 to 244.0	No	0.0995

Table 4.1 | Tukey's multiple comparisons of settling of unopsonised beads with different sizes in a 24-well plate

Manual count	Automated count	Relative error
2	2	0.000
3	3	0.000
6	6	0.000
23	23	0.000
26	26	0.000
27	27	0.000
28	28	0.000
28	28	0.000
28	28	0.000
29	29	0.000
30	30	0.000
30	30	0.000
33	33	0.000
38	38	0.000
38	38	0.000
44	44	0.000
46	46	0.000
49	48	0.020
49	49	0.000
50	50	0.000
50	50	0.000
50	50	0.000
51	51	0.000
51	51	0.000
56	56	0.000
58	58	0.000
72	72	0.000
86	86	0.000
86	88	0.023
238	238	0.000
250	249	0.004
255	250	0.020
260	260	0.000
270	270	0.000
281	281	0.000
283	285	0.007
283	283	0.000
284	280	0.014
289	289	0.000
294	294	0.000
297	295	0.007
297	297	0.000
298	298	0.000
299	299	0.000
299	299	0.000
306	306	0.000
306	308	0.007
398	398	0.000
497	498	0.002
514	515	0.002
534	532	0.004

Table 4.2 | Comparing manual and automated (*particle analysis)* counting of settled beads in a 24-well plate

4.4 Size of unopsonised spherical beads affects their uptake by macrophages

After determining the effect of size in settling of unopsonised beads, I then examined its role in the phagocytic uptake of spherical target by macrophages (MΦ). This is important to quantitate target size effect in phagocytosis which will enable us to predict how spherical pathogens of different sizes will be taken up by MΦ and, more importantly, probe the underlying mechanics of phagocytosis.

A healthy culture of J774 macrophage-like cells (1×10^5 cells/ml) was seeded into a 24-well plate with mounted glass coverslips. After overnight acclimatisation, they were then challenged with unopsonised beads of different sizes (in radius): 0.25 μm, 0.5 μm, 1.0 μm, 1.5 μm and 3.0 μm, and using a multiplicity of infection (MOI) of 1 MΦ: 10 beads. After 30 minutes of incubation, samples were then fixed, plated onto glass slides and examined using the previously described imaging set-up (section 4.2). Three images per replicate (a total of nine images per bead size) were acquired at random positions starting from the middle of a circular coverslip. Each image was then manually scored for the total MΦ count, MΦ in phagocytosis (i.e. MΦ with internalised beads), beads attached to MΦ and beads internalised by MΦ. All data were plotted and analysed for statistical significance.

Figure 4.4A shows raw data of beads internalised by MΦ according to bead size. Figure 4.4A was adjusted by multiplying with adjustment factors to account for settling differences between beads (table 4.1) using the formula:

$$Settling\ adjustment\ factor_x = \frac{Mean\ settling\ of\ reference\ bead}{Mean\ settling\ of\ bead_x} \quad \text{(4.2).}$$

The reference bead is the size with intermediate settling and, in cases where more than one bead size showed an intermediate value, the mean settling of those bead sizes was taken. In the experiment (Figure 4.3H), 0.5 μm, 1.5 μm and 3.0 μm beads displayed no statistically significant settling difference and showed an intermediate settling between 0.25 μm and 1.0 μm. Thus, their mean settling was computed which yielded adjustment factors of 3.65 and 0.69 in adjusting the phagocytic uptake of 0.25 μm and 1.0 μm beads by MΦ, respectively.

The adjusted values were plotted to produce the final graph (Figure 4.4B) of unopsonised bead uptake by J774 cells. A decrease in uptake at increasing bead size could readily be observed from the graph. Analysis using ordinary one-way ANOVA confirmed the effect of bead size ($F(4,27) = 16.13$, $p < 0.0001$) in their phagocytic uptake. Thus, a post hoc analysis using Tukey's test was done to further analyse the differences in uptake between bead

sizes. Results (table 4.3) showed that all bead size uptake comparisons had statistically significant differences except between 0.25 μm vs. 0.5 μm and 1.0 μm vs. 1.5 μm. Taken together, these indicate that size of an unopsonised spherical target could play a negative role in its phagocytic uptake by J774 cells.

I then checked if there were any significant differences in the number of macrophages scored per bead size which could have caused the differences in uptake. Statistical analysis using ordinary one-way ANOVA (Figure 4.4E) showed no significant difference ($F(4,28) = 1.233$, $p = 0.319$) in the number of macrophages counted across all bead sizes, indicating that the previously observed variation in bead uptake might not be due to the number of macrophages scored.

I next examined any differences in the attachment of MΦ to different bead sizes. This is important as increase in bead size provides more surface area for attachment, and hence increases the likelihood of being internalised. To investigate this, I computed the difference of attachment rate and detachment rate of beads to MΦ using the formula:

$$\kappa_a - \kappa_d = 2u + \kappa_i \qquad (4.3),$$

where κ_a (attached bead/MΦ·t) is the attachment rate, κ_d (detached bead/MΦ·t) is the detachment rate, u (attached bead/MΦ) is the number of beads attached to macrophages over the period of assay (Figure 4.4C) and κ_i (attached bead/MΦ·t) is the internalisation rate of beads by macrophages. κ_i was computed by dividing the total number of internalised beads over the total number of macrophages examined. The term $\kappa_a - \kappa_d$ will be referred hereafter as D. The potential effect of target geometry to its detachment to macrophages is discussed in the following subsection (4.11.3). Furthermore, only attachment rates of three bead sizes (0.5 μm, 1.5 μm and 3.0 μm) were compared as they completely represent the sizes in the experiment (table 4.3) with statistically significant differences in phagocytic uptake.

Results (Figure 4.4D) showed that there was no statistically significant difference in D of different bead sizes. These suggest that macrophages potentially contact beads of different surface areas at similar rates.

A

B

C

D

E
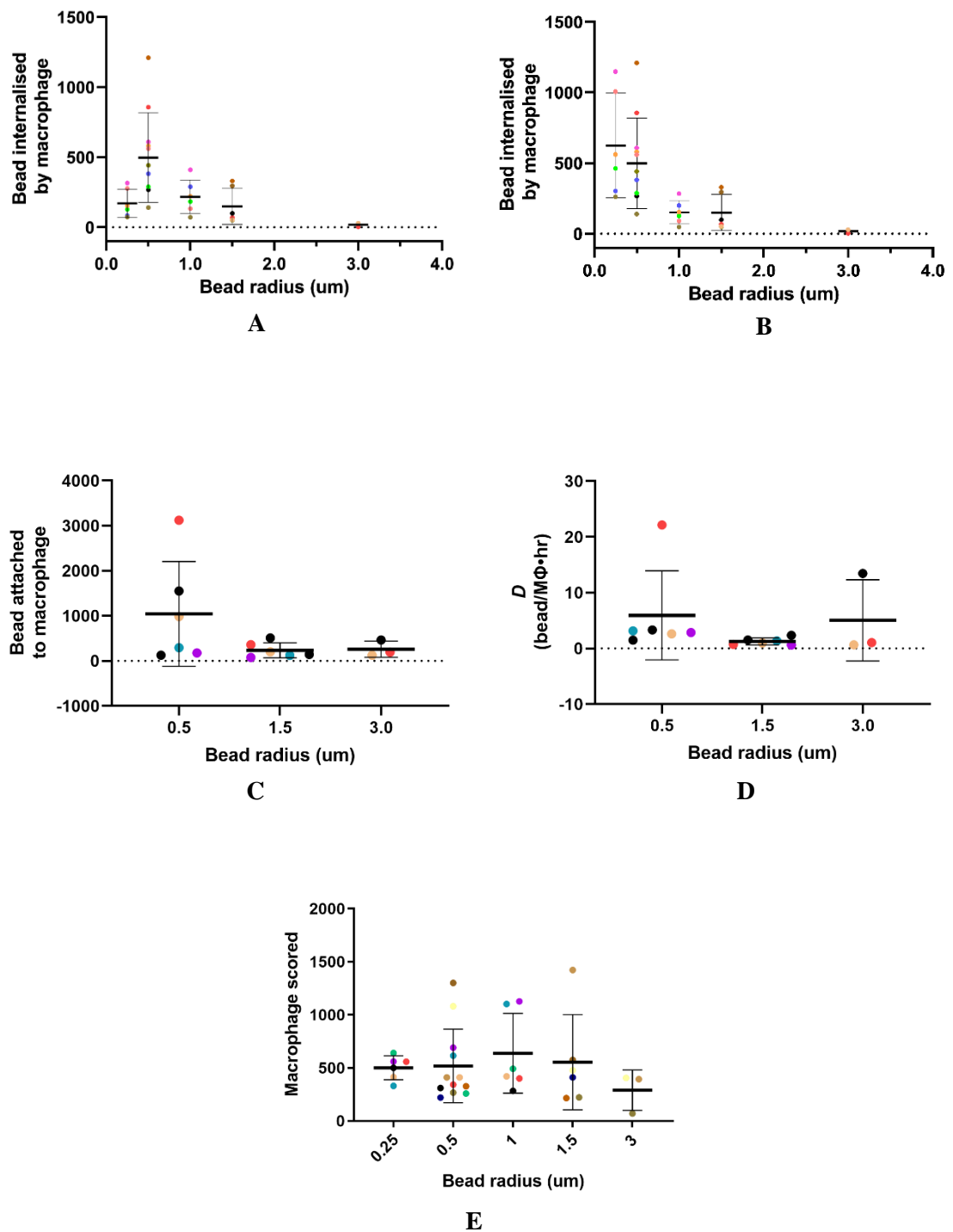
(Figure legend on next page)

Figure 4.4 | Size of unopsonised spherical beads affects their uptake by J774 macrophage-like cells. A healthy culture of J774 macrophage-like cells were seeded into a 24-well plate with glass coverslip, and allowed to acclimatise overnight. Cells were then incubated with different bead sizes (in radius): 0.25 μm, 0.5 μm, 1.0 μm, 1.5 μm and 3.0 μm, for 30 minutes in triplicates. Samples were fixed, mounted onto glass slides and imaged using a 60x oil immersion objective lens (1.4 NA Plan-Apo) in modified DIC and GFP channels (excitation: 470/40 nm, emission: 525/50 nm). Three images per replicate were taken, and phagocytosis was assessed by manually scoring each image for total number of macrophages (MΦ), MΦ in phagocytosis (i.e. with internalised beads), number of beads attached to MΦ and number of beads internalised by MΦ.

(A) Raw data of spherical beads internalised by MΦ according to size, number of repeats (n) according to increasing bead size are: 6, 12, 6, 6, 3 (each colour represents an experimental repeat), bars: mean (M) ± standard deviation (SD),

(B) Adjusted plot of A to account for settling differences of beads due to size using equation (4.2), and analysis of its log-transformed values using ordinary one-way ANOVA revealed a significant effect of bead size in their phagocytic uptake by J774 macrophage-like cells ($F_{(4,27)} = 16.13$, $p<0.0001$), bars: $M \pm SD$, a post hoc analysis using Tukey's test (table 4.3) was done to further examine uptake differences between bead sizes and determine statistically significant comparisons,

(C) Raw data of spherical beads attached to MΦ, n according to increasing bead size are: 6, 6, 3 (each colour represents an experimental repeat), bars: $M \pm SD$,

(D) Plot of D (i.e. attachment rate – detachment rate) calculated by equation (4.3). Size of spherical beads did not show any statistically significant effect on their attachment rate to MΦ, data was log transformed and analysed using ordinary one-way ANOVA ($F_{(2,12)} = 1.989$, $p = 0.179$), n according to increasing bead size are: 6, 6, 3 (each colour represents an experimental repeat), bars: $M \pm SD$,

(E) No statistically significant difference was found in the total number of MΦ scored across all bead sizes, data was log-transformed and analysed using ordinary one-way ANOVA ($F_{(4,28)} = 1.233$, $p = 0.319$), n according to increasing bead size are: 6, 12, 6, 6, 3 (each colour represents an experimental repeat) bars: $M \pm SD$.

Dependent variable: Number of beads internalised by macrophages Alpha = 0.05				
Bead size (um) comparison	**Mean difference**	**95% CI of difference**	**Significant?**	**Adjusted p value**
0.25 vs. 0.5	0.1197	-0.3658 to 0.6052	No	0.9501
0.25 vs. 1.0	0.6138	0.06147 to 1.166	Yes	0.0238
0.25 vs. 1.5	0.6890	0.1367 to 1.241	Yes	0.0091
0.25 vs. 3.0	1.606	0.9297 to 2.283	Yes	<0.0001
0.5 vs. 1.0	0.4941	0.008612 to 0.9796	Yes	0.0446
0.5 vs. 1.5	0.5693	0.08380 to 1.055	Yes	0.0156
0.5 vs. 3.0	1.486	0.8634 to 2.110	Yes	<0.0001
1.0 vs. 1.5	0.07519	-0.4771 to 0.6275	No	0.9944
1.0 vs. 3.0	0.9924	0.3160 to 1.669	Yes	0.0018
1.5 vs. 3.0	0.9172	0.2408 to 1.594	Yes	0.0041

Table 4.3 | Tukey's multiple comparisons of adjusted uptake of different unopsonised bead sizes by J774 macrophage-like cells

Finally, I investigated if the observed variation in bead uptake was due to another uptake mechanism called macropinocytosis which enables macrophages to capture small particles non-specifically and thus would increase the uptake of small (≤ 0.5 μm radius) beads. Hence, I performed an assay that inhibits macropinocytosis in macrophages using amiloride, and examined their uptake of 0.5 μm (radius) beads.

Results (Figure 4.5C) showed that there was no statistically significant difference in the uptake of 0.5 μm beads by macrophages with or without amiloride treatment. I then checked if the amiloride treatment was effective and was able to inhibit macropinocytosis by preventing membrane ruffle formation on the macrophage surface. Using scanning electron microscopy, I examined the surface of amiloride-treated macrophages (Figure 4.5B) and found that they have similar features as the untreated cells (Figure 4.5A) showing a predominance of membrane ridges and very rare occurrence of membrane ruffles. Unidentified membrane pits (Figure 4.5B yellow arrow) were observed to become very common in cells treated with amiloride indicating a previously uncharacterised effect of amiloride on these cells which was not further investigated due to time constraint. Overall, these suggest that J774 macrophage-like cells do not usually produce macropinocytic cups during *in vitro* phagocytosis assay, and small beads are most likely taken up by phagocytosis. The typical absence of membrane ruffles and macropinocytic cups in macrophages during the experiment could be very likely explained by the requirement of activation factors, such as LPS and M-CSF, to prime the macrophage cytoskeleton in producing these structures (Patel and Harrison, 2008).

A

B

C
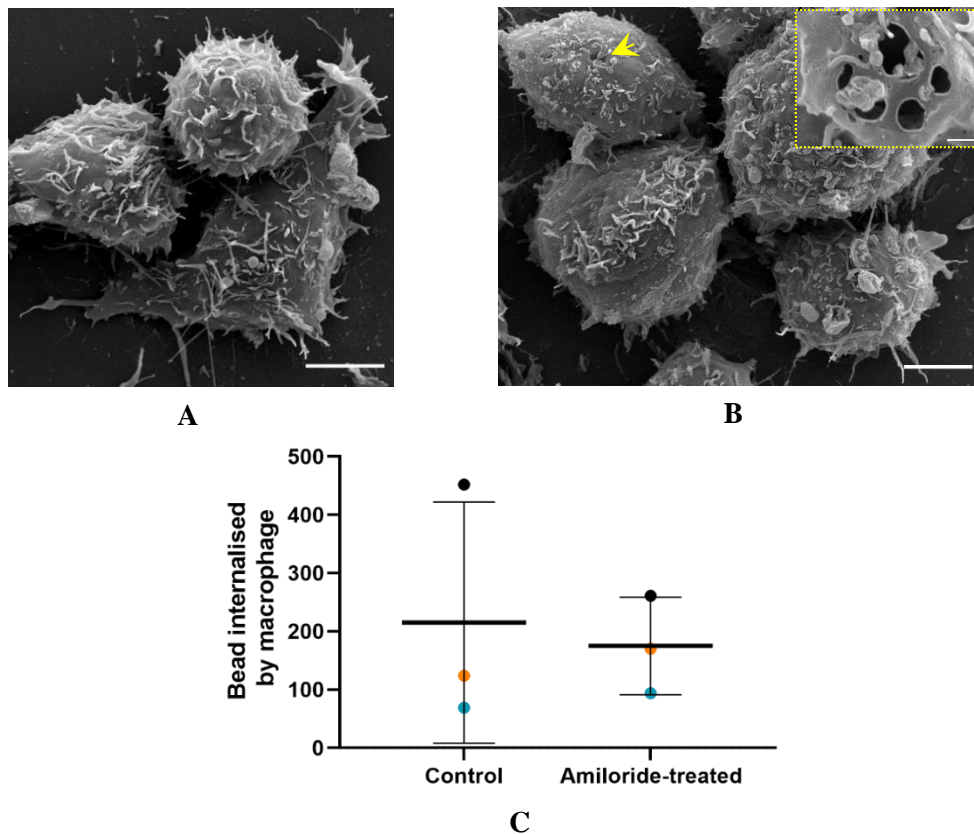
Figure 4.5 | Inhibition of macropinocytosis by amiloride does not affect the uptake of 0.5 μm (radius) beads by J774 macrophage-like cells. A healthy culture of J774 macrophage-like cells were seeded into a 24-well plate with glass coverslip, and allowed to acclimatise overnight. Cells were then incubated with 0.5 μm beads suspended in a serum-free media with 10 μM of amiloride for 30 minutes. After the assay, samples were fixed and imaged using a 60x oil immersion objective lens (1.4 NA Plan-Apo) in modified DIC and GFP channels (excitation: 470/40 nm, emission: 525/50 nm). Images were then manually scored for total number of beads internalised by MΦ. In parallel, samples from the assay were processed for SEM and imaged using a high vacuum, thermionic emission scanning electron microscope with an SE detector at 10 kV accelerating voltage. Three independent experimental repeats were done.

(A) SEM images of control (untreated) MΦ, **(B)** amiloride-treated MΦ showing similar ridge-enriched surfaces as untreated cells but with frequent occurrence of membrane pits (yellow arrow, inset), scale bars: main - 5 μm, inset – 500 nm

(C) No statistically significant difference was found in the uptake of 0.5 μm (radius) beads between control ($M = 215$; $SD = 207$) and amiloride-treated ($M = 175$; $SD = 84$) MΦ using unpaired t test ($t(4) = 0.31$, $p = 0.772$), $n = 3$(each colour represents an experimental repeat), bars: $M \pm SD$.

4.5 Opsonisation does not eliminate the size-dependent phagocytic uptake of spherical particles by J774 macrophage-like cells

After determining the effect of size in the phagocytic uptake of unopsonised spherical particles, I next examined if this property is conserved when changing the target surface or using another type of phagocytic receptor. The role of phagocytic receptors in mediating actin reorganisation during phagocytosis is well established (Gordon, 2016; Jamouille and Grinstein, 2011; Ostrowski et al., 2016). Unopsonised beads are believed to be taken up via a scavenger receptor known as macrophage receptor with collagenous domain (MARCO) (Palecanda et al., 1999; Kobzik, 1995). However, its surface could be modified by coating with complement proteins or antibodies, a process known as opsonisation, to further understand the mechanics of phagocytosis. This allows probing of any differences in the properties of phagocytic uptake according to the type of receptor involved. To investigate this, I used a monoclonal IgG antibody to quantitate the uptake of spherical targets with different sizes via Fc receptor (Burmeister et al., 1994).

The previously used unopsonised beads (section 4.4) were initially incubated with bovine serum albumin (BSA) overnight prior to antibody opsonisation (Figure 4.6B). They were then coated with IgG antibody at room temperature for an hour. Successful opsonisation was confirmed (Figure 4.6D) using an anti-IgG probe conjugated to AlexaFluor647 and widefield fluorescence imaging. A far-red dye was chosen because of the wide emission profile of beads in the visible light spectrum (Figure 4.6A) which might confound confirmatory results. After bead opsonisation, settling of each bead size was determined using the previously described method (section 4.3) and analysed for any statistical significance.

Results (Figure 4.6F) showed that opsonised bead settling was also influenced by particle size ($F(4,10) = 38.18$, $p < 0.0001$). However, compared to unopsonised beads, their settling displayed a different pattern with a very gradual increase from the smallest bead used (0.25 μm) and peaking at the largest bead size (3.0 μm). I accounted this settling behaviour to the attachment of coating materials to the bead surface; hence, I examined the relationship between bead settling and its surface area. Results (Figure 4.6G) showed a highly linear and positive correlation between these variables ($R^2 = 0.986$, $p = 0.0007$), indicating that bead surface area determines the settling of opsonised bead particles. This could be possibly explained by the increasing effect of the coating material at increasing bead size.
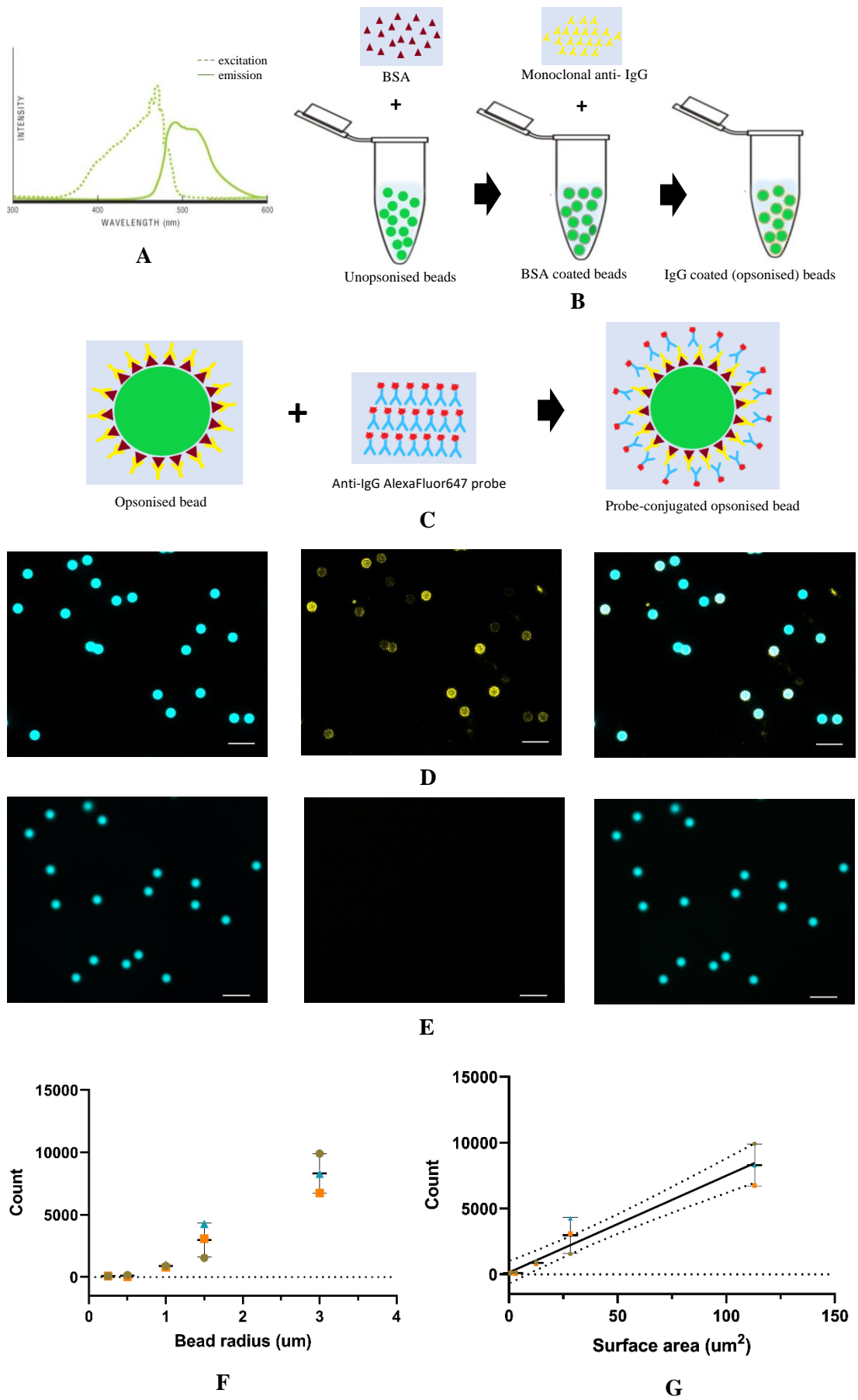
(Figure legend on next page)

Figure 4.6 | Opsonised spherical particles of different sizes have variable settling in a 24-well plate. Spherical beads of different sizes (in radius): 0.25 μm, 0.5 μm, 1.0 μm, 1.5 μm and 3.0 μm, were incubated with bovine serum albumin (BSA) overnight. Thereafter, beads were washed and incubated with a mouse monoclonal IgG for an hour. To confirm successful opsonisation, beads were incubated with an anti-mouse IgG conjugated to AlexaFluor647, and imaged with a 20x objective lens (0.45 NA S Plan-Flour) in GFP (excitation: 470/40 nm, emission: 525/50 nm) and Cy5 (excitation: 620/60 nm, emission: 700/75 nm) channels. Settling of each opsonised bead was examined using previous method (section 4.3). Three independent experimental repeats were done.

(A) Fluorescence profile of beads used (data courtesy of supplier Polysciences, Inc.),

(B) Schematic diagram of bead opsonisation protocol,

(C) Schematic diagram of opsonisation confirmatory test,

(D) Images of 1.5 μm (radius) **opsonised** beads (from left to right): bead fluorescence in GFP channel, anti-IgG probe fluorescence in Cy5 channel and overlay of both channels,

(E) Images of 1.5 μm (radius) **unopsonised** beads (negative control) showing similar channels in *D* from left to right, scale bar in all images - 20 μm,

(F) Size has statistically significant effect in settling of opsonised beads as shown by ordinary one-way ANOVA of log-transformed data ($F(4,10) = 38.18$, $p < 0.0001$), $n = 3$ (each colour represents an experimental repeat), bars: mean (*M*) ± standard deviation (*SD*), a post hoc analysis (table 4.4) using Tukey's test was used to further examine settling differences between bead sizes and determine statistically significant comparisons.

(G) Linear regression analysis revealed positive correlation between settling of opsonised beads and its surface area ($R^2 = 0.986$, $p = 0.0007$, y = 73.46x + 155.6), $n = 3$ (each colour represents an experimental repeat), bars: $M \pm SD$.

Dependent variable: Particle count Alpha = 0.05				
Bead size (um) in radius comparison	**Mean Difference**	**95.00% CI of Difference**	**Significant?**	**Adjusted p value**
0.25 vs. 0.5	0.07918	-0.5866 to 0.7450	No	0.9942
0.25 vs. 1.0	-0.9610	-1.627 to -0.2952	Yes	0.0054
0.25 vs. 1.5	-1.452	-2.118 to -0.7859	Yes	0.0002
0.25 vs. 3.0	-1.929	-2.595 to -1.264	Yes	<0.0001
0.5 vs. 1.0	-1.040	-1.706 to -0.3744	Yes	0.0031
0.5 vs. 1.5	-1.531	-2.197 to -0.8651	Yes	0.0001
0.5 vs. 3.0	-2.009	-2.674 to -1.343	Yes	<0.0001
1.0 vs. 1.5	-0.4907	-1.157 to 0.1751	No	0.1854
1.0 vs. 3.0	-0.9683	-1.634 to -0.3025	Yes	0.0052
1.5 vs. 3.0	-0.4776	-1.143 to 0.1882	No	0.2033

Table 4.4 | Tukey's multiple comparisons test of settling of opsonised beads with different sizes in a 24-well plate for 30 minutes

I then performed a phagocytosis assay using these opsonised beads to determine if the previously observed size-dependent uptake of spherical particles (section 4.4) is conserved using Fc receptor. Using the same *in vitro* phagocytosis experimental set-up and analysis (section 4.4.), I examined the uptake of different opsonised beads by J774 cells. The uptake results were also adjusted as in previous analysis (section 4.4) to account for any settling differences of opsonised particles. Finally, I compared the uptake of opsonised beads to unopsonised ones to examine the separate and combined effects of target size and surface chemistry in phagocytosis of a spherical target .

To account for any bead settling differences, I adjusted the raw phagocytic uptake data of opsonised beads (Figure 4.7A) using equation (4.2). Opsonised beads with 1.0 μm and 1.5 μm radii showed an intermediate settling amongst the bead sizes used in the experiment. In addition, they were found to have no statistically significant difference on their settling (table 4.4), hence I computed their mean settling and used it to adjust the uptake of the rest of bead sizes. These yielded adjustment factors of 9.05, 8.07 and 0.11 to amend the phagocytic uptake of 0.25 μm, 0.5 μm and 3.0 μm opsonised beads, respectively.

Results (Figure 4.7B) revealed that the phagocytic uptake of opsonised beads by J774 macrophages was also size dependent ($F(4,20) = 5.148$, $p = 0.005$), showing a general trend of decrease in uptake at increasing particle size. As previously done (section 4.4), I then checked if there were any differences in D and in the total number of macrophages scored for each bead size that might explain the observed uptake differences (Figure 4.7B). Results revealed no statistically significant differences in D (Figure 4.7D) nor macrophages scored (Figure 4.7E) across all bead sizes, reiterating the critical importance of size as a physical parameter in the phagocytic uptake of spherical targets. This could be possibly explained by

the prevailing biophysical events in the host cell that govern phagocytosis such as the kinetics of phagocytic receptors (reviewed by Richard and Endres, 2017) or the more direct source of engulfment forces, actin dynamics, which is mainly responsible in bending the membrane to allow target internalisation (explored further in section 4.6).

Although a general trend of decrease in phagocytic uptake at increasing target size was observed for both unopsonised and opsonised beads, some key differences in the uptake of very small particles ($\leq$ 0.5 um radius) and in the magnitude of uptake in almost all bead sizes (Figure 4.7F) could be observed. Hence, I further examined the combined effect of surface chemistry and particle size in the phagocytic uptake of spherical targets.

IgG-opsonised beads were generally taken up better than their unopsonised counterparts (Figure 4.7F), suggesting a more efficient phagocytic uptake of spherical particles by macrophages using Fc receptor than MARCO. Statistical analysis using two-way ANOVA (Figure 4.7F) further confirmed the dominant effect of opsonisation in the phagocytosis of spherical targets with different sizes. Opsonisation explained 49% of the uptake variation compared with 30% explained by target size. In addition, the analysis revealed a significant interaction or combined effect of opsonisation and target size in phagocytosis of spherical particles which accounted to 15% of the observed variation. Finally, it can be observed that the smallest bead (0.25 μm) did not show any statistically significant increase in uptake after opsonisation (Figure 4.7F). This suggests that other factors, such as target curvature, membrane topography and bending properties of the host cell membrane, might be playing a more dominant role than surface chemistry and size in phagocytosis of spherical targets in this size regime.
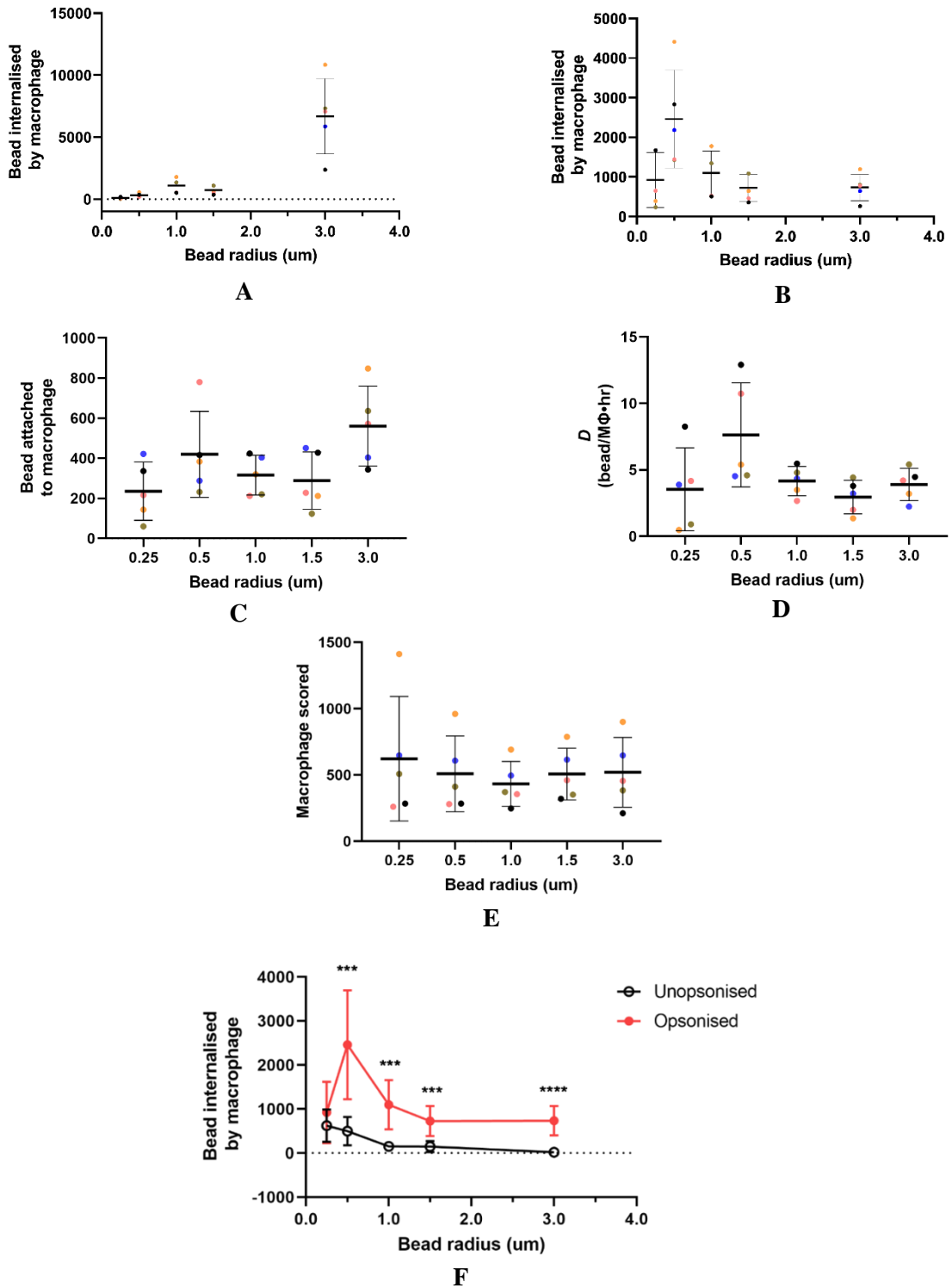
(Figure legend on next page)

Figure 4.7 | Phagocytic uptake of opsonised spherical particles by J774 macrophages is size dependent, and opsonisation plays a more dominant role than target size. A healthy culture of J774 cells were seeded into a 24-well plate with glass coverslip, and allowed to acclimatise overnight. Cells were then incubated with opsonised beads of different sizes (in radius): 0.25 μm, 0.5 μm, 1.0 μm, 1.5 μm and 3.0 μm, for 30 minutes. A triplicate for each bead size was prepared for the assay. Samples were then fixed, imaged and manually scored for phagocytosis as done previously with unopsonised beads (section 4.4). Five independent experimental repeats were done to assess phagocytosis of opsonised spherical beads.

(A) Raw data of opsonised spherical beads internalised by macrophages with respect to bead size, $n = 5$ (each colour represents an experimental repeat), bars: mean (M) ± standard deviation (SD),

(B) Adjusted plot of A to account for settling differences of opsonised beads of different sizes (equation (4.2)), and its analysis using ordinary one-way ANOVA revealed significant effect of size in the phagocytic uptake of opsonised spherical beads by J774 macrophage-like cells ($F(4,20) = 5.148$, $p = 0.005$), bars: $M \pm SD$, a post hoc analysis using Tukey's test (table 4.5) was done to further examine uptake differences between bead sizes and determine statistically significant comparisons,

(C) Raw data of opsonised spherical beads attached to J774 macrophages after a 30-minute phagocytosis assay, $n = 5$ (each colour represents an experimental repeat), bars: $M \pm SD$,

(D) Plot of attachment rate calculated by equation (4.3). Size of opsonised spherical beads did not show any statistically significant effect on their attachment rate to J774 macrophages as confirmed by ordinary one-way ANOVA of log-transformed data ($F(4,20) = 2.886$, $p = 0.104$), $n = 5$ (each colour represents an experimental repeat), bars: $M \pm SD$,

(E) No statistically significant difference was found in the total number of macrophages scored for phagocytic uptake across different bead sizes as shown by ordinary one-way ANOVA of log-transformed data ($F(4,20) = 0.125$, $p = 0.972$), $n = 5$ (each colour represents an experimental repeat), bars: $M \pm SD$,

(F) There was a statistically significant interaction between size and opsonisation state in the phagocytic uptake of spherical beads by J774 macrophages as revealed by two-way ANOVA ($F(4,47) = 7.606$, $p < 0.0001$). Sidak's multiple comparisons test between opsonised and unopsonised beads showed significantly higher uptake of 0.5 μm (***$p = 0.0002$), 1.0 μm (***$p = 0.0001$), 1.5 μm (***$p = 0.0005$) and 3.0 μm (****$p <0.0001$) opsonised beads compare to their unopsonised counterparts. However, opsonisation have no statistically significant effect in the uptake of 0.25 μm beads ($p = 0.979$). The main effect of opsonisation

state yielded an effect size of 0.49 ($F(1, 47) = 99.23$, $p < 0.0001$), indicating that 49% of total variation in bead uptake could be explained by whether beads were opsonised or not. On the other hand, size had 0.30 effect size ($F(4, 47) = 15.38$, $p < 0.0001$), indicating that 30% of total variation in the bead uptake by J774 cells could be explained by size.

Dependent variable: Number of beads internalised by macrophages				
Alpha = 0.05				
Bead size (um) comparison	**Mean Difference**	**95% CI of Difference**	**Significant?**	**Adjusted p value**
0.25 vs. 0.5	-1535	-2891 to -179.9	Yes	0.0217
0.25 vs. 1.0	-175.2	-1531 to 1180	No	0.9949
0.25 vs. 1.5	198.2	-1157 to 1554	No	0.9918
0.25 vs. 3.0	188.8	-1167 to 1544	No	0.9932
0.5 vs. 1.0	1360	4.689 to 2715	Yes	0.0490
0.5 vs. 1.5	1733	378.1 to 3089	Yes	0.0083
0.5 vs. 3.0	1724	368.7 to 3079	Yes	0.0087
1.0 vs. 1.5	373.4	-981.9 to 1729	No	0.9199
1.0 vs. 3.0	364.0	-991.3 to 1719	No	0.9264
1.5 vs. 3.0	-9.400	-1365 to 1346	No	>0.9999

Table 4.5 | Tukey's multiple comparisons of adjusted uptake of opsonised beads of different sizes by J774 macrophage-like cells

4.6 The role of actin in the phagocytic uptake of spherical targets

The very striking mechanical property of phagocytosis, which involves deformation of the host cell membrane to internalise particles, led us to probe the role of actin to potentially explain the size dependence of phagocytosis in taking up spherical particles. Moreover, the importance of actin in phagocytosis was previously hypothesised using theoretical and experimental models of phagocytic engulfment (Herant et al., 2006; Herant et al, 2011). These excellent works however did not illustrate the specific mechanisms involved in actin growth during phagocytosis and its implications in engulfing particles with different physical properties such as size. Thus, in collaboration with physicists, Dr. James Bradford and Dr. Rhoda Hawkins, of the Department of Physics and Astronomy in University of Sheffield, we looked at the dynamics of actin during phagosome formation and examined its role in phagocytic uptake of spherical targets with different sizes. Briefly, our collaborators developed a 2D simulation of actin growth based on critical parameters that define actin dynamics *in vitro* which include nucleation, branching, capping and anti-capping. These were then incorporated within an inextensible membrane model to simulate phagosome formation and growth during phagocytic uptake (Figure 4.8; Bradford, 2021).

Using the same target sizes as in the *in vitro* phagocytosis experiment (section 4.4 and 4.5), an *in silico* assay (Figure 4.8) was performed by our collaborators to investigate the phagocytosis of spherical targets as mediated by actin during phagosome formation. The physical interaction between the target (green) surface and host cell membrane (red line) results to an activated region (purple box), which depicts the activation of phagocytic receptors inducing actin polymerisation during engulfment. As expected, actin (purple lines) growth was seen to push the cell membrane around the target during the simulation, leading to a highly dense actin network around the target (Figure 4.8C red arrow). This recapitulates the advancing pseudopodia that is supported by actin during actual phagosome formation (Figure 4.9A and 4.9B, yellow arrow). Taken together, these underscore the important role of actin in shaping and providing critical membrane features of the host cell during phagocytic uptake.

Results from our simulation (Figure 4.10) revealed differences in membrane fusion timing (i.e. time to complete phagosome formation) to take up spherical particles of different sizes. Particle size with 1 μm radius was taken up the quickest (i.e. lowest time required for membrane fusion), whilst that with 3 μm radius did not result to any membrane fusion within the simulation period of 60 seconds. Interestingly, unopsonised beads with 3 μm radius were barely taken up by macrophages in our *in vitro* experiments as well (Figure 4.4B). Taken together, these data suggest that actin dynamics during phagosome formation might influence the phagocytic uptake of spherical particles with different sizes. However, in comparison with previous *in vitro* experimental results (Figure 4.7F), the trend of phagocytic uptake according to size where the smallest beads (≤ 0.5 μm radius) were usually taken up better and thus should have the shortest timing of fusion in the simulation was not observed. This could be explained by a few caveats when comparing these experiments. Aside from only one repeat in our simulation due to time constraints, other factors in phagocytic interaction such as activation of receptors through clustering (Sobota et al., 2005), receptor diffusion (Freeman et al., 2016), myosin recruitment (Swanson et al., 1999) and potential role of cortical actin (Nelsen et al., 2020) were not incorporated in our model. These might have direct or indirect effects on actin architecture and dynamics during engulfment, but understanding these variables could allow us to provide a more accurate picture of phagocytosis and understanding its mechanics.
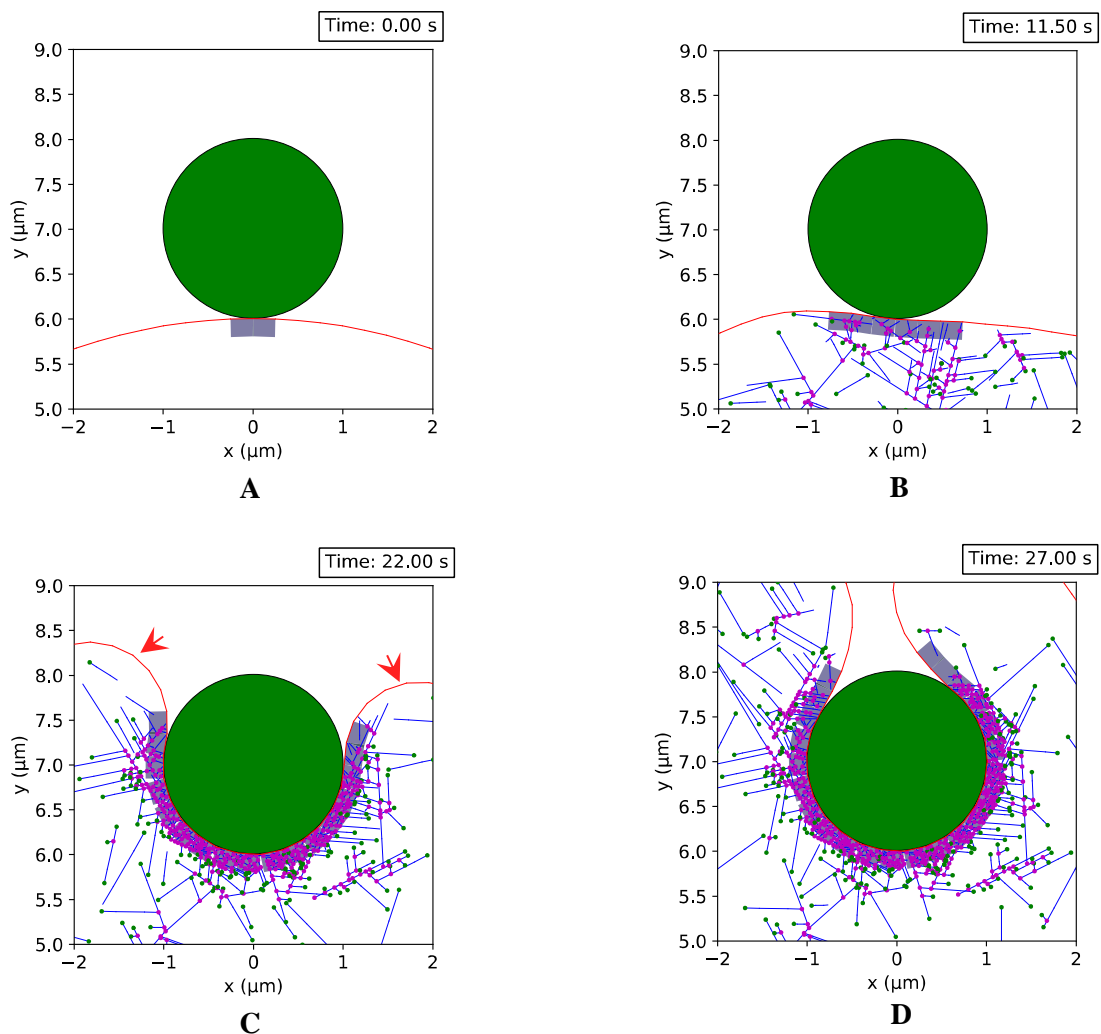
Figure 4.8 | Actin growth within host cell membrane leads to phagosome formation that drives the phagocytic uptake of spherical target. An *in silico* model of phagocytosis through actin filament growth within host cell membrane was developed by our physicist collaborators. Important parameters describing actin dynamics- nucleation, branching, capping and anti-capping were derived from *in vitro* experiments and were used to simulate the actin dynamics. Snapshots from *in silico* experiment to highlight the morphological changes in the host cell membrane due to actin growth during phagosome formation. Data courtesy of Dr. James Bradford.

(A) At 0 second, an initial contact between host cell membrane (red line) and spherical target (green circle) activated phagocytic receptors which caused an activated region (purple box) where actin filaments (purple line) assembled,

(B) Activation continued at both sides of initial receptor-ligand contact,

(C) As engulfment progressed further, actin pushed the membrane around the target resulting in an actin-rich protrusion (red arrow) similar to pseudopodia/phagocytic cup of actual phagocytosis,

(D) As actin continued to grow around the target, the opposite membranes of phagocytic cup contact each other and fuse to form a phagosome and complete phagocytic uptake.

A **B**
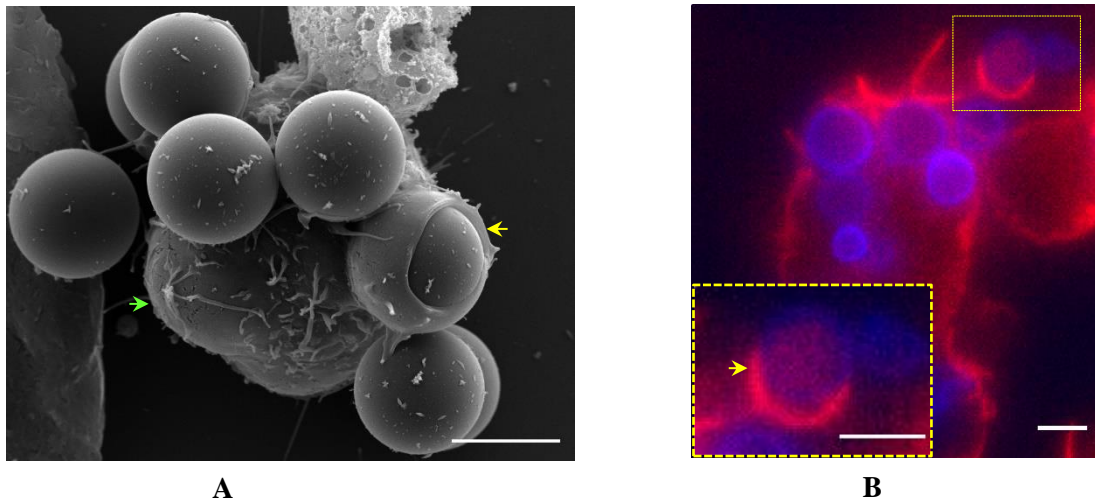
Figure 4.9 | Actin shapes and supports the growing phagosome during engulfment of spherical targets. J774 macrophage-like cells were incubated *in vitro* with spherical phagocytic targets, beads and *Cryptococcus neoformans*. Samples were then fixed and prepared accordingly for SEM and fluorescence microscopy. For SEM, samples were imaged using a high vacuum, thermionic emission scanning electron microscope with an SE detector at 10 kV accelerating voltage. On the other hand, fluorescence imaging was done using 60x oil immersion objective (1.4 NA Plan-Apo) in DAPI (excitation: 436/20 nm, emission: 480/40 nm) and mCherry (excitation: 560/40 nm, emission: 630/75 nm) channels of a widefield microscope.

(A) An SEM image of J774 cell during phagocytic uptake of 6 um spherical beads, the pseudopodia of growing phagosome (yellow arrow) could be seen wrapping around the bead to be internalised

(B) A fluorescence image of actin filaments (red) supporting the pseudopodia of growing phagosome (yellow arrow) around a Cryptococcal cell (blue), scale bar in all images – 5 um.
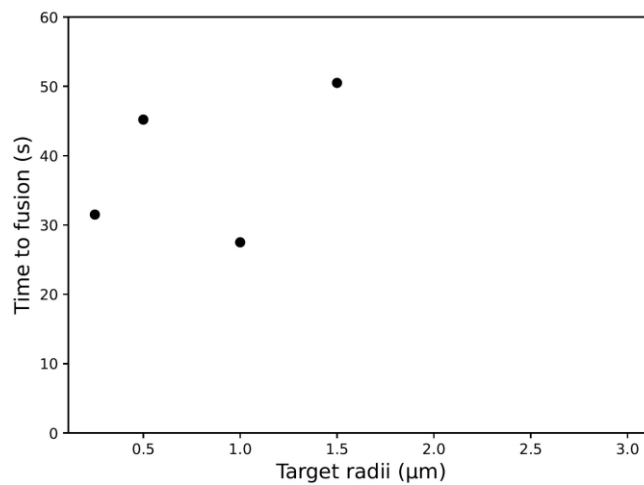
Figure 4.10 | Preliminary data in simulating actin growth during phagocytosis show different timing in completing the uptake of spherical targets with different sizes . Using our *in silico* model of phagocytosis, the time required to complete phagosome sealing or to fuse the opposite membranes of phagocytic cup around the target was recorded for each spherical particle size (target radii). Spherical target with 1 μm radius was found to be internalised the quickest (i.e. shortest time to fusion), whilst that with 3 μm radius did not result to any membrane fusion within the simulation period of 60 seconds. Data courtesy of Dr. James Bradford.

4.7 Investigating the phagocytic uptake of a spherical fungal pathogen *Cryptococcus neoformans*

After determining that size and surface chemistry are important factors in the phagocytic uptake of spherical targets by macrophages, I then examined if these are replicated in the uptake of an actual pathogen. Using *Cryptococcus neoformans* (Cn), a spherical fungal pathogen of immunocompromised host, I examined the phagocytosis of its two variants: **H99** (serotype A) - a wild type variant possessing capsule and **CAP59** - an acapsular variant.

Prior to setting up an *in vitro* phagocytosis experiment, I examined any differences in settling of different types of Cn that will be used in the assay. Cryptococcal cells grown in yeast extract peptone dextrose (YPD) agar media were cultured in a YPD broth overnight. H99 cells were then washed with phosphate buffered saline (PBS) solution three times whilst PBS-Tween was used to wash CAP59 cells to discourage cell clustering. Each type of Cn

(H99, CAP59, 18B7-opsonised H99) was stained with calcoflour white and resuspended in a serum free DMEM media before plating into a 24-well dish in triplicate. After 2 hours incubation, three images per replicate in phase and DAPI channels of a widefield microscope were taken starting at the bottom central of each well. As previously done to quantitate bead settling (section 4.3), *particle analysis* was used to estimate the number of Cryptococcal cells settled for each type.

Microscopic examination (Figure 4.11A-D) showed and confirmed the spherical shape of Cryptococcal cells *in vitro*. Buds (Figure 4.11D yellow arrow), which were outgrowths from the mother cell (green arrow), were found to be a common feature of Cn regardless of their variant (H99 or CAP59). Thus, to exclude them in particle counting, their mean size (Figure 4.11G) was determined ($M = 2.5$, $SD = 0.6$), and used as a threshold parameter in automated particle analysis.

Results showed that capsule possession (Figure 4.11E) and cell opsonisation (Figure 4.11F) did not have any statically significant effect in settling of Cryptococcal cells. *In vitro* experiments using Cn commonly use different types of media depending on the requirements of the host cell (Pline, 2019). Thus, I also investigated any effect of the type of media used in settling of H99 cells. Results (Figure 4.11H) revealed no statistically significant difference in settling of Cryptococcal cells with respect to the media used across different cell concentrations (table 4.6).

A

B

C

D

E

F

G

H
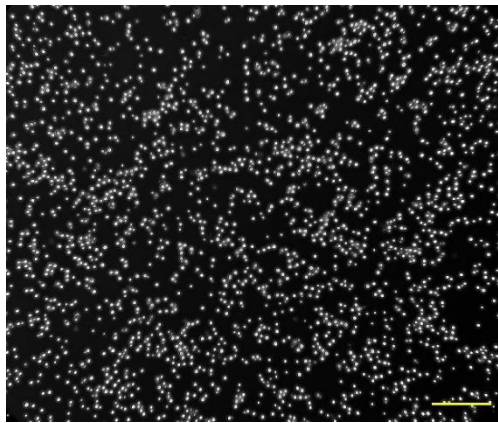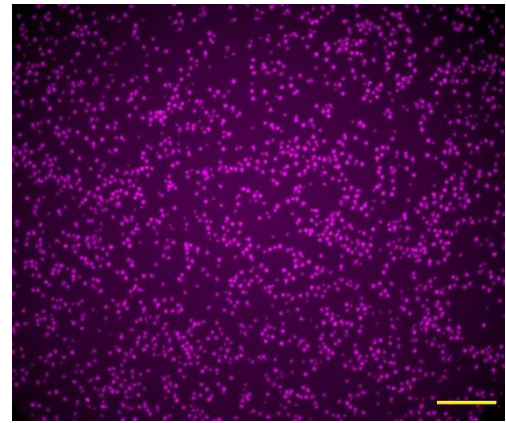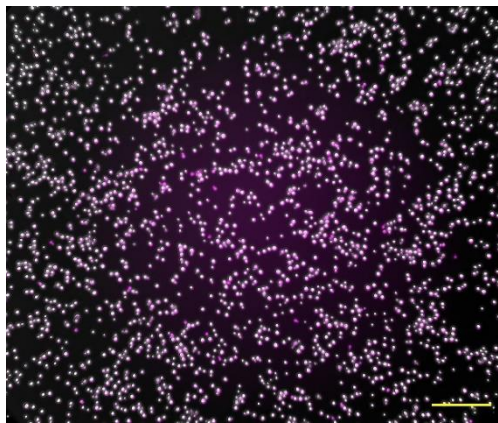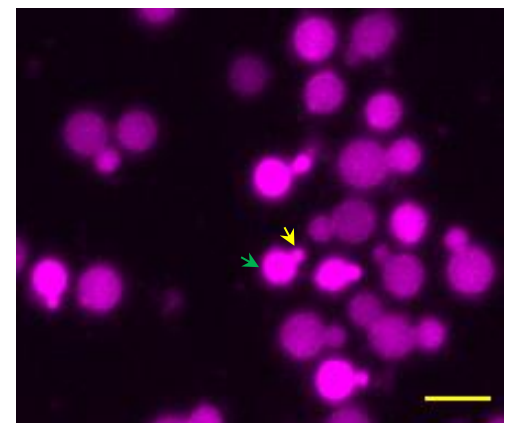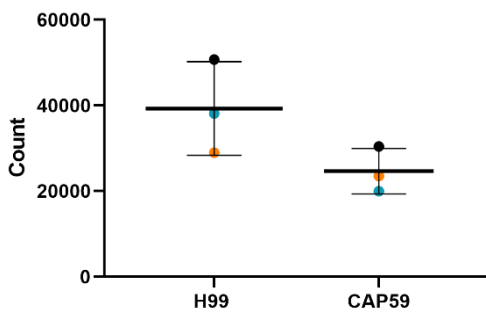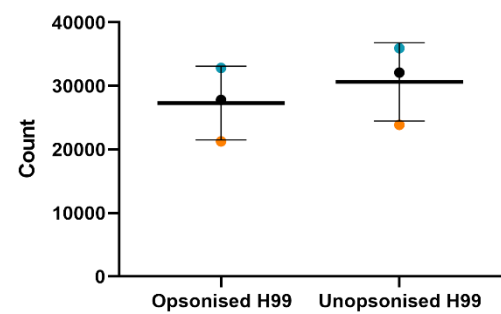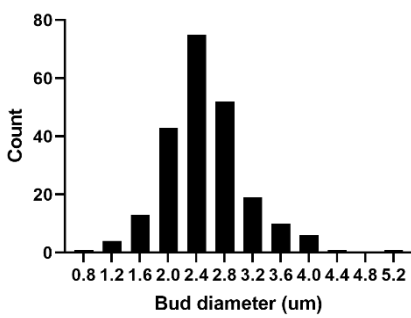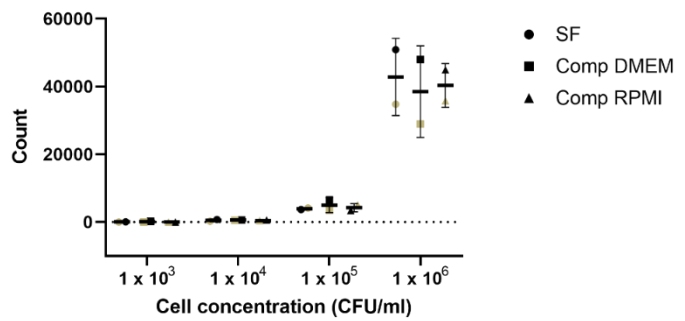
(Figure legend on next page)

Figure 4.11 | Capsule possession, cell opsonisation and type of media do not affect the settling of *C. neoformans* in vitro. Cryptococcal cells grown in a yeast extract peptone dextrose (YPD) agar media were cultured in a YPD broth overnight. Cells were then washed and processed before adjusting to a final concentration of 1×10^6 CFU/ml. One ml per well of each type of Cn (unopsonised H99, CAP59 and 18B7-opsonised H99) was prepared in a 24-well plate in triplicates. Samples were incubated for 2 hours, and then imaged using 20x objective lens (0.45 NA S Plan-Flour) in phase contrast and DAPI (excitation: 436/20 nm, emission: 480/40 nm) channels of a widefield microscope. Automated counting was done using the previously described method based on *particle analysis* (section 4.3). Three independent experimental repeats were done.

(A) Phase contrast image of settled H99 Cn,

(B) Fluorescence image of *A* revealing the cell wall of Cryptococcal cells,

(C) Overlay of image *A* and *B*, scale bar - 100 μm,

(D) Zoomed-in fluorescence image of cell wall showing a bud (yellow arrow) from the mother cell (green arrow), scale bar - 10 μm,

(E) There was no statistically significant difference found between the settling of capsular H99 ($M = 39, 290$; $SD = 10, 918$) and acapsular CAP59 ($M = 24, 659$; $SD = 5, 311$) Cn variants *in vitro* using unpaired t test ($t(4) = 2.087$, $p = 0.105$), $n = 3$ (each colour represents an experimental repeat), bars: mean (*M*) ± standard deviation (*SD*),

(F) No statistically significant difference was found between settling of unopsonised H99 cells ($M = 30, 638$; $SD = 10, 918$) and opsonised H99 cells ($M = 27, 309$; $SD = 5, 803$) *in vitro* using unpaired t test ($t(4) = 0.6810$, $p = 0.533$), $n = 3$ (each colour represents an experimental repeat), bars: $M \pm SD$,

(G) Bud size histogram of H99 *C. neoformans* ($n = 225$ buds, $M = 2.5$, $SD = 0.6$),

(H) The type of media used in preparing H99 Cryptococcal cells did not have any statistically significant effect in their settling as revealed by two-way ANOVA ($F(2,12) = 0.043$, $p < 0.9582$), $n = 2$ (each colour represents an experimental repeat), bars: $M \pm SD$, post hoc analysis using Tukey's test (table 4.6) specifically showed that type of media does not have any statistically significant effect on Cn settling across different cell concentrations.

Dependent variable: Cell count Alpha = 0.05				
Media comparison at different cell concentrations	**Mean Difference**	**95.00% CI of Difference**	**Significant?**	**Adjusted p value**
1 X 10³ CFU/ml				
SF VS. COMP DMEM	-75.00	-14708 to 14558	No	0.9999
SF VS. COMP RPMI	17.50	-14615 to 14650	No	>0.9999
COMP DMEM VS. COMP RPMI	92.50	-14540 to 14725	No	0.9998
1 X 10⁴ CFU/ml				
SF VS. COMP DMEM	-50.50	-14683 to 14582	No	>0.9999
SF VS. COMP RPMI	13.00	-14620 to 14646	No	>0.9999
COMP DMEM VS. COMP RPMI	63.50	-14569 to 14696	No	>0.9999
1 X 10⁵ CFU/ml				
SF VS. COMP DMEM	-1085	-15718 to 13548	No	0.9787
SF VS. COMP RPMI	-342.0	-14975 to 14291	No	0.9979
COMP DMEM VS. COMP RPMI	743.0	-13890 to 15376	No	0.9899
1 X 10⁶ CFU/ml				
SF VS. COMP DMEM	4342	-10291 to 18974	No	0.7151
SF VS. COMP RPMI	2493	-12140 to 17126	No	0.8934
COMP DMEM VS. COMP RPMI	-1849	-16481 to 12784	No	0.9396

Table 4.6 | Tukey's multiple comparisons of Cryptococcal cell settling *in vitro* at different cell concentrations and using different type of culture media.

4.8 Capsule possession and not cell size determines the phagocytic uptake of *C. neoformans*

After determining that settling of Cn is not affected by capsule possession nor opsonisation, I then examined the effect of Cryptococcus cell size on its phagocytic uptake. Acapsular Cn, such as CAP59, were reported to be larger than their capsular counterparts (Garcia-Rivera et al., 2004), potentially due to the restrictive effect of capsule on cell expansion during Cryptococcus lifetime. Thus, to investigate any differences in size and phagocytic uptake between capsular H99 and acapsular CAP59 variants, I used an *in vitro* phagocytosis assay set-up and immunofluorescence microscopy.

As in the previously described settling assay (section 4.7), Cryptococcal cells were processed according to cell type to prevent cell clustering. An MOI of 1 MΦ: 10 Cn was used in a 2-hour *in vitro* phagocytosis assay with J774 macrophage-like cells. When the assay was finished, samples were fixed and processed for immunofluorescence microscopy to evaluate phagocytic interactions and measure cellular features such as cell size and capsule size of Cn. Meanwhile, immunofluorescence microscopy was also used to obtain size measurements of those Cryptococcal cells in culture (general population). Comparisons between these measurements were done to determine any size preference during phagocytic uptake of Cn and quantitate the effect of capsule in Cn phagocytosis.

Immunofluorescence microscopy confirmed the spherical shape of Cn (Figure 4.12A and 4.12B) and the absence of capsule in CAP59 variant (Figure 4.12B). The size of Cryptococcal cells was measured by manually drawing a line across the cell (through its largest diameter, if not perfectly spherical) using the cell wall (Figure 4.12A and 4.12B left image) as a reference border. However, compared to a previous report by Garcia-Rivera (2004) and colleagues, our results (Figure 4.12C) showed no statistically significant difference between cell size of capsular H99 ($M = 2.2$, $SD = 0.2$) and acapsular CAP59 ($M = 2.6$, $SD = 0.2$) variants. These discrepancies might be due to some key differences between these experiments such as variants used, experimental set-up and experimental repeats considered to draw statistical conclusions. Garcia-Rivera (2004) and co-workers used capsular B3501 (serotype D) and acapsular B4131 (*cap59* missense mutation) strains whilst I used the capsular H99 (serotype A) and acapsular CAP59 (gene deletion by homologous recombination) which, as previously determined, might have different physical properties such as capsule thickness (Rachini et al. 2007), expression of capsule related genes and biofilm thickness (Lee et al., 2019). Furthermore, Garcia-Rivera (2004) and colleagues cultured cells in yeast nitrogen base (YNB) with 150 rpm shaking compared to YPD grown cells and 20 rpm disturbance used in my experiment. Lastly, the authors considered one experimental repeat with 150 cell size measurements compare to three independent repeats of 127 to 473 measurements in my experiment before doing any statistical analysis.

Higher resolution microscopy using SEM and helium ion microscopy (HIM) of Cn variants revealed the different properties of their surfaces (Figure 4.12C-F). The surface of uninduced H99 cells (Figure 4.12C) can be characterised by a short, highly branched polysaccharide capsule covering, whilst CAP59 surface (Figure 4.12D), which reveals the cell wall of Cryptococcal cells, was found to be smoother with some occasional puncta (red arrow). Interestingly, when surface properties of our uninduced H99 cells are compared to induced cells (Figure 4.12E and 4.12F) subjected to different media conditions from the independent work of Araujo (2016) and colleagues, the shorter polysaccharide branching close to the cell wall (Figure 4.12F yellow arrow) similar to surface properties of uninduced cells (Figure 4.12C yellow arrow) was found to extend outward (Figure 4.12E and F green arrow) and interact laterally to form thicker fibre bundles. HIM imaging is believed to illustrate structures close to its native state as it does not involve a coating step unlike SEM (Araujo et al., 2016). Nevertheless, our SEM imaging data using our optimised specimen preparation protocol (Chapter 2.3) also captured similar capsule features observed by HIM. Taken together, these results suggest that the capsule of Cn is a highly complex structure that is sensitive to its environment and can possess different levels of structural organisation.

A

B

C

D

E

F

G
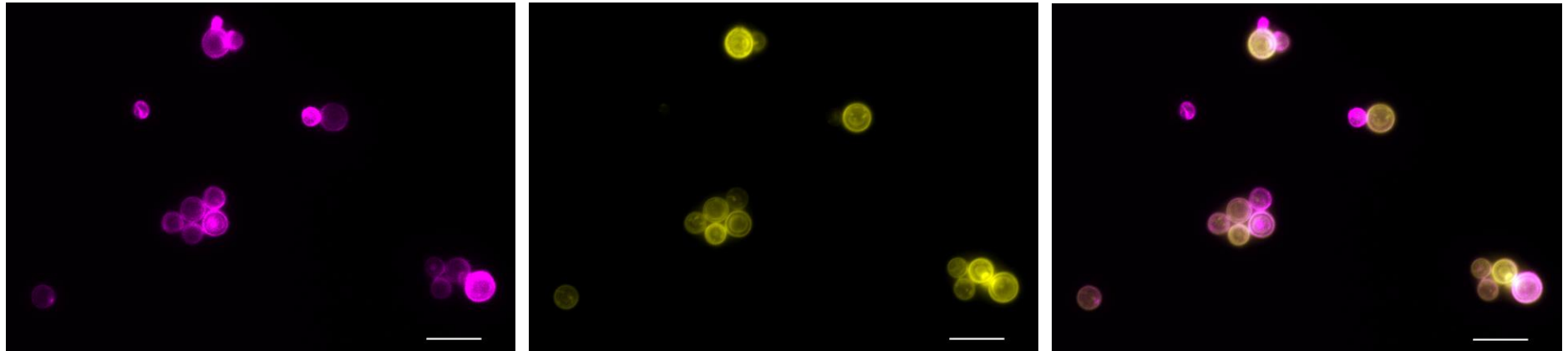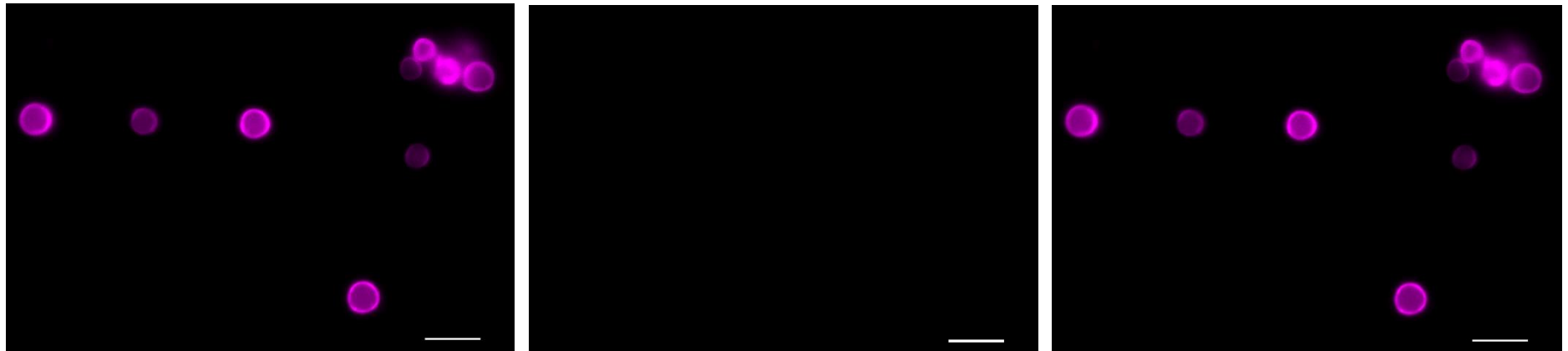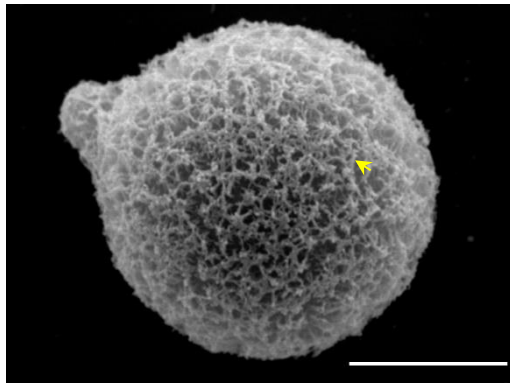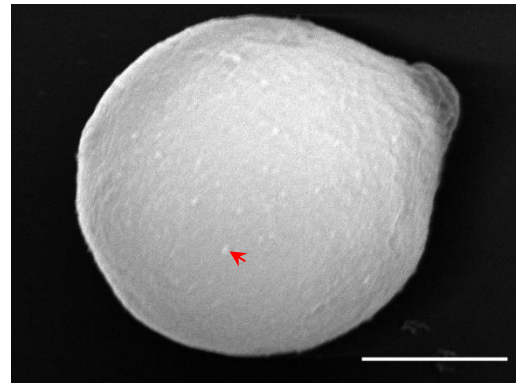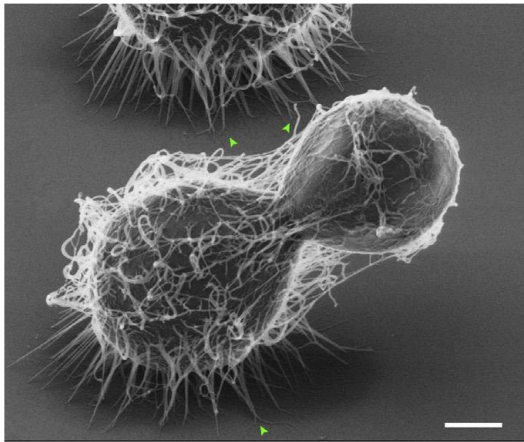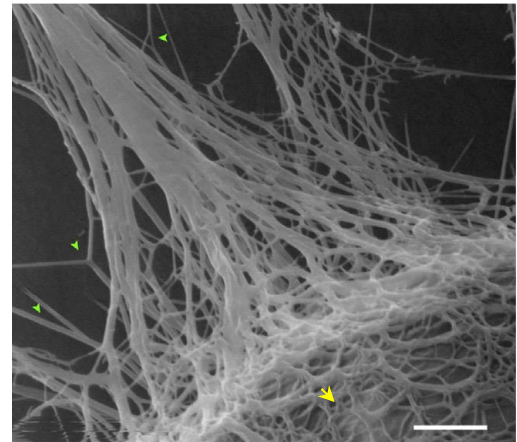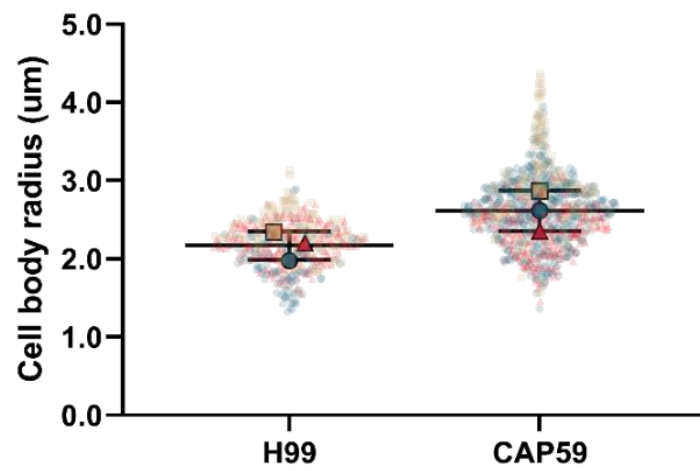
(Figure legend on next page)

Figure 4.12 | Immunofluorescence and SEM imaging reveal the morphologies of H99 and CAP59 *C. neoformans* **and show no statistically significant difference in their cell size.** Capsular H99 and acapsular CAP59 Cn were cultured overnight in a YPD broth media. They were then washed and incubated with calcoflour and 18B7 with anti-mouse IgG conjugated to FITC to label the cell wall and capsule, respectively. Samples were fixed, mounted onto glass slides and imaged with a 60x oil immersion objective (1.4 NA Plan-Apo) in DAPI (excitation: 436/20 nm, emission: 480/40 nm) and GFP (excitation: 470/40 nm, emission: 525/50 nm) channels of a widefield microscope. SEM examination of each variant was also done in parallel. Three independent experimental repeats were performed. Fluorescence images from left to right are maximum intensity projections of cell wall, capsule and overlay of the previous two images.

(A) Immunofluorescence images of H99 and **(B)** CAP59 Cn cultured *in vitro*, scale bar-10μm, **(C)** SEM images of capsular H99 and **(D)** CAP59, scale bar – 2 μm,

(E) Helium ion microscopy of induced Cn capsule (scale bar – 1 μm) and **(F)** an image with higher magnification showing adhesion fibres (green arrow) and those close to the cell wall (yellow arrow), scale bar – 200 nm, Images were taken from Araujo et al. 2016 (for reprint permission see appendix 3)

(G) There was no statistically significant difference between size of H99 (M = 2.2, SD=0.2) and CAP59 (M = 2.6, SD = 0.2) cells as revealed by unpaired t test ($t(4)$=2.424, p = 0.072), n=3, 127-473 cells measured per repeat (each colour represents an experimental repeat), bars: $M \pm SD$.

After investigating the size of CAP59 and H99 cells, I then examined any differences in their phagocytic uptake by MΦ. This is to verify previous findings that capsule possession plays an important role in phagocytosis of Cn (Bojarczuk et al., 2016; McQuiston and Poeta, 2014; Kozel, 1977). Immunofluorescence images (Figure 4.13) from the phagocytosis assay were used to manually score each variant for cells internalised by MΦ, cells attached to MΦ and total MΦ count. Results (Figure 4.14A) revealed that acapsular CAP59 cells were taken up better than H99 cells ($t(4)$ = 8.080, p = 0.0013), suggesting that capsule negatively impacts phagocytosis of Cn and validating previous reports of its anti-phagocytic property (Kozel and Gotsclich, 1982; Small and Mitchell, 1989). To further confirm that there was no size preference in the uptake of Cn by J774 macrophage-like cells, I compared cell sizes of those internalised (assay) from those in the culture (general population) for each variant. Results revealed no statistically significant difference for both H99 (Figure 4.14B) and CAP59 (Figure 4.14C) cells. Taken together, these suggest that capsule possession of the spherical pathogen Cn affects their phagocytic uptake by MΦ but not their cell size.
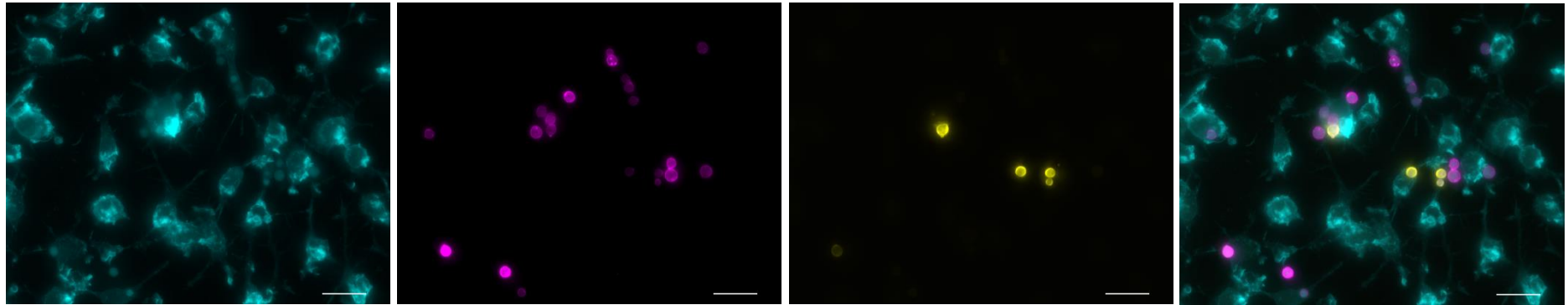
A
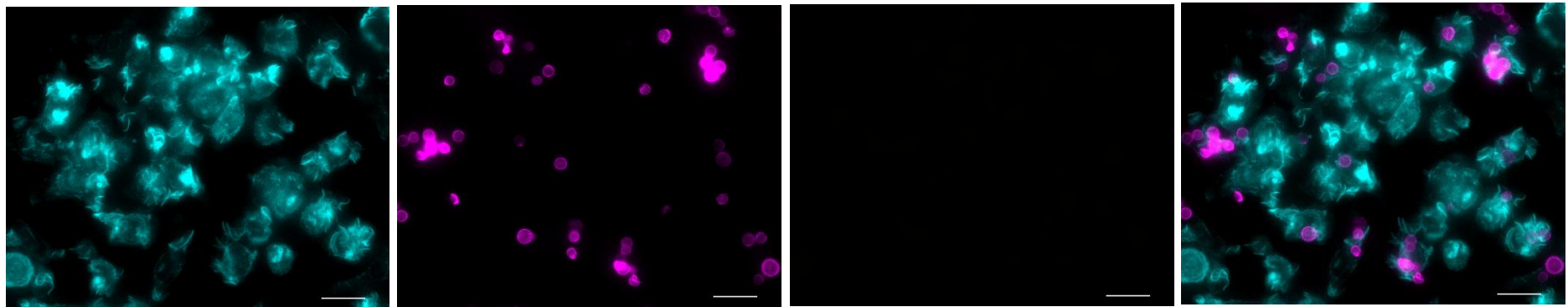
B

(Figure legend on next page)

Figure 4.13 | Immunofluorescence microscopy enables visualisation of different cell structures to examine the phagocytic interaction between *C. neoformans* and J774 macrophage-like cells. Capsular H99 and acapsular CAP59 *C. neoformans* (Cn) were grown overnight in YPD broth with constant 20 rpm rotation. In parallel, a healthy culture of J774 macrophage-like cells were seeded in a 24-well plate with glass coverslips. On the next day, J774 macrophages were challenged with either H99 or CAP59 cells with pre-labelled cell wall in triplicates for 2 hours. Samples were then fixed, permeabilised and incubated with 18B7 and anti-mouse IgG-FITC to label the capsule, and phalloidin-TRITC to label the actin filaments. Imaging was done using a 60x oil immersion objective (1.4 NA Plan-Apo) in DAPI (excitation: 436/20 nm, emission: 480/40 nm), GFP (excitation: 470/40 nm, emission: 525/50 nm) and Cy3 (excitation: 545/25 nm, emission: 605/70 nm) channels of a widefield microscope. Three fields of view were imaged per replicate (a total of nine per variant) starting at the centre of each coverslip, and three independent experimental repeats were done. Images are from a single field of view showing maximum intensity projections of (left to right images) actin filament, cell wall, capsule and overlay of all images.

(A) Immunofluorescence images of a J774 macrophage-like cells phagocytosis assay with H99 Cn and **(B)** CAP59 Cn, scale bar - 20 μm.
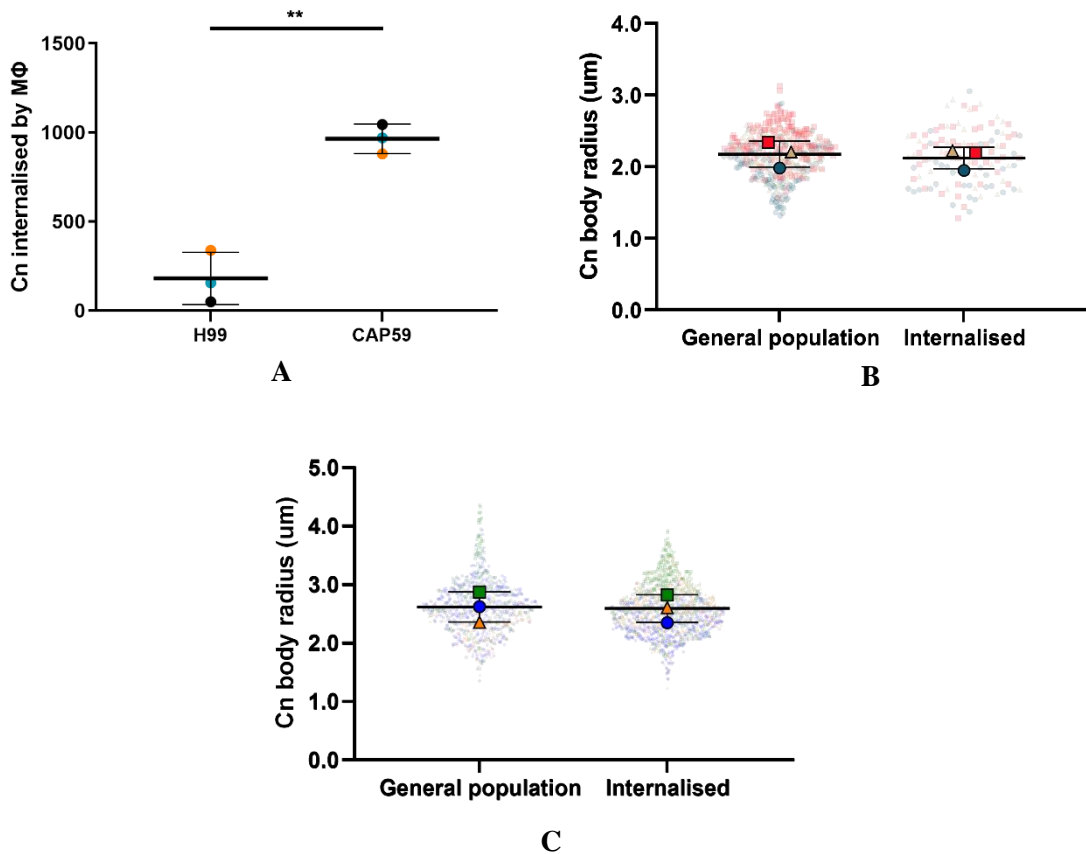
Figure 4.14 | Capsule possession and not cell size determines the phagocytic uptake of *C. neoformans* by J774 macrophage-like cells. Immunofluorescence images from phagocytosis assay using H99 and CAP59 Cn were used to evaluate phagocytic uptake of Cryptococcal cells. Each image was scored for Cn internalised by macrophages (MΦ), Cn attached to MΦ, MΦ in phagocytosis and total number of MΦ.

(A) H99 cells ($M = 181$; $SD = 146$) were taken up less than CAP59 cells ($M = 964$; $SD = 83$) by J774 macrophage-like cells as confirmed by unpaired t test ($t(4) = 8.080$, **$p = 0.0013$), $n=3$ (each colour represents an experimental repeat), bars: mean (M) ± standard deviation (SD),

(B) There was no statistically significant difference in cell size of H99 internalised by MΦ and those in the culture (general population) as revealed by unpaired t test ($t(4) = 0.388$, $p = 0.718$), $n = 3$, 33-169 cells per repeat (each colour represents experimental repeat), bars: $M \pm SD$,

(C) Similarly, no statistically significant difference was found in cell size of CAP59 internalised by MΦ and those in the culture as confirmed by unpaired t test ($t(4) = 0.13$, $p = 0.903$), $n = 3$, 200-515 cells per repeat (each colour represents an experimental repeat), bars: $M \pm SD$.

198

I next explored how capsule possession inhibits the phagocytic uptake of H99 cells by J774 macrophage-like cells. Firstly, I hypothesised that there was preferential uptake of cells with smaller capsule by macrophages as previously reported *in vivo* by Bojarczuk (2016) and colleagues. Thus, using the immunofluorescence data, I attempted to compare the capsule size of cells in culture with those internalised by macrophages. Measurement of capsule of cells grown in culture however was unsuccessful, yielding mostly 0 and negative values. This was potentially due to nonspecific labelling of probes, autofluorescence of Cryptococcal cells (data not shown) or a combination of both. On the other hand, most cells that were internalised have successfully labelled capsule and thus I focussed in analysing these results to probe the effect of capsule in Cn phagocytosis.

Results (Figure 4.15A) revealed that there was statistically significant difference ($F(2,108) = 9.767$, $p = 0.0001$) in capsule size of internalised cells across different repeats. More specifically, those in the first repeat had the thickest mean capsule which was significantly thicker than the other two repeats (table 4.7). This implies significant differences in the capsule size of H99 cells in different culture set-ups. The most probable explanation for this variation is the sensitivity of capsule to different variables which is further explained later in subsection (4.11.5).

After determining significant differences in the capsule size of internalised H99 cells, I then examined how these cells were internalised by J774 macrophage-like cells by computing their internalisation rate (κ_i) using the formula:

$$\kappa_i = \frac{N_{Cn}}{N_{M\Phi}t} \qquad (4.4),$$

where N_{Cn} is the number of Cryptococcal cells internalised by macrophages, $N_{M\Phi}$ is the total macrophages scored and t is the duration of the assay. Results (table 4.8) showed that internalisation rate across different repeats were also variable, with the first repeat having the lowest rate. Thus, I next checked if there was any correlation between capsule size and internalisation rate. Results (Figure 4.15B) revealed a highly negative correlation ($R^2 = 0.999$, $p = 0.022$) of capsule size to its internalisation rate which is summarised by the following equation:

$$y = -0.7317x + 1.339 \qquad (4.5),$$

where y-axis represents the internalisation rate of H99 Cn by J774 cells whilst x-axis represents H99 mean capsule thickness. Furthermore, this regression analysis predicts a 95% confidence that in the absence of capsule (x = 0), internalisation rate of Cryptococcal cells would be between 1.087 and 1.591 μm Cn/MΦ·hr. This was verified in our experimental data (table 4.8) as the mean internalisation rate of acapsular CAP59 cells was found to be 1.586 Cn/MΦ·hr. On the other hand, a complete inhibition of Cryptococcus uptake (y = 0) would be expected with 95% confidence when capsule size is between 1.498 and 2.686. Overall, these results revealed the striking effect of Cn capsule size on its phagocytic uptake. It is however important to point out the limitations of this analysis which was based on three experimental repeats due to a painstaking manual image analysis involved to accurately derive these quantities. Additional data might allow us to test our experimental data with the polymer physics-based model equations developed by our physics collaborators (unpublished) to fully understand the role of capsule in phagocytosis of Cn.

As in my previous phagocytosis assay analysis, I examined if there were any differences in D (equation 4.3 but changing the coefficient 2 to ½ due to a different incubation period) between H99 and CAP59 cells, which might explain the higher uptake of CAP59 variant than H99 due to attachment rate. Results (Figure 4.15C) showed a statistically significant difference ($t(4) = 5.027$, $p = 0.007$) between their attachment rates. This could be potentially explained by exposure of adhesive proteins found on the fungal cell wall (Klis et al., 2009) in the absence of capsule. Moreover, acapsular cells freely display their mannans and β-glucans (Cross and Bancroft, 1995) which promote phagocytic uptake via mannose receptor (Garcia-Aguilar et al., 2016; Ezekowitz et al., 1991) and dectin 1 (Brown and Gordon, 2001), respectively. Therefore, the increased in internalisation of CAP59 cells might be due to the increased accessibility of epitopes by phagocytic receptors on the macrophage surface, a mechanism also conjectured by Zaragoza (2019).

Meanwhile, I also analysed any differences in the total number of MΦ scored for each variant and found no statistically significant results (Figure 4.15D), indicating no significant variation in MΦ scoring across experimental repeats.
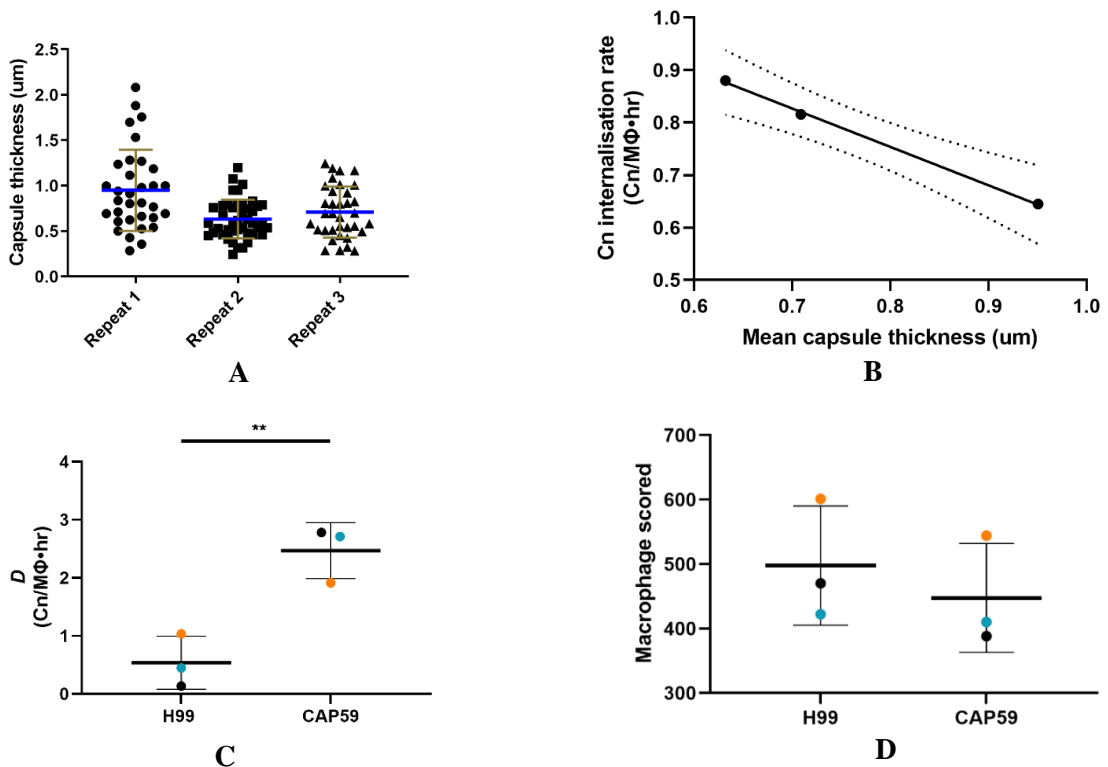
Figure 4.15 | Capsule thickness of H99 *C. neoformans* is negatively correlated to its phagocytic uptake by J774 macrophage-like cells. Immunofluorescence images of the phagocytosis assay from three independent repeats were used to manually measure capsule thickness of H99 cells, and compare it with their internalisation rate (table 4.8). Attachment rate and macrophage scored for each variant were also examined to account for uptake difference.

(A) There was statistically significant difference in the capsule thickness of internalised H99 cells across different experimental repeats as shown by ordinary one-way ANOVA ($F(2,108)$ = 9.767, p = 0.0001) bars: mean (M) ± standard deviation (SD), a post hoc analysis using Tukey's test (table 4.7) was done to further examine capsule thickness differences between bead repeats and determine statistically significant comparisons,

(B) There was negative correlation between capsule thickness and phagocytic uptake of H99 cells by J774 macrophages as shown by simple linear regression (R^2 = 0.999, p = 0.022,

y = -0.7317x + 1.339),

(C) Acapsular CAP59 cells had higher attachment rate than capsular H99 cells with J774 macrophages as revealed by unpaired t test ($t(4)$ = 5.027, **p = 0.007), n = 3 (each colour represents experimental repeat), bars: $M ± SD$,

(D) There was no statistically significant difference in the number of macrophages scored between H99 (M = 498, SD = 93) and CAP59 (M = 447, SD = 84) in examining results of

phagocytosis assay as confirmed by unpaired t test ($t(4) = 0.696$, $p = 0.525$), $n = 3$ (each colour represents experimental repeat), bars: $M \pm SD$

Dependent variable: Capsule thickness Alpha = 0.05				
Repeat comparison	**Mean Difference**	**95.00% CI of difference**	**Significant?**	**Adjusted p value**
Repeat (R)1 vs. R2	0.3185	0.1432 to 0.4938	Yes	0.0001
R1 vs. R3	0.2417	0.05796 to 0.4255	Yes	0.0064
R2 vs. R3	-0.07672	-0.2492 to 0.09572	No	0.5426

Table 4.7 | Tukey's multiple comparisons of capsule thickness of internalised Cryptococcal cells in different phagocytosis assay repeats

Variant	**Repeat 1**	**Repeat 2**	**Repeat 3**	**Mean internalisation rate**
H99	0.6447	0.8802	0.8158	0.7802
CAP59	1.7575	1.4086	1.5938	1.5866

Table 4.8 | Internalisation rate of capsular H99 and acapsular CAP59 Cn by J774 macrophage-like cells in different experimental repeats

4.9 Opsonisation enhances phagocytic uptake of *C. neoformans*

As previously seen in the uptake of spherical beads (section 4.5), opsonisation generally enhances the uptake of spherical targets. Thus, to investigate if this is also true for *C. neoformans*, I used 18B7 (Mukherjee et al., 1993) which is known to opsonise Cn serotypes A and D (Casadevall et al., 1998). In brief, H99 cells grown in YPD broth overnight were washed and resuspended in PBS. They were then incubated with 18B7 for an hour before performing phagocytosis assay with J774 macrophage-like cells.

Results (Figure 4.16) showed that opsonised H99 cells ($M = 136$, $SD = 15$) were taken up better than their unopsonised counterpart ($M = 25$, $SD = 21$) as revealed by unpaired t test ($t(4) = 7.403$, $p = 0.002$). This agrees with previous findings (Figure 4.7) predicting that an increase in phagocytic uptake would be expected in this size regime (~2 μm radius) of spherical target following opsonisation.

To determine whether the attachment rate of H99 cells to macrophages was changed after opsonisation, I estimated this for each type of H99 using equation 4.3 and changing the

coefficient to ½ as the assay period was 2 hours. Results (Figure 4.16B) showed no statistically significant difference between unopsonised and opsonised H99 cells. Lastly, I also examined any differences in the number of MΦ scored between each type during the analysis (Figure 4.16B) and found no statistically significant differences.
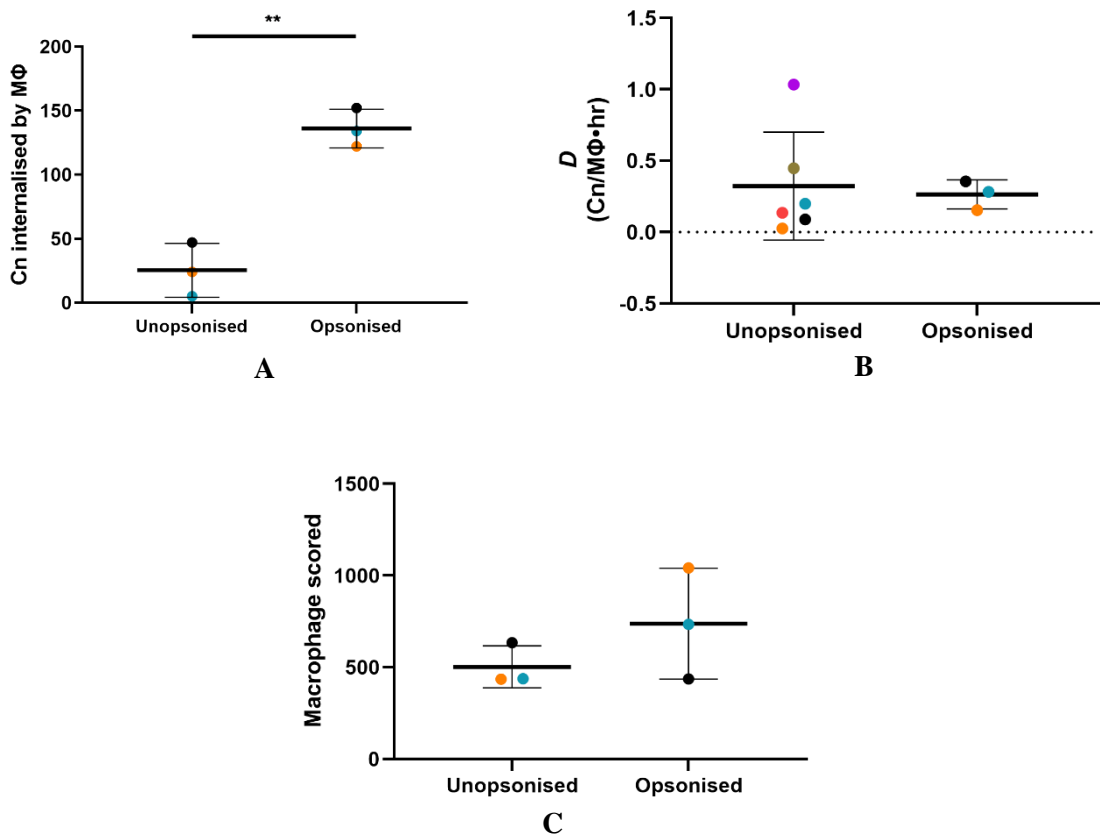
Figure 4.16 | Opsonised H99 Cn are taken up better by J774 macrophage-like cells than their unopsonised counterpart. An *in vitro* phagocytosis assay using unopsonised and 18B7-opsonised H99 was done using previous protocol (section 4.8, figure 4.12) with immunofluorescence microscopy. A triplicate for each condition was prepared, and three fields of view per replicate were imaged (a total of nine images per condition) starting at the centre of each coverslip. Each image was then scored for Cn internalised by MΦ, Cn attached to MΦ, MΦ in phagocytosis and total number of MΦ. Three independent experimental repeats were performed.

(A) There was statistically significant difference in Cryptococcal cells internalised by MΦ between unopsonised ($M = 25$, $SD = 21$) and opsonised ($M = 136$, $SD = 15$) H99 as confirmed by unpaired t test ($t(4) = 7.403$, $**p = 0.002$), $n = 3$ (each colour represents an experimental repeat), bars: mean (M) ± standard deviation (SD),

(B) No statistically significant difference was found in the attachment rate of unopsonised (*M* = 0.322, *SD* = 0.379) and opsonised (*M* = 0.264, *SD* = 0.102) H99 to J774 macrophage-like cells as shown by unpaired t test *t*(7) = 0.250, *p* = 0.810), *n* = 3-6 (each colour represents an experimental repeat), bars: *M* ± *SD*,

(C) No statistically significant difference was found in the number of macrophages scored between unopsonised (*M* = 502, *SD* = 114) and opsonised (*M* = 738, *SD* = 303) H99 during assessment of their phagocytic uptake as confirmed by unpaired t test *t*(4) = 1.261, *p* = 0.276), *n*=3 (each colour represents an experimental repeat), bars: *M* ± *SD*,

4.10 General Discussion

Phagocytosis is a dynamic cellular event that has evolved in innate immune cells as a fundamental mechanism of infection and homeostasis control. The striking mechanical properties of this process relying on the biophysical properties of the host cell to generate structures for target engulfment suggest that physical parameters should be considered to fully understand its dynamics. In this chapter, I presented our investigation on the role of size and surface properties in the phagocytic uptake of spherical targets. Using an improvised imaging approach, we determined that the optimal size in taking up spherical particles is 0.5 μm (radius). This strikingly corresponds to the size of most common bacteria (Kubitschek, 1969), suggesting that physical properties of the target might be an important aspect in the emergence of mechanical properties of phagocytosis during the course of evolution.

By specifically quantifying the uptake of spherical particles, we were able to illustrate trends in phagocytosis of spherical targets with respect to their size and surface properties. This is important to infer uptake of important spherical pathogens and its relation to infection outcomes. Furthermore, this is also relevant in designing microparticles to target immune cells for efficient drug delivery and other therapeutics.

Finally, we have shown an important application of our approach in understanding the relationship between the biophysical properties of the target to its phagocytic fate by probing the phagocytosis of fungal pathogen *Cryptococcus neoformans* by J774 cells. We have shown that capsule thickness rather than cell size determines the phagocytic uptake of *C. neoformans*. As revealed by our data in using polystyrene beads, opsonisation enhances the phagocytic uptake of spherical targets in Cryptococcus size range which was verified in our experiment. Overall, this study iterates the importance of accurately quantitating the effect of biophysical parameters in phagocytic uptake to fully understand its mechanics and make critical inferences.

4.11 Specific Discussions

This chapter investigated the biophysical underpinnings of phagocytosis using inorganic and organic spherical targets. As previously mentioned, amongst the important properties of phagocytosis is its dependence on the physical properties of the target. Phagocytosis is central to the roles of innate immune cells such as neutrophils, macrophages and dendritic cells in controlling infection and maintaining tissue homeostasis (Gordon, 2016). Hence, describing its fundamental properties is paramount in understanding cellular behaviour which might have greater implications in explaining disease outcome.

4.11.1 Using imaging to investigate phagocytosis *in vitro*

Imaging is amongst the important tools to investigate the properties of dynamic cellular processes such as phagocytosis. A simple yet reliable set-up to identify cellular features is particularly advantageous in examining phagocytic interactions of host cells with different types of target. In this chapter, I described a bespoke imaging set-up I used to illustrate the phagocytic uptake of spherical beads by J774 macrophage-like cells. A modified differential interference contrast (DIC) configuration which uses all common DIC components apart from the polariser was seen to be useful in profiling bead localisation with respect to macrophages ($M\Phi$). Features of the macrophage membrane, such as the possession of ridges, were used to determine whether beads were internalised by macrophages or not. However, this set-up was not without any imaging drawbacks. A halo was found to become more pronounced as the focus is shifted away from the cell body. This is believed to be due to the attenuation of low spatial frequency wavefronts diffracted by the specimen, and the absence of destructive interference between undeviated light waves and these low spatial frequencies (Murphy et al., 2021). To rectify this, most spatial frequencies from the specimen must be captured (Murphy et al., 2021), thus I made sure that the main body of $M\Phi$ was in focus throughout imaging experiments.

I also used bead fluorescence to discriminate them from spherical features within the cell such as intracellular vesicles. However, due to the proportionality of bead fluorescence along the optical axis to its size (Kunding et al., 2008), small beads are most likely to be missed when imaging a single optical section. Thus, I used multiple z stacks to profile small beads and accurately determine their localisation after the assay.

4.11.2 Settling of spherical particles *in vitro*

The phagocytosis assay I set-up requires incubation of seeded J774 $M\Phi$ in a 24-well plate with bead suspension of different sizes. Hence, I examined any differences in the settling

of bead particles which might affect target availability and, subsequently, the results of phagocytosis assay.

Results revealed statistically significant differences in settling of beads with different sizes for both unopsonised and opsonised types, confirming size effect on settling of spherical particles as previously reported (Gibbs et al., 1971; Ayoub et al., 1983). For small spheres, settling velocity in a fluid medium can be estimated using the Stoke's equation (Polysciences, 2016):

$$V = 2ga^2(\rho_1 - \rho_2)/9\eta \qquad\qquad (4.6),$$

where V is the settling velocity, g is the acceleration of gravity, a is the particle radius, ρ_1 is the density of the particle, ρ_2 is the density of suspending media, and η is the coefficient of viscosity. Assuming all parameters are constant in the experimental set-up, this equation predicts a quadratic growth in bead settling with respect to size. This might be true for opsonised beads (Figure 4.6F); however, for unopsonised ones (Figure 4.3H), increase in settling appears to reach a peak at 1 μm (radius) which gradually slows down thereafter. If the Stoke's principle is applied, which is assumed to be true for particles less than 50 μm (Rhodes, 2017), this would predict higher settling velocity at increasing particle size that could lead to higher settling rate. The contribution of particle size to the viscosity of the system is very minimal compared to its solid fraction (Pavlik, 2009; Konijn et al., 2014). Thus, other factors that explain the behaviour of particles in this size range, such as Brownian motion (Einstein, 1956), size distribution variability (Rhodes, 2017) and hindered settling effect (Dey et al., 2019) might be important to explore to understand settling of unopsonised beads *in vitro*. Nevertheless, this allowed us to determine bead settling as an important variable to consider in examining the phagocytic uptake of different bead sizes by MΦ *in vitro*.

4.11.3 The role of target size in phagocytosis of spherical particles

After examining the settling of beads used in the experiment, I then explored how they are taken up by MΦ with respect to their size. Results revealed size dependence in phagocytic uptake, with smaller beads (≤ 1μm) generally taken up better than larger ones. I then examined if these could be possibly explained by differences in target attachment to MΦ. Results showed no statistically significant difference in the attachment of MΦ to different bead sizes which had statistically significant difference in uptake. However, the equation used to derive bead attachment did not consider particle detachment. Cell-target adhesion during

phagocytosis is believed to be mainly mediated by weak, noncovalent molecular interactions between the membrane receptor and the target (Heinrich, 2015), which could result in detachment of the target when the bonds formed are not strong enough. On the other hand, the geometry and the size of the target is also reported to be important in sustaining its engagement with the host cell. A previous study proposed that the shape of the particle determines the complexity of actin structure that must be created to initiate phagocytosis and expand the membrane around the target (Champion and Mitragotri, 2006). Furthermore, previous reports showed that uptake of large (≥ 3 μm radius) particles is dependent on myosin which implies more complex mechanics in taking up larger particles. Barger (2019) and colleagues showed that class 1 myosins- myosin 1e and myosin 1f, colocalise with membrane receptors to mediate important actin processes during phagocytic uptake such as actin adhesion to the membrane and actin polymerisation. This agrees with the theoretical model proposed by Herant (2006) and collaborators which requires the interaction between the membrane and actin cytoskeleton for successful internalisation. Meanwhile, Swanson (1999) and colleagues showed that other types of myosins - myosin Ic, II, V and IXb could be found in a developing phagocytic cup. Myosin Ic appears at later stage during closure of the phagocytic cup, which led to a notion of it being important during contraction to close the phagocytic cup and internalise the target (Swanson et al., 1999). Indeed, the final stages of a frustrated phagocytosis model identified the important role of myosin during late-stage contraction events (Kovari et al., 2016) which suggests a more complex mechanical requirement in taking up larger particles. Taken together, we can predict that extremely small beads with high curvature and extremely large beads with large surface area would have lower uptake than those beads with intermediate size due to the required membrane bending energy to initiate the uptake of the former whilst a high extension energy to complete the uptake of the latter. However, our showed that small (≤ 1 μm) unopsonised beads generally have the highest uptake by MΦ, suggesting that bending energy might not be relevant in this type of phagocytic target/MARCO receptor and size regime. Lower uptake for smaller beads (0.25 μm vs 0.5 μm radii) was only seen after bead opsonisation with IgG, suggesting curvature effect might only be important in this type of target.

To possibly explain the target size dependence of phagocytic process, we used an *in silico* model of actin growth during phagosome formation. Actin is essential to generate the force required to internalise a phagocytic target (Herant et al., 2006); thus, we hypothesised that increase in particle size would increase the engulfment time due to the physical requirements of wrapping the target with an actin-rich phagosome for its successful internalisation. Subsequently, this would decrease phagocytic uptake at increasing size of a spherical target which would lead to a size-dependent feature. Our model predicted non uptake

of the largest spherical particle considered (3 μm radius) within the simulation period of 60 seconds, suggesting that target size influences the phagocytic uptake of spherical particles. Interestingly, this corresponds to the bead size that was taken up the least in both unopsonised and opsonised phagocytosis assay experiments. However, it did not completely recapitulate the trends seen *in vitro*. Aside from having only one repeat, this was accounted to other caveats, as previously mentioned (4.6), and more importantly this highlights complexities of phagocytosis as a mechanical process.

4.11.4 Opsonisation enhances phagocytic uptake

Modifying the surface of spherical beads by coating with IgG antibody was shown to significantly increase the phagocytic uptake of almost all bead sizes. This suggests that Fc-receptor mediated phagocytosis is more efficient in taking up spherical targets than MARCO within this size range. Our results also revealed the dominant effect of particle opsonisation over particle size, indicating that the type of receptor is more significant than particle size in determining the phagocytic uptake of spherical targets within this size range. This highly efficient phagocytosis via Fc receptor could be possibly due to the high number of Fc receptor variants expressed in phagocytes (Mellman et al., 1988). These receptors can act synergistically for more efficient binding and internalisation of different phagocytic targets (Konderman, 2019). For instance, the receptor FcγRIIIb was found to have strong adhesion to IgG opsonised particles that are internalised via FcγRIIa (Williams et al., 2000). Furthermore, Fc receptors can interact with other types of membrane receptor such as integrins (Ortiz-Stern and Rosales, 2003) and toll-like receptors (van Egmond et al., 2015) to further enhance phagocytic activities. The mechanistic process of taking up unopsonised particles through MARCO (Arredouani et al., 2005; Kobzik, 1995) on the other hand is poorly understood. A single naturally occurring variant called MARCOII was reported but does not seem to cooperate in phagocytic uptake (Novakowski et al., 2016).

Our data can also be used to infer the phagocytic uptake of spherical pathogen of certain size according to the dominant receptor present in the phagocyte membrane as will be discussed in the next subsection. Finally, to our knowledge, analysis of mechanistic differences in phagocytic uptake of spherical particles with different sizes via different receptors had not been reported. Previous studies (Pacheco et al., 2013; Champion et al., 2008; Tabata and Ikada, 1990; Kawaguchi et al., 1986) have shown the size-dependence of spherical particle uptake by macrophages with varying conclusions on optimal size for uptake. Bead radius of 0.25 μm (Pacheco et al., 2013), 1.5 μm (Champion et al., 2008) and 1 μm (Tabata and Ikada, 1990) were reported to be taken up the most by MΦ. However, the different

methods used such as flow cytometry (Pacheco et al., 2013; Champion et al., 2008) and an ill-defined set-up (Tabata and Ikada, 1990) do not allow direct comparisons with our data.

4.11.5 Capsule possession and not cell size determines the phagocytic uptake of *C. neoformans*

After illustrating the effect of size and surface properties in the phagocytic uptake of inorganic polystyrene beads, I then used these results to infer the uptake of a spherical pathogen, *C. neoformans,* by MΦ. Using capsular H99 and acapsular CAP59 variants, I compared their cell sizes and found no statistically significant difference (Figure 4.12G). Additionally, there was no size preference in the phagocytic uptake of cells within these variants (Figure 4.14B and 4.14C). This could be potentially explained by looking at the size effect in phagocytic uptake of spherical targets (Figure 4.7F). A size range between 1.5 and 3μm seem to have very small differences in uptake for both unopsonised and opsonised spherical targets. This indicates that particles within this size range, such as Cryptococcal cells (2.2 – 2.6 μm), might not show any differences on their phagocytic uptake as seen in our results.

On the other hand, comparing the phagocytic uptake of H99 and CAP59 by MΦ showed a statistically significant lower uptake of H99 than its acapsular counterpart. Having no significant size difference, the physical feature that could explain these results is the possession of capsule. Thus, I analysed the capsule size measurements from different experimental repeats and remarkably found statistically significant differences. Capsule growth is a highly sensitive process which is reported to be influenced by various factors such as CO_2 concentration (Granger et al., 1985), iron availability (Vartivarian et al., 1993), culture media composition (Zaragoza and Casadevall, 2004) and age of the cell (Charlier et al., 2005, Zaragoza et al., 2006). Though the exact source of capsule size variation in my experiment was not identified, these findings of capsule sensitivity to a multitude of internal and external factors would suggest that capsule size variation is very common in *in vitro* experiments.

Using the acquired capsule measurements, I examined any relationship of capsule thickness to phagocytic uptake of H99 cells. Statistical analysis revealed a highly significant negative correlation between capsule thickness and H99 uptake by MΦ, validating previous reports of an anti-phagocytic role of its capsule.

The physical mechanism by which capsule inhibits phagocytic uptake is not fully understood. The most straightforward explanation is that it masks crucial phagocytic receptors hence preventing uptake (Kozel and Gotschlich, 1982). However, capsule is a highly regulated

and dynamic structure whose physical properties are affected by different environmental and intrinsic cellular variables as previously stated. For instance, *in vitro* experiments of Feldmesser (2000) and co-workers showed that capsular Cn are taken up as much as their acapasular counterpart by J774 macrophage-like cells. The capsular variant used in their experiment, 3501 serotype (D), is however different from the one we used, H99 serotype (A), and consequently the media and growth conditions they applied. Our equation (eq. 4.5) predicts that even a slight (~hundreds of nanometre) reduction of capsule thickness below 0.7 um would enhance the phagocytic uptake of Cn. These suggest a very likely difference in capsule thickness between the serotypes used in our experiment and that of Feldmesser (2000) and colleagues which led to different conclusions.

4.11.6 Opsonisation enhances the phagocytic uptake of *C. neoformans*

I then examined how opsonisation will affect the phagocytic uptake of Cn. Using the bead uptake data according to size (Figure 4.7F), we can infer an increase in Cn uptake following opsonisation. Indeed, our data showed a 5-fold increase in H99 uptake after being opsonised (Figure 4.16A). Phagocytic uptake of Cn is known to be enhanced by opsonins such as monoclonal antibodies (Nussbaum et al., 1997) and complement proteins (Taborda and Casadevall, 2002). However, this is a nonlinear relationship that reaches a maximum concentration thereafter due to receptor saturation (Macura et al., 2007).

On the other hand, very little is known about the uptake of unopsonised Cryptococcus. Due to the inhibitory effect of their capsule (Kozel, 1977;Kozel and Gotschlich, 1982), it was presumed that there is essentially no uptake in the absence of opsonins (Casadevall et al., 2019). However, a report showed that the scavenger receptor MARCO plays an important role in their phagocytic uptake and control of infection (Xu et al, 2017). MARCO, as previously described, is used in the uptake of unopsonised particles including beads, titanium oxide, ferric oxide, silicon dioxide and other dust particles in the environment (Palecanda et al., 1999; Kobzik, 1995). It is therefore not surprising that it is mostly expressed in the lungs as revealed by transcriptomic data of more than 20 human organs (Fagerberg et al., 2014). Moreover, amongst the different types of scavenger receptor expressed by alveolar macrophages, MARCO was found to play the most important role in binding with unopsonised particles and bacteria (Arredouani et al., 2005). Taken together, these findings suggest that in the absence of antibodies and complement proteins in the lungs, a MARCO-mediated uptake of Cn serves for their internalisation which, as our data predict, would lead to a poor phagocytosis outcome with respect to their size and surface composition.

4.12 Conclusions and future work

We have shown in this study that size and surface properties of the target are important parameters in understanding phagocytosis. Our robust quantitative data that represent the roles of these variables in phagocytosis of spherical targets was found to be useful in predicting the phagocytic uptake of *C. neoformans* by macrophages *in vitro*. However, there are areas worth exploring to gain a better understanding of the mechanical properties of phagocytosis. Firstly, we have no accurate picture of the density and actual arrangement of actin filaments during phagocytic uptake. Very recent studies showed the presence of podosomes in Fc-receptor mediated phagocytosis (Tertrais et al., 2021; Ostrowski et al., 2019) which creates a diffusional barrier that concentrates key signalling molecules. This might be an important difference between unopsonised and opsonised bead uptake as it was shown that the architecture of phagosome-associated podosomes is target-dependent and found only with IgG opsonised particles (Tertrais et al., 2021). But how the actin is organised during phagocytosis and what causes the size dependence in uptake are still unclear. Secondly, there is no current consensus on the role of myosin in phagocytosis. Works using large (> 3 μm radius) particles showed that myosin is important during uptake (Barger et al., 2019), which is presumed to have an important role in contraction to close the phagocytic cup (Vorselen et al., 2020). However, other studies reported that myosin has limited effect in phagocytosis (Rotty et al., 2017) and has no role in increasing the effective membrane tension during the uptake (Masters et al., 2013). Finally, the role of capsule thickness in phagocytosis of *C. neoformans* requires further investigation. Additional data might allow us to test the polymer physics-based model equations developed by our physics collaborators (unpublished) that explains the role of capsule in masking ligands during phagocytosis of Cn. The physical properties and dynamics of capsule during interaction with phagocytes *in vivo* will be essential to further our understanding of host-pathogen interactions and outcomes of Cryptococcal infection.

CHAPTER 5

The dynamics of the membrane and actin cytoskeleton of macrophages during infection with *Cryptococcus neoformans*

5.1 Introduction

Cryptococcal infection is amongst the most important invasive human fungal infections with an estimated annual global cases of over 200,000 (Rajasingham et al., 2017). The causative agent, *Cryptococcus* spp., is a remarkable pathogen, both morphologically and mechanistically, on its means of interacting and surviving within the host's immune cells. *Cryptococcus* is known to have developed strategies that allow it to proliferate within macrophages (Evans et al., 2019; Bojarczuck et al., 2016; Feldmesser et al., 2001) and escape from the phagosome following phagocytosis (Alvarez and Casadevall, 2006; Ma et al., 2006). Furthermore, manipulation (Smith et al., 2015) and permeabilisation (Tucker and Casadevall, 2002; Johnston and May, 2010) of phagosomes containing Cryptococcus are also reported, suggesting a complex interplay between Cryptococcus and host cell during infection.

As described in the previous chapter (Chapter 3), macrophages (MΦ) are highly dynamic immune cells that possess a multitude of physical and functional properties. They are amongst the first line of defence during microbial infection, and their interaction with Cryptococcus is believed to be crucial in determining disease outcome (Pline, 2019; Bojarczuck et al., 2016; Johnston and May, 2013). This was particularly seen during their experimental depletion in a zebrafish model which caused accelerated fungal infection and increased mortality (Bojarczuck et al., 2016). Thus, changes in MΦ during interaction with Cryptococcus should be carefully dissected to understand the complexities of Cryptococcal infection and cellular mechanisms of host-pathogen interaction.

In this chapter, I will present my findings on investigating MΦ critical structures, cell membrane and actin cytoskeleton during their interaction with *Cryptococcus neoformans*. Using scanning electron microscopy (SEM), fluorescence microscopy and image analysis, I will compare the geometrical properties and dynamics of two dominant MΦ membrane features, membrane ridges and dorsal ruffles, in early stages of Cryptococcal infection. I will then describe salient changes in actin cytoskeleton of MΦ during infection and correlate these changes with the membrane features they possess. Finally, I will illustrate the importance of actin-rich membrane protrusions of MΦ in their physical interaction and phagocytic uptake of *Cryptococcus neoformans*.

5.2 Macrophages possess distinct membrane features during *in vitro* infection with *Cryptococcus neoformans*

As shown in the previous chapter (Chapter 3), the membrane surface of MΦ cultured *in vitro* is characterised by a high density of nanoscopic sheet-like protrusions I called membrane ridges. I first examined any changes in MΦ surface properties with respect to these structures during infection with *C. neoformans* (Cn).

J774 macrophage-like cells were seeded into a 24-well plate and allowed to acclimatise overnight. On the following day, they were incubated with H99 Cn for 0, 30 and 120 minutes. Samples were then fixed and processed for SEM to examine membrane features of MΦ at each timepoint.

Results (Figure 5.1) showed that the surface of MΦ had notably distinct features at each infection timepoint. At 0 minute post infection and as expected, a predominance of membrane ridges could be seen on the MΦ surface (Figure 5.1A, 5.1D green arrow). These were then replaced by giant dorsal ruffles (Figure 5.1B and 5.1E green arrow) 30 minutes post infection (PI); whilst the most dramatic change was seen 120 minutes PI where tail-like (Figure 5.1F green arrow) and bleb-like (yellow arrow) structures became prominent surface features of these infected cells. Incubation with beads (data not shown) was also carried out at similar timepoints, but this did not result in any surface changes in MΦ showing persistence of ridges throughout the course of incubation.

I next examined the geometrical properties of these dorsal ruffles and compared them with membrane ridges. Using the ridge detection (RD) image analysis described in the previous chapter (section 3.4), I profiled the thickness and length of dorsal ruffles produced by MΦ upon exposure to H99 Cn. Results (Figure 5.2B) showed that dorsal ruffles of these cells had an average thickness of 218 nm ($SD = 40$) which was significantly higher (Figure 5.2F, $p < 0.0001$) than membrane ridges ($M = 142$ nm, $SD = 24$). On the other hand, the average length of dorsal ruffles (1,300 nm) was also found to be significantly greater (Figure 5.2E, $p = 0.0004$) than ridges (820 nm).

Apart from differences in their geometrical properties, I also compared these structures with respect to their lifetime dynamics, architecture and stimulation (summarised in table 5.2). As seen in the previous chapter (section 3.8), ridges have a relatively simpler life cycle characterised by emergence from the membrane surface and growth on their opposite ends before collapsing back to the surface. On the other hand, dorsal ruffles have a more complex behaviour which tend to form a circle (circularise) from top view, their ends meeting to form a macropinocytic cup followed by constriction and membrane fusion to form an endocytic vesicle called macropinosome (Condon et al., 2018).

Membrane ridges have also simpler architecture than ruffles which is formed by a single sheet-like body without any structural derivatives whilst dorsal ruffles can produce secondary structures such filopodia and membrane ridges on their bodies. Finally, ridges do not usually require induction signals for their production whilst generation of dorsal ruffles is commonly induced by LPS, M-CSF and PMA (Patel and Harrison, 2008; Yoshida et al., 2015).

A

B

C

D

E

F
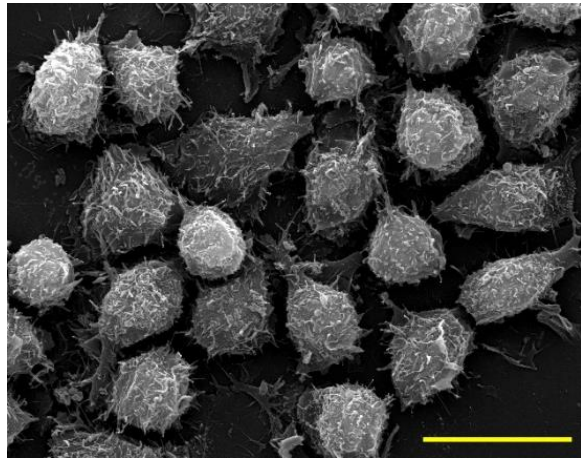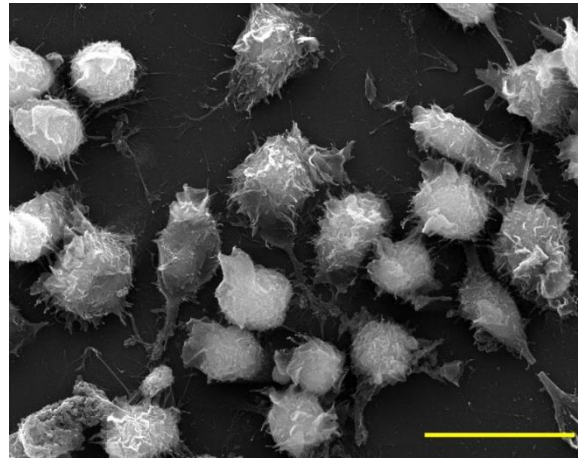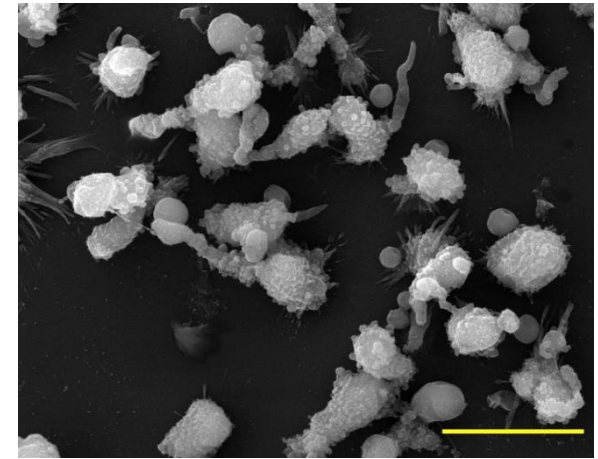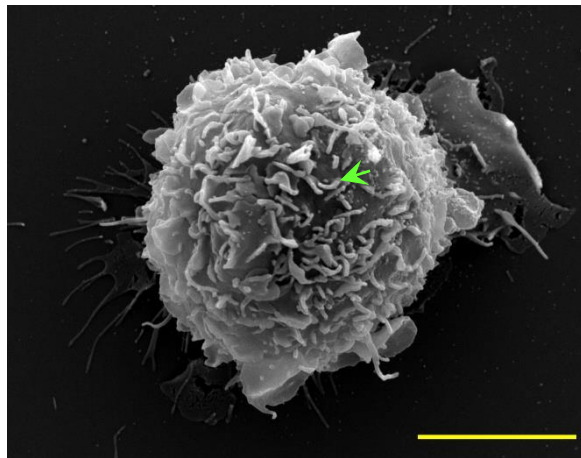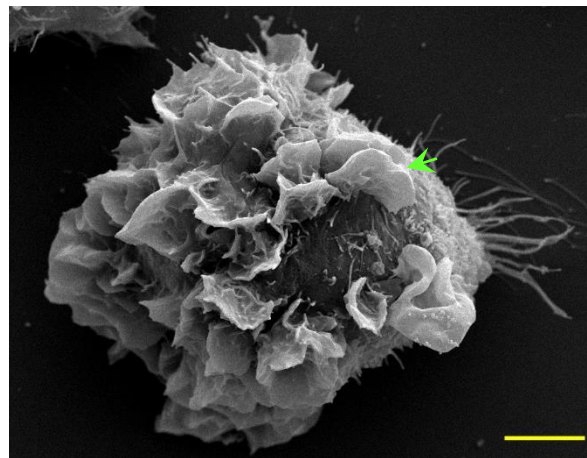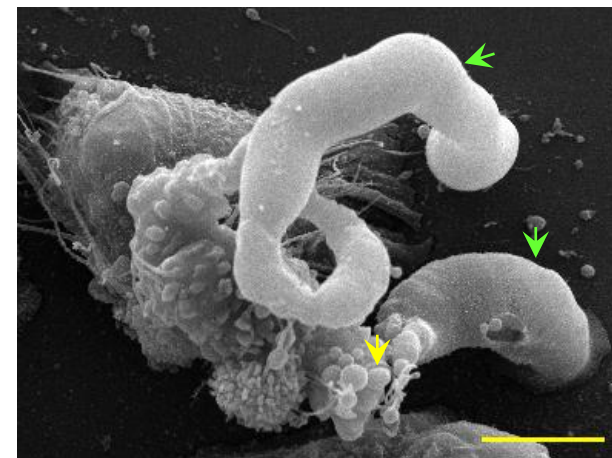
(Figure legend on next page)

Figure 5.1 | *In vitro* **infection of macrophages with** *Cryptococcus neoformans* **is marked by distinct changes in the macrophage membrane surface.** A healthy culture of J774 macrophage-like cells was seeded into 24-well plate with glass coverslip overnight. They were then incubated with H99 *C. neoformans* (Cn) at 0, 30 and 120 minutes timepoints. Samples were then fixed, processed for SEM examination and imaged using a high vacuum, thermionic emission scanning electron microscope with SE detector system at 10 kV accelerating voltage, 9 mm working distance, 63 nm spot size and 0° stage tilt. Images are a representative of more than 100 imaging frames from 3 independent *in vitro* infection experiments.

(A) An SEM image of J774 cell population *in vitro* after infection with H99 Cn at 0 minute, **(B)** 30 minutes and **(C)** 120 minutes,

(D) Single cell SEM imaging of J774 cells showing the most common surface features observed after infection with H99 at 0 minute: membrane ridges (green arrow), **(E)** 30 minutes: dorsal ruffles (green arrow) and **(F)** 120 minutes: tail-like protrusion (green arrow) and bleb-like structure (yellow arrow). Image scale bar: **A-C** – 20 μm; **D-F** – 5 μm.

A

B

C

D

E

F
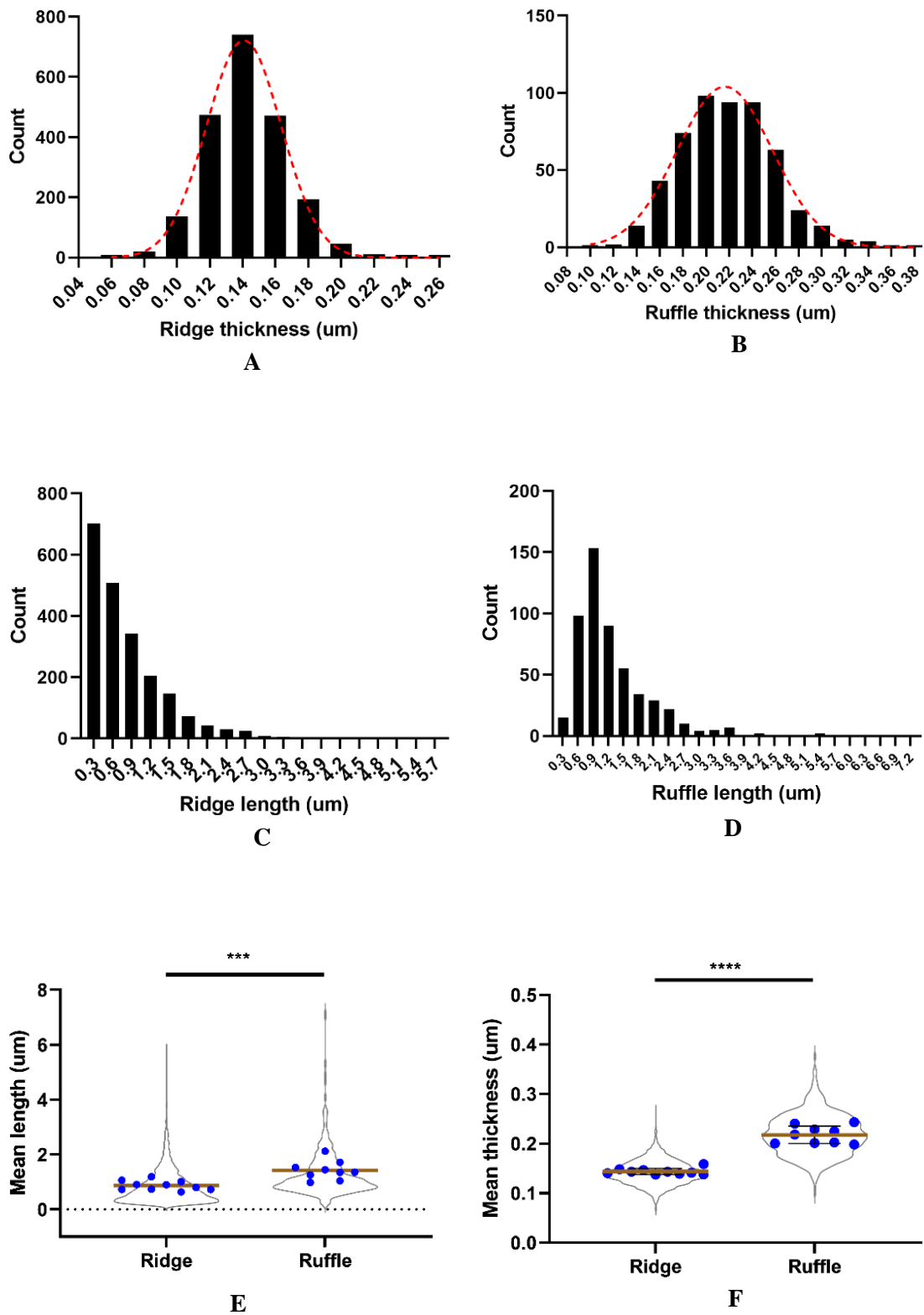
(Figure legend on next page)

Figure 5.2 | Membrane ridges can be distinguished from dorsal ruffles by their geometrical properties. Single cell SEM images of J774 macrophage-like cells producing ridges or ruffles were examined using the image processing routine described in the previous section (3.4). Nine to twelve cells from three independent experimental repeats were used to measure thickness and length of membrane ridges and dorsal ruffles of J774 cells.

(A) A combined thickness histogram of all membrane ridges of J774 cells examined with a Gaussian fit (red curve) ($R^2 = 0.997$, $n = 10$ cells (2097 ridges), Mean (M) = 0.142, standard deviation (SD) = 0.024),

(B) A combined thickness histogram of all J774 dorsal ruffles examined with a Gaussian fit (red curve) ($R^2 = 0.987$, $n = 9$ cells (531 ruffles), $M = 0.218$, $SD = 0.040$),

(C) Combined length histogram of all J774 membrane ridges profiled ($n = 10$ cells (2097 ridges), skewness (g_1) = 1.962, median = 0.648, the rest of descriptive statistics are shown in table 5.1),

(D) Combined length histogram of all J774 dorsal ruffles profiled ($n = 9$ cells (531 ruffles), skewness (g_1) = 2.619, median = 1.048, the rest of descriptive statistics are summarised in table 5.1),

(E) Dorsal ruffles (Median = 1.360) were significantly longer than membrane ridges (Median=0.852) as confirmed by Mann-Whitney test (n = 9-10 mean length values, ***$p = 0.0004$), bar: median,

(F) Dorsal ruffles ($M = 0.218$, $SD = 0.018$) were significantly thicker than membrane ridges ($M = 0.144$, $SD = 0.006$) as revealed by unpaired t-test ($t(17) = 12.35$, ****$p < 0.0001$), n = 9-10 mean thickness values, bars: $M \pm SD$.

	Membrane ridge	Dorsal ruffle
Number of values	2098	531
Minimum	0.159	0.205
25% percentile	0.375	0.782
Median	0.648	1.048
75% percentile	1.067	1.584
Maximum	5.798	7.187
Range	5.639	6.982
Mean	0.821	1.300
Std. deviation	0.622	0.847
Std. error of mean	0.014	0.037
Skewness	1.962	2.619

Table 5.1 | Comparison of length distribution between membrane ridges and dorsal ruffles

218

Criterion	Membrane ridge	Dorsal ruffle
Thickness	142 ± 23 nm	218 ± 40 nm
Length	820 nm	1300 nm
Life cycle dynamics	Does not usually circularise nor fuse at their extreme ends	Circularises and forms a macropinocytic cup before collapsing back to the membrane surface (Condon et al., 2018)
Can generate other types of membrane protrusion?	No	Yes, filopodia are commonly found on their edges whilst membrane ridges are typically seen on their main body
Known stimulants/ activation factors	Does not usually require any induction signal for its production in differentiated phagocytes	Commonly requires LPS, M-CSF and PMA to induce expression (Patel and Harrison, 2008; Yoshida et al., 2015)

Table 5.2 | Comparative summary of membrane ridges and dorsal ruffles of macrophages

5.3 Production of membrane ridges shows an opposite trend to generation of dorsal ruffles in the first 30 minutes of infection

I next estimated the amount of membrane ridges and dorsal ruffles produced by J774 cells exposed to Cn at different infection timepoints. J774 cells that were acclimatised overnight in a 24-well plate were incubated with capsular H99 or acapsular CAP59 Cn at 0, 5, 10, 20, 30, 60 and 120 minutes. Samples were then fixed at each timepoint and processed for SEM. Ten cells were randomly chosen and imaged for single cell SEM examination. The area density of their membrane ridges was computed using RD analysis and equation (3.2) whilst ruffles area density was obtained by manually tracing the border of each ruffle (Figure 5.3B) and using Fiji (Schindelin et al., 2012) to measure the total area enclosed by ruffles. In cases where both ridges and ruffles were present in a cell, ruffles were first isolated and measured. Each image was then reanalysed using RD to acquire ridge area density.

Results (Figure 5.3C and 5.3D) showed that ridge production in both H99 and CAP59 infected MΦ was drastically reduced in the first hour of infection. This was concurrent with a sharp increase in ruffle generation by these cells that reached a peak at 30 minutes PI in both

H99 and CAP59-infected MΦ. It is worth noting that this peak is almost at similar level with the maximum ridge area density at 0-minute PI (Figure 5.3C and 5.3D) and coincides with a low ridge density in H99-infected MΦ (Figure 5.3C) and lowest ridge density in CAP59-infected ones (Figure 5.3D). These suggest that ridges might potentially being used to generate dorsal ruffles. I also examined if Cryptococcus variant influenced ridge and ruffle densities at different infection timepoint. Results (table 5.3) showed that there was no statistically significant difference in ruffle production in all timepoints between variants ($F(1,23) = 2.072$, $p = 0.164$). Conversely, ridges (table 5.4) were found to be more repressed during CAP59 exposure than H99 ($F(1,131) = 46.51$, $p < 0.0001$). I also measured ruffle height and found that it was almost invariable throughout infection with H99 (Figure 5.3E) or CAP59 (Figure 5.3F) with a peak reaching 2.25 μm. Finally, ridge recovery seemed to occur at 120 minutes PI in both H99 and CAP59 infections, but this was not further investigated due to time constraint, hence I focussed on analysing structural changes in MΦ within the first 2 hours of infection.

I also noted that ridges and ruffles seemed to have inverse area densities up to 30 minutes PI in both H99 (Figure 5.3C) and CAP59-infected (Figure 5.3D) MΦ . This trend was more apparent in CAP59 than H99 infection. Moreover, ridge repression was more pronounced after CAP59 infection showing almost complete inhibition 30 minutes PI (Figure 5.3D). Taken together, these indicate that MΦ membrane surface changes in the presence of *C. neoformans* independent of capsule possession. The opposite trends of ridge and ruffle productions in early periods of *C. neoformans* infection potentially suggests a mechanism that converts membrane ridges to ruffles whereby ridges act as membrane and actin sources.

A

B

C

D

E

F
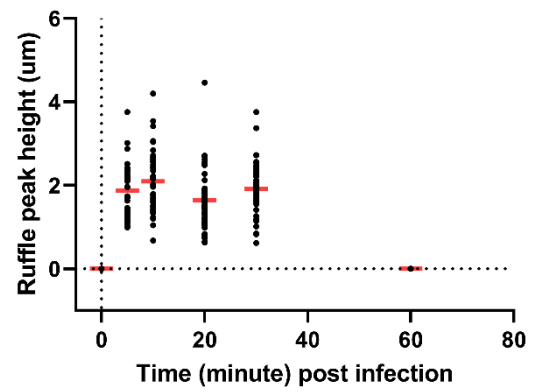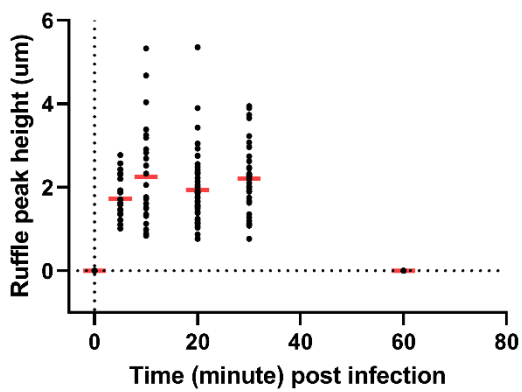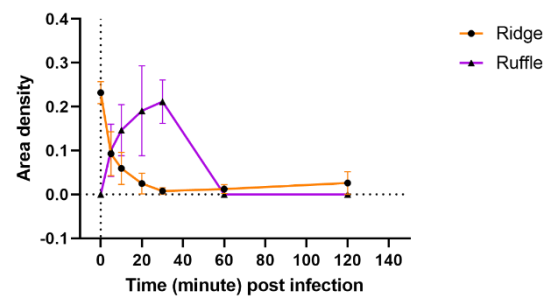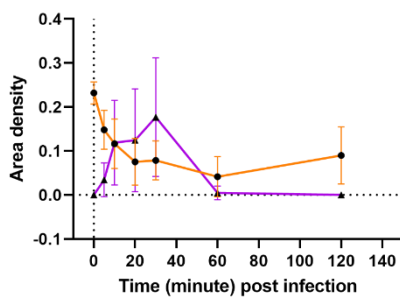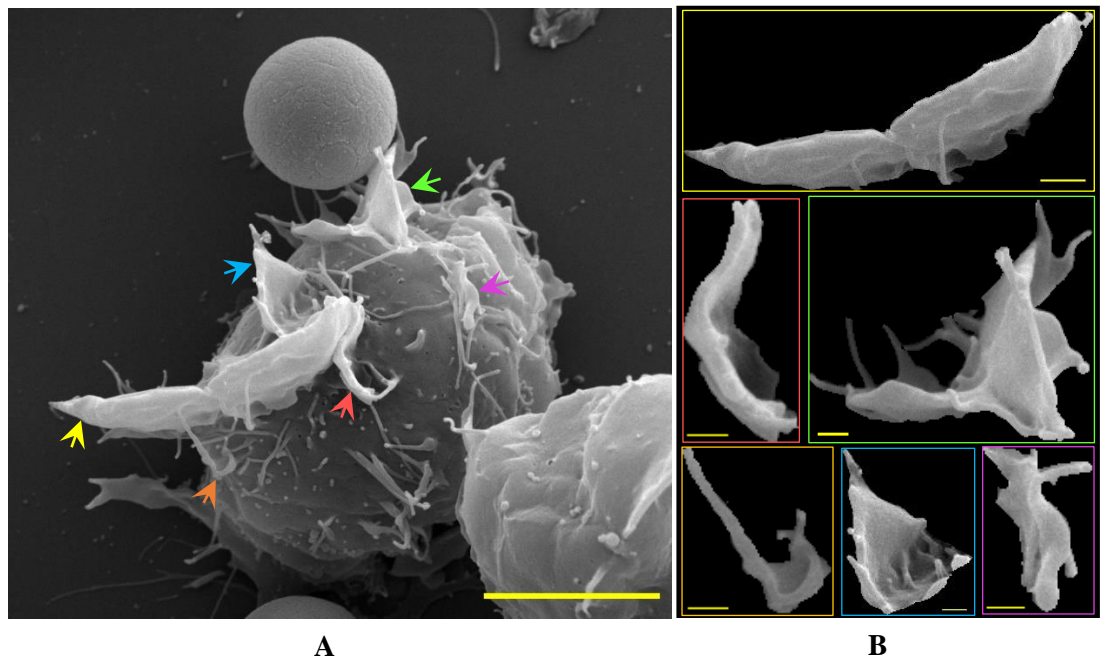
(Figure legend on next page)

Figure 5.3 | Membrane ridge and dorsal ruffle productions during *in vitro* infection with *C. neoformans* are highly dynamic and show opposite trends up to 30 minutes post infection. A healthy culture of J774 cells was seeded and allowed to acclimatise overnight in a 24-well plate with glass coverslip. They were then challenged with H99 or CAP59 Cn on the following day at 0, 5, 10, 20, 30, 60 and 120-minute timepoints. Samples were fixed and processed at each timepoint for SEM examination. Single cell SEM imaging was done using a high vacuum, thermionic emission scanning electron microscope with SE detector system at 10 kV accelerating voltage, 9 mm working distance, 63 nm spot size and 0° stage tilt. Image is a representative of more than 100 images taken from a single experimental repeat.

(A) An SEM image of CAP59-infected macrophage after 30 minutes showing extensive dorsal ruffle (arrows) production, scale bar – 5 μm,

(B) Manually isolated ruffles of *A* with colour-coded border according to colour of reference arrow in *A*, scale bar – 500 nm,

(C) Membrane ridge and dorsal ruffle production by MΦ showed opposite trends within the first 30 minutes of H99 infection with ridge density declining abruptly simultaneous with sharp increase in ruffle density, $n = 10$-15 cells per timepoint, points: mean (*M*), bars: standard deviation (*SD*), post hoc analyses using Sidak's test (table 5.3 and 5.4) were carried out to determine any effect of Cryptococcus variant in ridge and ruffle production of MΦ at different timepoints.

(D) Infection with CAP59 Cn also showed similar trend with H99 infection but displayed a much clearer inverse relationship between MΦ ridge and ruffle productions within the first 30 minutes of infection, $n = 10$ cells per timepoint, points: *M*, bars: *SD*,

(E) There was no statistically significant difference in the height of dorsal ruffles produced by macrophages across different timepoints of H99 infection as shown by Kruskal-Wallis test ($H(4) = 4.862$, $p = 0.182$), $n = 22$-46 ruffles, bars: *M*,

(F) There was statistically significant difference in the height of macrophage dorsal ruffles after CAP59 infection as revealed by Kruskal-Wallis test ($H(4) = 10.17$, *$p = 0.017$), $n = 31$-47 ruffles, bars: *M*, a post hoc analysis using Dunn's test (table 5.5) was done to further examine height differences between timepoints.

Dependent variable: Ruffle area density (um) Alpha = 0.05				
Time post infection (minute)	**Predicted (LS) mean difference**	**95.00% CI of difference**	**Significant?**	**Adjusted p value**
0	0.006876	-0.07843 to 0.09218	No	>0.9999
5	-0.05903	-0.1443 to 0.02628	No	0.3589
10	-0.02030	-0.1056 to 0.06500	No	0.9939
20	-0.06607	-0.1440 to 0.01187	No	0.1468
30	-0.02772	-0.1130 to 0.05759	No	0.9638
60	0.01177	-0.07354 to 0.09708	No	0.9998
120	0.006876	-0.07843 to 0.09218	No	>0.9999

Table 5.3 | Sidak's multiple comparisons of ruffle area density between H99- and CAP59-infected MΦ at each infection timepoint

Dependent variable: Ridge area density (um) Alpha = 0.05				
Time post infection (minute)	**Predicted (LS) mean difference**	**95.00% CI of difference**	**Significant?**	**Adjusted p value**
0	0.000	-0.04983 to 0.04983	No	>0.9999
5	0.05532	0.005494 to 0.1051	Yes	0.0207
10	0.05678	0.006952 to 0.1066	Yes	0.0162
20	0.05041	0.004923 to 0.09589	Yes	0.0211
30	0.07087	0.02104 to 0.1207	Yes	0.0012
60	0.02891	-0.02091 to 0.07874	No	0.5788
120	0.06365	0.01382 to 0.1135	Yes	0.0047

Table 5.4 | Sidak's multiple comparisons of ridge area density between H99- and CAP59-infected MΦ at each infection timepoint

Dependent variable: Ruffle height (um) Alpha = 0.05			
Timepoint comparison	**Mean rank difference**	**Significant?**	**Adjusted p value**
5 minutes vs. 10 minutes	-14.62	No	>0.9999
5 minutes vs. 20 minutes	16.74	No	0.7620
5 minutes vs. 30 minutes	-4.785	No	>0.9999
10 minutes vs. 20 minutes	31.35	Yes	0.0119
10 minutes vs. 30 minutes	9.830	No	>0.9999
20 minutes vs. 30 minutes	-21.52	No	0.1779

Table 5.5 | Dunn's multiple comparisons test of ruffle height of CAP59-infected J774 cells at different timepoints

5.4 Membrane surface changes in MΦ during Cn infection are also accompanied by changes in their actin cytoskeleton

To illustrate the physical features of MΦ actin cytoskeleton during Cn infection, I performed a fluorescence imaging experiment labelling actin filaments with phalloidin-TRITC to examine their spatial organisation. Briefly, J774 cells that were seeded overnight into a 24-well plate were incubated with either H99 Cn for 30 and 120 minutes or 1 μm beads for 120 minutes. These timepoints were chosen as dramatic changes in MΦ membrane surface during Cn interaction were seen at these periods (Figure 5.1E and 5.2F), and I hypothesised that MΦ cytoskeleton was also modified during these events. Samples were then fixed and processed for fluorescence imaging using a widefield microscope. Lastly, images were deconvolved (Ayers and Dainty, 1988) to improve visualisation of MΦ actin structures.

Results showed that MΦ incubated with beads possessed similar actin features as uninfected cells, exhibiting actin ridges (Figure 5.4B and 5.4D yellow arrow) on their dorsalmost regions. Their actin cortices (Figure 5.4A and 5.4C green arrow) were also visible which confirmed their role in supporting cell shape. Meanwhile, the MΦ actin cytoskeleton 30 minutes PI with H99 (Figure 5.4E) displayed extensive ruffling (yellow arrow) which also formed a macropinocytic cup (Figure 5.4F yellow arrow). Ridges were rarely seen (Figure 5.4F) in these cells, confirming my previous findings of very low ridge density and peak ruffle expression at this timepoint (Figure 5.3C and 5.3D). After 2 hours of H99 incubation, MΦ cortical actin (Figure 5.4G and 5.4H green arrow) became more distinct showing a more well-defined boundary around each cell. The cells were found to become more elongated than control (uninfected) cells (Figure 5.4A) verifying SEM findings (Figure 5.1C). Furthermore, tail-like features (Figure 5.4G red arrow) seen in previous SEM examination (Figure 5.1F green arrow) were also seen in these cells, which were found to possess an actin filament border. Finally, membrane ridges were rarely seen in these cells (Figure 5.4H) whilst ruffles were occasionally found (yellow arrow) and some actin puncta (Figure 5.4G yellow arrow) on the dorsal cell region.

A B C D

E F G H
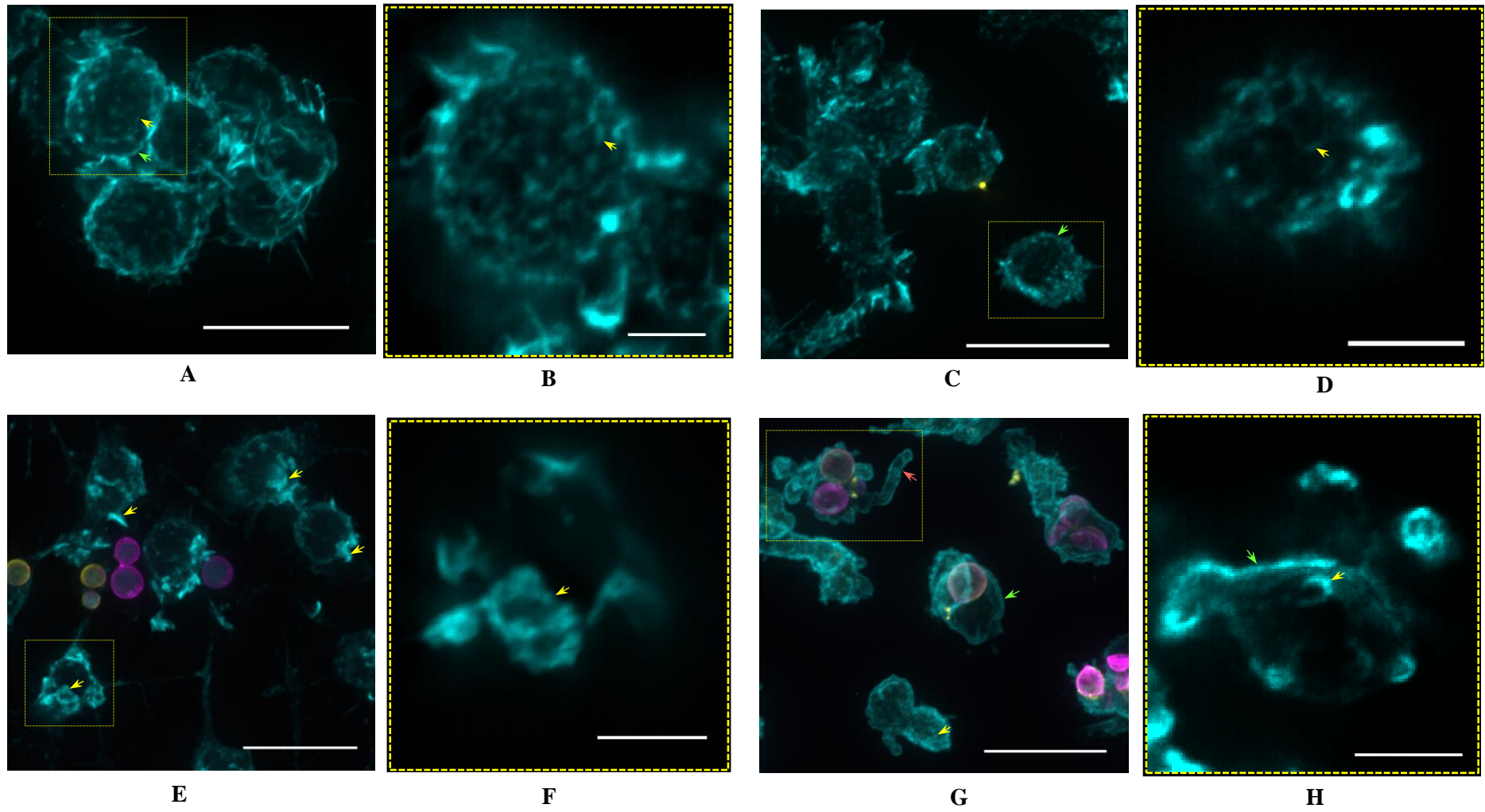
(Figure legend on next page)

Figure 5.4 | Changes in the macrophage actin cytoskeleton are also observed during *in vitro* infection with *C. neoformans*. A healthy culture of J774 macrophage-like cells was seeded into 24-well plate with glass coverslip overnight. They were then challenged with either 1-μm bead for 2 hours or H99 Cn for half an hour and 2 hours. Samples were fixed thereafter, permeabilised and incubated with phalloidin-TRITC to label the actin filaments, 18B7 and anti-mouse IgG-FITC to label the capsule and calcoflour white to label the cell wall. Imaging was done using a 60x oil immersion objective (1.4 NA Plan-Apo) in DAPI (excitation: 436/20 nm, emission: 480/40 nm), GFP (excitation: 470/40 nm, emission: 525/50 nm) and Cy3 (excitation: 545/25 nm, emission: 605/70 nm) channels of a widefield microscope. Images were blindly deconvolved using NIS Elements deconvolution software. Images are a representative subsection of 277 x 234 μm widefield images from 90 imaging frames of 3 independent experimental repeats.

(A) Maximum intensity projection of actin filaments of unchallenged (negative control) J774 cells showing its actin cortex (green arrow) and membrane ridges (yellow arrow)

(B) The upper 1.5 μm axial section of a cell in *A* (yellow box) revealing the high density of membrane ridges (yellow arrow) in unchallenged J774 cells,

(C) Maximum intensity projection of actin filaments (cyan) and bead (yellow) of macrophages challenged with 1-μm bead after 2 hours with visible actin cortex (green arrow),

(D) Upper 1.5 μm axial section of a cell in *C* (yellow box) showing conserved expression of membrane ridges in J774 cells after challenging with beads,

(E) Maximum intensity projection of actin filaments (cyan), cell wall (magenta) and capsule (yellow) of H99-incubated J774 cells after 30 minutes showing extensive production of ruffles (yellow arrow)

(F) Upper 3 μm axial section of a cell in *E* (yellow box) showing its actin filaments forming ruffles that usually produce a macropinocytic cup (yellow arrow) whilst membrane ridges were rarely observed,

(G) Maximum intensity projection of actin filaments (cyan), cell wall (magenta) and capsule (yellow) of H99-incubated J774 cells after 2 hours showing the commonly seen and uncharacterised tail-like feature (red arrow) in these cells and very distinct actin cortex (green arrow),

(H) The upper 3 μm axial section of a cell in *G* (yellow box) revealing its actin cortex (green arrow) and occasional dorsal ruffles (yellow arrow). Scale bars: **A, C, E, G** – 20 μm; **B, D, F, H** – 5 μm.

5.5 Actin surrounding phagosomes is a common feature of internalised Cryptococcus

After inspecting the types of actin-rich protrusions found on the dorsal region of H99 infected MΦ and their actin cortices, I next examined any structures that were formed by actin filaments in more interior region of these cells. A very distinct actin signal was observed within the vicinity of internalised H99 cells (Figure 5.5B yellow arrow). A closer examination of these actin-rich regions revealed that they enclosed the phagosomes containing Cryptococcal cells (Figure 5.5E yellow arrow). I then checked if these were autofluorescence from Cryptococcus capsule by inspecting multiple channels of a single z slice. Results (Figure 5.5F) revealed no overlapping signal of these actin structures (yellow arrow) with the capsule (green arrow), indicating that these were actual assemblies of actin filaments surrounding the phagosome.

I next looked at the architecture of these actin cages by examining multiple z sections of a MΦ (Figure 5.5G-P). Results revealed that they were anisotropic structures with actin puncta (Figure 5.5M red arrow) and blocks (yellow arrow) of actin constituting them. Furthermore, these actin cages were not only found around phagosomes with single Cryptococcus but also with multiple cargoes (Figure 5.5J and 5.5O orange arrow). Overall, these highlighted the importance of actin not only in generating membrane protrusions and phagocytic uptake of Cn but also in surrounding phagosomes containing Cn within MΦ.

Actin cages were found to persist throughout the two-hour incubation with H99 Cn so I examined if there were any differences in their frequency at different timepoints of infection which showed different MΦ actin features. I used 30 and 120 minutes PI as dramatic changes in actin cytoskeleton were observed at these timepoints (Figure 5.4E-H). Results (Figure 5.5Q) revealed that actin cages were more common ($p = 0.0014$) 30 minutes PI where 93% of phagosomes was seen with actin cages compared with 79% at 120 minutes PI. This indicates that actin cages were more common at earlier infection periods which is presumably due to the amount of actin used in building the phagocytic cup during Cryptococcus uptake.

(Figure legend on next page)

Q
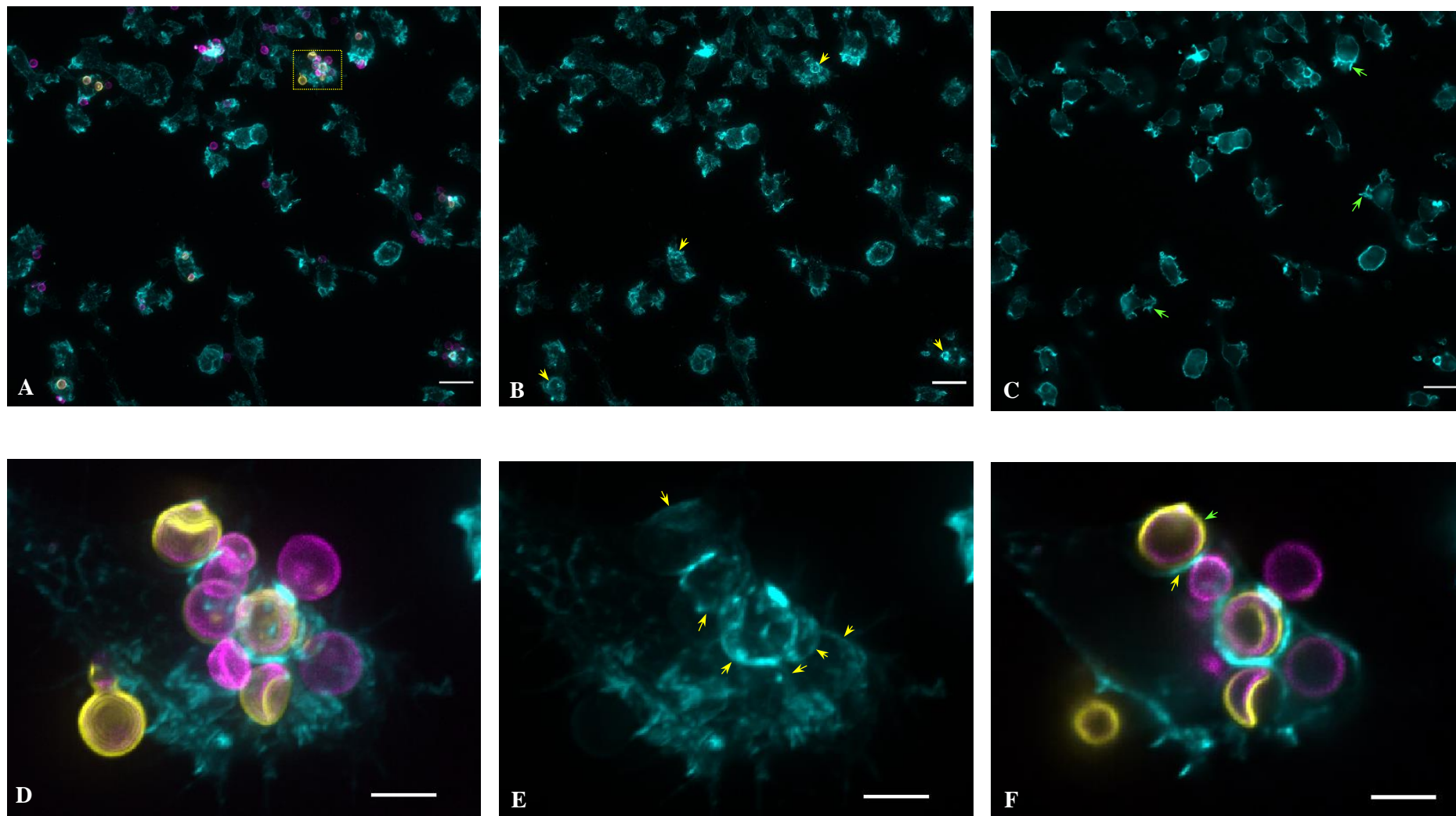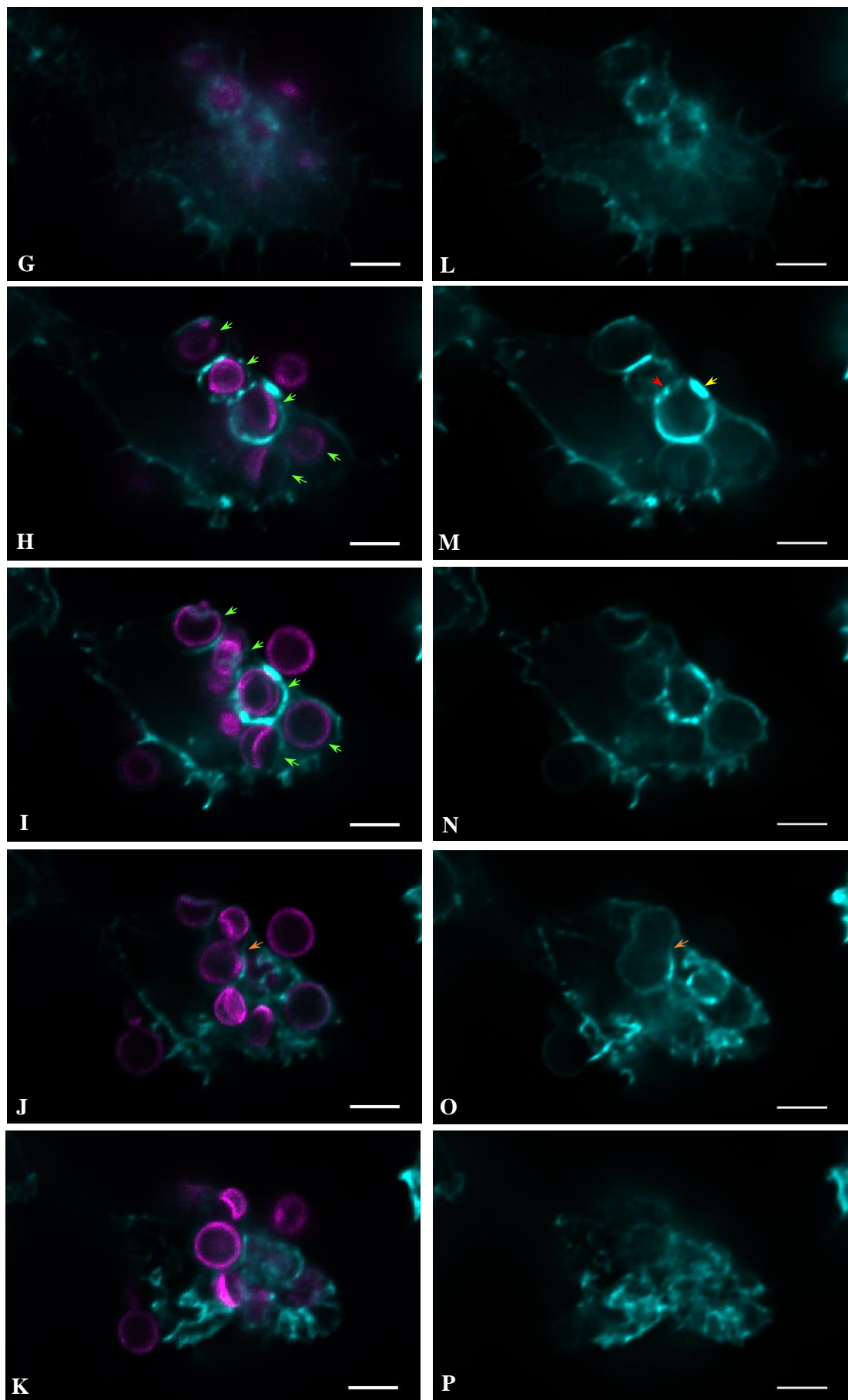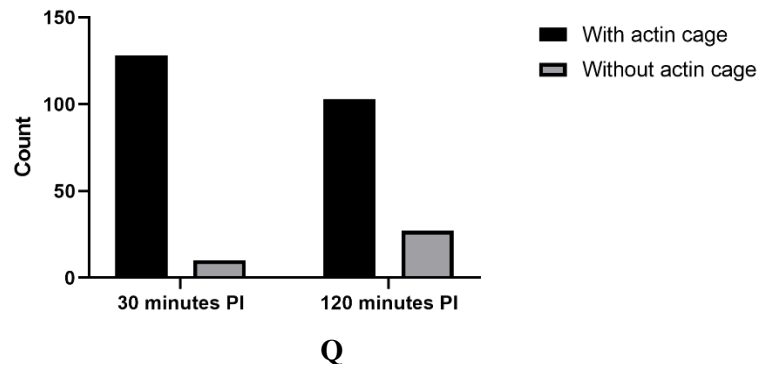
Figure 5.5 | Phagocytic interaction with *C. neoformans* is characterised by actin filaments enclosing phagosomes. A healthy culture of J774 macrophage-like cells was seeded into 24-well plate with glass coverslip, and allowed to acclimatise overnight. They were then incubated with H99 Cn for 30 minutes on the following day. Thereafter, samples were prepared and examined for immunofluorescence microscopy as in previous (Figure 5.4). Images were blindly deconvolved (Ayers and Dainty, 1988) using NIS Elements deconvolution software. Images are a representative of 24 widefield images from 2 independent experimental repeats.

(A) A maximum intensity projection of J774 cells infected with H99 cells after 30 minutes revealing the actin filaments (cyan), cell wall (magenta) and capsule (yellow),

(B) A maximum intensity projection of *A* showing actin filaments only to illustrate the structure they form (yellow arrow) around intracellular phagosomes,

(C) A mid z section of *A* revealing the absence of intracellular compartments (compare with Figure 5.5B) and similar round cortical actin morphology as uninfected cells (Figure 5.5A) but with robust ruffle actin (green arrow),

(D) A maximum intensity projection of a MΦ in *A* (yellow box) showing its actin filaments (cyan), Cryptococcus cell wall (magenta) and capsule (yellow),

(E) Maximum intensity projection of *D* showing only the actin filaments to reveal the actin cages of phagosomes,

(F) A mid z section of *D* to illustrate that actin cages were not due to capsule autofluorescence,

(G-K) Axial sections of *D* revealing phagosome actin cages (green arrow) containing H99 Cn, images from top to bottom start from the basal most up to the uppermost axial region of *D* with 1.5 μm sectioning interval,

(**L-P**) Axial sections of *D* showing only actin filaments and also corresponding to images on its left to highlight the spatial organisation of actin filaments surrounding the phagosomes. Scale bars: **A, C** – 20 μm; **D-P** – 5 μm,

(**Q**) Actin cages were more common 30 minutes post infection (PI) than 120 minutes as revealed by two-sided Fisher's exact test ($p = 0.0014$), the contingency table and statistical analyses were shown in table 5.6.

Timepoint	With actin cage	Without actin cage	Total
30 minutes	128	10	138
120 minutes	103	27	130
Total	231	37	268
Percentage of row total	**With actin cage**	**Without actin cage**	
30 minutes	92.75%	7.25%	
120 minutes	79.23%	20.77%	
Percentage of column total	**With actin cage**	**Without actin cage**	
30 minutes	55.41%	27.03%	
120 minutes	44.59%	72.97%	
Percentage of grand total	**With actin cage**	**Without actin cage**	
30 minutes	47.76%	3.73%	
120 minutes	38.43%	10.07%	

Table 5.6 A contingency table showing the proportion of phagosomes with and without actin cages at 30- and 120-minutes post infection

5.6 MΦ infected with H99 Cn exhibits compartments 2 hours post infection

I further investigated how actin filaments of MΦ are organised at later stages (i.e. 2 hours PI) of infection with H99. The actin cortex was very striking in these cells (Figure 5.6B yellow arrow) and appeared to be more distinct (greater signal intensity) than cells not exposed to H99 (Figure 5.6A). Another salient feature of these cells is the partitioning of their body into compartments (Figure 5.6L 1-3) that were not entirely disconnected from one other (i.e. having a common border and opening with respect to its actin component). Prominent constricted regions I termed "necks" (Figure 5.6K-M green arrow) were usually seen at the border of each compartment. Using this feature, I determined the frequency of MΦ with compartments 2 hours post infection with H99 and found that 94% (650/695) of these cells possessed compartments during this infection period.
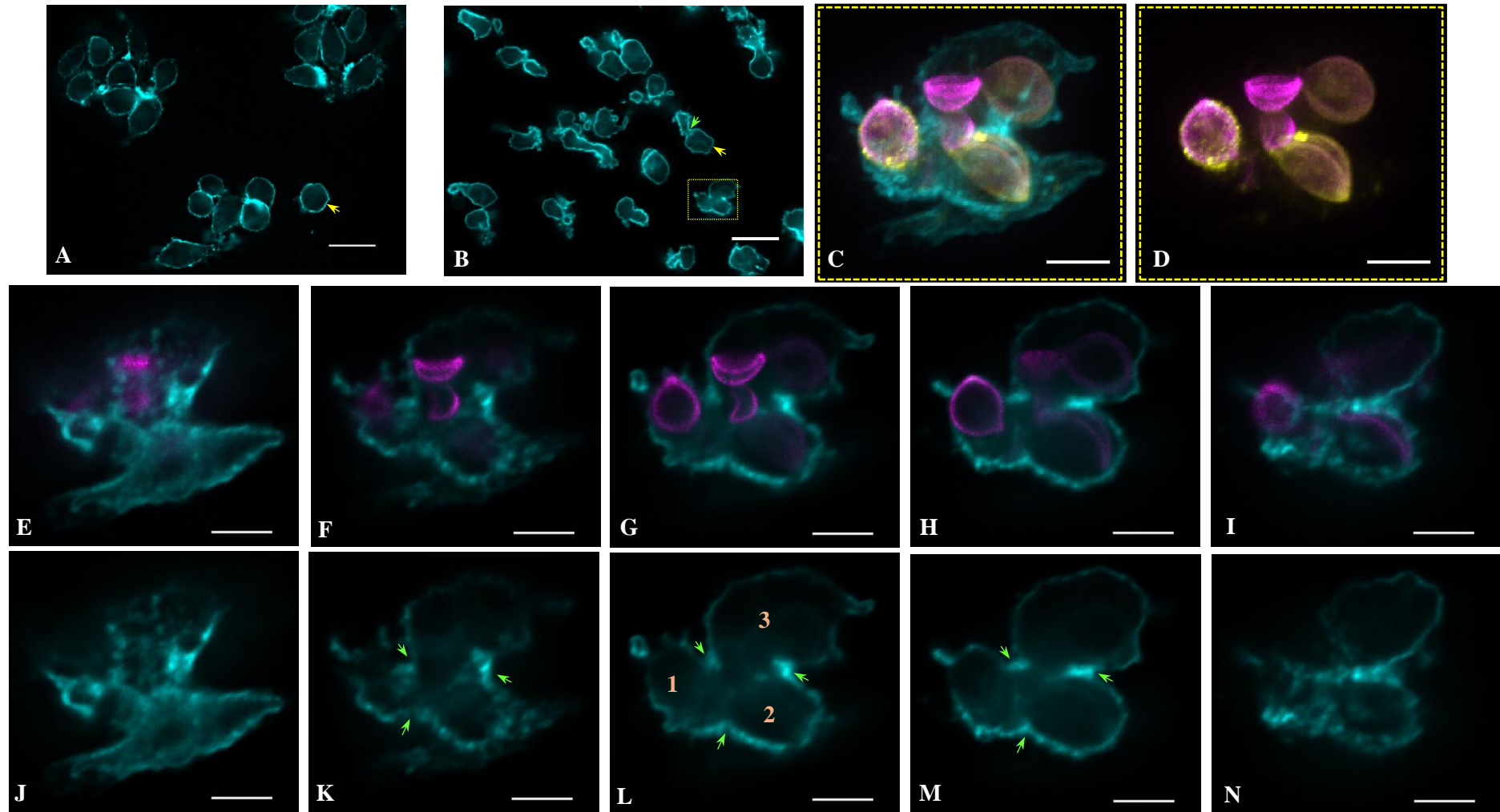
(Figure legend on next page)

Figure 5.6 | Macrophage actin cytoskeleton shows striking compartmentalisation 2 hours post infection with *C. neoformans*. A healthy culture of J774 macrophage-like cells was seeded into 24-well plate with glass coverslip, and allowed to acclimatise overnight. They were then incubated with H99 Cn for 2 hours on the following day. Samples were immediately prepared and examined for immunofluorescence microscopy as in previous (Figure 5.4). Images were blindly deconvolved (Ayers and Dainty, 1988) using NIS Elements deconvolution software. Images are a representative subsection of 277 x 234 μm widefield images from 36 imaging frames of 3 independent experimental repeats.

(A) A mid z-section of J774 cells not infected with H99 (negative control) showing the organisation of their actin filaments that mainly line the cell's body to form a cortical actin layer (yellow arrow),

(B) A mid z-section of J774 cell infected with H99 for 2 hours revealing the organisation of their actin filaments into distinct but interconnected intracellular compartments within a single cell, a "neck" (green arrow) which appears like a constricted region usually borders each compartment,

(C) A maximum intensity projection of a single cell in *B* (yellow box) showing the actin filaments (cyan), cell wall (magenta) and capsule (yellow),

(D) Maximum intensity projection of H99 Cn internalised by a J774 cell in *C* revealing its cell wall (magenta) and capsule (yellow),

(E-I) Axial sections of *C* revealing the different intracellular compartments after a 2-hour infection with H99 Cn, images from left to right start from the basal most up to the uppermost axial region of *C* with 1.5 μm sectioning interval,

(J-N) Axial sections of *C* showing only the actin filaments which also correspond to the images directly above them, the characteristic constrictions "neck" (green arrow) between compartments (**L**: 1-3) could be observed. Scale bars: **A, B** – 20 μm; **C-N** – 5 μm.

5.7 Actin-rich membrane protrusions are important in physical contact of MΦ with *C. neoformans*

Because actin-rich protrusions are very prominent structures during interaction with *C. neoformans* (Cn), I next investigated how MΦ used these in contacting and internalising Cn. Using single cell SEM images acquired from the previous experiment (section 5.2), I examined how MΦ were attached to Cn. Results (Figure 5.7 A-C) showed that MΦ used different protrusions to contact Cn. Finger-like filopodia (Figure 5.7A and 1) were seen extending towards Cn. Sheet-like membrane ridges (Figure 5.7B and 2) and dorsal ruffles (Figure 5.7C and 3) were also found to contact Cn. The actin filaments supporting these structures and providing them with their characteristic forms were revealed using fluorescence microscopy (Figure 5.7D-F).

I then looked at how these membrane protrusions were used during interaction with capsular H99 and acapsular CAP59 Cn. Using the fluorescence data from previous experiment (section 4.8), I initially analysed Cn attachment to MΦ whether with or without protrusion. Results (Figure 5.8A) showed that Cn had greater attachment to MΦ surface with membrane protrusion (over 80% of attached Cn – table 5.7 row percentage total) than without any protrusion. This attachment property was independent of capsule possession ($p = 0.704$). I next examined if there was any preference to the type of protrusion that Cn attach to. It was difficult to discriminate ridges from ruffles using fluorescence images hence I categorised Cn protrusion according to their geometry as sheet-like or finger-like protrusion. Results (Figure 5.8B) revealed that Cn had higher attachment to a sheet-like (over 70% of Cn – table 5.8 row percentage total) than finger-like protrusion geometry. Moreover, this attachment feature was also not influenced by capsule possession ($p = 0.124$).

I next examined how opsonisation could affect MΦ attachment to Cn. Using my previous phagocytosis data of opsonised Cn (section 4.9), I did a similar contingency table analysis as in figure 5.8 but with Cryptococcus variant replaced by opsonisation state. Results (Figure 5.9) revealed higher attachment of opsonised H99 to MΦ surface with protrusion (~70% of attached 18B7-opsonised Cn – table 5.9 row percentage total). However, opsonisation seemed to have increased attachment to surface without any protrusion (Figure 5.9A, $p < 0.0001$) showing 30% of opsonised H99 attached to MΦ surface without any protrusion compared with 9% of unopsonised H99. I then examined any attachment preference of opsonised Cn according to protrusion geometry. Results (Figure 5.9B) showed that opsonised H99 had higher attachment to sheet-like than finger-like protrusion. This property was similar to the previous finding (Figure 5.8B) and was independent of opsonisation state ($p=0.124$).
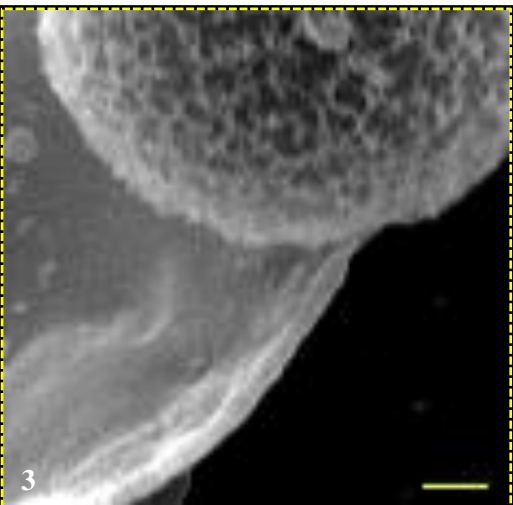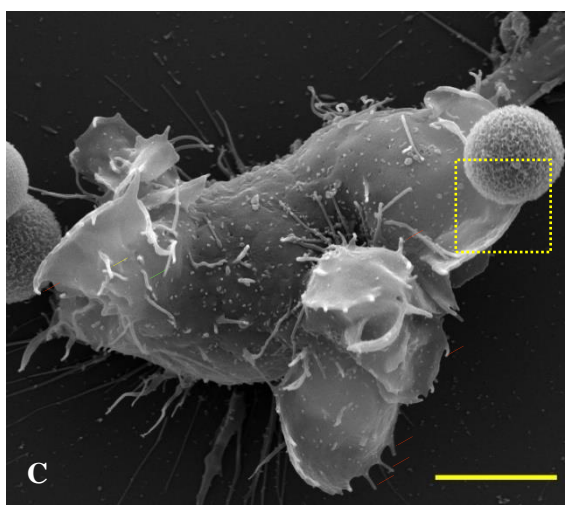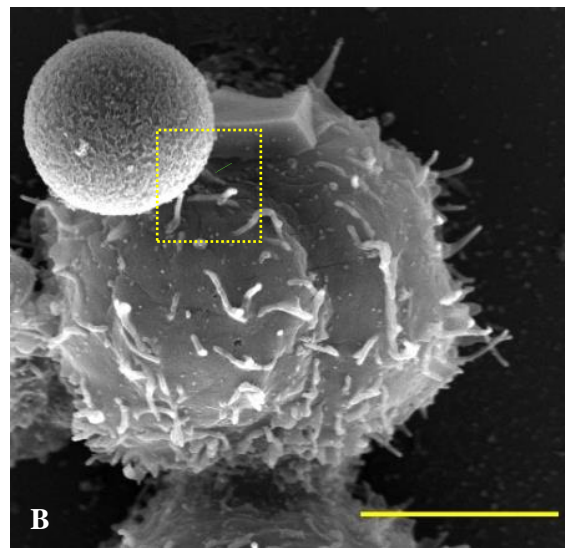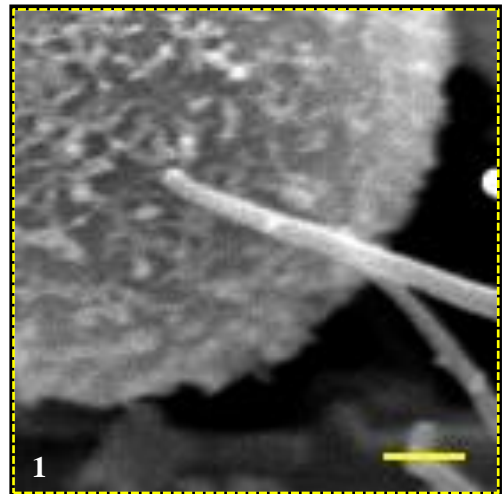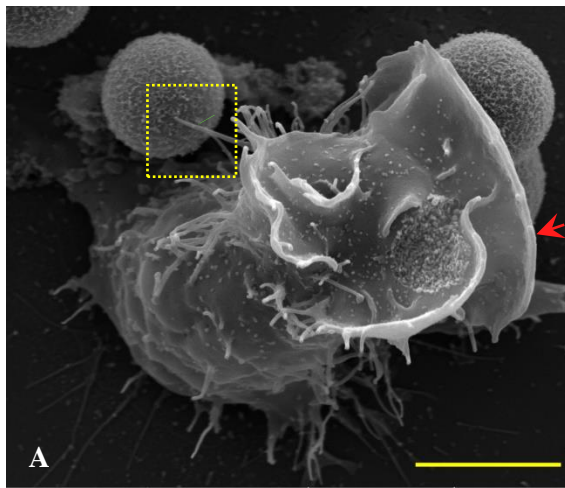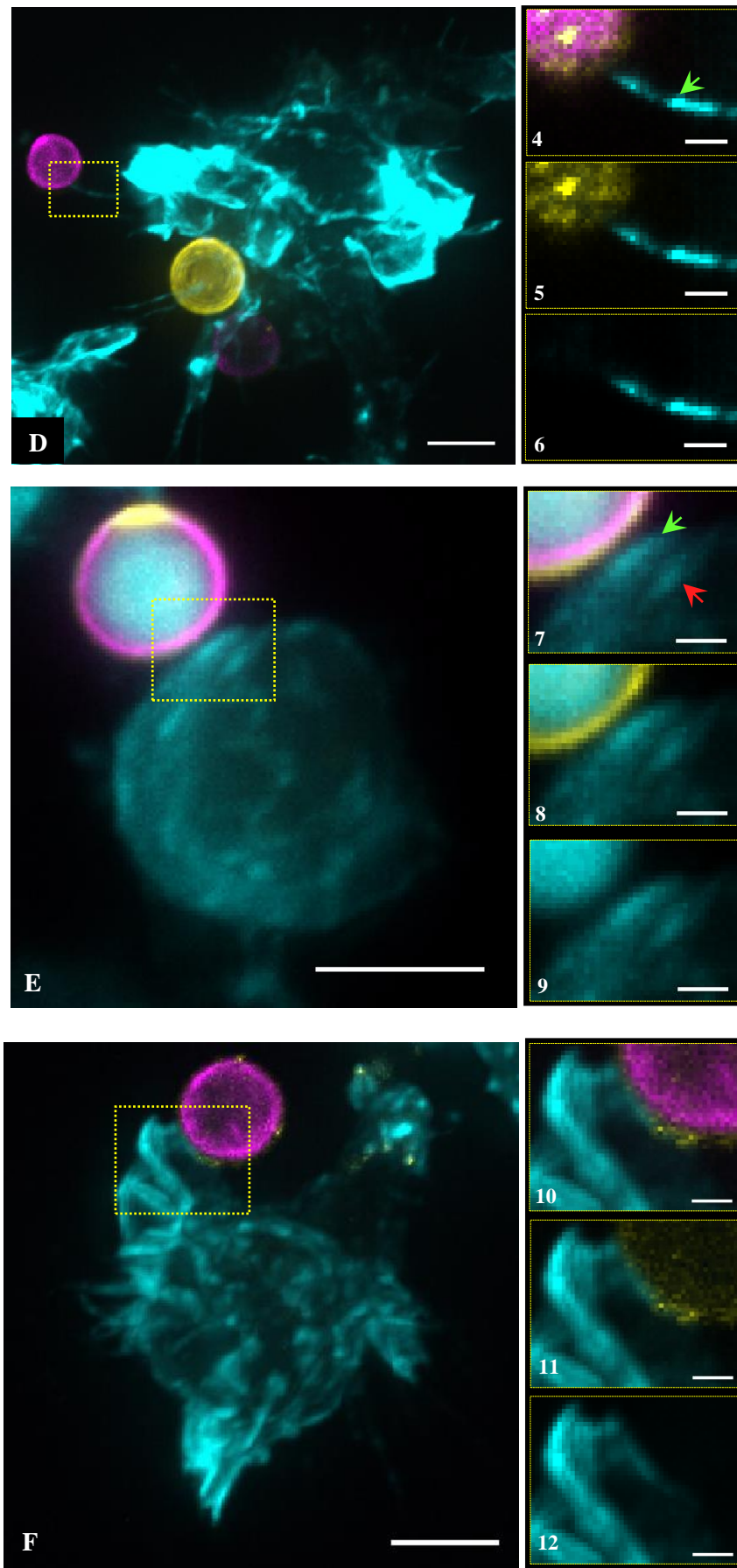
(Figure legend on next page)

Figure 5.7 | Macrophage actin-rich membrane protrusions are used in physical contact with *C. neoformans*. A healthy culture of J774 macrophage-like cells was seeded into 24-well plate with glass coverslip, and allowed to acclimatise overnight. They were then incubated with H99 Cn for 30 minutes the next day and processed for single cell SEM and immunofluorescence (Figure 5.4) examinations. **Left-** main panel, scale bar in all images – 5 μm, **Right**- zoomed in section of a region (yellow box) in the left image with different channels shown for immunofluorescence images (from top to bottom): overlay of all channels, actin and capsule only and actin only, scale bar: SEM – 500 nm; fluorescence – 1 μm. Zoomed in images were enhanced by improving image brightness and contrast using LUTs in Fiji (Schindelin et al., 2012).

(A) An SEM image of J774 cell contacting an H99 cell through its filopodia (green arrow), other H99 cells could also be seen surrounded by giant ruffles (red arrow),

(1) Zoomed in region of *A* (yellow box) showing a filopodium touching the outermost fibrous surface (capsule) of an H99 cell,

(B) An SEM image of J774 cell contacting an H99 cell through a membrane ridge (green arrow),

(2) Zoomed in region of *B* (yellow box) showing a membrane ridge in physical contact with H99 through its capsule, other membrane ridges (red arrow) within the vicinity could also be seen,

(C) An SEM image of J774 cell showing highly elaborated dorsal ruffles that can generate filopodia on its edges (red arrow) or its main body (yellow arrow), membrane ridges (green arrow) were also commonly seen on its main body,

(3) Zoomed in section of an H99 cell resting on top of a giant dorsal ruffle in *C* (yellow box),

(D) An immunofluorescence image of J774 cell with H99 cells rendered in maximum intensity projection (maxIP) showing actin filaments (cyan), cell wall (magenta) and capsule (yellow),

(4-6) Zoomed in region of *D* illustrating the finger-like filopodial actin touching H99 capsule

(E) A maxIP immunofluorescence image of J774 cell contacting H99 cell through membrane ridge,

(7-9) Zoomed in region of *E* showing membrane ridge in contact (green arrow) and not in contact (red arrow) with H99,

(F) A maxIP immunofluorescence image of a J774 touching an H99 by its ruffles,

(10-12) Zoomed in region of *F* illustrating ruffle actin contacting an H99 cell.
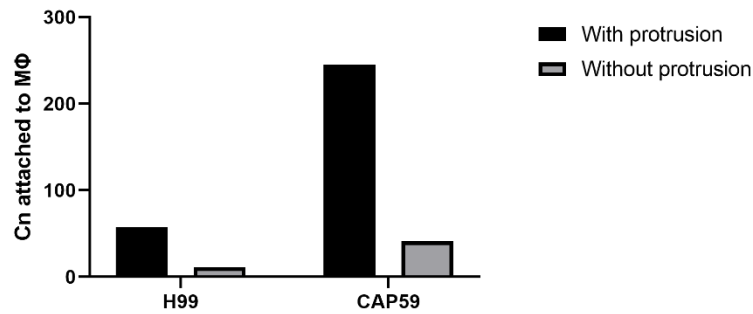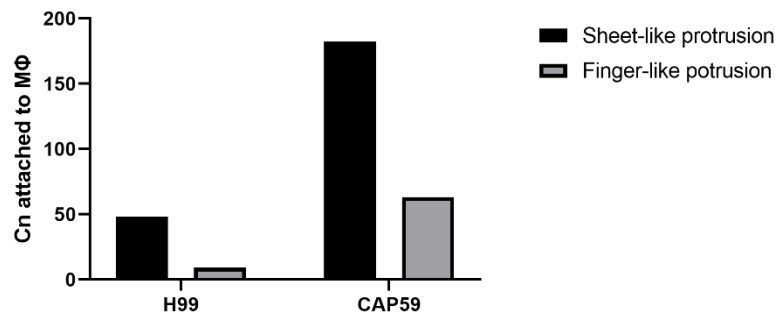
Figure 5.8 | *C. neoformans* **shows higher attachment to MΦ surface with membrane protrusion than without any protrusion whose proportion is not affected by capsule possession.** Immunofluorescence images from a single repeat (9 images) of previous experiment (Figure 4.13) were analysed for the attachment of capsular H99 Cn and acapsular CAP59 Cn to J774 macrophage-like cells. As previously shown (Figure 5.7), Cryptococcus can attach to different types of actin-rich membrane protrusion. Data were then recorded in a contingency table (table 5.7 and 5.8) and analysed using Fisher's exact test for any correlation.

(A) Both H99 and CAP59 Cn showed higher attachment to MΦ surface with protrusion than without any protrusion; Capsule possession did not influence Cn attachment to the type of MΦ surface (i.e. with or without membrane protrusion) as revealed by two-sided Fisher's exact test ($p = 0.704$), the contingency table used for analysis is given in table 5.7,

(B) Both H99 and CAP59 Cn showed higher attachment to a sheet-like protrusion geometry, and capsule possession did not affect this attachment feature during Cn-MΦ interaction as shown by two-sided Fisher's exact test ($p = 0.124$), contingency table for this analysis can be found in table 5.8.

Cryptococcus variant	With protrusion	Without protrusion	Total
H99	57	11	68
CAP59	245	41	286
Total	302	52	354
Percentage of row total	**With protrusion**	**Without protrusion**	
H99	83.82%	16.18%	
CAP59	85.66%	14.34%	
Percentage of column total	**With protrusion**	**Without protrusion**	
H99	18.87%	21.15%	
CAP59	81.13%	78.85%	
Percentage of grand total	**With protrusion**	**Without protrusion**	
H99	16.10%	3.11%	
CAP59	69.21%	11.58%	

Table 5.7 | A contingency table showing the proportion of Cn attached to MΦ with or without protrusion 120 minutes post infection

Cryptococcus variant	Sheet-like protrusion	Finger-like protrusion	Total
H99	48	9	57
CAP59	182	63	245
Total	230	72	302
Percentage of row total	**Sheet-like protrusion**	**Finger-like protrusion**	
H99	84.21%	15.79%	
CAP59	74.29%	25.71%	
Percentage of column total	**Sheet-like protrusion**	**Finger-like protrusion**	
H99	20.87%	12.50%	
CAP59	79.13%	87.50%	
Percentage of grand total	**Sheet-like protrusion**	**Finger-like protrusion**	
H99	15.89%	2.98%	
CAP59	60.26%	20.86%	

Table 5.8 | A contingency table showing the proportion of Cn attached to MΦ with or without protrusion 120 minutes post infection

A

B
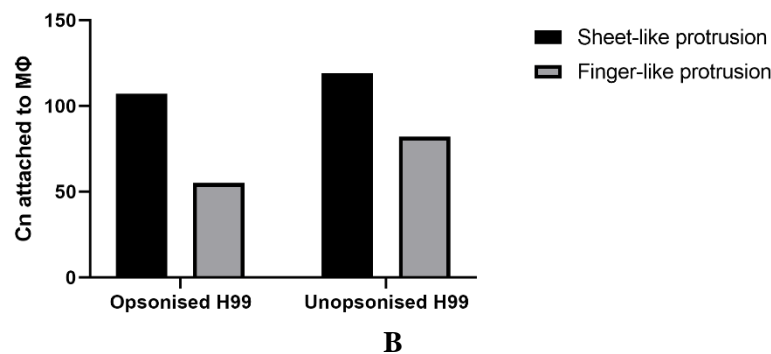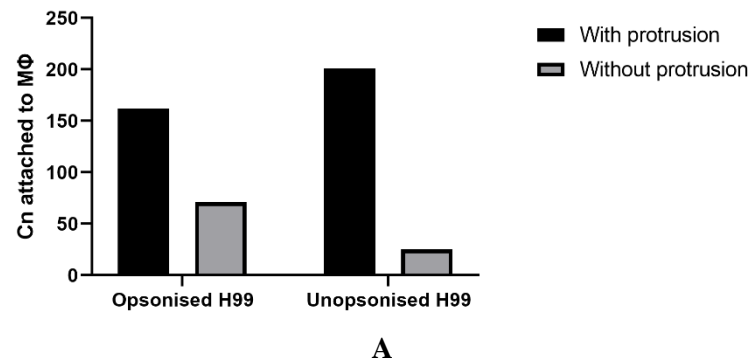
Figure 5.9 | Opsonised H99 also has higher attachment to MΦ membrane surface with protrusion than without protrusion but shows increased in attachment to surface without protrusion. Immunofluorescence images from 3 experimental repeats (27 images) of previous phagocytosis assay (Figure 4.16) were analysed for the type of membrane protrusion H99 cells adhered to by scanning multiple z sections of each image. Data were then summarised in a contingency table (table 5.9 and 5.10) and analysed using Fisher's exact test for any correlation.

(A) Opsonisation maintained higher attachment to surface with protrusion than without protrusion, but also resulted in increased attachment to surface without protrusion as revealed by two-sided Fisher's exact test ($p < 0.0001$), the contingency table used for analysis is given in table 5.9,

(B) Opsonisation maintained higher attachment to a sheet-like protrusion than finger-like geometry by H99 cells as shown by two-sided Fisher's exact test ($p = 0.124$), contingency table for this analysis can be found in table 5.10.

Opsonisation state	With protrusion	Without protrusion	Total
Opsonised H99	162	71	233
Unopsonised H99	201	25	226
Total	363	96	459
Percentage of row total	With protrusion	Without protrusion	
Opsonised H99	69.53%	30.47%	
Unopsonised H99	88.94%	11.06%	
Percentage of column total	With protrusion	Without protrusion	
Opsonised H99	44.63%	73.96%	
Unopsonised H99	55.37%	26.04%	
Percentage of grand total	With protrusion	Without protrusion	
Opsonised H99	35.29%	15.47%	
Unopsonised H99	43.79%	5.45%	

Table 5.9 | A contingency table showing the proportion of opsonised and unopsonised Cn attached to MΦ with or without protrusion 120 minutes post infection

Opsonisation state	Sheet-like protrusion	Finger-like protrusion	Total
Opsonised H99	107	55	162
Unopsonised H99	119	82	201
Total	226	137	363
Percentage of row total	Sheet-like	Finger-like	
Opsonised H99	66.05%	33.95%	
Unopsonised H99	59.20%	40.80%	
Percentage of column total	Sheet-like	Finger-like	
Opsonised H99	47.35%	40.15%	
Unopsonised H99	52.65%	59.85%	
Percentage of grand total	Sheet-like	Finger-like	
Opsonised H99	29.48%	15.15%	
Unopsonised H99	32.78%	22.59%	

Table 5.10 | A contingency table showing the proportion of opsonised and unopsonised Cn attached to sheet-like or finger-like MΦ protrusions 120 minutes post infection

5.8 Inhibition of membrane ridges reduces phagocytic uptake of acapsular Cryptococcus

I next investigated the importance of membrane ridges in phagocytosis of Cn. As revealed in my previous experiment (Figure 5.3D), ridges were almost completely inhibited 30 minutes post infection with CAP59 Cn. Using this knowledge, I designed an *in vitro* phagocytosis imaging assay that would allow quantitation of internalised Cn when ridges are repressed. Briefly, J774 cells that were acclimatised overnight in a 24-well plate were challenged with CAP59 Cn on the following day using 1MΦ:10Cn MOI. After 30 minutes, these cells were then challenged with either H99 or CAP59 with pre-labelled cell wall to differentiate them from the previous batch of Cn. Samples were then fixed after 2 hours, processed for immunofluorescence (section 4.8) without cell wall labelling and examined using a widefield microscope. Three fields of view per replicate/well were imaged using a 60x oil immersion lens at random position with multiple z sections of 15-μm thickness. The total number of internalised Cn from all nine frames of each set-up was then recorded and used for statistical analysis.

Results (Figure 5.10) showed that loss of ridges reduced uptake of both capsular H99 and acapsular CAP59 Cn. I then used a 2-way ANOVA analysis to determine individual and combined contributions of capsule possession and ridge repression to phagocytosis of Cn. Statistical analysis revealed greater effect of ridge repression than capsule possession in the phagocytic uptake of Cn. Ridge repression explained 32% of uptake variation compared with 28% explained by capsule possession. This analysis further revealed a combined effect of ridge repression and capsule possession in phagocytosis of Cn which accounted for 24% of variation. However, it should be noted that only CAP59 uptake was significantly reduced after pre-incubation with CAP59 cells. Furthermore, it is worth to try if pre-incubation with H99 or treatment with IL-10 which represses membrane ridges also leads to similar result of reduction of phagocytic uptake by macrophages.
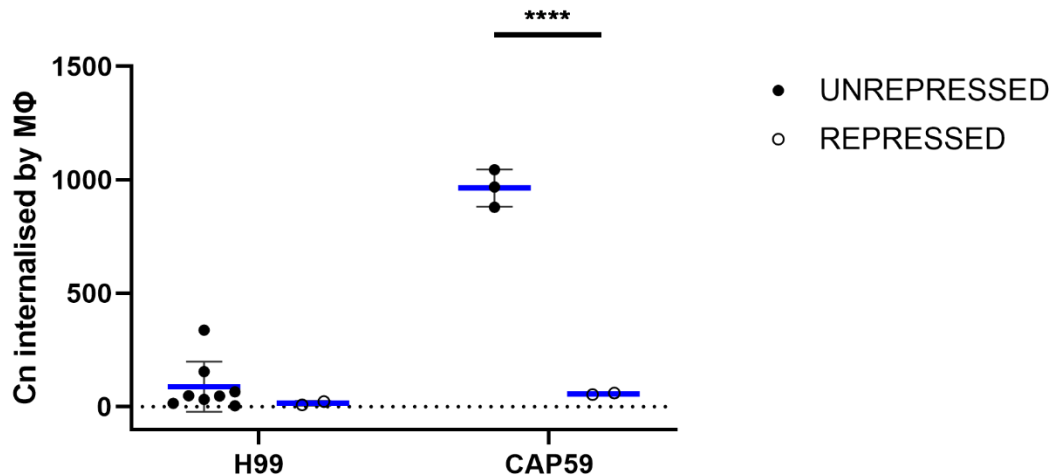
Figure 5.10 | Loss of membrane ridges impairs phagocytic uptake of acapsular CAP59
C. neoformans. A healthy culture of J774 macrophage-like cells was seeded into 24-well plate
with glass coverslip overnight. On the following day, they were challenged with CAP59 Cn
for half hour to inhibit ridge production. Cells were washed, and media were replaced with
either H99 or CAP59 cells that were both pre-labelled to discriminate them from previous Cn
cells. Samples were incubated for 2 hours and fixed thereafter. They were processed for
immunofluorescence microscopy as in previous (Figure 4.13) without cell wall labelling, and
examined using a widefield microscope. Three images per replicate (a total of nine frames per
set-up) were scored for the number of Cn internalised by MΦ. Two-way ANOVA analysis
revealed that there was a statistically significant correlation between capsule possession an
ridge repression ($F(1,11) = 52.70$, $p < 0.0001$) in Cryptococcus phagocytic uptake. Sidak's
multiple comparisons test however showed that only CAP59 uptake was affected by ridge
repression ($p < 0.0001$). H99 uptake did not show any statistically significant change
following ridge repression ($p < 0.585$). The main effect of ridge repression yielded an effect
size of 0.32 ($F(1, 11) = 72.60$, $p < 0.0001$), indicating that 32% of total variation in
Cryptococcus uptake could be explained by whether MΦ possessed ridges or not. On the other
hand, capsule possession recorded a 0.28 effect size ($F(1, 11) = 63.56$, $p < 0.0001$), indicating
that 28% of total variation in Cryptococcus phagocytosis could be explained by whether or
not they had capsule.

5.9 MΦ exposed to Cn for 2 hours show intracellular capsule and cell wall fragments

Finally, I examined another feature of MΦ-Cn interaction which is the presence of capsule and cell wall residues within the cytoplasm (Figure 5.11). Using the immunofluorescence images from my previous experiment (section 4.9), I manually inspected MΦ for any intracellular localisation of capsule and cell wall fragments. Images were deconvolved and background subtracted to improve fragment visualisation. All nine frames per experimental repeat (three) were then scored for intracellular capsule or cell wall residues in MΦ.

Results revealed that the occurrence of cell wall fragments (Figure 5.11D red arrow) within MΦ after 2 hours of infection with H99 was a rare event with less than 3% of cells showing cell wall residues (table 5.11 – row percentage). I then examined if this is influenced by opsonisation of Cn as it enhances phagocytic uptake as revealed in my previous experiment (Figure 4.16A). Unexpectedly, results (Figure 5.11E) showed that opsonisation decreased the number of MΦ with cell wall fragments ($p = 0.0073$).

I next examined capsule residues (Figure 5.11C green arrow) in H99-infected MΦ with 2 hours PI. Results revealed that only MΦ incubated with opsonised H99 possessed capsule residues in their cytoplasm (table 5.12). The frequency of MΦ-containing capsule fragments (4.56%) was slightly higher than those with cell wall residues (1.58%). Taken together, these suggest that both cell wall and capsule residues could be found intracellularly in MΦ interacting with Cn *in vitro* after 2 hours. Opsonisation increased the frequency of cells with intracellular capsule fragments, and the opposite was true for cell wall residue.
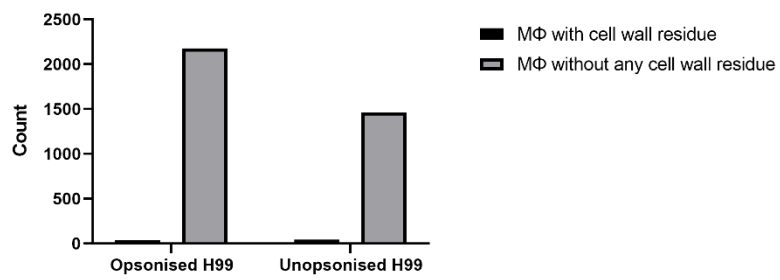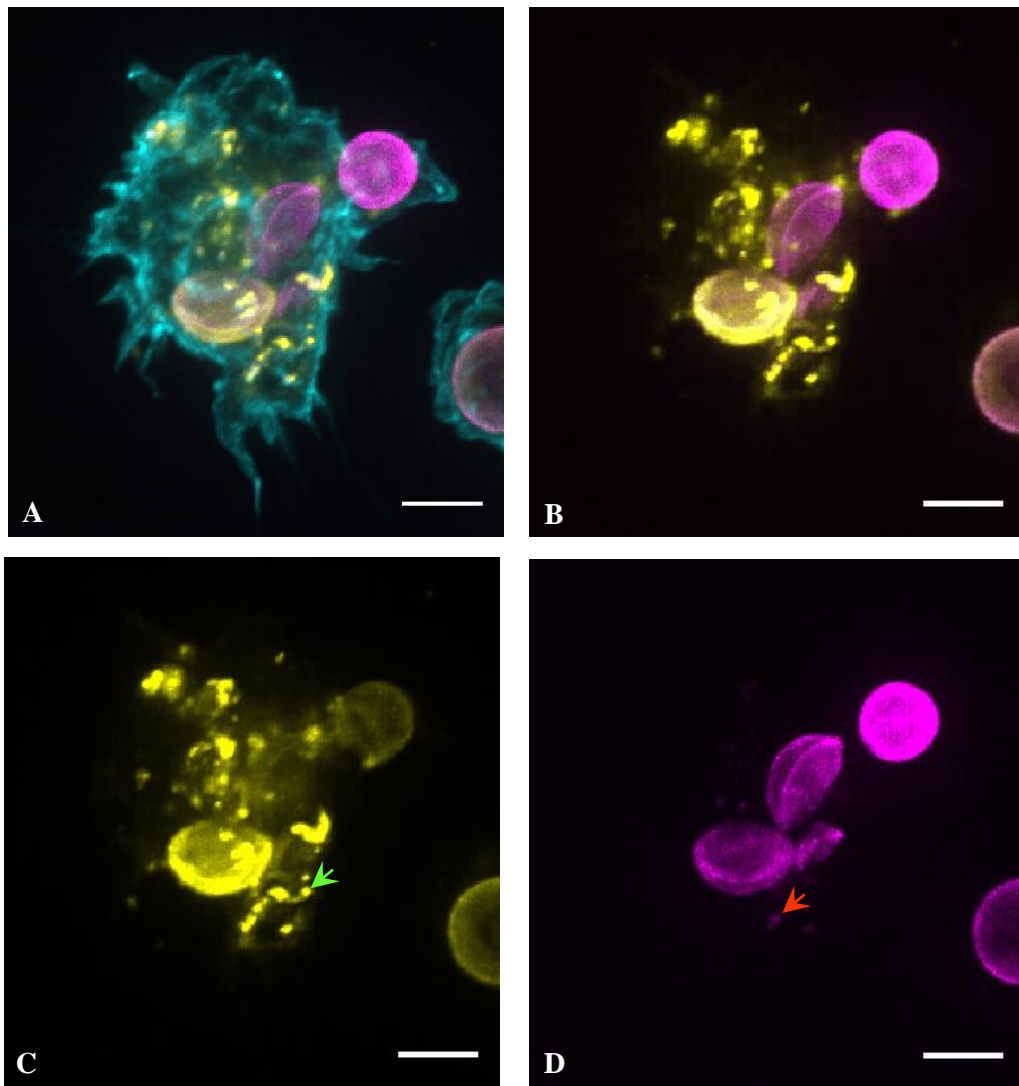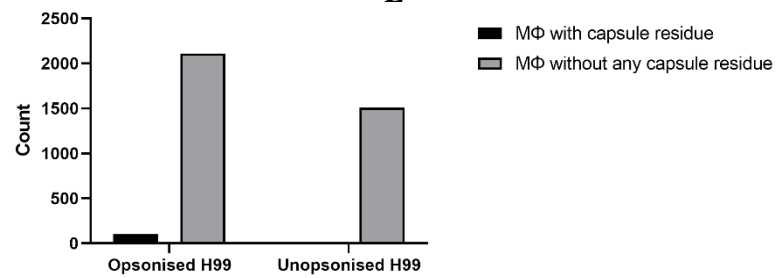
(Figure legend on next page)

Figure 5.11 | Macrophages possess capsule and cell wall residues after incubation with *C. neoformans* **in vitro for 2 hours.** Immunofluorescence images from previous experiment (section 4.9) were manually scored for intracellular fragments of Cryptococcus cell wall and capsule. Results were then examined by contingency table analysis for any correlation between fragment possession and Cn opsonisation.

(A) A J774 cell with internalised Cn and profuse intracellular capsule and cell wall fragments, image is a maximum intensity projection of capsule (yellow), cell wall (magenta) and actin filaments (cyan),

(B) The same image as *A* showing only capsule (yellow) and cell wall (magenta),

(C) The same image as *A* showing only the capsule and capsule fragments visible (green arrow),

(D) The same image as *A* showing only cell wall and its residues visible (red arrow), scale bar in all images – 5 μm.

(E) Opsonisation reduced the frequency of MΦ with intracellular capsule residue as confirmed by two-sided Fisher's exact test ($p = 0.0073$), the contingency table used for analysis is given in table 5.11,

(F) Opsonisation increased the number of MΦ with capsular fragments as revealed by two-sided Fisher's exact test ($p < 0.0001$), contingency table for this analysis can be found in table 5.12.

Opsonisation state	MΦ with cell wall residue	MΦ without any cell wall residue	Total
Opsonised H99	35	2178	2213
Unopsonised H99	44	1463	1507
Total	79	3641	3720
Percentage of row total	MΦ with cell wall residue	MΦ without any cell wall residue	
Opsonised H99	1.58%	98.42%	
Unopsonised H99	2.92%	97.08%	
Percentage of column total	MΦ with cell wall residue	MΦ without any cell wall residue	
Opsonised H99	44.30%	59.82%	
Unopsonised H99	55.70%	40.18%	
Percentage of grand total	MΦ with cell wall residue	MΦ without any cell wall residue	
Opsonised H99	0.94%	58.55%	
Unopsonised H99	1.18%	39.33%	

Table 5.11 | A contingency table showing the proportion of MΦ with cell wall residues 120 minutes post infection with opsonised and unopsonised H99

Opsonisation state	MΦ with capsule residue	MΦ without any capsule residue	Total
Opsonised H99	101	2112	2213
Unopsonised H99	0	1507	1507
Total	101	3619	3720
Percentage of row total	MΦ with capsule residue	MΦ without any capsule residue	
Opsonised H99	4.56%	95.44%	
Unopsonised H99	0.00%	100.00%	
Percentage of column total	MΦ with capsule residue	MΦ without any capsule residue	
Opsonised H99	100.00%	58.36%	
Unopsonised H99	0.00%	41.64%	
Percentage of grand total	MΦ with capsule residue	MΦ without any capsule residue	
Opsonised H99	2.72%	56.77%	
Unopsonised H99	0.00%	40.51%	

Table 5.12 | A contingency table showing the proportion of MΦ with capsule residues 120 minutes post infection with opsonised and unopsonised H99

5.9 General Discussion

Macrophages are a highly specialised group of cells that perform diverse roles from infection control to tissue homeostasis. They are known to be critical for host defence against many types of fungal infection by destroying the infectious agent through phagocytosis and priming an adaptive immune response (Erwig and Gow, 2016). Amongst these infections with high clinical importance is Cryptococcosis, caused by the fungal species *Cryptococcus neformans* and *C. gatti* (Maziarz and Perfect, 2016).

As previously shown by our lab (Bojarczuck et al., 2016) and others (Davis et al., 2016; Tenor et al., 2015), macrophages play key a role in the early immune response to Cryptococcal infection. To clear out Cryptococcal cells, macrophages require efficient means of detecting, engulfing and digesting these microbes. However, *Cryptococcus* are poised with structural and biochemical properties which allow them to overcome antimicrobial responses of macrophages leading to a more complex infection dynamics. Their capsule enables them to evade phagocytosis (Kozel and Gotsclich, 1982; Small and Mitchell, 1989) through an unknown mechanism, and also possesses antioxidant properties (Zaragoza et al., 2008) which favour cell survival in phagolysosomes enriched with free radicals. Moreover, *Cryptococcus* can manipulate the composition of phagolysosome by urease secretion which can neutralise its acidity through conversion of urea to ammonia and carbon dioxide (Fu et al., 2018). They can also dissolve phagolysosomal membrane in an undefined mechanism (Tucker and Casadevall, 2002) which makes it leaky that subsequently results to alteration of its content and, ultimately, functional impairment. Overall, these features do not only show some of the adaptive responses of *Cryptococcus* during infection but also imply changes in macrophages due to their interaction with *Cryptococcus*.

Using different imaging modalities, I investigated changes in macrophage membrane and actin cytoskeleton during early stages (i.e. first 2 hours) of Cryptococcal infection. I found that the membrane surface of macrophages cultured *in vitro* was drastically transformed after exposure to *Cryptococcus*, from a highly dense ridge surface to a ruffle-rich structure. These membrane structures were found to have different geometrical properties which is useful in discriminating one from the other. The inverse relationship of ridge expression with dorsal ruffles wherein ridge reduction showed concomitant increase in dorsal ruffle production highly suggests that conversion between these sheet-like membrane features is one of the early structural responses of macrophages to Cryptococcal infection.

Through fluorescence microscopy, I was also able to describe changes in macrophage actin cytoskeleton during interaction with *Cryptococcus*. At thirty minutes post infection, their actin-rich ruffles were seen as the dominant protrusion whilst actin ridges were very rarely

observed, agreeing with my previous SEM findings of membrane surface changes during Cryptococcal infection. Furthermore, actin surrounding the phagosomes called actin cages were also commonly seen during this period. Further exposure of MΦ for 2 hours revealed that ridges and ruffles were rarely present at this timepoint, which was also corroborated by my SEM data. A more defined actin cortex was rather seen in these cells suggesting of critical importance of maintaining cell shape after ingestion of Cryptococcal cells.

I also examined the physical interaction between MΦ and *Cryptococcus* and the effect of membrane ridge repression in the phagocytic uptake of *Cryptococcus*. Using SEM and fluorescence microscopy, the different membrane protrusions: filopodia, membrane ridges and dorsal ruffles, were found to be used by MΦ to contact Cryptococcal cells. Contact through sheet-like protrusion was found to be more common than finger-like protrusion even after opsonisation. In addition, opsonisation also enhances *Cryptococcus* contact with MΦ surface without any protrusion. Finally, repression of membrane ridges was found to negatively impact the phagocytic uptake of *Cryptococcus*. This however needs to be verified as the experimental set-up relied on pre-exposure of MΦ to *Cryptococcus* which very likely altered not just their ridge density after initial engulfment of Cryptococcal cells but also their other biophysical properties such as cortical or membrane tension, cytoplasmic viscosity and membrane reserves which are all implicated in phagocytosis (Herant et al., 2005; Evans, 1989; Petty 1981).

5.10 Specific Discussions

Structural changes in macrophages during early interaction with *Cryptococcus neoformans* were investigated in this chapter. Using scanning electron microscopy, fluorescence microscopy and image analysis, these morphological changes at specific timepoints of infection were described and quantitated. Through this approach, early structural changes with respect to membrane and actin cytoskeleton of MΦ were tracked and analysed following Cryptococcal infection.

5.10.1 Cell surface changes during interaction with *Cryptococcus*

The plasma membrane is an important outermost cellular structure in almost all eukaryotic cells which allows them to interact with their external environment (Alberts et al., 2015). As a frontline defence against invading pathogens, macrophages rely on their membrane surfaces to perform functions critical to infection control such as migration to sites of infection, detection of infectious agents and their phagocytic uptake for intracellular degradation. It is therefore essential to describe changes in the macrophage surface during early stages of infection which will allow us to understand their behaviour and physical interaction with pathogens that might predict infection outcomes.

Immediately after infection with *Cryptococcus neoformans* (i.e. within 5 minutes PI), a remarkable transformation in the membrane surface of MΦ cultured *in vitro* was observed. It should also be noted that I also attempted to examine Cryptococcus-infected MΦ at an earlier timepoint - 2 minutes PI, and ruffles were already seen predominating the macrophage surface. The highly ridged surface was converted into dorsal ruffles within the first 30 minutes of infection with increasing ruffle density at decreasing ridge density. This suggests an undescribed mechanism that changes membrane ridges to ruffles in MΦ during early stages of Cryptococcal infection. Furthermore, ruffles were found to be structurally more complex than ridges with larger geometrical features (i.e. length and thickness) and possessing other secondary protrusions, filopodia and ridges, extending from its edges or main body.

At later infection timepoints (i.e. 2 hours PI), membrane ridges and dorsal ruffles were rarely seen on the MΦ surface. Instead, bleb-like and tail-like structures became a very common feature of these cells. Membrane blebbing is known to be a key apoptotic signature during infection which favours infection control as it results in cell death without lysis that could otherwise disseminate the infectious agent (Behar et al., 2011). For a comprehensive review of molecular pathways involved in blebbing and apoptosis, the reader is referred to Coleman (2001). Blebs appear when the cell membrane delaminates from the cortical cytoskeletal network to form blisters that are expanded by hydrostatic pressure (Charras et al., 2005). It was previously shown by Tinevez (2009) and colleagues that blebs are positively regulated by cortical tension which could potentially explain the predominance of bleb-like features 2 hours PI with *Cryptococcus* concurrent with a well-defined cortical actin possessed by MΦ at this timepoint. The physical properties of cortical actin however were not further investigated which could have revealed more insights about infection control at the cellular level.

5.10.2 Features of the actin cytoskeleton during Cryptococcal infection

Changes in MΦ actin cytoskeleton were also examined at different infection timepoints. Fluorescence imaging revealed that 30 minutes PI actin ridges were rarely seen in MΦ concomitant to actin ruffles becoming the dominant type of protrusion. Actin surrounding phagosomes called actin cages were also a common feature of MΦ at this stage of infection. At 2 hours PI, distinct cellular compartments containing internalised *Cryptococcus* which were surrounded by the cortical actin was found to be a salient feature of MΦ actin cytoskeleton together with a highly defined actin cortex. Taken together, these suggest that early Cryptococcal infection is marked by changes in the cellular actin architecture of MΦ.

5.10.2.1 Dorsal ruffles

Immediately after Cryptococcal infection, ruffles were found to be extensively produced by MΦ. Ruffle production however is not an exclusive feature of Cryptococcal infection. This is also seen in other infection models including *Salmonella typhymurium* (Hanisch et al., 2010), *Staphylococcus aureus* (Flannagan and Heinrich, 2020), *Shigella* spp. (Ohya et al., 2005) and *Neisseria gonorrhoeae* (Edwards et al., 2000) where molecular mechanisms of ruffle induction have been well-characterised through identification of different effector proteins secreted by these pathogens to promote actin remodelling. In the first 30 minutes of Cryptococcal infection, an inverse correlation between ridge density and ruffle density was found suggesting a mechanism of converting ridges to ruffles upon exposure to *Cryptococcus*. Guerra (2014) and colleagues suggested that these ruffles enhance the uptake of both capsular (H99) and acapsular (CAP59) *Cryptococcus* which led to their conclusion that capsule is not important in *Cryptococcus* uptake. However, their analysis of phagocytic uptake was based on examining SEM images of fixed cell surface by which confirmation of whether target was internalised or not was unclear. Furthermore, the use of cytochalasin to inhibit ruffling would very likely impact phagocytosis as well as demonstrated by Rotty (2017) and colleagues. My results on the other hand showed no statistically significant difference in ruffle production between H99- and CAP59-infected macrophages during the entire incubation period of 2 hours (table 5.3). There was however significant difference in the phagocytic uptake between these variants (Figure 4.14A) which, I accounted to capsule possession and thickness (Figure 4.14 and 4.15).

5.10.2.2 Actin cages

The presence of actin around a phagosome containing *Cryptococcus* was previously reported in the seminal paper of Johnston and May (2010). They showed that this structure is important to prevent a non-lytic escape of *Cryptococcus* from the host cell which could otherwise contribute to its dissemination (Johnston and May, 2010). The anisotropic distribution of actin around the phagosome (Figure 5.5) potentially indicates that this is produced by actin polymerisation at different timepoints. However, I was not able to further investigate and verify this property due to time constraints of setting up a live cell imaging experiment and analysing timelapse data. One feature that is known about these structures is that they are highly dynamic that is capable of producing short pulses termed actin flash with at least 2 minutes interval for C3bi-opsonised targets (Poirier et al., 2020) and 20-30 actin flashes for *Cryptococcus* targets within 18 hours of phagocytic uptake (Johnston and May, 2010), suggesting cyclical events of actin polymerisation.

Actin cage was also reported by Liebl and Griffith (2009) who concluded that this structure delays phagosome maturation by preventing fusion with lysosomes. Observations

using *Dictyostelium discoideum* seem to support this notion as clustering of late-endosomal vacuoles was prevented by actin's presence around the phagosome (Drengk et al., 2003). Other reports of actin structures around a phagosome demonstrated that the phagocytic receptor used for uptake influences the amount of recruited actin (Bohdanowicz et al., 2010). Bohdanowicz (2010) and collaborators showed that CR3-mediated phagocytosis can recruit actin post engulfment by phosphatidylinositol-3-phosphate-dependent actin polymerisation which then forms as an actin tail that transports the phagosome within the host cell. Finally, Poirier (2020) and colleagues showed that actin flashes can serve in mechanical deformation of phagosomal content via recruitment of myosin IIA. This could be important in *Cryptococcus* engulfment as actin intensity around the phagosome seemed to be greater in those with thicker capsule (Figure 5.5D-P)

5.10.2.3 Intracellular compartmentalisation

After 2 hours of Cryptococcal infection, MΦ actin cytoskeleton was found to be organised in different compartments with a very distinct actin cortex. Ruffles and ridges were rarely seen in these cells, however actin puncta on the dorsal cell region (Figure 5.4G yellow arrow) and tail-like actin features (red arrow) were commonly observed. This compartmentalised feature of the cytoplasm is possibly a consequence of phagocytic load as the size and number of *Cryptococcus* taken up seemed to correlate with the size of the compartment (Figure 5.6G and 5.6L). This effect was confirmed by incubating MΦ with 6 um beads (Figure 4.9A) which showed the compartments (green arrow) from the outer cell perspective. These features at later stages of Cryptococcal infection are very likely influenced by the properties of the actin cortex which is yet to be explored.

5.10.3 Importance of actin-rich MΦ protrusions in Cryptococcal infection

The importance of actin-rich membrane protrusions in interaction of MΦ with *Cryptococcus* was also demonstrated. SEM imaging revealed MΦ use their protrusions: filopodia, membrane ridges and dorsal ruffles to contact *Cryptococcus*. Fluorescence examination after *in vitro* infection showed that more than 70% of *Cryptococcus* were attached to MΦ surface with protrusion (table 5.7 and 5.9). This agrees with the observation of Flannagan (2010) and colleagues who demonstrated that binding with different types of phagocytic target was greatly reduced upon inhibition of MΦ to form these membrane protrusions.

5.10.4 Other features of MΦ during early periods of Cryptococcal interaction

Finally, MΦ incubated with *Cryptococcus* for 2 hours showed intracellular residues of cell wall and capsule. A potential mechanism for this is shedding from the leaky phagosomes where *Cryptococcus* were contained (Tucker and Casadevall, 2002). However, it

was also observed that dorsal ruffles contact fragments of capsule and cell wall before they were internalised (data not shown). This indicates that macropinocytosis could be a possible mechanism by which fragments are internalised by macrophages. Deformed Cryptococcal cells that were not completely internalised and remains on the surface with parts of macrophage membrane surrounding them resembling a trogocytosis phenomenon (Joly and Hudrisier, 2003) was also rarely observed, suggesting that it is another plausible mechanism of capsule and cell wall internalisation.

5.11 Conclusions and future work

The early features of *Cryptococcus*-macrophage interaction were explored here using different imaging techniques. Salient changes in the macrophage membrane and actin cytoskeleton were found within the first 2 hours of infection. Membrane ridges were replaced by dorsal ruffles immediately after Cryptococcal exposure whilst bleb-like features, actin compartments and a highly distinct actin cortex were features found at later infection stage. These underpin the importance of actin dynamics in infection, which is directly responsible for structural features used by MΦ for pathogen interaction and maintaining cellular integrity. Furthermore, genetic mutations involved in actin cytoskeleton regulation were found to have deleterious effects in immune response (Sprenkeler et al., 2020). These are collectively called immunological actinophaties, which further implicate actin in the paradigm of infection.

Infection with *Cryptococcus* was found to strongly induce ruffle production by MΦ. This was however not seen with *Candida albicans*, a similar yeast pathogen, after incubation at 30 minutes, 1- and 2-hours using SEM and fluorescence imaging (data not shown). Report of Tsarfaty (2000) and colleagues showed that *C. albicans* have rather anti-ruffling effect through their secretion of actin-rearranging *Candida*-secreted factor (arcsf).

Ruffling was reported to have an adverse effect in some infections such as *Staphylococcus aureus*, wherein fluid uptake by macropinocytosis is utilised by the pathogen as a nutrient source (Flannagan and Heinrich, 2020). In *Cryptococcus*, the influence of these ruffles on pathogen survival and infection outcome is not yet explored. It would be useful to illustrate the role of these membrane structures in Cryptococcal infection as membrane ridges appear to promote phagocytic uptake. Hence, transition to a ruffle phenotype could be potentially targeted to modulate infection outcome.

Finally, the role of actin cortex in infection is an exciting research avenue. Technological improvements in both specimen preparation and cell imaging in recent years had transformed our understanding on the role of cortical actin in different cellular processes such as cell shape regulation, cell division, cell motility and bleb growth (Chugh and Paluch, 2018). In immune cells, the importance of actin cortex in cellular mechanics had only been recently appreciated as advances in superresolution live imaging enabled its direct

examination (Colin-York et al., 2019). Understanding changes in the properties of the cortical actin during infection will provide us a better understanding of the biophysical underpinnings of infection control by macrophages. The very dramatic changes in macrophage actin cytoskeleton during Cryptococcal infection uncovered in here would be good starting points to further inquire and fill the wide knowledge gap in cellular mechanics during early stages of infection.

CHAPTER 6

Final Discussion

6.1 Membrane ridges: architecture, dynamics and responses to different factors

In this thesis I presented my findings on the biophysical properties of the macrophage surface, focussing on membrane ridges, and the mechanics of phagocytic uptake of spherical targets. Using a combination of electron and superresolution microscopy techniques, I described the ultrastructural features of the dorsal surface of different types of macrophages cultured *in vitro*. I found short-lived (i.e. less than one minute average lifetime), wavy and sheet-like protrusions with consistent thickness produced by these cells which I referred to as membrane ridges due to their appearance on the macrophage surface using 3D SEM. I found membrane ridges to be a highly conserved feature amongst phagocytic cells, from unicellular amoeba *Dictyostelium discoideum* up to human macrophages. Label-free imaging using DIC enabled me to describe their dynamics on the surface which is characterised by splitting and fusion events. Remarkably, their thickness is highly maintained throughout these processes and their lifetime indicating the importance of maintaining this geometric feature in generating membrane ridges.

Comparing the membrane ridges with other actin-based structures in macrophages, I found that its thickness is very similar to cortical actin. Moreover, I also found that the prominent cortical actin nucleator Arp2/3 (Bovellan et al., 2014) was also enriched in membrane ridges alongside nucleation promoting factor WASH. Liu (2009) and colleagues showed that WASH links branched and linear actin nucleation by acting downstream of Rho1 and Arp2/3. This suggests that both branched and linear actin filaments might be present in ridges, however the more frequent expression of Arp2/3 in ridges suggests that branched actin filaments might be its predominant actin architecture. Determining whether or not capping proteins are enriched in ridges could help shed light on this matter as capping rate was seen to be higher at increasing branching rate in sheet-like protrusions like lamellipodia (Schaub et al., 2007). Mechanically, shorter filaments are also more stable than longer ones in pushing the membrane as they are more rigid (Mogilner and Oster, 1996), showing its relevance in producing transient nanoscopic protrusions with conserved geometry.

The production of membrane ridges was also found to be influenced by different factors including genetic, chemical and mechanical variables. Suppression of pro-inflammatory genes *trib1* and *trib3* were found to reduce the expression of membrane ridges. This is corroborated by exposing macrophages to cytokines that yield a pro-inflammatory or

an anti-inflammatory phenotype. After I subjected cells to IL-10, a potent anti-inflammatory cytokine, ridges were almost entirely inhibited. Meanwhile, cells that were subjected to pro-inflammatory cytokines, LPS and IFNγ, did not show any statistically significant difference in ridge density with unstimulated macrophages, suggesting that ridges might play an important role in key pro-inflammatory responses such as phagocytosis which involves physical interactions with a target. Interestingly, IL-4 activation which is considered an anti-inflammatory cytokine also resulted to a conserved ridge density on the macrophage surface. An important immunological event that is mediated by both IL-4 and IFNγ is antigen presentation (Hart et al., 1996; Smiley and Grusby, 1998), which allow macrophages to present antigens from degraded pathogen to T cells for their activation. Furthermore, IL10 is well known to have immunosuppressive activity by inhibiting antigen presentation (Mittal and Roche, 2015).

Finally, I found that media osmolarity can affect the production of membrane ridges by macrophages. After I subjected macrophages to extremely hypoosmotic media (0.2% NaCl), membrane ridges were almost completely repressed, suggesting a negative regulation of membrane ridges by osmotic pressure. Interestingly, when I examined changes in macrophage filopodia with respect to their count and area density at different osmotic conditions, they seem to be unchanged compared to membrane ridges. This indicates that membrane ridges are more sensitive to osmotic stress than filopodia which could be exploited when examining physiological responses of macrophages in organs with pronounced changes in osmolarity such as kidney (Burg et al., 2007) and liver (Schliess et al., 2007).

6.2 Phagocytosis of spherical particles

Phagocytosis is a highly dynamic process with very striking mechanical attributes to internalise targets and process them intracellularly. Previous studies (Pacheco et al., 2013; Champion et al., 2008; Champion and Mitragotri, 2006; Richard and Endres, 2016; Sosale et al., 2015; Beningo and Wang, 2002) have shown the effect of the target's physical properties on its phagocytic fate, however how these physical properties play a role in the uptake of actual pathogens is less understood. Initially, I examined how spherical beads of different sizes are taken up by macrophages. I found size-dependence in the uptake of spherical targets with smaller beads generally taken up better than larger ones. More importantly, by examining the uptake of specific bead sizes, I determined trends in taking up unopsonised and opsonised beads. Whilst both showed size-dependence in their uptake, opsonised beads were generally taken up better than their unopsonised counterpart. Moreover, in opsonised beads, those with 0.25 um radius were taken up less than those with 0.5 um radius compared to unopsonised beads where no statistically significant uptake difference was found between these sizes

(Figure 4.7F). These could be potentially explained by subtle mechanistic differences in the uptake of these targets with respect to the phagocytic receptors involved.

Using my beads phagocytic uptake data, I analysed the phagocytosis of spherical fungal pathogen *Cryptococcus neoformans*. I found that its surface property (i.e. absence or presence of capsule) rather than its size determines its uptake with acapsular Cryptococcus taken up better than their capsular counterpart. Moreover, as capsule thickness increases, the rate of uptake decreases indicating its antiphagocytic role. This appears to be supported by my bead uptake data (Figure 4.7F) as targets in this size regime (2.2 – 2.6 um radius) would be poorly taken up by macrophages when interpolating from this data, except if they were opsonised. This was confirmed when capsular H99 Cryptococcus were opsonised, and a 5-fold increase in phagocytic uptake was found.

6.3 Actin cytoskeletal changes in macrophages during interaction with Cryptococcus

Finally, using SEM and fluorescence microscopy, I explored the dynamics of macrophage-Cryptococcus interaction, specifically during the early periods (i.e. within 2 hours) of infection. I found a remarkable transformation of the macrophage surface immediately after exposure to capsular or acapsular Cryptococcus (within 5 minutes) from high ridge density to predominance of dorsal ruffles. By comparing the area density of these two actin-rich structures at different infection timepoints, I found an inverse relationship between them suggesting that ridges are converted into ruffles during infection. Further following the course of infection, membrane ridges and dorsal ruffles are both repressed 60 minutes post infection, and membrane blebs are commonly seen on the surface. I also observed that actin cortex became more distinct at this timepoint suggesting the importance of regulating cell shape during phagocytic uptake of Cryptococcus. Intracellular compartments whose size seemed to be influenced by the number of Cryptococcus internalised were seen to be prominent on this late infection timepoint. I was not able to examine whether this compartmentalisation phenotype has a physiological implication as well such that cargo processing could be more efficient when segregating internalised target according to size to deliver the necessary amount of degradative enzymes according to cargo size.

Using my previous observation that ridges are repressed 60 minutes post infection, I examined their role in the phagocytic uptake of Cryptococcus. My results showed that both capsular H99 and acapsular CAP59 Cryptococcus had reduced phagocytosis upon ridge inhibition, however only CAP59 showed a statistically significant reduction. Furthermore, due to the experimental design in this assay where macrophages were pre-exposed to Cryptococcus in determining the role of ridges in Cryptococcus phagocytosis, it should be

clearly dissected if the reduction in uptake is due to absence of membrane ridges or alteration in the mechanical properties of macrophages due to previous Cryptococcus uptake. Hence, this experiment could be repeated by pharmacological treatment of macrophages such as IL10 to inhibit ridges or using Cryptococcus conditioned media to repress ridges and then measuring phagocytic uptake.

6.4 Conclusions and future outlook

This thesis showed the indispensable role of imaging in studying the structural and dynamic properties of macrophages and the biophysical nature of phagocytosis. The striking mechanical attributes of macrophages could be seen in their ability to produce different types of membrane protrusions. Amongst these structures that was extensively investigated in this thesis is the membrane ridge. The regularity of their thickness throughout their lifetime suggests that a tight regulation in their production exists despite their relatively transient nature. This perhaps reflects how macrophages operate in nature, which is marked by a fine-tuned control of their features amidst their highly sophisticated role of responding to various external perturbations.

The striking results revealed in this thesis pose important questions to further understand phagocyte biology and the mechanics of phagocytosis. The extremely consistent thickness of membrane ridges throughout their lifetime suggests that a highly regulated actin dynamics exists in producing these membrane protrusions. Known regulators of actin polymerisation such as capping proteins and nucleators could be further examined through an imaging approach to understand how their interaction, if any, might result into such protrusion phenotype. A very important nucleator candidate that is shown to localised in membrane ridges in this thesis is Arp2/3. It would be critical to confirm the presence of capping proteins in membrane ridges to further explore the notion of a "fine balance" between capping rate and branching rate (Schaub et al., 2006) by simulations to generate a sheet-like protrusion with consistent thickness. The sensitivity of membrane ridges to different factors such as cytokines and osmotic stress is also worth investigating further which might inform how cytoskeletal changes amongst macrophages are regulated. By exploring gene pathways implicating ridges, macrophage activation and stress response such as trib3, which was also revealed in this thesis, the role of cytoskeleton in producing different macrophage phenotypes could be determined which would be very useful in manipulating macrophages for desired outcomes in infection, development and other areas where they play a critical role. Finally, the mechanics of phagocytosis is still unclear as to how it appears to be target size and surface property dependent. Exploring membrane energetics as to how actin generates the force required to overcome the elastic resistance of the membrane to engulf phagocytic targets would be a huge advancement towards understanding phagocytosis and its inherent biophysical properties.

REFERENCES

Aamri, F. E., Remuzgo-Martínez, S., Acosta, F., Real, F., Ramos-Vivas, J., Icardo, J. M., & Padilla, D. (2015). Interactions of *Streptococcus iniae* with phagocytic cell line. *Microbes and Infection*, *17*(4). https://doi.org/10.1016/j.micinf.2014.06.006

Abel, A. M., Yang, C., Thakar, M. S., & Malarkannan, S. (2018). Natural Killer Cells: Development, Maturation, and Clinical Utilization. *Frontiers in Immunology*, *9*, 1869. https://doi.org/10.3389/fimmu.2018.01869

Abercrombie, M., Heaysman, J. E. M., & Pegrum, S. M. (1971). The locomotion of fibroblasts in culture. *Experimental Cell Research*, *67*(2). https://doi.org/10.1016/0014-4827(71)90420-4

Agudo-Canalejo, J., & Lipowsky, R. (2016). Stabilization of membrane necks by adhesive particles, substrate surfaces, and constriction forces. *Soft Matter*, *12*(39), 8155–8166. https://doi.org/10.1039/C6SM01481J

Akira, S., Uematsu, S., & Takeuchi, O. (2006). Pathogen Recognition and Innate Immunity. *Cell*, *124*(4), 783–801. https://doi.org/10.1016/j.cell.2006.02.015

Aksenov, S. I., Babyeva, I. P., & Golubev, V. I. (1973). On the mechanism of adaptation of micro-organisms to conditions of extreme low humidity. *Life Sciences and Space Research*, *11*, 55–61.

Albert, M. L., Kim, J. I., & Birge, R. B. (2000). α(v)β5 Integrin recruits the CrkII-Dock180-Rac1 complex for phagocytosis of apoptotic cells. *Nature Cell Biology*, *2*(12). https://doi.org/10.1038/35046549

Alberts, B., Johnson, A., Lewis, J., Morgan, D., Raff, M., Roberts, K., & Walter, P. (2015). *Molecular Biology of the cell* (6th ed.). Garland.

Albuschies, J., & Vogel, V. (2013). The role of filopodia in the recognition of nanotopographies. *Scientific Reports*, *3*. https://doi.org/10.1038/srep01658

Ali, A. K., Komal, A. K., Almutairi, S. M., & Lee, S. H. (2019). Natural Killer Cell-Derived IL-10 Prevents Liver Damage During Sustained Murine Cytomegalovirus Infection. *Frontiers in Immunology*, *10*. https://doi.org/10.3389/fimmu.2019.02688

Alvarez, M., & Casadevall, A. (2006). Phagosome Extrusion and Host-Cell Survival after Cryptococcus neoformans Phagocytosis by Macrophages. *Current Biology*, *16*(21). https://doi.org/10.1016/j.cub.2006.09.061

Anand, P. K., Tait, S. W. G., Lamkanfi, M., Amer, A. O., Nunez, G., Pagès, G., Pouysségur, J., McGargill, M. A., Green, D. R., & Kanneganti, T. D. (2011). TLR2 and RIP2 pathways mediate autophagy of Listeria monocytogenes via extracellular signal-regulated kinase (ERK)

activation. *Journal of Biological Chemistry*, *286*(50). https://doi.org/10.1074/jbc.M111.310599

Anderson, C. L., Shen, L., Eicher, D. M., Wewers, M. D., & Gill, J. K. (1990). Phagocytosis mediated by three distinct Fcγ receptor classes on human leukocytes. *Journal of Experimental Medicine*, *171*(4). https://doi.org/10.1084/jem.171.4.1333

Anderson, K. I. (1998). The Keratocyte Cytoskeleton: A Dynamic Structural Network. In D. A. Beysens & G. Forgacs (Eds.), *Dynamical Networks in Physics and Biology* (pp. 27–40). Springer Berlin Heidelberg.

Araki, N., Hatae, T., Furukawa, A., & Swanson, J. A. (2003). Phosphoinositide-3-kinase-independent contractile activities associated with Fcγ-receptor-mediated phagocytosis and macropinocytosis in macrophages. *Journal of Cell Science*, *116*(2), 247–257. https://doi.org/10.1242/jcs.00235

Araújo, G. R., Fontes, G. N., Leão, D., Rocha, G. M., Pontes, B., Sant'Anna, C., de Souza, W., & Frases, S. (2016). Cryptococcus neoformans capsular polysaccharides form branched and complex filamentous networks viewed by high-resolution microscopy. *Journal of Structural Biology*, *193*(1), 75–82. https://doi.org/10.1016/j.jsb.2015.11.010

Arndt, L., Dokas, J., Gericke, M., Kutzner, C. E., Müller, S., Jeromin, F., Thiery, J., & Burkhardt, R. (2018). Tribbles homolog 1 deficiency modulates function and polarization of murine bone marrow– derived macrophages. *Journal of Biological Chemistry*, *293*(29), 11527–11536. https://doi.org/10.1074/jbc.RA117.000703

Arredouani, M. S., Palecanda, A., Koziel, H., Huang, Y.-C., Imrich, A., Sulahian, T. H., Ning, Y. Y., Yang, Z., Pikkarainen, T., Sankala, M., Vargas, S. O., Takeya, M., Tryggvason, K., & Kobzik, L. (2005). MARCO Is the Major Binding Receptor for Unopsonized Particles and Bacteria on Human Alveolar Macrophages. *The Journal of Immunology*, *175*(9), 6058–6064. https://doi.org/10.4049/jimmunol.175.9.6058

Ayers, G. R., & Dainty, J. C. (1988). Iterative blind deconvolution method and its applications. In *OPTICS LETTERS* (Vol. 13, Issue 7).

Ayoub, A. M., Klinzing, G. E., & Ekmann, J. M. (1983). Effect of particle size and shape on settling using an integral approach. *Powder Technology*, *35*(1). https://doi.org/10.1016/0032-5910(83)85027-X

Bainton, D. F., & Farquhar, M. G. (1971). The development of neutrophilic polymorphonuclear leukocytes in human bone marrow origin and content of azurophil and specific granules. 28.

Barger, S. R., Reilly, N. S., Shutova, M. S., Li, Q., Maiuri, P., Heddleston, J. M., Mooseker, M. S., Flavell, R. A., Svitkina, T., Oakes, P. W., Krendel, M., & Gauthier, N. C. (2019). Membrane-cytoskeletal crosstalk mediated by myosin-I regulates adhesion turnover during phagocytosis. *Nature Communications*, *10*(1). https://doi.org/10.1038/s41467-019-09104-1

Barrangou, R., Fremaux, C., Deveau, H., Richards, M., Boyaval, P., Moineau, S., Romero, D. A., & Horvath, P. (2007). CRISPR Provides Acquired Resistance Against Viruses in Prokaryotes. *Science*, *315*(5819), 1709–1712. https://doi.org/10.1126/science.1138140

Becker, T., Volchuk, A., & Rothman, J. E. (2005). Differential use of endoplasmic reticulum membrane for phagocytosis in J774 macrophages. In *PNAS March* (Vol. 15, Issue 11, pp. 4022–4026). www.pnas.orgcgidoi10.1073pnas.0409219102

Bedoui, S., Gebhardt, T., Gasteiger, G., & Kastenmüller, W. (2016). Parallels and differences between innate and adaptive lymphocytes. *Nature Immunology*, *17*(5), 490–494. https://doi.org/10.1038/ni.3432

Behar, S. M., Martin, C. J., Booty, M. G., Nishimura, T., Zhao, X., Gan, H.-X., Divangahi, M., & Remold, H. G. (2011). Apoptosis is an innate defense function of macrophages against Mycobacterium tuberculosis. *Mucosal Immunology*, *4*(3), 279–287. https://doi.org/10.1038/mi.2011.3

Belay, T., Cherniak, R., O'Neill, E. B., & Kozel, T. R. (1996). Serotyping of Cryptococcus neoformans by dot enzyme assay. *Journal of Clinical Microbiology*, *34*(2), 466–470. https://doi.org/10.1128/jcm.34.2.466-470.1996

Beningo, K. a, & Wang, Y. (2002). Fc-receptor-mediated phagocytosis is regulated by mechanical properties of the target. *Journal of Cell Science*, *115*, 849–856. https://doi.org/10.1146/annurev.immunol.17.1.593

Berenson, C. S., Kruzel, R. L., Eberhardt, E., & Sethi, S. (2013). Phagocytic dysfunction of human alveolar macrophages and severity of chronic obstructive pulmonary disease. *The Journal of Infectious Diseases*, *208*(12), 2036–2045. https://doi.org/10.1093/infdis/jit400

Bian, H., Li, F., Wang, W., Zhao, Q., Gao, S., Ma, J., Li, X., Ren, W., Qin, C., & Qi, J. (2017). MAPK/p38 regulation of cytoskeleton rearrangement accelerates induction of macrophage activation by TLR4, but not TLR3. *International Journal of Molecular Medicine*, *40*(5), 1495–1503. https://doi.org/10.3892/ijmm.2017.3143

Blystone, S. D., Graham, I. L., Lindberg, F. P., & Brown, E. J. (1994). Integrin α(v)β3 differentially regulates adhesive and phagocytic functions of the fibronectin receptor α5β1. *Journal of Cell Biology*, *127*(4). https://doi.org/10.1083/jcb.127.4.1129

Bohdanowicz, M., Cosío, G., Backer, J. M., & Grinstein, S. (2010). Class I and class III phosphoinositide 3-kinases are required for actin polymerization that propels phagosomes. *Journal of Cell Biology*, *191*(5), 999–1012. https://doi.org/10.1083/jcb.201004005

Bohdanowicz, M., & Grinstein, S. (2013). Role of phospholipids in endocytosis, phagocytosis, and macropinocytosis. *Physiological Reviews*, *93*(1), 69–106. https://doi.org/10.1152/physrev.00002.2012

Bohdanowicz, M., Schlam, D., Hermansson, M., Rizzuti, D., Fairn, G. D., Ueyama, T., Somerharju, P., Du, G., & Grinstein, S. (2013). Phosphatidic acid is required for the constitutive ruffling and macropinocytosis of phagocytes. *Molecular Biology of the Cell*, *24*(11), 1700–1712. https://doi.org/10.1091/mbc.E12-11-0789

Bojarczuk, A., Miller, K. A., Hotham, R., Lewis, A., Ogryzko, N. V., Kamuyango, A. A., Frost, H., Gibson, R. H., Stillman, E., May, R. C., Renshaw, S. A., & Johnston, S. A. (2016). Cryptococcus neoformans Intracellular Proliferation and Capsule Size Determines Early Macrophage Control of Infection. *Scientific Reports*, *6*(February), 1–15. https://doi.org/10.1038/srep21489

Bonnett, C. R., Cornish, E. J., Harmsen, A. G., & Burritt, J. B. (2006). Early Neutrophil Recruitment and Aggregation in the Murine Lung Inhibit Germination of *Aspergillus fumigatus* Conidia. *Infection and Immunity*, *74*(12), 6528–6539. https://doi.org/10.1128/IAI.00909-06

Borle, A. B., Freudenrich, C. C., & Snowdowne, K. W. (1986). A simple method for incorporating aequorin into mammalian cells. *American Journal of Physiology - Cell Physiology*, *251*(2 (20/2)). https://doi.org/10.1152/ajpcell.1986.251.2.c323

Bornschlögl, T. (2013). How filopodia pull: What we know about the mechanics and dynamics of filopodia: Bornschlögl. *Cytoskeleton*, *70*(10), 590–603. https://doi.org/10.1002/cm.21130

Bovellan, M., Romeo, Y., Biro, M., Boden, A., Chugh, P., Yonis, A., Vaghela, M., Fritzsche, M., Moulding, D., Thorogate, R., Jégou, A., Thrasher, A. J., Romet-Lemonne, G., Roux, P. P., Paluch, E. K., & Charras, G. (2014). Cellular control of cortical actin nucleation. *Current Biology*, *24*(14), 1628–1635. https://doi.org/10.1016/j.cub.2014.05.069

Bradford, J. E. (2021). *Modelling actin polymerisation and phagocytosis*. Doctoral dissertation, University of Sheffield.

Bresser, P., Out, T. A., van ALPHEN, L., Jansen, H. M., & Lutter, R. (2000). Airway Inflammation in Nonobstructive and Obstructive Chronic Bronchitis with Chronic *Haemophilus influenzae* Airway Infection: Comparison with Noninfected Patients with Chronic Obstructive Pulmonary Disease. *American Journal of Respiratory and Critical Care Medicine*, *162*(3), 947–952. https://doi.org/10.1164/ajrccm.162.3.9908103

Brinkmann, V., Reichard, U., Goosmann, C., Fauler, B., Uhlemann, Y., Weiss, D. S., Weinrauch, Y., & Zychlinsky, A. (2004). Neutrophil Extracellular Traps Kill Bacteria. *Science*, *303*(5663). https://doi.org/10.1126/science.1092385

Brown, G. D., & Gordon, S. (2001). Immune recognition. A new receptor for beta-glucans. *Nature*, *413*(September).

Buchmann, K. (2014). Evolution of innate immunity: Clues from invertebrates via fish to mammals. *Frontiers in Immunology*, *5*(SEP). https://doi.org/10.3389/fimmu.2014.00459

Buracco, S., Claydon, S., & Insall, R. (2019). Control of actin dynamics during cell motility. *F1000Research*, *8*, 1977. https://doi.org/10.12688/f1000research.18669.1

Burg, M. B., Ferraris, J. D., & Dmitrieva, N. I. (2007). Cellular response to hyperosmotic stresses. *Physiological Reviews*, *87*(4), 1441–1474. https://doi.org/10.1152/physrev.00056.2006

Burmeister, W. P., Huber, A. H., & Bjorkman, P. J. (1994). Crystal structure of the complex of rat neonatal Fc receptor with Fc. *Nature*, *372*(6504). https://doi.org/10.1038/372379a0

Burwen, S. J., & Satir, B. H. (1977). Plasma Membrane Folds on the Mast Cell Surface and Their Relationship to Secretory. In *Source: The Journal of Cell Biology* (Vol. 74, Issue 3, pp. 690–697). https://about.jstor.org/terms

Butcher, L., Ahluwalia, M., Örd, T., Johnston, J., Morris, R. H., Kiss-Toth, E., Örd, T., & Erusalimsky, J. D. (2017). Evidence for a role of TRIB3 in the regulation of megakaryocytopoiesis. *Scientific Reports*, *7*(1), 6684. https://doi.org/10.1038/s41598-017-07096-w

Byrne, A. J., Mathie, S. A., Gregory, L. G., & Lloyd, C. M. (2015). Pulmonary macrophages: Key players in the innate defence of the airways. *Thorax*, *70*(12), 1189–1196. https://doi.org/10.1136/thoraxjnl-2015-207020

Byrnes, E. J., Li, W., Lewit, Y., Ma, H., Voelz, K., Ren, P., Carter, D. A., Chaturvedi, V., Bildfell, R. J., May, R. C., & Heitman, J. (2010). Emergence and Pathogenicity of Highly Virulent Cryptococcus gattii Genotypes in the Northwest United States. *PLoS Pathogens*, *6*(4), e1000850. https://doi.org/10.1371/journal.ppat.1000850

Cammarota, E., Soriani, C., Taub, R., Morgan, F., Sakai, J., Veatch, S. L., Bryant, C. E., & Cicuta, P. (2020). Criticality of plasma membrane lipids reflects activation state of macrophage cells. *Journal of the Royal Society Interface*, *17*(163). https://doi.org/10.1098/rsif.2019.0803

Campellone, K. G., & Welch, M. D. (2010). A nucleator arms race: Cellular control of actin assembly. *Nature Reviews Molecular Cell Biology*, *11*(4), 237–251. https://doi.org/10.1038/nrm2867

Campesino, L. M., Johnston, J., Kiss-Toth, E., & Wilson, H. (2018). *114 TRIB3-mediated regulation of macrophage phenotype*. https://doi.org/10.1136/heartjnl-2018-bcs.113

Capilla, J., Maffei, C. M. L., Clemons, K. V., Sobel, R. A., & Stevens, D. A. (2006). Experimental systemic infection with *Cryptococcus neoformans* var. *Grubii* and *Cryptococcus gattii* in

normal and immunodeficient mice. *Medical Mycology*, *44*(7), 601–610. https://doi.org/10.1080/13693780600810040

Carey, B., & Trapnell, B. C. (2010). The molecular basis of pulmonary alveolar proteinosis. *Clinical Immunology*, *135*(2), 223–235. https://doi.org/10.1016/j.clim.2010.02.017

Casadevall, A., Cleare, W., Feldmesser, M., Glatman-Freedman, A., Goldman, D. L., Kozel, T. R., Lendvai, N., Mukherjee, J., Pirofski, L.-A., Rivera, J., Rosas, A. L., Scharff, M. D., Valadon, P., Westin, K., & Zhong, A. Z. (1998). *Characterization of a Murine Monoclonal Antibody to Cryptococcus neoformans Polysaccharide That Is a Candidate for Human Therapeutic Studies* (Vol. 42, Issue 6, pp. 1437–1446).

Casadevall, A., Coelho, C., Cordero, R. J. B., Dragotakes, Q., Jung, E., Vij, R., & Wear, M. P. (2019). The capsule of *Cryptococcus neoformans*. *Virulence*, *10*(1), 822–831. https://doi.org/10.1080/21505594.2018.1431087

Castro, S. A., Collighan, R., Lambert, P. A., Dias, I. H., Chauhan, P., Bland, C. E., Milic, I., Milward, M. R., Cooper, P. R., & Devitt, A. (2017). Porphyromonas gingivalis gingipains cause defective macrophage migration towards apoptotic cells and inhibit phagocytosis of primary apoptotic neutrophils. *Cell Death and Disease*, *8*(3), e2644-9. https://doi.org/10.1038/cddis.2016.481

Chalut, K. J., & Paluch, E. K. (2016). The Actin Cortex: A Bridge between Cell Shape and Function. *Developmental Cell*, *38*(6), 571–573. https://doi.org/10.1016/j.devcel.2016.09.011

Champion, J. A., & Mitragotri, S. (2006). Role of target geometry in phagocytosis. *Proceedings of the National Academy of Sciences*, *103*(13), 4930–4934. https://doi.org/10.1073/pnas.0600997103

Champion, J. A., & Mitragotri, S. (2009). Shape induced inhibition of phagocytosis of polymer particles. *Pharmaceutical Research*, *26*(1), 244–249. https://doi.org/10.1007/s11095-008-9626-z

Champion, J. A., Walker, A., & Mitragotri, S. (2008). Role of particle size in phagocytosis of polymeric microspheres. *Pharmaceutical Research*, *25*(8), 1815–1821. https://doi.org/10.1007/s11095-008-9562-y

Chaplin, D. D. (2010). Overview of the immune response. *Journal of Allergy and Clinical Immunology*, *125*(2 SUPPL. 2). https://doi.org/10.1016/j.jaci.2009.12.980

Charlier, C., Chrétien, F., Baudrimont, M., Mordelet, E., Lortholary, O., & Dromer, F. (2005). Capsule Structure Changes Associated with Cryptococcus neoformans Crossing of the Blood-Brain Barrier. *The American Journal of Pathology*, *166*(2), 421–432. https://doi.org/10.1016/S0002-9440(10)62265-1

Charras, G. T., Yarrow, J. C., Horton, M. A., Mahadevan, L., Mitchison, T. J., & Charras, G. (2005). Non-equilibration of hydrostatic pressure in blebbing cells. In *Nature* (Vol. 435, Issue 7040, pp. 365–369).

Cherniak, R., Reiss, E., Slodki, M. E., Plattner, R. D., & Blumer, S. O. (1980). Structure and antigenic activity of the capsular polysaccharide of Cryptococcus neoformans serotype A. *Molecular Immunology*, *17*(8). https://doi.org/10.1016/0161-5890(80)90096-6

Chu, V. T., Fröhlich, A., Steinhauser, G., Scheel, T., Roch, T., Fillatreau, S., Lee, J. J., Löhning, M., & Berek, C. (2011). Eosinophils are required for the maintenance of plasma cells in the bone marrow. *Nature Immunology*, *12*(2). https://doi.org/10.1038/ni.1981

Chugh, P., Clark, A. G., Smith, M. B., Cassani, D. A. D., Dierkes, K., Ragab, A., Roux, P. P., Charras, G., Salbreux, G., & Paluch, E. K. (2017). Actin cortex architecture regulates cell surface tension. *Nature Cell Biology*, *19*(6), 689–697. https://doi.org/10.1038/ncb3525

Chugh, P., & Paluch, E. K. (2018). The actin cortex at a glance. *Journal of Cell Science*, *131*(14). https://doi.org/10.1242/jcs.186254

Ciano, C. D., Nie, Z., Sza, K., Lewis, A., Uruno, T., Zhan, X., Rotstein, O. D., Mak, A., Kapus, S., Ciano, D., szi, K. S., & Kapus, A. (2002). Osmotic stress-induced remodeling of the cortical cytoskeleton. *Am J Physiol Cell Physiol*, *283*, 850–865. https://doi.org/10.1152/ajpcell.00018.2002.-Osmotic

Cisse, B., Caton, M. L., Lehner, M., Maeda, T., Scheu, S., Locksley, R., Holmberg, D., Zweier, C., Hollander, N. S. den, Kant, S. G., Holter, W., Rauch, A., Zhuang, Y., & Reizis, B. (2008). Transcription Factor E2-2 Is an Essential and Specific Regulator of Plasmacytoid Dendritic Cell Development. *Cell*, *135*(1). https://doi.org/10.1016/j.cell.2008.09.016

Clark, A. G., Dierkes, K., & Paluch, E. K. (2013). Monitoring actin cortex thickness in live cells. *Biophysical Journal*, *105*(3), 570–580. https://doi.org/10.1016/j.bpj.2013.05.057

Coleman, M. L., Sahai, E. A., Yeo, M., Bosch, M., Dewar, A., & Olson, M. F. (2001). Membrane blebbing during apoptosis results from caspase-mediated activation of ROCK I. In *NATURE CELL BIOLOGY* (Vol. 3). http://cellbio.nature.com

Colin-York, H., Li, D., Korobchevskaya, K., Chang, V. T., Betzig, E., Eggeling, C., & Fritzsche, M. (2019). Cytoskeletal actin patterns shape mast cell activation. *Communications Biology*, *2*(1), 1–12. https://doi.org/10.1038/s42003-019-0322-9

Condon, N. D., Heddleston, J. M., Chew, T. L., Luo, L., Mcpherson, P. S., Ioannou, M. S., Hodgson, L., Stow, J. L., & Wall, A. A. (2018). Macropinosome formation by tent pole ruffling in macrophages. *Journal of Cell Biology*, DOI: 10.1083/jcb.201804137. https://doi.org/10.1083/jcb.201804137

Cordero, R. J. B., Pontes, B., Guimarães, A. J., Martinez, L. R., Rivera, J., Fries, B. C., Nimrichter, L., Rodrigues, M. L., Viana, N. B., & Casadevall, A. (2011). Chronological aging is associated

with biophysical and chemical changes in the capsule of Cryptococcus neoformans. *Infection and Immunity*, *79*(12). https://doi.org/10.1128/IAI.05789-11

Cornelissen, S., Botha, A., Conradie, W. J., & Wolfaardt, G. M. (2003). Shifts in community composition provide a mechanism for maintenance of activity of soil yeasts in the presence of elevated copper levels. *Canadian Journal of Microbiology*, *49*(7), 425–432. https://doi.org/10.1139/w03-057

Couper, K. N., Blount, D. G., & Riley, E. M. (2008). IL-10: The Master Regulator of Immunity to Infection. *The Journal of Immunology*, *180*(9), 5771–5777. https://doi.org/10.4049/jimmunol.180.9.5771

Cowland, J. B., & Borregaard, N. (2016). Granulopoiesis and granules of human neutrophils. *Immunological Reviews*, *273*(1), 11–28. https://doi.org/10.1111/imr.12440

Crispe, I. N. (2014). Immune tolerance in liver disease. *Hepatology (Baltimore, Md.)*, *60*(6), 2109–2117. https://doi.org/10.1002/hep.27254

Cross, C. E., & Bancroft, G. J. (1995). Ingestion of Acapsular Cryptococcus neoformans Occurs via Mannose and-Glucan Receptors, Resulting in Cytokine Production and Increased Phagocytosis of the Encapsulated Form. In *INFECTION AND IMMUNITY* (Vol. 63, Issue 7, pp. 2604–2611). https://journals.asm.org/journal/iai

Cuevas, C. D., & Ross, S. R. (2014). Toll-Like Receptor 2-Mediated Innate Immune Responses against Junín Virus in Mice Lead to Antiviral Adaptive Immune Responses during Systemic Infection and Do Not Affect Viral Replication in the Brain. *Journal of Virology*, *88*(14). https://doi.org/10.1128/jvi.00050-14

Daëron, M., Malbec, O., Bonnerot, C., Latour, S., Segal, D. M., & Fridman, W. H. (1994). Tyrosine-containing activation motif-dependent phagocytosis in mast cells. *The Journal of Immunology*, *152*(2), 783.

Davenport, M. P., Smith, N. L., & Rudd, B. D. (2020). Building a T cell compartment: How immune cell development shapes function. *Nature Reviews Immunology*, *20*(8), 499–506. https://doi.org/10.1038/s41577-020-0332-3

Davies, L. C., Jenkins, S. J., Allen, J. E., & Taylor, P. R. (2013). Tissue-resident macrophages. *Nature Immunology*, *14*(10), 986–995. https://doi.org/10.1038/ni.2705

Davis, J. M., Huang, M., Botts, M. R., Hull, C. M., & Huttenlocher, A. (2016). A zebrafish model of cryptococcal infection reveals roles for macrophages, endothelial cells, and neutrophils in the establishment and control of sustained fungemia. *Infection and Immunity*, *84*(10). https://doi.org/10.1128/IAI.00506-16

DeLeo, F. R., Otto, M., Kreiswirth, B. N., & Chambers, H. F. (2010). Community-associated meticillin-resistant Staphylococcus aureus. *The Lancet*, *375*(9725), 1557–1568. https://doi.org/10.1016/S0140-6736(09)61999-1

Delneste, Y., Lassalle, P., Jeannin, P., Joseph, M., Tonnel, A. B., & Gosset, P. (1994). Histamine induces IL-6 production by human endothelial cells. *Clinical and Experimental Immunology*, *98*(2). https://doi.org/10.1111/j.1365-2249.1994.tb06148.x

Deng, Z., Zink, T., Chen, H. Y., Walters, D., Liu, F. T., & Liu, G. Y. (2009). Impact of actin rearrangement and degranulation on the membrane structure of primary mast cells: A combined atomic force and laser scanning confocal microscopy investigation. *Biophysical Journal*, *96*(4), 1629–1639. https://doi.org/10.1016/j.bpj.2008.11.015

Dey, S., Zeeshan Ali, S., & Padhi, E. (2019). Terminal fall velocity: The legacy of Stokes from the perspective of fluvial hydraulics. *Proceedings of the Royal Society A: Mathematical, Physical and Engineering Sciences*, *475*(2228), 20190277. https://doi.org/10.1098/rspa.2019.0277

Divangahi, M., King, I. L., & Pernet, E. (2015). Alveolar macrophages and type I IFN in airway homeostasis and immunity. *Trends in Immunology*, *36*(5), 307–314. https://doi.org/10.1016/j.it.2015.03.005

Dohlsten, M., Kalland, T., Sjögren, H. O., & Carlsson, R. (1988). Histamine inhibits interleukin 1 production by lipopolysaccharide-stimulated human peripheral blood monocytes. *Scandinavian Journal of Immunology*, *27*(5), 527–532. https://doi.org/10.1111/j.1365-3083.1988.tb02379.x

Doering, T. L., Nosanchuk, J. D., Roberts, W. K., & Casadevall, A. (1999). Melanin as a potential cryptococcal defence against microbicidal proteins. *Medical Mycology*, *37*(3), 175–181.

Dowrick, P., Kenworthy, P., McCann, B., & Warn, R. (1993). Circular ruffle formation and closure lead to macropinocytosis in hepatocyte growth factor/scatter factor-treated cells. *European Journal of Cell Biology*, *61*(1).

Drengk, A., Fritsch, J., Schmauch, C., Rühling, H., & Maniak, M. (2003). A Coat of Filamentous Actin Prevents Clustering of Late-Endosomal Vacuoles in Vivo. *Current Biology*, *13*(20). https://doi.org/10.1016/j.cub.2003.09.037

Dries, K. V. D., Schwartz, S. L., Byars, J., Meddens, M. B. M., Bolomini-Vittori, M., Lidke, D. S., Figdor, C. G., Lidke, K. A., & Cambi, A. (2013). Dual-color superresolution microscopy reveals nanoscale organization of mechanosensory podosomes. *Molecular Biology of the Cell*, *24*(13). https://doi.org/10.1091/mbc.E12-12-0856

D'Souza, C. A., Kronstad, J. W., Taylor, G., Warren, R., Yuen, M., Hu, G., Jung, W. H., Sham, A., Kidd, S. E., Tangen, K., Lee, N., Zeilmaker, T., Sawkins, J., McVicker, G., Shah, S., Gnerre, S., Griggs, A., Zeng, Q., Bartlett, K., … Cuomo, C. A. (2011). Genome Variation in

Cryptococcus gattii, an Emerging Pathogen of Immunocompetent Hosts. *MBio*, *2*(1). https://doi.org/10.1128/mBio.00342-10

Earl, C. S., An, S., & Ryan, R. P. (2015). The changing face of asthma and its relation with microbes. *Trends in Microbiology*, *23*(7), 408–418. https://doi.org/10.1016/j.tim.2015.03.005

Edwards, J. L., Shao, J. Q., Ault, K. A., & Apicella, M. A. (2000). Neisseria gonorrhoeae Elicits Membrane Ruffling and Cytoskeletal Rearrangements upon Infection of Primary Human Endocervical and Ectocervical Cells. In *INFECTION AND IMMUNITY* (Vol. 68, Issue 9, pp. 5354–5363). https://journals.asm.org/journal/iai

Effler, J. C., Kee, Y. S., Berk, J. M., Tran, M. N., Iglesias, P. A., & Robinson, D. N. N. (2006). Mitosis-Specific Mechanosensing and Contractile-Protein Redistribution Control Cell Shape. *Current Biology*, *16*(19). https://doi.org/10.1016/j.cub.2006.08.027

Eke, P. I., Dye, B. A., Wei, L., Thornton-Evans, G. O., & Genco, R. J. (2012). Prevalence of Periodontitis in Adults in the United States: 2009 and 2010. *Journal of Dental Research*, *91*(10), 914–920. https://doi.org/10.1177/0022034512457373

Epelman, S., Lavine, K. J., & Randolph, G. J. (2014). Origin and Functions of Tissue Macrophages. *Immunity*, *41*(1), 21–35. https://doi.org/10.1016/j.immuni.2014.06.013

Erdman N., Bell D.C., Reichelt R. (2019) Scanning Electron Microscopy. In: Hawkes P.W., Spence J.C.H. (eds) Springer Handbook of Microscopy. Springer Handbooks. Springer, Cham. https://doi.org/10.1007/978-3-030-00069-1_5

Erhardt, A., Biburger, M., Papadopoulos, T., & Tiegs, G. (2007). IL-10, regulatory T cells, and Kupffer cells mediate tolerance in concanavalin A-induced liver injury in mice. *Hepatology*, *45*(2), 475–485. https://doi.org/10.1002/hep.21498

Erwig, L. P., & Gow, N. A. R. (2016). Interactions of fungal pathogens with phagocytes. *Nature Reviews Microbiology*, *14*(3), 163–176. https://doi.org/10.1038/nrmicro.2015.21

Eswarappa, S. M., Pareek, V., & Chakravortty, D. (2008). Role of actin cytoskeleton in LPS-induced NF-κB activation and nitric oxide production in murine macrophages. *Innate Immunity*, *14*(5), 309–318. https://doi.org/10.1177/1753425908096856

Evans, E. (1989). Kinetics of granulocyte phagocytosis: Rate limited by cytoplasmic viscosity and constrained by cell size. *Cell Motility and the Cytoskeleton*, *14*(4). https://doi.org/10.1002/cm.970140411

Evans, E., & Yeung, A. (1989). Apparent viscosity and cortical tension of blood granulocytes determined by micropipet aspiration. *Biophysical Journal*, *56*(1), 151–160. https://doi.org/10.1016/S0006-3495(89)82660-8

Evans, R. J., Pline, K., Loynes, C. A., Needs, S., Aldrovandi, M., Tiefenbach, J., Bielska, E., Rubino, R. E., Nicol, C. J., May, R. C., Krause, H. M., O'Donnell, V. B., Renshaw, S. A., &

Johnston, S. A. (2019). 15-keto-prostaglandin e2 activates host peroxisome proliferator-activated receptor gamma (Ppar-γ) to promote cryptococcus neoformans growth during infection. *PLoS Pathogens*, *15*(3). https://doi.org/10.1371/journal.ppat.1007597

Falus, A. (1994). Inflammation: the role of histamine. In *Histamine and Inflammation*. A. Falus, ed. R. G. Landes, TX, Austin, p. 63.

Falus, A., & Merétey, K. (1992). Histamine: An early messenger in inflammatory and immune reactions. *Immunology Today*, *13*(5), 154–156. https://doi.org/10.1016/0167-5699(92)90117-P

Ezekowitz, R. A. B., Williams, D. J., Koziel, H., Armstrong, M. Y. K., Warner, A., Richards, F. F., & Rose, R. M. (1991). Uptake of Pneumocystis carinii mediated by the macrophage mannose receptor. *Nature*, *351*(6322). https://doi.org/10.1038/351155a0

Fagerberg, L., Hallstrom, B. M., Oksvold, P., Kampf, C., Djureinovic, D., Odeberg, J., Habuka, M., Tahmasebpoor, S., Danielsson, A., Edlund, K., Asplund, A., Sjostedt, E., Lundberg, E., Szigyarto, C. A. K., Skogs, M., Takanen, J. O., Berling, H., Tegel, H., Mulder, J., … Uhlen, M. (2014). Analysis of the human tissue-specific expression by genome-wide integration of transcriptomics and antibody-based proteomics. *Molecular and Cellular Proteomics*, *13*(2), 397–406. https://doi.org/10.1074/mcp.M113.035600

Farber, D. L., Netea, M. G., Radbruch, A., Rajewsky, K., & Zinkernagel, R. M. (2016). Immunological memory: Lessons from the past and a look to the future. *Nature Reviews Immunology*, *16*(2), 124–128. https://doi.org/10.1038/nri.2016.13

Faust, J. J., Balabiyev, A., Heddleston, J. M., Podolnikova, N. P., Baluch, D. P., Chew, T. L., & Ugarova, T. P. (2019). An actin-based protrusion originating from a podosome-enriched region initiates macrophage fusion. *Molecular Biology of the Cell*, *30*(17), 2254–2267. https://doi.org/10.1091/mbc.E19-01-0009

Feldmesser, M., Kress, Y., & Casadevall, A. (2001). Dynamic changes in the morphology of Cryptococcus neoformans during murine pulmonary infection. *Microbiology*, *147*(8). https://doi.org/10.1099/00221287-147-8-2355

Feldmesser, M., Kress, Y., Novikoff, P., & Casadevall, A. (2000). Cryptococcus neoformans Is a Facultative Intracellular Pathogen in Murine Pulmonary Infection. In *INFECTION AND IMMUNITY* (Vol. 68, Issue 7, pp. 4225–4237). https://journals.asm.org/journal/iai

Figard, L., & Sokac, A. M. (2014). A membrane reservoir at the cell surface: Unfolding the plasma membrane to fuel cell shape change. *BioArchitecture*, *4*(2), 39–46. https://doi.org/10.4161/bioa.29069

Flajnik, M. F., & Pasquier, L. D. (2004). Evolution of innate and adaptive immunity: Can we draw a line? *Trends in Immunology*, *25*(12), 640–644. https://doi.org/10.1016/j.it.2004.10.001

Flannagan, R. S., Harrison, R. E., Yip, C. M., Jaqaman, K., & Grinstein, S. (2010). Dynamic macrophage "probing" is required for the efficient capture of phagocytic targets. *Journal of Cell Biology*, *191*(6), 1205–1218. https://doi.org/10.1083/jcb.201007056

Flannagan, R. S., & Heinrichs, D. E. (2020). Macrophage-driven nutrient delivery to phagosomal Staphylococcus aureus supports bacterial growth. *EMBO Reports*, *21*(8). https://doi.org/10.15252/embr.202050348

Fossati, G., Moots, R. J., Bucknall, R. C., & Edwards, S. W. (2002). Differential role of neutrophil Fcγ receptor IIIb (CD16) in phagocytosis, bacterial killing, and responses to immune complexes. *Arthritis and Rheumatism*, *46*(5). https://doi.org/10.1002/art.10230

Freeman, S. A., Goyette, J., Furuya, W., Woods, E. C., Bertozzi, C. R., Bergmeier, W., Hinz, B., Merwe, P. A. V. D., Das, R., & Grinstein, S. (2016). Integrins Form an Expanding Diffusional Barrier that Coordinates Phagocytosis. *Cell*, *164*(1–2), 128–140. https://doi.org/10.1016/j.cell.2015.11.048

Freitas-Lopes, M., Mafra, K., David, B., Carvalho-Gontijo, R., & Menezes, G. (2017). Differential Location and Distribution of Hepatic Immune Cells. *Cells*, *6*(4), 48. https://doi.org/10.3390/cells6040048

Fritzsche, M., Fernandes, R. A., Chang, V. T., Colin-York, H., Clausen, M. P., Felce, J. H., Galiani, S., Erlenkämper, C., Santos, A. M., Heddleston, J. M., Pedroza-Pacheco, I., Waithe, D., Serna, J. B. D. L., Lagerholm, B. C., Liu, T.-L., Chew, T.-L., Betzig, E., Davis, S. J., & Eggeling, C. (2017). *Cytoskeletal actin dynamics shape a ramifying actin network underpinning immunological synapse formation*. http://advances.sciencemag.org/

Fritzsche, M., Li, D., Colin-York, H., Chang, V. T., Moeendarbary, E., Felce, J. H., Sezgin, E., Charras, G., Betzig, E., & Eggeling, C. (2017). Self-organizing actin patterns shape membrane architecture but not cell mechanics. *Nature Communications*, *8*. https://doi.org/10.1038/ncomms14347

Frohman, E. M., Racke, M. K., & Raine, C. S. (2006). Multiple Sclerosis—The Plaque and Its Pathogenesis. *New England Journal of Medicine*, *354*(9), 942–955. https://doi.org/10.1056/NEJMra052130

Fu, M. S., Coelho, C., Leon-Rodriguez, C. M. D., Rossi, D. C. P., Camacho, E., Jung, E. H., Kulkarni, M., & Casadevall, A. (2018). Cryptococcus neoformans urease affects the outcome of intracellular pathogenesis by modulating phagolysosomal pH. *PLoS Pathogens*, *14*(6). https://doi.org/10.1371/journal.ppat.1007144

Fu, R., Shen, Q., Xu, P., Luo, J. J., & Tang, Y. (2014). Phagocytosis of microglia in the central nervous system diseases. *Molecular Neurobiology*, *49*(3), 1422–1434. https://doi.org/10.1007/s12035-013-8620-6

Galli, S. J., Nakae, S., & Tsai, M. (2005). Mast cells in the development of adaptive immune responses. *Nature Immunology*, *6*(2), 135–142. https://doi.org/10.1038/ni1158

Garcia-Aguilar, T., Espinosa-Cueto, P., Magallanes-Puebla, A., & Mancilla, R. (2016). The mannose receptor is involved in the phagocytosis of mycobacteria-induced apoptotic cells. *Journal of Immunology Research*, *2016*. https://doi.org/10.1155/2016/3845247

García-García, E., Nieto-Castañeda, G., Ruiz-Saldaña, M., Mora, N., & Rosales, C. (2009). FcgammaRIIA and FcgammaRIIIB mediate nuclear factor activation through separate signaling pathways in human neutrophils. *Journal of Immunology (Baltimore, Md. : 1950)*, *182*(8), 4547–4556. https://doi.org/10.4049/jimmunol.0801468

García-Rivera, J., Chang, Y. C., Kwon-Chung, K. J., & Casadevall, A. (2004). Cryptococcus neoformans CAP59 (or Cap59p) is involved in the extracellular trafficking of capsular glucuronoxylomannan. *Eukaryotic Cell*. https://doi.org/10.1128/EC.3.2.385-392.2004

Gasteiger, G., D'Osualdo, A., Schubert, D. A., Weber, A., Bruscia, E. M., & Hartl, D. (2017). Cellular Innate Immunity: An Old Game with New Players. *Journal of Innate Immunity*, *9*(2), 111–125. https://doi.org/10.1159/000453397

Gautier, E. L., Jakubzick, C., & Randolph, G. J. (2009). Regulation of the migration and survival of monocyte subsets by chemokine receptors and its relevance to atherosclerosis. *Arteriosclerosis, Thrombosis, and Vascular Biology*, *29*(10), 1412–1418. https://doi.org/10.1161/ATVBAHA.108.180505

Gekara, N. O., & Weiss, S. (2008). Mast cells initiate early anti-Listeria host defences. *Cellular Microbiology*, *10*(1). https://doi.org/10.1111/j.1462-5822.2007.01033.x

Ghiran, I., Barbashov, S. F., Klickstein, L. B., Tas, S. W., Jensenius, J. C., & Nicholson-Weller, A. (2000). Complement receptor 1/CD35 is a receptor for mannan-binding lectin. *Journal of Experimental Medicine*, *192*(12). https://doi.org/10.1084/jem.192.12.1797

Ghosh, H. S., Cisse, B., Bunin, A., Lewis, K. L., & Reizis, B. (2010). Continuous Expression of the Transcription Factor E2-2 Maintains the Cell Fate of Mature Plasmacytoid Dendritic Cells. *Immunity*, *33*(6). https://doi.org/10.1016/j.immuni.2010.11.023

Giannone, G., Dubin-Thaler, B. J., Rossier, O., Cai, Y., Chaga, O., Jiang, G., Beaver, W., Döbereiner, H. G., Freund, Y., Borisy, G., & Sheetz, M. P. (2007). Lamellipodial Actin Mechanically Links Myosin Activity with Adhesion-Site Formation. *Cell*, *128*(3), 561–575. https://doi.org/10.1016/j.cell.2006.12.039

Gibbs, R. J., & Matthews, M.D. (1971). The Relationship Between Sphere Size And Settling Velocity. *SEPM Journal of Sedimentary Research*, *Vol. 41*. https://doi.org/10.1306/74D721D0-2B21-11D7-8648000102C1865D

Golay, J., Roit, F. D., Bologna, L., Ferrara, C., Leusen, J. H., Rambaldi, A., Klein, C., & Introna, M. (2013). Glycoengineered CD20 antibody obinutuzumab activates neutrophils and mediates phagocytosis through CD16B more efficiently than rituximab. *Blood*, *122*(20). https://doi.org/10.1182/blood-2013-05-504043

Goodman, S., Naphade, S., Khan, M., Sharma, J., & Cherqui, S. (2019). Macrophage polarization impacts tunneling nanotube formation and intercellular organelle trafficking. *Scientific Reports*, *9*(1). https://doi.org/10.1038/s41598-019-50971-x

Gordon, S. (2016). Phagocytosis: An Immunobiologic Process. *Immunity*, *44*(3), 463–475. https://doi.org/10.1016/j.immuni.2016.02.026

Graham, T. (1854). The Bakerian Lecture: On Osmotic Force. In *Philosophical Transactions of the Royal Society of London* (Vol. 144, pp. 177–228). https://www.jstor.org/stable/108498

Granger, D. L., Perfect, J. R., & Durack, D. T. (1985). Virulence of Cryptococcus neoformans: Regulation of capsule synthesis by carbon dioxide. *Journal of Clinical Investigation*, *76*(2). https://doi.org/10.1172/JCI112000

Greenberg, M. E., Sun, M., Zhang, R., Febbraio, M., Silverstein, R., & Hazen, S. L. (2006). Oxidized phosphatidylserine-CD36 interactions play an essential role in macrophage-dependent phagocytosis of apoptotic cells. *Journal of Experimental Medicine*, *203*(12). https://doi.org/10.1084/jem.20060370

Greenlee-Wacker, M. C., Rigby, K. M., Kobayashi, S. D., Porter, A. R., DeLeo, F. R., & Nauseef, W. M. (2014). Phagocytosis of *Staphylococcus aureus* by Human Neutrophils Prevents Macrophage Efferocytosis and Induces Programmed Necrosis. *The Journal of Immunology*, *192*(10), 4709–4717. https://doi.org/10.4049/jimmunol.1302692

Grinstein, S., Rothstein, A., Sarkadi, B., & Gelfand, E. W. (1984). Responses of lymphocytes to anisotonic media: Volume-regulating behavior. *American Journal of Physiology-Cell Physiology*, *246*(3), C204–C215. https://doi.org/10.1152/ajpcell.1984.246.3.C204

Groulx, N., Boudreault, F., Orlov, S. N., & Grygorczyk, R. (2006). Membrane reserves and hypotonic cell swelling. *Journal of Membrane Biology*, *214*(1–2), 43–56. https://doi.org/10.1007/s00232-006-0080-8

Guerra, C. R., Seabra, S. H., Souza, W. D., & Rozental, S. (2014). Cryptococcus neoformans is internalized by receptor-mediated or "triggered" phagocytosis, dependent on actin recruitment. *PLoS ONE*, *9*(2), 1–10. https://doi.org/10.1371/journal.pone.0089250

Guilliams, M., Bruhns, P., Saeys, Y., Hammad, H., & Lambrecht, B. N. (2014). The function of Fcγ receptors in dendritic cells and macrophages. *Nature Reviews Immunology*, *14*(2), 94–108. https://doi.org/10.1038/nri3582

Guilliams, M., Kleer, I. D., Henri, S., Post, S., Vanhoutte, L., Prijck, S. D., Deswarte, K., Malissen, B., Hammad, H., & Lambrecht, B. N. (2013). Alveolar macrophages develop from fetal

monocytes that differentiate into long-lived cells in the first week of life via GM-CSF. *Journal of Experimental Medicine*, *210*(10). https://doi.org/10.1084/jem.20131199

Guimarães, A. J., Frases, S., Cordero, R. J. B., Nimrichter, L., Casadevall, A., & Nosanchuk, J. D. (2010). Cryptococcus neoformans responds to mannitol by increasing capsule size in vitro and in vivo. *Cellular Microbiology*, *12*(6). https://doi.org/10.1111/j.1462-5822.2010.01430.x

Häger, M., Cowland, J. B., & Borregaard, N. (2010). Neutrophil granules in health and disease. *Journal of Internal Medicine*, *268*(1), 25–34. https://doi.org/10.1111/j.1365-2796.2010.02237.x

Halanych, K. M. (2004). Invertebrates; Invertebrate Zoology: A Functional Evolutionary Approach. In *Systematic Biology* (Vol. 53, Issue 4). https://doi.org/10.1080/10635150490472977

Hammami, S., Willumsen, N. J., & Klaerke, D. A. (2007). Cell volume and membrane stretch independently control K + channel activity. *The FASEB Journal*, *21*(5). https://doi.org/10.1096/fasebj.21.5.a539-b

Hänisch, J., Ehinger, J., Ladwein, M., Rohde, M., Derivery, E., Bosse, T., Steffen, A., Bumann, D., Misselwitz, B., Hardt, W. D., Gautreau, A., Stradal, T. E. B., & Rottner, K. (2010). Molecular dissection of Salmonella-induced membrane ruffling versus invasion. *Cellular Microbiology*, *12*(1), 84–98. https://doi.org/10.1111/j.1462-5822.2009.01380.x

Harris, L., Foster, S., & Richards, R. (2002). An introduction to staphylococcus aureus, and techniques for identifying and quantifying s. aureus adhesins in relation to adhesion to biomaterials: Review. *European Cells and Materials*, *4*, 39–60. https://doi.org/10.22203/eCM.v004a04

Hart, P. H., Bonder, C. S., Jones, C. A., & Finlay-Jones, J. J. (1996). Control of major histocompatibility complex class II expression on human monocytes by interleukin-4: Regulatory effect of lipopolysaccharide. *Immunology*, *89*(4), 599–605. https://doi.org/10.1046/j.1365-2567.1996.d01-779.x

He, C., Hu, X., Weston, T. A., Jung, R. S., Sandhu, J., Huang, S., Heizer, P., Kim, J., Ellison, R., Xu, J., Kilburn, M., Bensinger, S. J., Riezman, H., Tontonoz, P., Fong, L. G., Jiang, H., & Young, S. G. (2018). Macrophages release plasma membrane-derived particles rich in accessible cholesterol. *Proceedings of the National Academy of Sciences of the United States of America*, *115*(36), E8499–E8508. https://doi.org/10.1073/pnas.1810724115

Hed, J., & Stendahl, O. (1982). Differences in the ingestion mechanisms of IgG and C3b particles in phagocytosis by neutrophils. *Immunology*, *45*(4), 727–736.

Heinrich, V. (2015). Controlled One-on-One Encounters between Immune Cells and Microbes Reveal Mechanisms of Phagocytosis. *Biophysical Journal*, *109*(3), 469–476. https://doi.org/10.1016/j.bpj.2015.06.042

Helfrich, W. (1973). Elastic Properties of Lipid Bilayers: Theory and Possible Experiments. In *Z. Naturforsch. 28 c* (Vol. 6, p. 3).

Heming, T. A., Tuazon, D. M., Davé, S. K., Chopra, A. K., Peterson, J. W., & Bidani, A. (2001). Post-transcriptional effects of extracellular pH on tumour necrosis factor-α production in RAW 246.7 and J774 A.1 cells. *Clinical Science*, *100*(3). https://doi.org/10.1042/CS20000192

Herant, M. (2006). Mechanics of neutrophil phagocytosis: Experiments and quantitative models. *Journal of Cell Science*, *119*(9), 1903–1913. https://doi.org/10.1242/jcs.02876

Herant, M., Heinrich, V., & Dembo, M. (2005). Mechanics of neutrophil phagocytosis: Behavior of the cortical tension. *Journal of Cell Science*, *118*(9), 1789–1797. https://doi.org/10.1242/jcs.02275

Herant, M., Lee, C. Y., Dembo, M., & Heinrich, V. (2011). Protrusive push versus enveloping embrace: Computational model of phagocytosis predicts key regulatory role of cytoskeletal membrane anchors. *PLoS Computational Biology*, *7*(1), 1–6. https://doi.org/10.1371/journal.pcbi.1001068

Herre, J., Marshall, A. S. J., Caron, E., Edwards, A. D., Williams, D. L., Schweighoffer, E., Tybulewicz, V., Sousa, C. R. E., Gordon, S., & Brown, G. D. (2004). Dectin-1 uses novel mechanisms for yeast phagocytosis in macrophages. *Blood*, *104*(13). https://doi.org/10.1182/blood-2004-03-1140

Hildner, K., Edelson, B. T., Purtha, W. E., Diamond, M., Matsushita, H., Kohyama, M., Calderon, B., Schraml, B. U., Unanue, E. R., Diamond, M. S., Schreiber, R. D., Murphy, T. L., & Murphy, K. M. (2008). Batf3 deficiency reveals a critical role for CD8α+ dendritic cells in cytotoxic T cell immunity. *Science*, *322*(5904). https://doi.org/10.1126/science.1164206

Hilligan, K. L., & Ronchese, F. (2020). Antigen presentation by dendritic cells and their instruction of CD4+ T helper cell responses. *Cellular & Molecular Immunology*, *17*(6), 587–599. https://doi.org/10.1038/s41423-020-0465-0

Hirst, J., Jones, W., & Cohn, M. (1971). Characterization of a BALB/c myeloma library. *J. Immunol*, *107*, 926–927.

Hoang, L. M. N., Maguire, J. A., Doyle, P., Fyfe, M., & Roscoe, D. L. (2004). Cryptococcus neoformans infections at Vancouver Hospital and Health Sciences Centre (1997-2002): Epidemiology, microbiology and histopathology. *Journal of Medical Microbiology*, *53*(Pt 9), 935–940. https://doi.org/10.1099/jmm.0.05427-0

Hocdé, S. A., Hyrien, O., & Waugh, R. E. (2009). Cell adhesion molecule distribution relative to neutrophil surface topography assessed by TIRFM. *Biophysical Journal*, *97*(1), 379–387. https://doi.org/10.1016/j.bpj.2009.04.035

Hochmuth, R. M., Ting-Beall, H. P., Beaty, B. B., Needham, D., & Tran-Son-Tay, R. (1993). Viscosity of passive human neutrophils undergoing small deformations. *Biophysical Journal*, *64*(5), 1596–1601. https://doi.org/10.1016/S0006-3495(93)81530-3

Hodge, S., Hodge, G., Ahern, J., Jersmann, H., Holmes, M., & Reynolds, P. N. (2007). Smoking alters alveolar macrophage recognition and phagocytic ability: Implications in chronic obstructive pulmonary disease. *American Journal of Respiratory Cell and Molecular Biology*, *37*(6), 748–755. https://doi.org/10.1165/rcmb.2007-0025OC

Hoffmann, P. R., DeCathelineau, A. M., Ogden, C. A., Leverrier, Y., Bratton, D. L., Daleke, D. L., Ridley, A. J., Fadok, V. A., & Henson, P. M. (2001). Phosphatidylserine (PS) induces PS receptor-mediated macropinocytosis and promotes clearance of apoptotic cells. *Journal of Cell Biology*, *155*(4), 649–659. https://doi.org/10.1083/jcb.200108080

Hoon, J.-L., Wong, W.-K., & Koh, C.-G. (2012). Functions and regulation of circular dorsal ruffles. *Molecular and Cellular Biology*, *32*(21), 4246–4257. https://doi.org/10.1128/MCB.00551-12

Horn, J., Stelzner, K., Rudel, T., & Fraunholz, M. (2018). Inside job: Staphylococcus aureus host-pathogen interactions. *International Journal of Medical Microbiology*, *308*(6), 607–624. https://doi.org/10.1016/j.ijmm.2017.11.009

Horsthemke, M., Bachg, A. C., Groll, K., Moyzio, S., Müther, B., Hemkemeyer, S. A., Wedlich-Söldner, R., Sixt, M., Tacke, S., Bähler, M., & Hanley, P. J. (2017). Multiple roles of filopodial dynamics in particle capture and phagocytosis and phenotypes of Cdc42 and Myo10 deletion. *Journal of Biological Chemistry*, *292*(17), 7258–7273. https://doi.org/10.1074/jbc.M116.766923

Houk, A. R., Jilkine, A., Mejean, C. O., Boltyanskiy, R., Dufresne, E. R., Angenent, S. B., Altschuler, S. J., Wu, L. F., & Weiner, O. D. (2012). Membrane Tension Maintains Cell Polarity by Confining Signals to the Leading Edge during Neutrophil Migration. *Cell*, *148*(1–2), 175–188. https://doi.org/10.1016/j.cell.2011.10.050

Hudrisier, D., & Bongrand, P. (2003). Intercellular transfer of antigen-presenting cell determinants onto T cells: Molecular mechanisms and biological significance. *The FASEB Journal*, *16*(6), 477–486. https://doi.org/10.1096/fj.01-0933rev

Hume, D. A. (2008). Macrophages as APC and the Dendritic Cell Myth. *The Journal of Immunology*, *181*(9). https://doi.org/10.4049/jimmunol.181.9.5829

Innocenti, M. (2018). New insights into the formation and the function of lamellipodia and ruffles in mesenchymal cell migration. *Cell Adhesion and Migration*, *12*(5), 401–416. https://doi.org/10.1080/19336918.2018.1448352

Insall, R. H., & Machesky, L. M. (2009). Actin Dynamics at the Leading Edge: From Simple Machinery to Complex Networks. *Developmental Cell*, *17*(3), 310–322. https://doi.org/10.1016/j.devcel.2009.08.012

Ip, W. K. E., Sokolovska, A., Charriere, G. M., Boyer, L., Dejardin, S., Cappillino, M. P., Yantosca, L. M., Takahashi, K., Moore, K. J., Lacy-Hulbert, A., & Stuart, L. M. (2010). Phagocytosis and Phagosome Acidification Are Required for Pathogen Processing and MyD88-Dependent Responses to Staphylococcus aureus. *The Journal of Immunology*, *184*(12). https://doi.org/10.4049/jimmunol.1000110

Ishibashi, H., Nakamura, M., Komori, A., Migita, K., & Shimoda, S. (2009). Liver architecture, cell function, and disease. *Seminars in Immunopathology*, *31*(3), 399–409. https://doi.org/10.1007/s00281-009-0155-6

Ishikawa, E., Ishikawa, T., Morita, Y. S., Toyonaga, K., Yamada, H., Takeuchi, O., Kinoshita, T., Akira, S., Yoshikai, Y., & Yamasaki, S. (2009). Direct recognition of the mycobacterial glycolipid, trehalose dimycolate, by C-type lectin Mincle. *Journal of Experimental Medicine*, *206*(13). https://doi.org/10.1084/jem.20091750

Itoh, T., & Hasegawa, J. (2013). Mechanistic insights into the regulation of circular dorsal ruffle formation. *Journal of Biochemistry*, *153*(1), 21–29. https://doi.org/10.1093/jb/mvs138

Iyer, S. S., & Cheng, G. (2012). *Role of Interleukin 10 Transcriptional Regulation in Inflammation and Autoimmune Disease*.

Jacobsen, E. A., Ochkur, S. I., Pero, R. S., Taranova, A. G., Protheroe, C. A., Colbert, D. C., Lee, N. A., & Lee, J. J. (2008). Allergic pulmonary inflammation in mice is dependent on eosinophil-induced recruitment of effector T cells. *The Journal of Experimental Medicine*, *205*(3), 699–710. https://doi.org/10.1084/jem.20071840

Jacobson, E. S., Ayers, D. J., Harrell, A. C., & Nicholas, C. C. (1982). Genetic and phenotypic characterization of capsule mutants of Cryptococcus neoformans. *Journal of Bacteriology*, *150*(3), 1292–1296. https://doi.org/10.1128/jb.150.3.1292-1296.1982

Janeway, C. A. (1989). Approaching the asymptote? Evolution and revolution in immunology. Cold spring harb symp quant biol. 1989. 54: 1-13. *Cold Spring Harbor Symp Quant Biol*, *54*.

Janeway, C. A., Travers, P., Walport, M., & Shlomchik, M. (2001). *Immunobiology: The Immune System in Health and Disease.* (5th ed.). Garland Science.

Jantsch, J., Binger, K. J., MÃ¼ller, D. N., & Titze, J. (2014). Macrophages in homeostatic immune function. *Frontiers in Physiology*, *5*. https://doi.org/10.3389/fphys.2014.00146

Jaumouillé, V., & Grinstein, S. (2011). Receptor mobility, the cytoskeleton, and particle binding during phagocytosis. *Current Opinion in Cell Biology*, *23*(1), 22–29. https://doi.org/10.1016/j.ceb.2010.10.006

Jeannin, P., Delneste, Y., Gosset, P., Molet, S., Lassalle, P., Hamid, Q., Tsicopoulos, A., & Tonnel, A. B. (1994). Histamine induces interleukin-8 secretion by endothelial cells. *Blood*, *84*(7). https://doi.org/10.1182/blood.v84.7.2229.bloodjournal8472229

Jemail, L., Miyao, M., Kotani, H., Kawai, C., Minami, H., Abiru, H., & Tamaki, K. (2018). Pivotal roles of Kupffer cells in the progression and regression of DDC-induced chronic cholangiopathy. *Scientific Reports*, *8*(1). https://doi.org/10.1038/s41598-018-24825-x

Johnston, S. A., & May, R. C. (2010). The human fungal pathogen Cryptococcus neoformans escapes macrophages by a phagosome emptying mechanism that is inhibited by arp2/3 complex- mediated actin polymerisation. *PLoS Pathogens*, *6*(8), 27–28. https://doi.org/10.1371/journal.ppat.1001041

Johnston, S. A., & May, R. C. (2013). *Cryptococcus* interactions with macrophages: Evasion and manipulation of the phagosome by a fungal pathogen: *Cryptococcus* interactions with macrophages. *Cellular Microbiology*, *15*(3), 403–411. https://doi.org/10.1111/cmi.12067

Joly, E., & Hudrisier, D. (2003). What is trogocytosis and what is its purpose? *Nature Immunology*, *4*(9), 815–815. https://doi.org/10.1038/ni0903-815

Jumaa, M. A. A., Dewitt, S., & Hallett, M. B. (2017). Topographical interrogation of the living cell surface reveals its role in rapid cell shape changes during phagocytosis and spreading. *Scientific Reports*, *7*(1), 1–11. https://doi.org/10.1038/s41598-017-09761-6

Jung, Y., Riven, I., Feigelson, S. W., Kartvelishvily, E., Tohya, K., Miyasaka, M., Alon, R., & Haran, G. (2016). Three-dimensional localization of T-cell receptors in relation to microvilli using a combination of superresolution microscopies. *Proceedings of the National Academy of Sciences of the United States of America*, *113*(40), E5916–E5924. https://doi.org/10.1073/pnas.1605399113

Kalinski, M. L. K. P., Schuitemaker, J. H. N., & U, C. M. (2021). *Prostaglandin E2 induces the final maturation of IL-12-deficient CD1a+CD83+ dendritic cells: The levels of IL-12 are determined during the final dendritic cell maturation and are resistant to further modulation*. http://www.jimmunol.org/content/161/6/2804

Kambayashi, T., & Laufer, T. M. (2014). Atypical MHC class II-expressing antigen-presenting cells: Can anything replace a dendritic cell? *Nature Reviews Immunology*, *14*(11), 719–730. https://doi.org/10.1038/nri3754

Karlsson, T., Bolshakova, A., Magalhães, M. A. O., Loitto, V. M., & Magnusson, K. E. (2013). Fluxes of Water through Aquaporin 9 Weaken Membrane-Cytoskeleton Anchorage and Promote Formation of Membrane Protrusions. *PLoS ONE*, *8*(4), 1–14. https://doi.org/10.1371/journal.pone.0059901

Kaverina, I., Stradal, T. E. B., & Gimona, M. (2003). Podosome formation in cultured A7r5 vascular smooth muscle cells requires Arp2/3-dependent denovo actin polymerization at discrete microdomains. *Journal of Cell Science*, *116*(24). https://doi.org/10.1242/jcs.00818

Kawaguchi, H., Koiwai, N., Ohtsuka, Y., Miyamoto, M., & Sasakawa, S. (1986). Phagocytosis of latex particles by leucocytes. I. Dependence of phagocytosis on the size and surface potential of particles. *Biomaterials*, *7*(1), 61–66. https://doi.org/10.1016/0142-9612(86)90091-8

Kay, A. B. (2015). The early history of the eosinophil. *Clinical & Experimental Allergy*, *45*(3), 575–582. https://doi.org/10.1111/cea.12480

Kerrigan, A. M., & Brown, G. D. (2009). C-type lectins and phagocytosis. *Immunobiology*, *214*(7), 562–575. https://doi.org/10.1016/j.imbio.2008.11.003

Kiely, D. G., Elliot, C. A., Sabroe, I., & Condliffe, R. (2013). Pulmonary hypertension: Diagnosis and management. *BMJ*, *346*(apr16 1), f2028–f2028. https://doi.org/10.1136/bmj.f2028

Kiessling, R., Klein, E., Pross, H., & Wigzell, H. (1975). "Natural" killer cells in the mouse. II. Cytotoxic cells with specificity for mouse Moloney leukemia cells. Characteristics of the killer cell. *European Journal of Immunology*, *5*(2). https://doi.org/10.1002/eji.1830050209

Kirkham, P. A., Spooner, G., Rahman, I., & Rossi, A. G. (2004). Macrophage phagocytosis of apoptotic neutrophils is compromised by matrix proteins modified by cigarette smoke and lipid peroxidation products. *Biochemical and Biophysical Research Communications*, *318*(1), 32–37. https://doi.org/10.1016/j.bbrc.2004.04.003

Klose, C. S. N., & Artis, D. (2020). Innate lymphoid cells control signaling circuits to regulate tissue-specific immunity. *Cell Research*, *30*(6), 475–491. https://doi.org/10.1038/s41422-020-0323-8

Knolle, P. A., Uhrig, A., Hegenbarth, S., Löser, E., Schmitt, E., Gerken, G., & Lohse, A. W. (1998). IL-10 down-regulates T cell activation by antigen-presenting liver sinusoidal endothelial cells through decreased antigen uptake via the mannose receptor and lowered surface expression of accessory molecules. *Clinical and Experimental Immunology*, *114*(3). https://doi.org/10.1046/j.1365-2249.1998.00713.x

Kobayashi, N., Karisola, P., Peña-Cruz, V., Dorfman, D. M., Jinushi, M., Umetsu, S. E., Butte, M. J., Nagumo, H., Chernova, I., Zhu, B., Sharpe, A. H., Ito, S., Dranoff, G., Kaplan, G. G., Casasnovas, J. M., Umetsu, D. T., DeKruyff, R. H., & Freeman, G. J. (2007). TIM-1 and TIM-4 Glycoproteins Bind Phosphatidylserine and Mediate Uptake of Apoptotic Cells. *Immunity*, *27*(6). https://doi.org/10.1016/j.immuni.2007.11.011

Kobzik, L. (1995). Lung macrophage uptake of unopsonized environmental particulates. Role of scavenger-type receptors. *Journal of Immunology (Baltimore, Md. : 1950)*, *155*(1), 367–376.

Koenderman, L. (2019). Inside-Out Control of Fc-Receptors. *Frontiers in Immunology*, *10*, 544. https://doi.org/10.3389/fimmu.2019.00544

Koestler, S. A., Rottner, K., Lai, F., Block, J., Vinzenz, M., & Small, J. V. (2009). F- and G-actin concentrations in lamellipodia of moving cells. *PLoS ONE*, *4*(3), 3–7. https://doi.org/10.1371/journal.pone.0004810

Konijn, B. J., Sanderink, O. B. J., & Kruyt, N. P. (2014). Experimental study of the viscosity of suspensions: Effect of solid fraction, particle size and suspending liquid. *Powder Technology*, *266*, 61–69. https://doi.org/10.1016/j.powtec.2014.05.044

Köster, D. V., Husain, K., Iljazi, E., Bhat, A., Bieling, P., Mullins, R. D., Rao, M., & Mayor, S. (2016). Actomyosin dynamics drive local membrane component organization in an in vitro active composite layer. *Proceedings of the National Academy of Sciences of the United States of America*, *113*(12), E1645–E1654. https://doi.org/10.1073/pnas.1514030113

Köster, D. V., & Mayor, S. (2016). Cortical actin and the plasma membrane: Inextricably intertwined. *Current Opinion in Cell Biology*, *38*, 81–89. https://doi.org/10.1016/j.ceb.2016.02.021

Koval, M., Preiter, K., Adles, C., Stahl, P. D., & Steinberg, T. H. (1998). Size of IgG-Opsonized Particles Determines Macrophage Response during Internalization. *Experimental Cell Research*, *242*(1), 265–273. https://doi.org/10.1006/excr.1998.4110

Kovari, D. T., Wei, W., Chang, P., Toro, J. S., Beach, R. F., Chambers, D., Porter, K., Koo, D., & Curtis, J. E. (2016). Frustrated Phagocytic Spreading of J774A-1 Macrophages Ends in Myosin II-Dependent Contraction. *Biophysical Journal*, *111*(12), 2698–2710. https://doi.org/10.1016/j.bpj.2016.11.009

Kozel, T. R. (1977). Non encapsulated variant of Cryptococcus neoformans. II. Surface receptors for cryptococcal polysaccharide and their role in inhibition of phagocytosis by polysaccharide. *Infection and Immunity*, *16*(1). https://doi.org/10.1128/iai.16.1.99-106.1977

Kozel, T. R., & Gotschlich, E. C. (1982). *The capsule of cryptococcus neoformans passively inhibits phagocytosis of the yeast by macrophages.* 7.

Kraja, A. T., Vaidya, D., Pankow, J. S., Goodarzi, M. O., Assimes, T. L., Kullo, I. J., Sovio, U., Mathias, R. A., Sun, Y. V., Franceschini, N., Absher, D., Li, G., Zhang, Q., Feitosa, M. F., Glazer, N. L., Haritunians, T., Hartikainen, A.-L., Knowles, J. W., North, K. E., … Borecki, I. B. (2011). A bivariate genome-wide approach to metabolic syndrome: STAMPEED consortium. *Diabetes*, *60*(4), 1329–1339. https://doi.org/10.2337/db10-1011

Krouwels, F. H., Hol, B. E. A., Lutter, R., Bruinier, B., Bast, A., Jansen, H. M., & Out, T. A. (1998). Histamine affects interleukin-4, interleukin-5, and interferon-γ production by human T cell

clones from the airways and blood. *American Journal of Respiratory Cell and Molecular Biology*, *18*(5). https://doi.org/10.1165/ajrcmb.18.5.2909

Krueger, E. W., Orth, J. D., Cao, H., & McNiven, M. A. (2003). A dynamin-cortactin-Arp2/3 complex mediates actin reorganization in growth factor-stimulated cells. *Molecular Biology of the Cell*, *14*(3). https://doi.org/10.1091/mbc.E02-08-0466

Kubitschek, H. E. (1969). Growth During the Bacterial Cell Cycle: Analysis of Cell Size Distribution. *Biophysical Journal*, *9*(6). https://doi.org/10.1016/S0006-3495(69)86418-0

Kumar, B. V., Connors, T. J., & Farber, D. L. (2018). Human T Cell Development, Localization, and Function throughout Life. *Immunity*, *48*(2), 202–213. https://doi.org/10.1016/j.immuni.2018.01.007

Kunding, A. H., Mortensen, M. W., Christensen, S. M., & Stamou, D. (2008). A fluorescence-based technique to construct size distributions from single-object measurements: Application to the extrusion of lipid vesicles. *Biophysical Journal*, *95*(3), 1176–1188. https://doi.org/10.1529/biophysj.108.128819

Kusumi, A., Nakada, C., Ritchie, K., Murase, K., Suzuki, K., Murakoshi, H., Kasai, R. S., Kondo, J., & Fujiwara, T. (2005). Paradigm Shift of the Plasma Membrane Concept from the Two-Dimensional Continuum Fluid to the Partitioned Fluid: High-Speed Single-Molecule Tracking of Membrane Molecules. *Annual Review of Biophysics and Biomolecular Structure*, *34*(1), 351–378. https://doi.org/10.1146/annurev.biophys.34.040204.144637

Kwon-Chung, K. J. (1980). Nuclear Genotypes of Spore Chains in *Filobasidiella Neoformans* (*Cryptococcus Neoformans*). *Mycologia*, *72*(2), 418–422. https://doi.org/10.1080/00275514.1980.12021196

Kwon-Chung, K. J. (1976). Morphogenesis of *Filobasidiella Neoformans* , the Sexual State of *Cryptococcus Neoformans*. *Mycologia*, *68*(4), 821–833. https://doi.org/10.1080/00275514.1976.12019959

Kwon-Chung, K. J., & Bennett, J. E. (1984). EPIDEMIOLOGIC DIFFERENCES BETWEEN THE TWO VARIETIES OF CRYPTOCOCCUS NEOFORMANS1. *American Journal of Epidemiology*, *120*(1), 123–130. https://doi.org/10.1093/oxfordjournals.aje.a113861

Kwon-Chung, K. J., Fraser, J. A., Doering, T. L., Wang, Z., Janbon, G., Idnurm, A., & Bahn, Y.-S. (2014). Cryptococcus neoformans and Cryptococcus gattii, the etiologic agents of cryptococcosis. *Cold Spring Harbor Perspectives in Medicine*, *4*(7), a019760. https://doi.org/10.1101/cshperspect.a019760

Labernadie, A., Bouissou, A., Delobelle, P., Balor, S., Voituriez, R., Proag, A., Fourquaux, I., Thibault, C., Vieu, C., Poincloux, R., Charrière, G. M., & Maridonneau-Parini, I. (2014). Protrusion force microscopy reveals oscillatory force generation and mechanosensing activity

of human macrophage podosomes. *Nature Communications*, *5*. https://doi.org/10.1038/ncomms6343

Labernadie, A., Thibault, C., Vieu, C., Maridonneau-Parini, I., & Charrière, G. M. (2010). Dynamics of podosome stiffness revealed by atomic force microscopy. *Proceedings of the National Academy of Sciences of the United States of America*, *107*(49). https://doi.org/10.1073/pnas.1007835107

Lagier, B., Lebel, B., Bousquet, J., & Pène, J. (1997). Different modulation by histamine of IL-4 and interferon-gamma (IFN- γ) release according to the phenotype of human Th0, Th1 and Th2 clones. *Clinical and Experimental Immunology*, *108*(3). https://doi.org/10.1046/j.1365-2249.1997.3791276.x

Lam, J., Herant, M., Dembo, M., & Heinrich, V. (2009). Baseline mechanical characterization of J774 macrophages. *Biophysical Journal*, *96*(1), 248–254. https://doi.org/10.1529/biophysj.108.139154

Lee, H. H., Pozzo, J. D., Salamanca, S. A., Hernandez, H., & Martinez, L. R. (2019). Reduced phagocytosis and killing of Cryptococcus neoformans biofilm-derived cells by J774.16 macrophages is associated with fungal capsular production and surface modification. *Fungal Genetics and Biology*, *132*(April), 103258. https://doi.org/10.1016/j.fgb.2019.103258

Lee, W. L., Mason, D., Schreiber, A. D., & Grinstein, S. (2007). Quantitative Analysis of Membrane Remodeling at the Phagocytic Cup. *Molecular Biology of the Cell*, *18*(8), 2883–2892. https://doi.org/10.1091/mbc.E06-05-0450

Legg, J. A., Bompard, G., Dawson, J., Morris, H. L., Andrew, N., Cooper, L., Johnston, S. A., Tramountanis, G., & Machesky, L. M. (2007). N-WASP Involvement in Dorsal Ruffle Formation in Mouse Embryonic Fibroblasts □ D □ V. *Molecular Biology of the Cell*, *18*, 678–687. https://doi.org/10.1091/mbc.E06

Leijnse, N., Oddershede, L. B., & Bendix, P. M. (2015). Helical buckling of actin inside filopodia generates traction. *Proceedings of the National Academy of Sciences of the United States of America*, *112*(1), 136–141. https://doi.org/10.1073/pnas.1411761112

Lemaire, S., Mingeot-Leclercq, M. P., Tulkens, P. M., & Bambeke, F. V. (2014). Study of macrophage functions in murine J774 cells and human activated THP-1 cells exposed to oritavancin, a lipoglycopeptide with high cellular accumulation. *Antimicrobial Agents and Chemotherapy*, *58*(4), 2059–2066. https://doi.org/10.1128/AAC.02475-13

Levayer, R., & Lecuit, T. (2012). Biomechanical regulation of contractility: Spatial control and dynamics. *Trends in Cell Biology*, *22*(2), 61–81. https://doi.org/10.1016/j.tcb.2011.10.001

Liang, Z., Zhang, Q., Thomas, C. M. R., Chana, K. K., Gibeon, D., Barnes, P. J., Chung, K. F., Bhavsar, P. K., & Donnelly, L. E. (2014). Impaired macrophage phagocytosis of bacteria in severe asthma. *Respiratory Research*, *15*(1). https://doi.org/10.1186/1465-9921-15-72

Liebl, D., & Griffiths, G. (2009). Transient assembly of F-actin by phagosomes delays phagosome fusion with lysosomes in cargo-overloaded macrophages. *Journal of Cell Science*, *122*(16). https://doi.org/10.1242/jcs.048355

Lin, X., & Heitman, J. (2006). The Biology of the *Cryptococcus neoformans* Species Complex. *Annual Review of Microbiology*, *60*(1), 69–105. https://doi.org/10.1146/annurev.micro.60.080805.142102

Lin, X., Hull, C. M., & Heitman, J. (2005). Sexual reproduction between partners of the same mating type in Cryptococcus neoformans. *Nature*, *434*(7036), 1017–1021. https://doi.org/10.1038/nature03448

Linder, S., Higgs, H., Hüfner, K., Schwarz, K., Pannicke, U., & Aepfelbacher, M. (2000). The Polarization Defect of Wiskott-Aldrich Syndrome Macrophages Is Linked to Dislocalization of the Arp2/3 Complex. *The Journal of Immunology*, *165*(1). https://doi.org/10.4049/jimmunol.165.1.221

Lindmark, H., Rosengren, B., Hurt-Camejo, E., & Bruder, C. E. G. (2004). Gene expression profiling shows that macrophages derived from mouse embryonic stem cells is an improved in vitro model for studies of vascular disease. *Experimental Cell Research*, *300*(2). https://doi.org/10.1016/j.yexcr.2004.06.025

Liu, R., Abreu-Blanco, M. T., Barry, K. C., Linardopoulou, E. V., Osborn, G. E., & Parkhurst, S. M. (2009). Wash functions downstream of Rho and links linear and branched actin nucleation factors. *Development*, *136*(16), 2849–2860. https://doi.org/10.1242/dev.035246

Loitto, V. M., Huang, C., Sigal, Y. J., & Jacobson, K. (2007). Filopodia are induced by aquaporin-9 expression. *Experimental Cell Research*, *313*(7). https://doi.org/10.1016/j.yexcr.2007.01.023

Luxenburg, C., Geblinger, D., Klein, E., Anderson, K., Hanein, D., Geiger, B., & Addadi, L. (2007). The architecture of the adhesive apparatus of cultured osteoclasts: From podosome formation to sealing zone assembly. *PLoS ONE*, *2*(1). https://doi.org/10.1371/journal.pone.0000179

Ma, H., Croudace, J. E., Lammas, D. A., & May, R. C. (2006). Expulsion of Live Pathogenic Yeast by Macrophages. *Current Biology*, *16*(21), 2156–2160. https://doi.org/10.1016/j.cub.2006.09.032

MacDougall, L., Kidd, S. E., Galanis, E., Mak, S., Leslie, M. J., Cieslak, P. R., Kronstad, J. W., Morshed, M. G., & Bartlett, K. H. (2007). Spread of Cryptococcus gattii in British Columbia, Canada, and detection in the Pacific Northwest, USA. *Emerging Infectious Diseases*, *13*(1), 42–50. https://doi.org/10.3201/eid1301.060827

Macura, N., Zhang, T., & Casadevall, A. (2007). Dependence of macrophage phagocytic efficacy on antibody concentration. *Infection and Immunity*, *75*(4), 1904–1915. https://doi.org/10.1128/IAI.01258-06

Mahankali, M., Peng, H. J., Cox, D., & Gomez-Cambronero, J. (2011). The mechanism of cell membrane ruffling relies on a phospholipase D2 (PLD2), Grb2 and Rac2 association. *Cellular Signalling*, *23*(8). https://doi.org/10.1016/j.cellsig.2011.03.010

Malaviya, R., Ikeda, T., Ross, E., & Abraham, S. N. (1996). Mast cell modulation of neutrophil influx and bacterial clearance at sites of infection through TNF-α. *Nature*, *381*(6577). https://doi.org/10.1038/381077a0

Malaviya, R., Ross, E. A., MacGregor, J. I., Ikeda, T., Little, J. R., Jakschik, B. A., & Abraham, S. N. (1994). Mast cell phagocytosis of FimH-expressing enterobacteria. *Journal of Immunology (Baltimore, Md. : 1950)*, *152*(4).

Mantovani, A. (2010). The growing diversity and spectrum of action of myeloid-derived suppressor cells. *European Journal of Immunology*, *40*(12). https://doi.org/10.1002/eji.201041170

Mantovani, A., Sica, A., Sozzani, S., Allavena, P., Vecchi, A., & Locati, M. (2004). The chemokine system in diverse forms of macrophage activation and polarization. *Trends in Immunology*, *25*(12), 677–686. https://doi.org/10.1016/j.it.2004.09.015

Marshall, J. S., Warrington, R., Watson, W., & Kim, H. L. (2018). An introduction to immunology and immunopathology. *Allergy, Asthma & Clinical Immunology*, *14*(S2), 49. https://doi.org/10.1186/s13223-018-0278-1

Masters, T. A., Pontes, B., Viasnoff, V., Li, Y., & Gauthier, N. C. (2013). Plasma membrane tension orchestrates membrane trafficking, cytoskeletal remodeling, and biochemical signaling during phagocytosis. *Proceedings of the National Academy of Sciences of the United States of America*, *110*(29), 11875–11880. https://doi.org/10.1073/pnas.1301766110

Mattila, P. K., & Lappalainen, P. (2008). Filopodia: Molecular architecture and cellular functions. *Nature Reviews Molecular Cell Biology*, *9*(6), 446–454. https://doi.org/10.1038/nrm2406

Maus, U. A., Janzen, S., Wall, G., Srivastava, M., Blackwell, T. S., Christman, J. W., Seeger, W., Welte, T., & Lohmeyer, J. (2006). Resident alveolar macrophages are replaced by recruited monocytes in response to endotoxin-induced lung inflammation. *American Journal of Respiratory Cell and Molecular Biology*, *35*(2), 227–235. https://doi.org/10.1165/rcmb.2005-0241OC

Maziarz, E. K., & Perfect, J. R. (2016). Cryptococcosis. *Infectious Disease Clinics of North America*, *30*(1), 179–206. https://doi.org/10.1016/j.idc.2015.10.006

McClelland, C. M., Chang, Y. C., Varma, A., & Kwon-Chung, K. J. (2004). Uniqueness of the mating system in Cryptococcus neoformans. *Trends in Microbiology*, *12*(5), 208–212. https://doi.org/10.1016/j.tim.2004.03.003

McQuiston, T., & Poeta, M. D. (2014). The Interaction of *Cryptococcus neoformans* with Host MacroPhages and Neutrophils. In J. Heitman, T. R. Kozel, K. J. Kwon-Chung, J. R. Perfect, & A. Casadevall (Eds.), *Cryptococcus* (pp. 371–385). ASM Press. https://doi.org/10.1128/9781555816858.ch26

Maxson, M. E., Cook, E., Casadevall, A., & Zaragoza, O. (2007). The volume and hydration of the Cryptococcus neoformans polysaccharide capsule. *Fungal Genetics and Biology*, *44*(3). https://doi.org/10.1016/j.fgb.2006.07.010

McBeath, R., Pirone, D. M., Nelson, C. M., Bhadriraju, K., & Chen, C. S. (2004). Cell shape, cytoskeletal tension, and RhoA regulate stem cell lineage commitment. *Developmental Cell*, *6*(4). https://doi.org/10.1016/S1534-5807(04)00075-9

McClelland, E. E., Bernhardt, P., & Casadevall, A. (2006). Estimating the relative contributions of virulence factors for pathogenic microbes. *Infection and Immunity*, *74*(3). https://doi.org/10.1128/IAI.74.3.1500-1504.2006

McNeill, E., Iqbal, A. J., Patel, J., White, G. E., Regan-Komito, D., Greaves, D. R., & Channon, K. M. (2014). Contrasting in vitro vs. In vivo effects of a cell membrane-specific CC-chemokine binding protein on macrophage chemotaxis. *Journal of Molecular Medicine*, *92*(11). https://doi.org/10.1007/s00109-014-1194-6

McWhorter, F. Y., Wang, T., Nguyen, P., Chung, T., & Liu, W. F. (2013). Modulation of macrophage phenotype by cell shape. *Proceedings of the National Academy of Sciences of the United States of America*, *110*(43), 17253–17258. https://doi.org/10.1073/pnas.1308887110

Medzhitov, R., & Janeway, C. (2000). Advances in immunology: Innate immunity. *New England Journal of Medicine*, *343*(5). https://doi.org/10.1056/NEJM200008033430506

Mellman, I., Koch, T., Healey, G., Hunziker, W., Lewis, V., Plutner, H., Miettinen, H., Vaux, D., Moore, K., & Stuart, S. (1988). Structure and function of Fc receptors on macrophages and lymphocytes. In *J. Cell Sci. Suppl* (Vol. 9, pp. 45–65).

Merrifield, E. H., & Stephen, A. M. (1980). Structural investigations of two capsular polysaccharides from cryptococcus neoformans. *Carbohydrate Research*, *86*(1). https://doi.org/10.1016/S0008-6215(00)84582-6

Mittal, S. K., & Roche, P. A. (2015). Suppression of antigen presentation by IL-10. *Current Opinion in Immunology*, *34*, 22–27. https://doi.org/10.1016/j.coi.2014.12.009

Misharin, A. V., Morales-Nebreda, L., Reyfman, P. A., Cuda, C. M., Walter, J. M., McQuattie-Pimentel, A. C., Chen, C. I., Anekalla, K. R., Joshi, N., Williams, K. J. N., Abdala-Valencia,

H., Yacoub, T. J., Chi, M., Chiu, S., Gonzalez-Gonzalez, F. J., Gates, K., Lam, A. P., Nicholson, T. T., Homan, P. J., … Perlman, H. (2017). Monocyte-derived alveolar macrophages drive lung fibrosis and persist in the lung over the life span. *Journal of Experimental Medicine*, *214*(8). https://doi.org/10.1084/jem.20162152

Mizutani, K., Miki, H., He, H., Maruta, H., & Takenawa, T. (2002). Essential role of neural Wiskott-Aldrich syndrome protein in podosome formation and degradation of extracellular matrix in src-transformed fibroblasts. *Cancer Research*, *62*(3), 669–674.

Mócsai, A., Ruland, J., & Tybulewicz, V. L. J. (2010). The SYK tyrosine kinase: A crucial player in diverse biological functions. *Nature Reviews Immunology*, *10*(6), 387–402. https://doi.org/10.1038/nri2765

Moeendarbary, E., & Harris, A. R. (2014). Cell mechanics: Principles, practices, and prospects. *Wiley Interdisciplinary Reviews: Systems Biology and Medicine*, *6*(5), 371–388. https://doi.org/10.1002/wsbm.1275

Mogensen, T. H. (2009). Pathogen Recognition and Inflammatory Signaling in Innate Immune Defenses. *Clinical Microbiology Reviews*, *22*(2), 240–273. https://doi.org/10.1128/CMR.00046-08

Mogilner, A., & Oster, G. (1996). Cell motility driven by actin polymerization. *Biophysical Journal*, *71*(6). https://doi.org/10.1016/S0006-3495(96)79496-1

Möller, J., Luehmann, T., Hall, H., & Vogel, V. (2012). The race to the pole: How high-aspect ratio shape and heterogeneous environments limit phagocytosis of filamentous Escherichia coli bacteria by macrophages. *Nano Letters*, *12*(6), 2901–2905. https://doi.org/10.1021/nl3004896

Mondal, D., Mathur, A., & Chandra, P. K. (2016). Tripping on TRIB3 at the junction of health, metabolic dysfunction and cancer. *Biochimie*, *124*, 34–52. https://doi.org/10.1016/j.biochi.2016.02.005

Monypenny, J., Chou, H.-C., Bañón-Rodríguez, I., Thrasher, A. J., Antón, I. M., Jones, G. E., & Calle, Y. (2011). Role of WASP in cell polarity and podosome dynamics of myeloid cells. *European Journal of Cell Biology*, *90*(2–3), 198–204. https://doi.org/10.1016/j.ejcb.2010.05.009

Morita, H., He, F., Fuse, T., Ouwehand, A. C., Hashimoto, H., Hosoda, M., Mizumachi, K., & Kurisaki, J. I. (2002). Cytokine Production by the Murine Macrophage Cell Line J774.1 after Exposure to Lactobacilli. *Bioscience, Biotechnology and Biochemistry*, *66*(9), 1963–1966. https://doi.org/10.1271/bbb.66.1963

Mørland, B., & Kaplan, G. (1977). Macrophage activation in vivo and in vitro. *Experimental Cell Research*, *108*(2), 279–288. https://doi.org/10.1016/S0014-4827(77)80035-9

Mullins, R. D., Heuser, J. A., & Pollard, T. D. (1998). The interaction of Arp23 complex with actin: Nucleation, high affinity pointed end capping, and formation of branching networks of filaments. In *Cell Biology* (Vol. 95, pp. 6181–6186). www.pnas.org.

Mukherjee, J., Casadevall, A., & Scharff, M. D. (1993). Molecular characterization of the humoral responses to Cryptococcus neoformans infection and glucuronoxylomannan-tetanus toxoid conjugate immunization. *The Journal of Experimental Medicine*, *177*(4), 1105–1116. https://doi.org/10.1084/jem.177.4.1105

Muntjewerff, E. M., & Meesters, L. D. (2020). Antigen Cross-Presentation by Macrophages. *Frontiers in Immunology*, *11*, 12.

Murray, P. J., & Wynn, T. A. (2011). Protective and pathogenic functions of macrophage subsets. *Nature Reviews Immunology*, *11*(11), 723–737. https://doi.org/10.1038/nri3073

Murphy, D., Oldfield, R., Schwartz, S., & Davidson, M. (2021). *Introduction to Phase Contrast Microscopy*. https://www.microscopyu.com/techniques/phase-contrast/introduction-to-phase-contrast-microscopy

Murphy, T. F., Brauer, A. L., Schiffmacher, A. T., & Sethi, S. (2004). Persistent Colonization by *Haemophilus influenzae* in Chronic Obstructive Pulmonary Disease. *American Journal of Respiratory and Critical Care Medicine*, *170*(3), 266–272. https://doi.org/10.1164/rccm.200403-354OC

Nagaraj, S., & Gabrilovich, D. I. (2007). Myeloid-derived suppressor cells. *Advances in Experimental Medicine and Biology*, *601*, 213–223. https://doi.org/10.1007/978-0-387-72005-0_22

Nakahira, K., Kim, H. P., Geng, X. H., Nakao, A., Wang, X., Murase, N., Drain, P. F., Wang, X., Sasidhar, M., Nabel, E. G., Takahashi, T., Lukacs, N. W., Ryter, S. W., Morita, K., & Choi, A. M. K. (2006). Carbon monoxide differentially inhibits TLR signaling pathways by regulating ROS-induced trafficking of TLRs to lipid rafts. *Journal of Experimental Medicine*, *203*(10), 2377–2389. https://doi.org/10.1084/jem.20060845

Nelsen, E., Hobson, C. M., Kern, M. E., Hsiao, J. P., O'Brien, E. T., Watanabe, T., Condon, B. M., Boyce, M., Grinstein, S., Hahn, K. M., Falvo, M. R., & Superfine, R. (2020). Combined Atomic Force Microscope and Volumetric Light Sheet System for Correlative Force and Fluorescence Mechanobiology Studies. *Scientific Reports*, *10*(1). https://doi.org/10.1038/s41598-020-65205-8

Netea, M. G., Schlitzer, A., Placek, K., Joosten, L. A. B., & Schultze, J. L. (2019). Innate and Adaptive Immune Memory: An Evolutionary Continuum in the Host's Response to Pathogens. *Cell Host & Microbe*, *25*(1), 13–26. https://doi.org/10.1016/j.chom.2018.12.006

Niespolo, C. (2020). *Investigating the Post-transcriptional Regulation of Macrophage and Prostate Cancer Transcriptome by microRNAs with focus on Tribbles-1*. Doctoral dissertation, University of Sheffield.

Nilsen, N. J., Deininger, S., Nonstad, U., Skjeldal, F., Husebye, H., Rodionov, D., Aulock, S. von, Hartung, T., Lien, E., Bakke, O., & Espevik, T. (2008). Cellular trafficking of lipoteichoic acid and Toll-like receptor 2 in relation to signaling; role of CD14 and CD36. *Journal of Leukocyte Biology*, *84*(1), 280–291. https://doi.org/10.1189/jlb.0907656

Novakowski, K. E., Huynh, A., Han, S. J., Dorrington, M. G., Yin, C., Tu, Z., Pelka, P., Whyte, P., Guarné, A., Sakamoto, K., & Bowdish, D. M. E. (2016). A naturally occurring transcript variant of MARCO reveals the SRCR domain is critical for function. *Immunology and Cell Biology*, *94*(7), 646–655. https://doi.org/10.1038/icb.2016.20

Nussbaum, G., Cleare, W., Casadevall, A., Scharff, M. D., & Valadon, P. (1997). Epitope location in the Cryptococcus neoformans capsule is a determinant of antibody efficacy. *Journal of Experimental Medicine*, *185*(4). https://doi.org/10.1084/jem.185.4.685

Ochoa, G. C., Slepnev, V. I., Neff, L., Ringstad, N., Takei, K., Daniell, L., Kim, W., Cao, H., McNiven, M., Baron, R., & Camilli, P. D. (2000). A functional link between dynamin and the actin cytoskeleton at podosomes. *Journal of Cell Biology*, *150*(2). https://doi.org/10.1083/jcb.150.2.377

Odom, A., Muir, S., Lim, E., Toffaletti, D. L., Perfect, J., & Heitman, J. (1997). Calcineurin is required for virulence of Cryptococcus neoformans. *The EMBO Journal*, *16*(10), 2576–2589. https://doi.org/10.1093/emboj/16.10.2576

Ogden, B. E., & Hill, H. R. (1980). Histamine regulates lymphocyte mitogenic responses through activation of specific H1 and H2 histamine receptors. *Immunology*, *41*(1).

Ohya, K., Handa, Y., Ogawa, M., Suzuki, M., & Sasakawa, C. (2005). IpgB1 is a novel Shigella effector protein involved in bacterial invasion of host cells: Its activity to promote membrane ruffling via Rac1 and Cdc42 activation. *Journal of Biological Chemistry*, *280*(25), 24022–24034. https://doi.org/10.1074/jbc.M502509200

Orth, J. D., & McNiven, M. A. (2006). Get off my back! Rapid receptor internalization through circular dorsal ruffles. *Cancer Research*, *66*(23), 11094–11096. https://doi.org/10.1158/0008-5472.CAN-06-3397

Ortiz-Stern, A., & Rosales, C. (2003). Cross-talk between Fc receptors and integrins. *Immunology Letters*, *90*(2–3), 137–143. https://doi.org/10.1016/j.imlet.2003.08.004

Ostrowski, P. P., Freeman, S. A., Fairn, G., & Grinstein, S. (2019). Dynamic Podosome-Like Structures in Nascent Phagosomes Are Coordinated by Phosphoinositides. *Developmental Cell*, *50*(4), 397-410.e3. https://doi.org/10.1016/j.devcel.2019.05.028

Ostrowski, P. P., Grinstein, S., & Freeman, S. A. (2016). Diffusion Barriers, Mechanical Forces, and the Biophysics of Phagocytosis. *Developmental Cell*, *38*(2), 135–146. https://doi.org/10.1016/j.devcel.2016.06.023

Pacheco, P., White, D., & Sulchek, T. (2013). Effects of Microparticle Size and Fc Density on Macrophage Phagocytosis. *PLoS ONE*, *8*(4). https://doi.org/10.1371/journal.pone.0060989

Padmore, T., Stark, C., Turkevich, L. A., & Champion, J. A. (2017). Quantitative analysis of the role of fiber length on phagocytosis and inflammatory response by alveolar macrophages. *Biochimica et Biophysica Acta (BBA) - General Subjects*, *1861*(2), 58–67. https://doi.org/10.1016/j.bbagen.2016.09.031

Pal, M., Onda, C., & Hasegawa, A. (1990). Isolation of saprophytic Cryptococcus neoformans. *Nihon Juigaku Zasshi. The Japanese Journal of Veterinary Science*, *52*(6), 1171–1174. https://doi.org/10.1292/jvms1939.52.1171

Palecanda, A., Paulauskis, J., Al-Mutairi, E., Imrich, A., Qin, G., Suzuki, H., Kodama, T., Tryggvason, K., Koziel, H., & Kobzik, L. (1999). Role of the Scavenger Receptor MARCO in Alveolar Macrophage Binding of Unopsonized Environmental Particles. *The Journal of Experimental Medicine*, *189*(9), 1497–1506. https://doi.org/10.1084/jem.189.9.1497

Pappas, P. G., Lionakis, M. S., Arendrup, M. C., Ostrosky-Zeichner, L., & Kullberg, B. J. (2018). Invasive candidiasis. *Nature Reviews Disease Primers*, *4*(1), 18026. https://doi.org/10.1038/nrdp.2018.26

Park, S. Y., Jung, M. Y., Kim, H. J., Lee, S. J., Kim, S. Y., Lee, B. H., Kwon, T. H., Park, R. W., & Kim, I. S. (2007). Rapid cell corpse clearance by stabilin-2, a membrane phosphatidylserine receptor. *Cell Death and Differentiation*, *15*(1). https://doi.org/10.1038/sj.cdd.4402242

Patel, P. C., & Harrison, R. E. (2008). Membrane Ruffles Capture C3bi-opsonized Particles in Activated Macrophages. *Molecular Biology of the Cell*, *19*, 4628–4639. https://doi.org/10.1091/mbc.E08

Paul, D., Achouri, S., Yoon, Y. Z., Herre, J., Bryant, C. E., & Cicuta, P. (2013). Phagocytosis dynamics depends on target shape. *Biophysical Journal*, *105*(5), 1143–1150. https://doi.org/10.1016/j.bpj.2013.07.036

Paul, F., Arkin, Y., Giladi, A., Jaitin, D. A., Kenigsberg, E., Keren-Shaul, H., Winter, D., Lara-Astiaso, D., Gury, M., Weiner, A., David, E., Cohen, N., Lauridsen, F. K. B., Haas, S., Schlitzer, A., Mildner, A., Ginhoux, F., Jung, S., Trumpp, A., … Amit, I. (2015). Transcriptional Heterogeneity and Lineage Commitment in Myeloid Progenitors. *Cell*, *163*(7). https://doi.org/10.1016/j.cell.2015.11.013

Pavlik, M. (2009). The dependence of suspension viscosity on particle size, shear rate, and solvent viscosity. *College of Liberal Arts & Social Sciences Theses and Dissertations*, *71*. http://via.library.depaul.edu/etd/71

Peiser, L., Gough, P. J., Kodama, T., & Gordon, S. (2000). Macrophage class A scavenger receptor-mediated phagocytosis of Escherichia coli: Role of cell heterogeneity, microbial strain, and culture conditions in vitro. *Infection and Immunity*, *68*(4). https://doi.org/10.1128/IAI.68.4.1953-1963.2000

Peiser, L., Makepeace, K., Plüddemann, A., Savino, S., Wright, J. C., Pizza, M., Rappuoli, R., Moxon, E. R., & Gordon, S. (2006). Identification of Neisseria meningitidis nonlipopolysaccharide ligands for class A macrophage scavenger receptor by using a novel assay. *Infection and Immunity*, *74*(9). https://doi.org/10.1128/IAI.00124-06

Perfect, J. R. (2006). Cryptococcus neoformans: The yeast that likes it hot. *FEMS Yeast Research*, *6*(4), 463–468. https://doi.org/10.1111/j.1567-1364.2006.00051.x

Perrone, M. C., Veldhuis, J. H., & Brodland, G. W. (2016). Non-straight cell edges are important to invasion and engulfment as demonstrated by cell mechanics model. *Biomechanics and Modeling in Mechanobiology*, *15*(2), 405–418. https://doi.org/10.1007/s10237-015-0697-6

Peskin, C. S., Odell, G. M., & Oster, G. F. (1993). Cellular motions and thermal fluctuations: The Brownian ratchet. *Biophysical Journal*, *65*(1). https://doi.org/10.1016/S0006-3495(93)81035-X

Petty, H. R., Hafeman, D. G., & McConnell, H. M. (1981). Disappearance of macrophage surface folds after antibody-dependent phagocytosis. *Journal of Cell Biology*, *89*(2), 223–229. https://doi.org/10.1083/jcb.89.2.223

Pfaff, M., & Jurdic, P. (2001). Podosomes in osteoclast-like cells: Structural analysis and cooperative roles of paxillin, proline-rich tyrosine kinase 2 (Pyk2) and integrin αVβ3. *Journal of Cell Science*, *114*(15). https://doi.org/10.1242/jcs.114.15.2775

Pfeiffer, T. J., & Ellis, D. H. (1992). Environmental isolation of Cryptococcus neoformans var. Gattii from Eucalyptus tereticornis. *Journal of Medical and Veterinary Mycology: Bi-Monthly Publication of the International Society for Human and Animal Mycology*, *30*(5), 407–408.

Pillay, J., Braber, I. D., Vrisekoop, N., Kwast, L. M., Boer, R. J. D., Borghans, J. A. M., Tesselaar, K., & Koenderman, L. (2010). In vivo labeling with 2H2O reveals a human neutrophil lifespan of 5.4 days. *Blood*, *116*(4). https://doi.org/10.1182/blood-2010-01-259028

Pline, K. M. (2019). *Investigating the role of Cryptococcus neoformans-macrophage interactions on the outcome of cryptococcal infection*. Doctoral dissertation, University of Sheffield.

Poirier, M. B., Fiorino, C., Rajasekar, T. K., & Harrison, R. E. (2020). F-actin flashes on phagosomes mechanically deform contents for efficient digestion in macrophages. *Journal of Cell Science*, *133*(12). https://doi.org/10.1242/jcs.239384

Pollard, T. D. (2016). Actin and actin-binding proteins. *Cold Spring Harbor Perspectives in Biology*, *8*(8). https://doi.org/10.1101/cshperspect.a018226

Pollard, J. W. (2009). Trophic macrophages in development and disease. *Nature Reviews Immunology*, *9*(4), 259–270. https://doi.org/10.1038/nri2528

Pollard, T. D., & Borisy, G. G. (2003). Cellular motility driven by assembly and disassembly of actin filaments. *Cell*, *112*(4), 453–465. https://doi.org/10.1016/s0092-8674(03)00120-x

Pontes, B., Ayala, Y., Fonseca, A. C. C., Romão, L. F., Amaral, R. F., Salgado, L. T., Lima, F. R., Farina, M., Viana, N. B., Moura-Neto, V., & Nussenzveig, oysés M. (2013). Membrane Elastic Properties and Cell Function. *PLoS ONE*, *8*(7). https://doi.org/10.1371/journal.pone.0067708

Pontes, B., Monzo, P., Gole, L., Roux, A. L. L., Kosmalska, A. J., Tam, Z. Y., Luo, W., Kan, S., Viasnoff, V., Roca-Cusachs, P., Tucker-Kellogg, L., & Gauthier, N. C. (2017). Membrane tension controls adhesion positioning at the leading edge of cells. *Journal of Cell Biology*, *216*(9), 2959–2977. https://doi.org/10.1083/jcb.201611117

Pratten, M. K., & Lloyd, J. B. (1986). Pinocytosis and phagocytosis: The effect of size of a particulate substrate on its mode of capture by rat peritoneal macrophages cultured in vitro. *Biochimica et Biophysica Acta (BBA) - General Subjects*, *881*(3), 307–313. https://doi.org/10.1016/0304-4165(86)90020-6

Prineas, J. W., Kwon, E. E., Cho, E. S., Sharer, L. R., Barnett, M. H., Oleszak, E. L., Hoffman, B., & Morgan, B. P. (2001). Immunopathology of secondary-progressive multiple sclerosis. *Annals of Neurology*, *50*(5), 646–657. https://doi.org/10.1002/ana.1255

Pugliese, S. C., Poth, J. M., Fini, M. A., Olschewski, A., El Kasmi, K. C., & Stenmark, K. R. (2015). The role of inflammation in hypoxic pulmonary hypertension: From cellular mechanisms to clinical phenotypes. *American Journal of Physiology. Lung Cellular and Molecular Physiology*, *308*(3), L229-252. https://doi.org/10.1152/ajplung.00238.2014

Raab, M., Swift, J., Dingal, P. C. D. P., Shah, P., Shin, J. W., & Discher, D. E. (2012). Crawling from soft to stiff matrix polarizes the cytoskeleton and phosphoregulates myosin-II heavy chain. *Journal of Cell Biology*, *199*(4). https://doi.org/10.1083/jcb.201205056

Rabinovitch, M. (1995). Professional and non-professional phagocytes: An introduction. *Trends in Cell Biology*, *5*(3), 85–87. https://doi.org/10.1016/S0962-8924(00)88955-2

Rachini, A., Pietrella, D., Lupo, P., Torosantucci, A., Chiani, P., Bromuro, C., Proietti, C., Bistoni, F., Cassone, A., & Vecchiarelli, A. (2007). An anti-β-glucan monoclonal antibody inhibits

growth and capsule formation of Cryptococcus neoformans in vitro and exerts therapeutic, anticryptococcal activity in vivo. *Infection and Immunity*, *75*(11), 5085–5094. https://doi.org/10.1128/IAI.00278-07

Rajasingham, R., Smith, R. M., Park, B. J., Jarvis, J. N., Govender, N. P., Chiller, T. M., Denning, D. W., Loyse, A., & Boulware, D. R. (2017). Global burden of disease of HIV-associated cryptococcal meningitis: An updated analysis. *The Lancet Infectious Diseases*. https://doi.org/10.1016/S1473-3099(17)30243-8

Ralph, P., & Nakoinz, I. (1977). Antibody-dependent killing of erythrocyte and tumor targets by macrophage-related cell lines: Enhancement by PPD and LPS. *Journal of Immunology (Baltimore, Md. : 1950)*, *119*(3).

Raucher, D., & Sheetz, M. P. (2000). Cell spreading and lamellipodial extension rate is regulated by membrane tension. *Journal of Cell Biology*, *148*(1), 127–136. https://doi.org/10.1083/jcb.148.1.127

Rhodes, J. C., Polacheck, I., & Kwon-Chung, K. J. (1982). Phenoloxidase activity and virulence in isogenic strains of Cryptococcus neoformans. *Infection and Immunity*, *36*(3), 1175–1184. https://doi.org/10.1128/iai.36.3.1175-1184.1982

Rhodes, M. (Ed.). (2017). *Introduction to Particle Technology* (2nd ed.). Wiley. pp. 1-28.

Richards, D. M., & Endres, R. G. (2014). The mechanism of phagocytosis: Two stages of engulfment. *Biophysical Journal*, *107*(7), 1542–1553. https://doi.org/10.1016/j.bpj.2014.07.070

Richards, D. M., & Endres, R. G. (2016). Target shape dependence in a simple model of receptor-mediated endocytosis and phagocytosis. *Proceedings of the National Academy of Sciences*, *113*(22), 6113–6118. https://doi.org/10.1073/pnas.1521974113

Richards, D. M., & Endres, R. G. (2017). How cells engulf: A review of theoretical approaches to phagocytosis. *Reports on Progress in Physics*, *80*(12), 126601. https://doi.org/10.1088/1361-6633/aa8730

Rivas-Fuentes, S., García-García, E., Nieto-Castañeda, G., & Rosales, C. (2010). Fcγ receptors exhibit different phagocytosis potential in human neutrophils. *Cellular Immunology*, *263*(1), 114–121. https://doi.org/10.1016/j.cellimm.2010.03.006

Robinson, M. W., Harmon, C., & O'Farrelly, C. (2016). Liver immunology and its role in inflammation and homeostasis. *Cellular & Molecular Immunology*, *13*(3), 267–276. https://doi.org/10.1038/cmi.2016.3

Rocklin, R. E., & Greineder, D. (1977). Histamine-induced suppressor factor (HSF): Nature of stimulus and effect. *Journal of Allergy and Clinical Immunology*, *61*(3). https://doi.org/10.1016/0091-6749(78)90293-2

Romani, L. (2004). Immunity to fungal infections. *Nature Reviews Immunology*, *4*(1), 11–24. https://doi.org/10.1038/nri1255

Rosenberg, H. F., Dyer, K. D., & Foster, P. S. (2013). Eosinophils: Changing perspectives in health and disease. *Nature Reviews Immunology*, *13*(1), 9–22. https://doi.org/10.1038/nri3341

Ross, G. D., Reed, W., Dalzell, J. G., Becker, S. E., & Hogg, N. (1992). Macrophage cytoskeleton association with CR3 and CR4 regulates receptor mobility and phagocytosis of iC3b-opsonized erythrocytes. *Journal of Leukocyte Biology*, *51*(2). https://doi.org/10.1002/jlb.51.2.109

Rotty, J. D., Brighton, H. E., Craig, S. L., Asokan, S. B., Cheng, N., Ting, J. P., & Bear, J. E. (2017). Arp2/3 Complex Is Required for Macrophage Integrin Functions but Is Dispensable for FcR Phagocytosis and In Vivo Motility. *Developmental Cell*, *42*(5), 498-513.e6. https://doi.org/10.1016/j.devcel.2017.08.003

Roufosse, F. (2018). Targeting the Interleukin-5 Pathway for Treatment of Eosinophilic Conditions Other than Asthma. *Frontiers in Medicine*, *5*, 49. https://doi.org/10.3389/fmed.2018.00049

Ryan, J. J., Kashyap, M., Bailey, D., Kennedy, S., Speiran, K., Brenzovich, J., Barnstein, B., Oskeritzian, C., & Gomez, G. (2007). Mast cell homeostasis: A fundamental aspect of allergic disease. *Critical Reviews in Immunology*, *27*(1), 15–32. https://doi.org/10.1615/critrevimmunol.v27.i1.20

Sachs, F., & Sivaselvan, M. V. (2015). Cell volume control in three dimensions: Water movement without solute movement. *Journal of General Physiology*, *145*(5), 373–380. https://doi.org/10.1085/jgp.201411297

Sarantis, H., & Grinstein, S. (2012). Subversion of phagocytosis for pathogen survival. *Cell Host and Microbe*, *12*(4), 419–431. https://doi.org/10.1016/j.chom.2012.09.001

Savai, R., Pullamsetti, S. S., Kolbe, J., Bieniek, E., Voswinckel, R., Fink, L., Scheed, A., Ritter, C., Dahal, B. K., Vater, A., Klussmann, S., Ghofrani, H. A., Weissmann, N., Klepetko, W., Banat, G. A., Seeger, W., Grimminger, F., & Schermuly, R. T. (2012). Immune and inflammatory cell involvement in the pathology of idiopathic pulmonary arterial hypertension. *American Journal of Respiratory and Critical Care Medicine*, *186*(9). https://doi.org/10.1164/rccm.201202-0335OC

Schaub, S., Meister, J. J., & Verkhovsky, A. B. (2007). Analysis of actin filament network organization in lamellipodia by comparing experimental and simulated images. *Journal of Cell Science*, *120*(8), 1491–1500. https://doi.org/10.1242/jcs.03379

Schiff, D. E., Kline, L., Soldau, K., Lee, J. D., Pugin, J., Tobias, P. S., & Ulevitch, R. J. (1997). Phagocytosis of Gram-negative bacteria by a unique CD14-dependent mechanism. *Journal of Leukocyte Biology*, *62*(6). https://doi.org/10.1002/jlb.62.6.786

Schindelin, J., Arganda-Carreras, I., Frise, E., Kaynig, V., Longair, M., Pietzsch, T., Preibisch, S., Rueden, C., Saalfeld, S., Schmid, B., Tinevez, J.-Y., White, D. J., Hartenstein, V., Eliceiri, K., Tomancak, P., & Cardona, A. (2012). Fiji: An open-source platform for biological-image analysis. *Nature Methods*, *9*(7), 676–682. https://doi.org/10.1038/nmeth.2019

Schliess, F., Reinehr, R., & Häussinger, D. (2007). Osmosensing and signaling in the regulation of mammalian cell function: Osmosensing and signaling in mammalian cell function. *FEBS Journal*, *274*(22), 5799–5803. https://doi.org/10.1111/j.1742-4658.2007.06100.x

Schmid, C. D., Melchior, B., Masek, K., Puntambekar, S. S., Danielson, P. E., Lo, D. D., Sutcliffe, J. G., & Carson, M. J. (2009). Differential gene expression in LPS/IFNγ activated microglia and macrophages: In vitro versus in vivo. *Journal of Neurochemistry*, *109*(SUPPL. 1), 117–125. https://doi.org/10.1111/j.1471-4159.2009.05984.x

Scoville, S. D., Freud, A. G., & Caligiuri, M. A. (2017). Modeling human natural killer cell development in the era of innate lymphoid cells. *Frontiers in Immunology*, *8*(MAR). https://doi.org/10.3389/fimmu.2017.00360

Serda, R. E., Gu, J., Burks, J. K., Ferrari, K., Ferrari, C., & Ferrari, M. (2009). Quantitative mechanics of endothelial phagocytosis of silicon microparticles. *Cytometry Part A*, *75*(9), 752–760. https://doi.org/10.1002/cyto.a.20769

Simonetta, F., Pradier, A., & Roosnek, E. (2016). T-bet and Eomesodermin in NK Cell Development, Maturation, and Function. *Frontiers in Immunology*, *7*. https://doi.org/10.3389/fimmu.2016.00241

Sirois, J., Ménard, G., Moses, A. S., & Bissonnette, E. Y. (2000). Importance of Histamine in the Cytokine Network in the Lung Through H 2 and H 3 Receptors: Stimulation of IL-10 Production. *The Journal of Immunology*, *164*(6), 2964–2970. https://doi.org/10.4049/jimmunol.164.6.2964

Sironi, M., Cagliani, R., Forni, D., & Clerici, M. (2015). Evolutionary insights into host–pathogen interactions from mammalian sequence data. *Nature Reviews Genetics*, *16*(4), 224–236. https://doi.org/10.1038/nrg3905

Sitarska, E., & Diz-Muñoz, A. (2020). Pay attention to membrane tension: Mechanobiology of the cell surface. *Current Opinion in Cell Biology*, *66*, 11–18. https://doi.org/10.1016/j.ceb.2020.04.001

Small, J. M., & Mitchell, T. G. (1989). Strain Variation in Antiphagocytic Activity of Capsular Polysaccharides from Cryptococcus neoformans Serotype A. In *INFECTION AND IMMUNITY* (Vol. 57, Issue 12, pp. 3751–3756).

Small, J. V., Isenberg, G., & Celis, J. E. (1978). Polarity of actin at the leading edge of cultured cells. *Nature*, *272*(5654). https://doi.org/10.1038/272638a0

Smeets, B., Cuvelier, M., Pešek, J., & Ramon, H. (2018). The Effect of Cortical Elasticity and Active Tension on Cell Adhesion Mechanics. *Biophysical Journal*, *116*(5), 930–937. https://doi.org/10.1016/j.bpj.2019.01.015

Smiley, S. T., & Grusby, M. J. (1998). Interleukin 4. In *Encyclopedia of Immunology* (pp. 1451–1453). Elsevier. https://doi.org/10.1006/rwei.1999.0368

Smith, L. M., Dixon, E. F., & May, R. C. (2015). The fungal pathogen Cryptococcus neoformans manipulates macrophage phagosome maturation. *Cellular Microbiology*, *17*(5), 702–713. https://doi.org/10.1111/cmi.12394

Sobota, A., Strzelecka-Kiliszek, A., Gładkowska, E., Yoshida, K., Mrozińska, K., & Kwiatkowska, K. (2005). Binding of IgG-Opsonized Particles to FcγR Is an Active Stage of Phagocytosis That Involves Receptor Clustering and Phosphorylation. *The Journal of Immunology*, *175*(7), 4450–4457. https://doi.org/10.4049/jimmunol.175.7.4450

Solsona, C., Innocenti, B., & Fernández, J. M. (1998). Regulation of exocytotic fusion by cell inflation. *Biophysical Journal*, *74*(2 I), 1061–1073. https://doi.org/10.1016/S0006-3495(98)74030-5

Sosale, N. G., Rouhiparkouhi, T., Bradshaw, A. M., Dimova, R., Lipowsky, R., & Discher, D. E. (2015). Cell rigidity and shape override CD47's "self"-signaling in phagocytosis by hyperactivating myosin-II. *Blood*, *125*(3), 542–552. https://doi.org/10.1182/blood-2014-06-585299

Spagnoli, C., Beyder, A., Besch, S., & Sachs, F. (2008). Atomic force microscopy analysis of cell volume regulation. *Physical Review E - Statistical, Nonlinear, and Soft Matter Physics*, *78*(3). https://doi.org/10.1103/PhysRevE.78.031916

Speed, B., & Dunt, D. (1995). Clinical and Host Differences Between Infections with the Two Varieties of Cryptococcus neoformans. *Clinical Infectious Diseases*, *21*(1), 28–34. https://doi.org/10.1093/clinids/21.1.28

Sprenkeler, E. G. G., Webbers, S. D. S., & Kuijpers, T. W. (2021). When Actin is Not Actin' Like It Should: A New Category of Distinct Primary Immunodeficiency Disorders. *Journal of Innate Immunity*, *13*(1), 3–25. https://doi.org/10.1159/000509717

Spriel, A. B. V., Herik-Oudijk, I. E. V. D., Sorge, N. M. V., Vilé, H. A., Strijp, J. A. G. V., & Winkel, J. G. J. V. D. (1999). Effective phagocytosis and killing of Candida albicans via

targeting Fcγ/RI (CD64) or FcαRI (CD89) on neutrophils. *Journal of Infectious Diseases*, *179*(3). https://doi.org/10.1086/314643

Steenbergen, J. N., Shuman, H. A., & Casadevall, A. (2001). Cryptococcus neoformans interactions with amoebae suggest an explanation for its virulence and intracellular pathogenic strategy in macrophages. *Proceedings of the National Academy of Sciences of the United States of America*, *98*(26), 15245–15250. https://doi.org/10.1073/pnas.261418798

Steger, G. (1998). An unbiased detector of curvilinear structures. *IEEE Transactions on Pattern Analysis and Machine Intelligence*, *20*(2), 113–125. https://doi.org/10.1109/34.659930

Stijlemans, B., Korf, H., Baetselier, P. D., Brys, L., Ginderachter, J. A. V., Magez, S., & Trez, C. D. (2020). Hepatocyte-derived IL-10 plays a crucial role in attenuating pathogenicity during the chronic phase of T. congolense infection. *PLoS Pathogens*, *16*(2), e1008170. https://doi.org/10.1371/journal.ppat.1008170

Stone, K. D., Prussin, C., & Metcalfe, D. D. (2010). IgE, mast cells, basophils, and eosinophils. *Journal of Allergy and Clinical Immunology*, *125*(2 SUPPL. 2). https://doi.org/10.1016/j.jaci.2009.11.017

Stow, J. L., & Condon, N. D. (2016). The cell surface environment for pathogen recognition and entry. *Clinical and Translational Immunology*, *5*(4). https://doi.org/10.1038/cti.2016.15

Stradal, T. E. B., Rottner, K., Disanza, A., Confalonieri, S., Innocenti, M., & Scita, G. (2004). Regulation of actin dynamics by WASP and WAVE family proteins. *Trends in Cell Biology*, *14*(6), 303–311. https://doi.org/10.1016/j.tcb.2004.04.007

Svitkina, T. M. (2020). Actin Cell Cortex: Structure and Molecular Organization. *Trends in Cell Biology*, *30*(7), 556–565. https://doi.org/10.1016/j.tcb.2020.03.005

Svitkina, T. (2018). The actin cytoskeleton and actin-based motility. *Cold Spring Harbor Perspectives in Biology*, *10*(1). https://doi.org/10.1101/cshperspect.a018267

Svitkina, T. M., & Borisy, G. G. (1999). Arp2/3 complex and actin depolymerizing factor/cofilin in dendritic organization and treadmilling of actin filament array in lamellipodia. *Journal of Cell Biology*, *145*(5). https://doi.org/10.1083/jcb.145.5.1009

Svitkina, T. M., Bulanova, E. A., Chaga, O. Y., Vignjevic, D. M., Kojima, S. ichiro, Vasiliev, J. M., & Borisy, G. G. (2003). Mechanism of filopodia initiation by reorganization of a dendritic network. *Journal of Cell Biology*, *160*(3). https://doi.org/10.1083/jcb.200210174

Swanson, J. A. (2008). Shaping cups into phagosomes and macropinosomes. *Nature Reviews Molecular Cell Biology*, *9*(8), 639–649. https://doi.org/10.1038/nrm2447

Swanson, J. a, Johnson, M. T., Beningo, K., Post, P., Mooseker, M., & Araki, N. (1999). A contractile activity that closes phagosomes in macrophages. *Journal of Cell Science*, *112 (Pt 3*, 307–316.

Tabata, Y., & Ikada, Y. (1990). Phagocytosis of polymer microspheres by macrophages. *New Polymer Materials*, 107–141. https://doi.org/10.1007/BFb0043062

Taborda, C. P., & Casadevall, A. (2002). CR3 (CD11b/CD18) and CR4 (CD11c/CD18) are involved in complement-independent antibody-mediated phagocytosis of Cryptococcus neoformans. *Immunity*, *16*(6). https://doi.org/10.1016/S1074-7613(02)00328-X

Takayama, H., Katsumoto, T., & Takagi, A. (1976). Electron microscopic studies on macrophages II. Effect of colchicine and cytochalasin B on the cell cortex as revealed by ultrathin sectioning. *Microscopy*, *26*(1), 7–8. https://doi.org/10.1093/oxfordjournals.jmicro.a050045

Talmadge, J. E., & Gabrilovich, D. I. (2013). History of myeloid-derived suppressor cells. *Nature Reviews Cancer*, *13*(10), 739–752. https://doi.org/10.1038/nrc3581

Tamura, T., Tailor, P., Yamaoka, K., Kong, H. J., Tsujimura, H., O'Shea, J. J., Singh, H., & Ozato, K. (2005). IFN Regulatory Factor-4 and -8 Govern Dendritic Cell Subset Development and Their Functional Diversity. *The Journal of Immunology*, *174*(5). https://doi.org/10.4049/jimmunol.174.5.2573

Taylor, P. R., Martinez-Pomares, L., Stacey, M., Lin, H. H., Brown, G. D., & Gordon, S. (2005). Macrophage receptors and immune recognition. *Annual review of immunology*, *23*, 901–944. https://doi.org/10.1146/annurev.immunol.23.021704.115816

Tenor, J. L., Oehlers, S. H., Yang, J. L., Tobin, D. M., & Perfect, J. R. (2015). Live imaging of host-parasite interactions in a zebrafish infection model reveals cryptococcal determinants of virulence and central nervous system invasion. *MBio*, *6*(5). https://doi.org/10.1128/mBio.01425-15

Tertrais, M., Bigot, C., Martin, E., Poincloux, R., Labrousse, A., & Maridonneau-Parini, I. (2021). Phagocytosis is coupled to the formation of phagosome-associated podosomes and a transient disruption of podosomes in human macrophages. *European Journal of Cell Biology*, *100*(4), 151161. https://doi.org/10.1016/j.ejcb.2021.151161

Theret, M., Mounier, R., & Rossi, F. (2019). The origins and non-canonical functions of macrophages in development and regeneration. *Development (Cambridge)*, *146*(9). https://doi.org/10.1242/dev.156000

Thomas, C. F., & Limper, A. H. (2007). Current insights into the biology and pathogenesis of Pneumocystis pneumonia. *Nature Reviews Microbiology*, *5*(4), 298–308. https://doi.org/10.1038/nrmicro1621

Thompson, G. R., & Young, J.-A. H. (2021). Aspergillus Infections. *New England Journal of Medicine*, *385*(16), 1496–1509. https://doi.org/10.1056/NEJMra2027424

Tinevez, J. Y., Schulze, U., Salbreux, G., Roensch, J., Joanny, J. F., & Paluch, E. (2009). Role of cortical tension in bleb growth. *Proceedings of the National Academy of Sciences of the United States of America*, *106*(44), 18581–18586. https://doi.org/10.1073/pnas.0903353106

Tollis, S., Dart, A. E., Tzircotis, G., & Endres, R. G. (2010). *The zipper mechanism in phagocytosis: Energetic requirements and variability in phagocytic cup shape*. http://arxiv.org/abs/1011.0370

Treffers, L. W., Houdt, M. V., Bruggeman, C. W., Heineke, M. H., Zhao, X. W., Heijden, J. V. D., Nagelkerke, S. Q., Verkuijlen, P. J. J. H., Geissler, J., Lissenberg-Thunnissen, S., Valerius, T., Peipp, M., Franke, K., Bruggen, R. V., Kuijpers, T. W., Egmond, M. V., Vidarsson, G., Matlung, H. L., & Berg, T. K. V. D. (2019). FcγRIIIb restricts antibody-dependent destruction of cancer cells by human neutrophils. *Frontiers in Immunology*, *10*(JAN). https://doi.org/10.3389/fimmu.2018.03124

Triantafilou, M., Miyake, K., Golenbock, D. T., & Triantafilou, K. (2002). Mediators of innate immune recognition of bacteria concentrate in lipid rafts and facilitate lipopolysaccharide-induced cell activation. *Journal of Cell Science*, *115*(Pt 12), 2603–2611.

Tsarfaty, I., Sandovsky-Losica, H., Mittelman, L., Berdicevsky, I., & Segal, E. (2000). Cellular actin is affected by interaction with Candida albicans. *FEMS Microbiology Letters*, *189*(2), 225–232. https://doi.org/10.1111/j.1574-6968.2000.tb09235.x

Tucker, S. C., & Casadevall, A. (2002). Replication of Cryptococcus neoformans in macrophages is accompanied by phagosomal permeabilization and accumulation of vesicles containing polysaccharide in the cytoplasm. *Proceedings of the National Academy of Sciences*, *99*(5), 3165–3170. https://doi.org/10.1073/pnas.052702799

Turner, M. D., Nedjai, B., Hurst, T., & Pennington, D. J. (2014). Cytokines and chemokines: At the crossroads of cell signalling and inflammatory disease. *Biochimica et Biophysica Acta (BBA) - Molecular Cell Research*, *1843*(11), 2563–2582. https://doi.org/10.1016/j.bbamcr.2014.05.014

Underhill, D. M., & Goodridge, H. S. (2012). Information processing during phagocytosis. *Nature Reviews Immunology*, *12*(7), 492–502. https://doi.org/10.1038/nri3244

Underhill, D. M., Ozinsky, A., Hajjar, A. M., Stevens, A., Wilson, C. B., Bassetti, M., & Aderem, A. (1999). The Toll-like receptor 2 is recruited to macrophage phagosomes and discriminates between pathogens. *Nature*, *401*(6755). https://doi.org/10.1038/44605

Vachon, E., Martin, R., Plumb, J., Kwok, V., Vandivier, R. W., Glogauer, M., Kapus, A., Wang, X., Chow, C. W., Grinstein, S., & Downey, G. P. (2006). CD44 is a phagocytic receptor. *Blood*, *107*(10), 4149–4158. https://doi.org/10.1182/blood-2005-09-3808

van den Dries, K., Meddens, M. B. M., de Keijzer, S., Shekhar, S., Subramaniam, V., Figdor, C. G., & Cambi, A. (2013). Interplay between myosin IIA-mediated contractility and actin network integrity orchestrates podosome composition and oscillations. *Nature Communications*, *4*(1), 1412. https://doi.org/10.1038/ncomms2402

van der Laan, L. J. W., Döpp, E. A., Haworth, R., Pikkarainen, T., Kangas, M., Elomaa, O., Dijkstra, C. D., Gordon, S., Tryggvason, K., & Kraal, G. (1999). Regulation and Functional Involvement of Macrophage Scavenger Receptor MARCO in Clearance of Bacteria In Vivo. *The Journal of Immunology*, *162*(2), 939.

van Egmond, M., Vidarsson, G., & Bakema, J. E. (2015). Cross-talk between pathogen recognizing Toll-like receptors and immunoglobulin Fc receptors in immunity. *Immunological Reviews*, *268*(1), 311–327. https://doi.org/10.1111/imr.12333

van Kessel, K. P. M., Bestebroer, J., & van Strijp, J. A. G. (2014). Neutrophil-Mediated Phagocytosis of Staphylococcus aureus. *Frontiers in Immunology*, *5*. https://doi.org/10.3389/fimmu.2014.00467

van Liempt, E. van, Bank, C. M. C., Mehta, P., García-Vallejo, J. J., Kawar, Z. S., Geyer, R., Alvarez, R. A., Cummings, R. D., Kooyk, Y. van, & Die, I. van. (2006). Specificity of DC-SIGN for mannose- and fucose-containing glycans. *FEBS Letters*, *580*(26). https://doi.org/10.1016/j.febslet.2006.10.009

Vannier, E., Miller, L. C., & Dinarello, C. A. (1991). Histamine suppresses gene expression and synthesis of tumor necrosis factor α via histamine H2 receptors. *Journal of Experimental Medicine*, *174*(1). https://doi.org/10.1084/jem.174.1.281

Varricchi, G., Raap, U., Rivellese, F., Marone, G., & Gibbs, B. F. (2018). Human mast cells and basophils-How are they similar how are they different? *Immunological Reviews*, *282*(1), 8–34. https://doi.org/10.1111/imr.12627

Vartivarian, S. E., Anaissie, E. J., Cowart, R. E., Sprigg, H. A., Tingler, M. J., & Jacobson, E. S. (1993). Regulation of cryptococcal capsular polysaccharide by iron. *Journal of Infectious Diseases*, *167*(1). https://doi.org/10.1093/infdis/167.1.186

Veltman, D. M., Williams, T. D., Bloomfield, G., Chen, B. C., Betzig, E., Insall, R. H., & Kay, R. R. (2016). A plasma membrane template for macropinocytic cups. *ELife*, *5*(DECEMBER2016), 24. https://doi.org/10.7554/eLife.20085

Vignjevic, D., Kojima, S. I., Aratyn, Y., Danciu, O., Svitkina, T., & Borisy, G. G. (2006). Role of fascin in filopodial protrusion. *Journal of Cell Biology*, *174*(6). https://doi.org/10.1083/jcb.200603013

Vinzenz, M., Nemethova, M., Schur, F., Mueller, J., Narita, A., Urban, E., Winkler, C., Schmeiser, C., Koestler, S. A., Rottner, K., Resch, G. P., Maeda, Y., & Small, J. V. (2012). Actin

branching in the initiation and maintenance of lamellipodia. *Journal of Cell Science*, *125*(11), 2775–2785. https://doi.org/10.1242/jcs.107623

Vorselen, D., Wang, Y., Jesus, M. M. de, Shah, P. K., Footer, M. J., Huse, M., Cai, W., & Theriot, J. A. (2020). Microparticle traction force microscopy reveals subcellular force exertion patterns in immune cell–target interactions. *Nature Communications*, *11*(1). https://doi.org/10.1038/s41467-019-13804-z

Wang, F., Zhang, L., Zhang, G. L., Wang, Z. B., Cui, X. S., Kim, N. H., & Sun, S. C. (2014). WASH complex regulates Arp2/3 complex for actin-based polar body extrusion in mouse oocytes. *Scientific Reports*, *4*. https://doi.org/10.1038/srep05596

Wang, H.-B., Ghiran, I., Matthaei, K., & Weller, P. F. (2007). Airway Eosinophils: Allergic Inflammation Recruited Professional Antigen-Presenting Cells. *The Journal of Immunology*, *179*(11). https://doi.org/10.4049/jimmunol.179.11.7585

Wang Y. L. (1985). Exchange of actin subunits at the leading edge of living fibroblasts: possible role of treadmilling. *The Journal of cell biology*, *101*(2), 597–602. https://doi.org/10.1083/jcb.101.2.597

Wang, Y., & Casadevall, A. (1994). Susceptibility of melanized and nonmelanized Cryptococcus neoformans to nitrogen- and oxygen-derived oxidants. *Infection and Immunity*, *62*(7), 3004–3007. https://doi.org/10.1128/iai.62.7.3004-3007.1994

Ween, M., Ahern, J., Carroll, A., Hodge, G., Pizzutto, S., Jersmann, H., Reynolds, P., & Hodge, S. (2016). A small volume technique to examine and compare alveolar macrophage phagocytosis of apoptotic cells and non typeable Haemophilus influenzae (NTHi). *Journal of Immunological Methods*, *429*, 7–14. https://doi.org/10.1016/j.jim.2015.12.004

Werheim, E. R., Senior, K. G., Shaffer, C. A., & Cuadra, G. A. (2020). Oral Pathogen Porphyromonas gingivalis Can Escape Phagocytosis of Mammalian Macrophages. *Microorganisms*, *8*(9), 1432. https://doi.org/10.3390/microorganisms8091432

Wickes, B. L., Mayorga, M. E., Edman, U., & Edman, J. C. (1996). Dimorphism and haploid fruiting in Cryptococcus neoformans: Association with the alpha-mating type. *Proceedings of the National Academy of Sciences*, *93*(14), 7327–7331. https://doi.org/10.1073/pnas.93.14.7327

Williams, J. W., Giannarelli, C., Rahman, A., Randolph, G. J., & Kovacic, J. C. (2018). Macrophage Biology, Classification, and Phenotype in Cardiovascular Disease. *Journal of the American College of Cardiology*, *72*(18), 2166–2180. https://doi.org/10.1016/j.jacc.2018.08.2148

Williams, T. E., Nagarajan, S., Selvaraj, P., & Zhu, C. (2000). Concurrent and Independent Binding of Fcγ Receptors IIa and IIIb to Surface-Bound IgG. *Biophysical Journal*, *79*(4), 1867–1875. https://doi.org/10.1016/S0006-3495(00)76436-8

Wohlleber, D., & Knolle, P. A. (2016). The role of liver sinusoidal cells in local hepatic immune surveillance. *Clinical & Translational Immunology*, *5*(12), e117. https://doi.org/10.1038/cti.2016.74

Wolfe, J., Dowgert, M. F., & Steponkus, P. L. (1986). Mechanical study of the deformation and rupture of the plasma membranes of protoplasts during osmotic expansions. *The Journal of Membrane Biology*, *93*(1), 63–74. https://doi.org/10.1007/BF01871019

Wong, S. W., Kwon, M.-J., Choi, A. M. K., Kim, H.-P., Nakahira, K., & Hwang, D. H. (2009). Fatty Acids Modulate Toll-like Receptor 4 Activation through Regulation of Receptor Dimerization and Recruitment into Lipid Rafts in a Reactive Oxygen Species-dependent Manner. *Journal of Biological Chemistry*, *284*(40), 27384–27392. https://doi.org/10.1074/jbc.M109.044065

Worbs, T., Hammerschmidt, S. I., & Förster, R. (2017). Dendritic cell migration in health and disease. *Nature Reviews Immunology*, *17*(1), 30–48. https://doi.org/10.1038/nri.2016.116

Wu, N. Z., & Baldwin, A. L. (1992). Transient venular permeability increase and endothelial gap formation induced by histamine. *American Journal of Physiology - Heart and Circulatory Physiology*, *262*(4 31-4). https://doi.org/10.1152/ajpheart.1992.262.4.h1238

Wynn, T. A., Barron, L., Thompson, R. W., Madala, S. K., Wilson, M. S., Cheever, A. W., & Ramalingam, T. (2011). Quantitative Assessment of Macrophage Functions in Repair and Fibrosis. In J. E. Coligan, B. E. Bierer, D. H. Margulies, E. M. Shevach, & W. Strober (Eds.), *Current Protocols in Immunology* (p. im1422s93). John Wiley & Sons, Inc. https://doi.org/10.1002/0471142735.im1422s93

Wynn, T. A., Chawla, A., & Pollard, J. W. (2013). Macrophage biology in development, homeostasis and disease. *Nature*, *496*(7446), 445–455. https://doi.org/10.1038/nature12034

Xu, J., Flaczyk, A., Neal, L. M., Fa, Z., Eastman, A. J., Malachowski, A. N., Cheng, D., Moore, B. B., Curtis, J. L., Osterholzer, J. J., & Olszewski, M. A. (2017). Scavenger Receptor MARCO Orchestrates Early Defenses and Contributes to Fungal Containment during Cryptococcal Infection. *The Journal of Immunology*, 1700057. https://doi.org/10.4049/jimmunol.1700057

Yang, C., Czech, L., Gerboth, S., Kojima, S. I., Scita, G., & Svitkina, T. (2007). Novel roles of formin mDia2 in lamellipodia and filopodia formation in motile cells. *PLoS Biology*, *5*(11). https://doi.org/10.1371/journal.pbio.0050317

Yang, C., & Svitkina, T. (2011). Filopodia initiation: Focus on the Arp2/3 complex and formins. *Cell Adhesion and Migration*, *5*(5). https://doi.org/10.4161/cam.5.5.16971

Yoshida, S., Hoppe, A. D., Araki, N., & Swanson, J. A. (2009). Sequential signaling in plasma-membrane domains during macropinosome formation in macrophages. *Journal of Cell Science*, *122*(18), 3250–3261. https://doi.org/10.1242/jcs.053207

Yoshida, S., Pacitto, R., Yao, Y., Inoki, K., & Swanson, J. A. (2015). Growth factor signaling to mTORC1 by amino acid-laden macropinosomes. *Journal of Cell Biology*, *211*(1), 159–172. https://doi.org/10.1083/jcb.201504097

Yu, Y., Smoligovets, A. A., & Groves, J. T. (2013). Modulation of t cell signaling by the actin cytoskeleton. *Journal of Cell Science*, *126*(5). https://doi.org/10.1242/jcs.098210

Zambonin-Zallone, A., Teti, A., Grano, M., Rubinacci, A., Abbadini, M., Gaboli, M., & Marchisio, P. C. (1989). Immunocytochemical distribution of extracellular matrix receptors in human osteoclasts: A β3 integrin is colocalized with vinculin and talin in the podosomes of osteoclastoma giant cells. *Experimental Cell Research*, *182*(2). https://doi.org/10.1016/0014-4827(89)90266-8

Zaragoza, O. (2011). Multiple disguises for the same party: The concepts of morphogenesis and phenotypic variations in Cryptococcus neoformans. *Frontiers in Microbiology*, *2*(SEP). https://doi.org/10.3389/fmicb.2011.00181

Zaragoza, O. (2019). Basic principles of the virulence of Cryptococcus. *Virulence*, *10*(1), 490–501. https://doi.org/10.1080/21505594.2019.1614383

Zaragoza, O., & Casadevall, A. (2004). Experimental modulation of capsule size in Cryptococcus neoformans. In *Biological Procedures Online* • (Vol. 6, Issue 1, pp. 10–15). www.biologicalprocedures.com

Zaragoza, O., Chrisman, C. J., Castelli, M. V., Frases, S., Cuenca-Estrella, M., Rodríguez-Tudela, J. L., & Casadevall, A. (2008). Capsule enlargement in Cryptococcus neoformans confers resistance to oxidative stress suggesting a mechanism for intracellular survival. *Cellular Microbiology*, *10*(10). https://doi.org/10.1111/j.1462-5822.2008.01186.x

Zaragoza, O., Telzak, A., Bryan, R. A., Dadachova, E., & Casadevall, A. (2006). The polysaccharide capsule of the pathogenic fungus Cryptococcus neoformans enlarges by distal growth and is rearranged during budding. *Molecular Microbiology*, *59*(1), 67–83. https://doi.org/10.1111/j.1365-2958.2005.04928.x

Zawia, A., Arnold, N. D., West, L., Pickworth, J. A., Turton, H., Iremonger, J., Braithwaite, A. T., Cañedo, J., Johnston, S. A., Thompson, A. A. R., Miller, G., & Lawrie, A. (2021). Altered Macrophage Polarization Induces Experimental Pulmonary Hypertension and Is Observed in Patients with Pulmonary Arterial Hypertension. *Arteriosclerosis, Thrombosis, and Vascular Biology*, *41*(1), 430–445. https://doi.org/10.1161/ATVBAHA.120.314639

Zhang, X., Edwards, J. P., & Mosser, D. M. (2009). The expression of exogenous genes in macrophages: Obstacles and opportunities. *Methods in Molecular Biology*, *531*, 123–143. https://doi.org/10.1007/978-1-59745-396-7_9

Zhu, L. L., Zhao, X. Q., Jiang, C., You, Y., Chen, X. P., Jiang, Y. Y., Jia, X. M., & Lin, X. (2013). C-type lectin receptors dectin-3 and dectin-2 form a heterodimeric pattern-recognition

receptor for host defense against fungal infection. *Immunity*, *39*(2), 324–334. https://doi.org/10.1016/j.immuni.2013.05.017

Zhu, Y. P., Padgett, L., Dinh, H. Q., Marcovecchio, P., Blatchley, A., Wu, R., Ehinger, E., Kim, C., Mikulski, Z., Seumois, G., Madrigal, A., Vijayanand, P., & Hedrick, C. C. (2018). Identification of an Early Unipotent Neutrophil Progenitor with Pro-tumoral Activity in Mouse and Human Bone Marrow. *Cell Reports*, *24*(9). https://doi.org/10.1016/j.celrep.2018.07.097

APPENDIX 1 : Ridge curvature profiling script by Dr. James Bradford

```java
10 import ij.ImagePlus;
11 import ij.IJ;
12 import ij.process.FloatPolygon;
13 import ij.gui.Roi;
14 import ij.gui.Plot;
15 import ij.measure.ResultsTable;
16 import ij.gui.OvalRoi;
17 import ij.plugin.frame.RoiManager;
18
19 //Get ROI and then get all coordinates
20 ImagePlus imp   = IJ.getImage();    //  get the active image
21 IJ.run(imp, "Interpolate", "interval=1 smooth"); // This does the smoothing
22 rm = RoiManager.getInstance();
23 if (rm==null) {
24     rm = new RoiManager();
25 }
26     rm.reset();
27
28 FloatPolygon r = imp.getRoi().getFloatPolygon();
29 rm.addRoi(imp.getRoi());
30
31 rt = new ResultsTable();
32
33 points = new ResultsTable();
34 for (int i = 0; i < r.npoints; ++i)
35 {
36     points.incrementCounter();
37     points.addValue("X", r.xpoints[i] );
38     points.addValue("Y", r.ypoints[i] );
39 }
40 points.show("XYPoints");
41
42
43 // First calculate unit vectors of each subunit
44 // Also get the length of each sub (dS), which we'll need later
45
46 double[][] unitVecs = new double[r.npoints-1][2];
47 double[] dS = new double[r.npoints-1];
48 for (int i = 0; i < r.npoints-1; ++i)
49 {
50     double dX = r.xpoints[i+1] - r.xpoints[i];
51     double dY = r.ypoints[i+1] - r.ypoints[i];
52     double mag = Math.sqrt(dX*dX + dY*dY);
53     dS[i] = mag;
54     unitVecs[i][0] = dX/mag;
55     unitVecs[i][1] = dY/mag;
56 }
57
58 // Then calculate tangent vectors for each point
59 double[][] tanVecs = new double[r.npoints-2][2];
60 for (int i = 1; i < r.npoints-1; ++i)
61 {
62     int j = i-1;
63     double mag = Math.sqrt((unitVecs[i][0]+unitVecs[i-1][0])*(unitVecs[i][0]+
  unitVecs[i-1][0]) + (unitVecs[i][1]+unitVecs[i-1][1])*(unitVecs[i][1]+unitVecs[i-1
  ][1]));
64     tanVecs[j][0] = (unitVecs[i][0]+unitVecs[i-1][0])/mag;
65     tanVecs[j][1] = (unitVecs[i][1]+unitVecs[i-1][1])/mag;
66 }
67
68 // Then convert to angles
69 double[] tanAngles = new double[r.npoints-2];
70 for (int i = 0; i < r.npoints-2; ++i)
71 {
```

```
72      tanAngles[i] = Math.atan2(tanVecs[i][1], tanVecs[i][0]);
73 }
74
75
76 // Then calculate the change in angles from one to next
77 double[] dAngs = new double[r.npoints-3];
78 for (int i = 0; i < r.npoints-3; ++i)
79 {
80          double dAng = tanAngles[i+1] - tanAngles[i];
81          dAng = dAng - 2*Math.PI*Math.floor(dAng/(2*Math.PI)+0.5);
   // keep to between 0 and 2pi
82      dAngs[i] = dAng;
83 }
84
85 // Then calculate the radius of curvatures
86 double[] Rs = new double[r.npoints-3];
87 int divZero = 0; // Counter for number of divZero errors skipped
88 for (int i = 0; i < r.npoints-3; ++i)
89 {
90      int j = i+1;
91          if (dAngs[i] != 0)
92          {
93              Rs[i] = dS[j]/dAngs[i];
94          }
95          else
96          {
97                  divZero = divZero + 1;
98          }
99 }
100
101 for (int i = 0; i < r.npoints-3-divZero; ++i)
102 {
103     rt.incrementCounter();
104
105     if (Rs[i] > 0)
106     {
107       rt.addValue("Positive Radius", Rs[i] );
108       rt.addValue("Negative Radius", "");
109       rt.addValue("Positive Curvature", 1.0/Rs[i] );
110       rt.addValue("Negative Curvature", "");
111
112     }
113     else
114     {
115       rt.addValue("Positive Radius", "");
116       rt.addValue("Negative Radius", Rs[i] );
117       rt.addValue("Positive Curvature", "");
118       rt.addValue("Negative Curvature", 1.0/Rs[i] );
119     }
120 }
121
122 rt.show("RadiusSummary");
123
```

APPENDIX 2 : Reprint permission for the journal article "Cellular trafficking of lipoteichoic acid and Toll-like receptor 2 in relation to signaling; role of CD14 and CD36"

JOHN WILEY AND SONS LICENSE
TERMS AND CONDITIONS

Aug 04, 2021

This Agreement between Mr. Jaime Cañedo ("You") and John Wiley and Sons ("John Wiley and Sons") consists of your license details and the terms and conditions provided by John Wiley and Sons and Copyright Clearance Center.

License Number	5121881243222
License date	Aug 04, 2021
Licensed Content Publisher	John Wiley and Sons
Licensed Content Publication	JOURNAL OF LEUKOCYTE BIOLOGY
Licensed Content Title	Cellular trafficking of lipoteichoic acid and Toll-like receptor 2 in relation to signaling; role of CD14 and CD36
Licensed Content Author	Terje Espevik, Oddmund Bakke, Egil Lien, et al
Licensed Content Date	May 5, 2008
Licensed Content Volume	84
Licensed Content Issue	1

Licensed Content Pages	12
Type of use	Dissertation/Thesis
Requestor type	University/Academic
Format	Print and electronic
Portion	Figure/table
Number of figures/tables	1
Will you be translating?	No
Title	Ultrastructural study of phagocytic membrane and the biophysics of phagocytosis (tentative)
Institution name	University of Sheffield
Expected presentation date	Oct 2021
Portions	Figure 6
Requestor Location	Mr. Jaime Cañedo
	Firth Court
	BMS, University of Sheffield
	Sheffield, South Yorkshire S10 2TN
	United Kingdom
	Attn: Mr. Jaime Cañedo
Publisher Tax ID	EU826007151
Total	0.00 GBP

Terms and Conditions

TERMS AND CONDITIONS

This copyrighted material is owned by or exclusively licensed to John Wiley & Sons, Inc. or one of its group companies (each a"Wiley Company") or handled on behalf of a society with which a Wiley Company has exclusive publishing rights in relation to a particular work (collectively "WILEY"). By clicking "accept" in connection with completing this licensing transaction, you agree that the following terms and conditions apply to this transaction (along with the billing and payment terms and conditions established by the Copyright Clearance Center Inc., ("CCC's Billing and Payment terms and conditions"), at the time that you opened your RightsLink account (these are available at any time at http://myaccount.copyright.com).

Terms and Conditions

- The materials you have requested permission to reproduce or reuse (the "Wiley Materials") are protected by copyright.

- You are hereby granted a personal, non-exclusive, non-sub licensable (on a standalone basis), non-transferable, worldwide, limited license to reproduce the Wiley Materials for the purpose specified in the licensing process. This license, **and any CONTENT (PDF or image file) purchased as part of your order,** is for a one-time use only and limited to any maximum distribution number specified in the license. The first instance of republication or reuse granted by this license must be completed within two years of the date of the grant of this license (although copies prepared before the end date may be distributed thereafter). The Wiley Materials shall not be used in any other manner or for any other purpose, beyond what is granted in the license. Permission is granted subject to an appropriate acknowledgement given to the author, title of the material/book/journal and the publisher. You shall also duplicate the copyright notice that appears in the Wiley publication in your use of the Wiley Material. Permission is also granted on the understanding that nowhere in the text is a previously published source acknowledged for all or part of this Wiley Material. Any third party content is expressly excluded from this permission.

- With respect to the Wiley Materials, all rights are reserved. Except as expressly granted by the terms of the license, no part of the Wiley Materials may be copied, modified, adapted (except for minor reformatting required by the new Publication), translated, reproduced, transferred or distributed, in any form or by any means, and no derivative works may be made based on the Wiley Materials without the prior permission of the respective copyright owner.**For STM Signatory Publishers clearing permission under the terms of the STM Permissions Guidelines only, the terms of the license are extended to include subsequent editions and for editions in other languages, provided such editions are for the work as a whole in situ and does not involve the separate exploitation of the permitted figures or extracts,** You may not alter, remove or suppress in any manner any copyright, trademark or other notices displayed by the Wiley Materials. You may not license,

rent, sell, loan, lease, pledge, offer as security, transfer or assign the Wiley Materials on a stand-alone basis, or any of the rights granted to you hereunder to any other person.

- The Wiley Materials and all of the intellectual property rights therein shall at all times remain the exclusive property of John Wiley & Sons Inc, the Wiley Companies, or their respective licensors, and your interest therein is only that of having possession of and the right to reproduce the Wiley Materials pursuant to Section 2 herein during the continuance of this Agreement. You agree that you own no right, title or interest in or to the Wiley Materials or any of the intellectual property rights therein. You shall have no rights hereunder other than the license as provided for above in Section 2. No right, license or interest to any trademark, trade name, service mark or other branding ("Marks") of WILEY or its licensors is granted hereunder, and you agree that you shall not assert any such right, license or interest with respect thereto

- NEITHER WILEY NOR ITS LICENSORS MAKES ANY WARRANTY OR REPRESENTATION OF ANY KIND TO YOU OR ANY THIRD PARTY, EXPRESS, IMPLIED OR STATUTORY, WITH RESPECT TO THE MATERIALS OR THE ACCURACY OF ANY INFORMATION CONTAINED IN THE MATERIALS, INCLUDING, WITHOUT LIMITATION, ANY IMPLIED WARRANTY OF MERCHANTABILITY, ACCURACY, SATISFACTORY QUALITY, FITNESS FOR A PARTICULAR PURPOSE, USABILITY,

  INTEGRATION OR NON-INFRINGEMENT AND ALL SUCH WARRANTIES ARE HEREBY EXCLUDED BY WILEY AND ITS LICENSORS AND WAIVED BY YOU.

- WILEY shall have the right to terminate this Agreement immediately upon breach of this Agreement by you.

- You shall indemnify, defend and hold harmless WILEY, its Licensors and their respective directors, officers, agents and employees, from and against any actual or threatened claims, demands, causes of action or proceedings arising from any breach of this Agreement by you.

- IN NO EVENT SHALL WILEY OR ITS LICENSORS BE LIABLE TO YOU OR ANY OTHER PARTY OR ANY OTHER PERSON OR ENTITY FOR ANY SPECIAL, CONSEQUENTIAL, INCIDENTAL, INDIRECT, EXEMPLARY OR PUNITIVE DAMAGES, HOWEVER CAUSED, ARISING OUT OF OR IN CONNECTION WITH THE DOWNLOADING, PROVISIONING, VIEWING OR USE OF THE MATERIALS REGARDLESS OF THE FORM OF ACTION, WHETHER FOR BREACH OF CONTRACT, BREACH OF WARRANTY, TORT, NEGLIGENCE, INFRINGEMENT OR OTHERWISE (INCLUDING, WITHOUT LIMITATION, DAMAGES BASED ON LOSS OF PROFITS, DATA, FILES, USE, BUSINESS OPPORTUNITY OR CLAIMS OF THIRD PARTIES), AND WHETHER OR NOT THE PARTY HAS BEEN ADVISED OF THE POSSIBILITY OF SUCH DAMAGES. THIS LIMITATION SHALL APPLY NOTWITHSTANDING ANY FAILURE OF ESSENTIAL PURPOSE OF ANY LIMITED REMEDY PROVIDED HEREIN.

- Should any provision of this Agreement be held by a court of competent jurisdiction to be illegal, invalid, or unenforceable, that provision shall be deemed amended to achieve as nearly as possible the same economic effect as the original provision, and the legality, validity and enforceability of the remaining provisions of this Agreement shall not be affected or impaired thereby.

- The failure of either party to enforce any term or condition of this Agreement shall not constitute a waiver of either party's right to enforce each and every term and condition of this Agreement. No breach under this agreement shall be deemed waived or excused by either party unless such waiver or consent is in writing signed by the party granting such waiver or consent. The waiver by or consent of a party to a breach of any provision of this Agreement shall not operate or be construed as a waiver of or consent to any other or subsequent breach by such other party.

- This Agreement may not be assigned (including by operation of law or otherwise) by you without WILEY's prior written consent.

- Any fee required for this permission shall be non-refundable after thirty (30) days from receipt by the CCC.

- These terms and conditions together with CCC's Billing and Payment terms and conditions (which are incorporated herein) form the entire agreement between you and WILEY concerning this licensing transaction and (in the absence of fraud) supersedes all prior agreements and representations of the parties, oral or written. This Agreement may not be amended except in writing signed by both parties. This Agreement shall be binding upon and inure to the benefit of the parties' successors, legal representatives, and authorized assigns.

- In the event of any conflict between your obligations established by these terms and conditions and those established by CCC's Billing and Payment terms and conditions, these terms and conditions shall prevail.

- WILEY expressly reserves all rights not specifically granted in the combination of (i) the license details provided by you and accepted in the course of this licensing transaction, (ii) these terms and conditions and (iii) CCC's Billing and Payment terms and conditions.

- This Agreement will be void if the Type of Use, Format, Circulation, or Requestor Type was misrepresented during the licensing process.

- This Agreement shall be governed by and construed in accordance with the laws of the State of New York, USA, without regards to such state's conflict of law rules. Any legal action, suit or proceeding arising out of or relating to these Terms and Conditions or the breach thereof shall be instituted in a court of competent jurisdiction in New York County in the State of New York in the United States of America and each party hereby consents and submits to the personal jurisdiction of such court, waives any objection to venue in such court and consents to service of process by registered or certified mail, return receipt requested, at the last known address of such party.

WILEY OPEN ACCESS TERMS AND CONDITIONS

Wiley Publishes Open Access Articles in fully Open Access Journals and in Subscription journals offering Online Open. Although most of the fully Open Access journals publish open access articles under the terms of the Creative Commons Attribution (CC BY) License only, the subscription journals and a few of the Open Access Journals offer a choice of Creative Commons Licenses. The license type is clearly identified on the article.

The Creative Commons Attribution License

The Creative Commons Attribution License (CC-BY) allows users to copy, distribute and transmit an article, adapt the article and make commercial use of the article. The CC-BY license permits commercial and non-

Creative Commons Attribution Non-Commercial License

The Creative Commons Attribution Non-Commercial (CC-BY-NC)License permits use, distribution and reproduction in any medium, provided the original work is properly cited and is not used for commercial purposes.(see below)

Creative Commons Attribution-Non-Commercial-NoDerivs License

The Creative Commons Attribution Non-Commercial-NoDerivs License (CC-BY-NC-ND) permits use, distribution and reproduction in any medium, provided the original work is properly cited, is not used for commercial purposes and no modifications or adaptations are made. (see below)

Use by commercial "for-profit" organizations

Use of Wiley Open Access articles for commercial, promotional, or marketing purposes requires further explicit permission from Wiley and will be subject to a fee.

Further details can be found on Wiley Online Library
http://olabout.wiley.com/WileyCDA/Section/id-410895.html

Other Terms and Conditions:

v1.10 Last updated September 2015

Questions? customercare@copyright.com or +1-855-239-3415 (toll free in the US) or +1-978-646-2777.

APPENDIX 3 : Reprint permission for the journal article "*Cryptococcus neoformans* capsular polysaccharides form branched and complex filamentous networks viewed by high-resolution microscopy"

ELSEVIER LICENSE
TERMS AND CONDITIONS

Aug 04, 2021

This Agreement between Mr. Jaime Cañedo ("You") and Elsevier ("Elsevier") consists of your license details and the terms and conditions provided by Elsevier and Copyright Clearance Center.

License Number	5121920409905
License date	Aug 04, 2021
Licensed Content Publisher	Elsevier
Licensed Content Publication	Journal of Structural Biology
Licensed Content Title	Cryptococcus neoformans capsular polysaccharides form branched and complex filamentous networks viewed by highresolution microscopy
Licensed Content Author	Glauber R. de S. Araújo,Giselle N. Fontes,Daniela Leão,Gustavo Miranda Rocha,Bruno Pontes,Celso Sant'Anna,Wanderley de Souza,Susana Frases
Licensed Content Date	Jan 1, 2016
Licensed Content Volume	193
Licensed Content Issue	1

Licensed Content Pages	8
Start Page	75
End Page	82
Type of Use	reuse in a thesis/dissertation
Portion	figures/tables/illustrations
Number of figures/tables/illustrations	1
Format	both print and electronic
Are you the author of this Elsevier article?	No
Will you be translating?	No
Title	Ultrastructural study of phagocytic membrane and the biophysics of phagocytosis (tentative)
Institution name	University of Sheffield
Expected presentation date	Oct 2021
Portions	Figure 2. Helium Ion Microscopy (HIM) of the Cryptococcus neoformans polysaccharide capsule.

Requestor Location	Mr. Jaime Cañedo
	Firth Court
	BMS, University of Sheffield
	Sheffield, South Yorkshire S10 2TN
	United Kingdom
	Attn: Mr. Jaime Cañedo
Publisher Tax ID	GB 494 6272 12
Total	0.00 GBP

Terms and Conditions

INTRODUCTION

1. The publisher for this copyrighted material is Elsevier. By clicking "accept" in connection with completing this licensing transaction, you agree that the following terms and conditions apply to this transaction (along with the Billing and Payment terms and conditions established by Copyright Clearance Center, Inc. ("CCC"), at the time that you opened your Rightslink account and that are available at any time at http://myaccount.copyright.com).

GENERAL TERMS

2.   Elsevier hereby grants you permission to reproduce the aforementioned material subject tothe terms and conditions indicated.

3.   Acknowledgement: If any part of the material to be used (for example, figures) hasappeared in our publication with credit or acknowledgement to another source, permission must also be sought from that source. If such permission is not obtained then that material may not be included in your publication/copies. Suitable acknowledgement to the source must be made, either as a footnote or in a reference list at the end of your publication, as follows:

"Reprinted from Publication title, Vol /edition number, Author(s), Title of article / title of chapter, Pages No., Copyright (Year), with permission from Elsevier [OR APPLICABLE SOCIETY COPYRIGHT OWNER]." Also Lancet special credit - "Reprinted from The Lancet, Vol. number, Author(s), Title of article, Pages No., Copyright (Year), with permission from Elsevier."

4.   Reproduction of this material is confined to the purpose and/or media for whichpermission is hereby given.

5.   Altering/Modifying Material: Not Permitted. However figures and illustrations may bealtered/adapted minimally to serve your work. Any other abbreviations, additions, deletions and/or any other alterations shall be made only with prior written authorization

of Elsevier Ltd. (Please contact Elsevier's permissions helpdesk [here](#)). No modifications can be made to any Lancet figures/tables and they must be reproduced in full.

6.   If the permission fee for the requested use of our material is waived in this instance,please be advised that your future requests for Elsevier materials may attract a fee.

7.   Reservation of Rights: Publisher reserves all rights not specifically granted in thecombination of (i) the license details provided by you and accepted in the course of this licensing transaction, (ii) these terms and conditions and (iii) CCC's Billing and Payment terms and conditions.

8.   License Contingent Upon Payment: While you may exercise the rights licensedimmediately upon issuance of the license at the end of the licensing process for the transaction, provided that you have disclosed complete and accurate details of your proposed use, no license is finally effective unless and until full payment is received from you (either by publisher or by CCC) as provided in CCC's Billing and Payment terms and conditions. If full payment is not received on a timely basis, then any license preliminarily granted shall be deemed automatically revoked and shall be void as if never granted. Further, in the event that you breach any of these terms and conditions or any of CCC's Billing and Payment terms and conditions, the license is automatically revoked and shall be void as if never granted. Use of materials as described in a revoked license, as well as any use of the materials beyond the scope of an unrevoked license, may constitute copyright infringement and publisher reserves the right to take any and all action to protect its copyright in the materials.

9.   Warranties: Publisher makes no representations or warranties with respect to the licensedmaterial.

10.   Indemnity: You hereby indemnify and agree to hold harmless publisher and CCC, andtheir respective officers, directors, employees and agents, from and against any and all claims arising out of your use of the licensed material other than as specifically authorized pursuant to this license.

11.   No Transfer of License: This license is personal to you and may not be sublicensed,assigned, or transferred by you to any other person without publisher's written permission.

12.   No Amendment Except in Writing: This license may not be amended except in a writingsigned by both parties (or, in the case of publisher, by CCC on publisher's behalf).

13.   Objection to Contrary Terms: Publisher hereby objects to any terms contained in anypurchase order, acknowledgment, check endorsement or other writing prepared by you, which terms are inconsistent with these terms and conditions or CCC's Billing and Payment terms and conditions. These terms and conditions, together with CCC's Billing and Payment terms and conditions (which are incorporated herein), comprise the entire agreement between you and publisher (and CCC) concerning this licensing transaction. In the event of any conflict between your obligations established by these terms and conditions and those established by CCC's Billing and Payment terms and conditions, these terms and conditions shall control.

14.   Revocation: Elsevier or Copyright Clearance Center may deny the permissions describedin this License at their sole discretion, for any reason or no reason, with a full

refund payable to you. Notice of such denial will be made using the contact information provided by you. Failure to receive such notice will not alter or invalidate the denial. In no event will Elsevier or Copyright Clearance Center be responsible or liable for any costs, expenses or damage incurred by you as a result of a denial of your permission request, other than a refund of the amount(s) paid by you to Elsevier and/or Copyright Clearance Center for denied permissions.

LIMITED LICENSE

The following terms and conditions apply only to specific license types:

15. **Translation**: This permission is granted for non-exclusive world **English** rights only unless your license was granted for translation rights. If you licensed translation rights you may only translate this content into the languages you requested. A professional translator must perform all translations and reproduce the content word for word preserving the integrity of the article.

16. **Posting licensed content on any Website**: The following terms and conditions apply as follows: Licensing material from an Elsevier journal: All content posted to the web site must maintain the copyright information line on the bottom of each image; A hyper-text must be included to the Homepage of the journal from which you are licensing at http://www.sciencedirect.com/science/journal/xxxxx or the Elsevier homepage for books at http://www.elsevier.com; Central Storage: This license does not include permission for a scanned version of the material to be stored in a central repository such as that provided by Heron/XanEdu.

Licensing material from an Elsevier book: A hyper-text link must be included to the Elsevier homepage at http://www.elsevier.com . All content posted to the web site must maintain the copyright information line on the bottom of each image.

Posting licensed content on Electronic reserve: In addition to the above the following clauses are applicable: The web site must be password-protected and made available only to bona fide students registered on a relevant course. This permission is granted for 1 year only. You may obtain a new license for future website posting.

17. **For journal authors:** the following clauses are applicable in addition to the above:

Preprints:

A preprint is an author's own write-up of research results and analysis, it has not been peerreviewed, nor has it had any other value added to it by a publisher (such as formatting, copyright, technical enhancement etc.).

Authors can share their preprints anywhere at any time. Preprints should not be added to or enhanced in any way in order to appear more like, or to substitute for, the final versions of articles however authors can update their preprints on arXiv or RePEc with their Accepted Author Manuscript (see below).

If accepted for publication, we encourage authors to link from the preprint to their formal publication via its DOI. Millions of researchers have access to the formal publications on ScienceDirect, and so links will help users to find, access, cite and use the best available

version. Please note that Cell Press, The Lancet and some society-owned have different preprint policies. Information on these policies is available on the journal homepage.

Accepted Author Manuscripts: An accepted author manuscript is the manuscript of an article that has been accepted for publication and which typically includes authorincorporated changes suggested during submission, peer review and editor-author communications.

Authors can share their accepted author manuscript:

- immediately via their non-commercial person homepage or blog by
  - updating a preprint in arXiv or RePEc with the accepted manuscript via
  - their research institute or institutional repository for internal
  - institutional uses or as part of an invitation-only research collaboration work-group directly by providing copies to their students or to research collaborators for their personal use
  - for private scholarly sharing as part of an invitation-only work group on commercial sites with which Elsevier has an agreement
- After the embargo period via non-commercial hosting platforms such as their
  - institutional repository via commercial sites with which Elsevier has an
  - agreement

In all cases accepted manuscripts should:

- link to the formal publication via its DOI
- bear a CC-BY-NC-ND license - this is easy to
- do

  if aggregated with other manuscripts, for example in a repository or other site, be shared in alignment with our hosting policy not be added to or enhanced in any way to appear more like, or to substitute for, the published journal article.

Published journal article (JPA): A published journal article (PJA) is the definitive final record of published research that appears or will appear in the journal and embodies all value-adding publishing activities including peer review co-ordination, copy-editing, formatting, (if relevant) pagination and online enrichment.

Policies for sharing publishing journal articles differ for subscription and gold open access articles:

Subscription Articles: If you are an author, please share a link to your article rather than the full-text. Millions of researchers have access to the formal publications on ScienceDirect, and so links will help your users to find, access, cite, and use the best available version.

Theses and dissertations which contain embedded PJAs as part of the formal submission can be posted publicly by the awarding institution with DOI links back to the formal publications on ScienceDirect.

If you are affiliated with a library that subscribes to ScienceDirect you have additional private sharing rights for others' research accessed under that agreement. This includes use for classroom teaching and internal training at the institution (including use in course packs and courseware programs), and inclusion of the article for grant funding purposes.

Gold Open Access Articles: May be shared according to the author-selected end-user license and should contain a CrossMark logo, the end user license, and a DOI link to the formal publication on ScienceDirect.

Please refer to Elsevier's posting policy for further information.

18.   **For book authors** the following clauses are applicable in addition to the above: Authors are permitted to place a brief summary of their work online only. You are not allowed to download and post the published electronic version of your chapter, nor may you scan the printed edition to create an electronic version. **Posting to a repository:** Authors are permitted to post a summary of their chapter only in their institution's repository.

19.   **Thesis/Dissertation**: If your license is for use in a thesis/dissertation your thesis may be submitted to your institution in either print or electronic form. Should your thesis be published commercially, please reapply for permission. These requirements include permission for the Library and Archives of Canada to supply single copies, on demand, of the complete thesis and include permission for Proquest/UMI to supply single copies, on demand, of the complete thesis. Should your thesis be published commercially, please reapply for permission. Theses and dissertations which contain embedded PJAs as part of the formal submission can be posted publicly by the awarding institution with DOI links back to the formal publications on ScienceDirect.

Elsevier Open Access Terms and Conditions

You can publish open access with Elsevier in hundreds of open access journals or in nearly 2000 established subscription journals that support open access publishing. Permitted third party re-use of these open access articles is defined by the author's choice of Creative Commons user license. See our open access license policy for more information.

Terms & Conditions applicable to all Open Access articles published with Elsevier:

Any reuse of the article must not represent the author as endorsing the adaptation of the article nor should the article be modified in such a way as to damage the author's honour or reputation. If any changes have been made, such changes must be clearly indicated.

The author(s) must be appropriately credited and we ask that you include the end user license and a DOI link to the formal publication on ScienceDirect.

If any part of the material to be used (for example, figures) has appeared in our publication with credit or acknowledgement to another source it is the responsibility of the user to ensure their reuse complies with the terms and conditions determined by the rights holder.

Additional Terms & Conditions applicable to each Creative Commons user license:

CC BY: The CC-BY license allows users to copy, to create extracts, abstracts and new works from the Article, to alter and revise the Article and to make commercial use of the Article (including reuse and/or resale of the Article by commercial entities), provided the user gives appropriate credit (with a link to the formal publication through the relevant DOI), provides a link to the license, indicates if changes were made and the licensor is not represented as endorsing the use made of the work. The full details of the license are available at http://creativecommons.org/licenses/by/4.0.

CC BY NC SA: The CC BY-NC-SA license allows users to copy, to create extracts, abstracts and new works from the Article, to alter and revise the Article, provided this is not done for commercial purposes, and that the user gives appropriate credit (with a link to the formal publication through the relevant DOI), provides a link to the license, indicates if changes were made and the licensor is not represented as endorsing the use made of the work. Further, any new works must be made available on the same conditions. The full details of the license are available at http://creativecommons.org/licenses/by-nc-sa/4.0.

CC BY NC ND: The CC BY-NC-ND license allows users to copy and distribute the Article, provided this is not done for commercial purposes and further does not permit distribution of the Article if it is changed or edited in any way, and provided the user gives appropriate credit (with a link to the formal publication through the relevant DOI), provides a link to the license, and that the licensor is not represented as endorsing the use made of the work. The full details of the license are available at http://creativecommons.org/licenses/by-nc-nd/4.0. Any commercial reuse of Open Access articles published with a CC BY NC SA or CC BY NC ND license requires permission from Elsevier and will be subject to a fee.

Commercial reuse includes:

- Associating advertising with the full text of the Article
- Charging fees for document delivery or access
- Article aggregation
- Systematic distribution via e-mail lists or share buttons

Posting or linking by commercial companies for use by customers of those companies.

20. **Other Conditions**:

v1.10

Questions? **customercare@copyright.com** or **+1-855-239-3415 (toll free in the US) or +1-978-646-2777.**